



Norwegian University of  
Science and Technology

# Modelling of Window Glasses Exposed to Blast Loading

**Kristoffer Aune Brekken**  
**Petter Tønsberg Ingier**

Master of Science in Mechanical Engineering

Submission date: June 2016

Supervisor: Tore Børvik, KT

Co-supervisor: Odd Sture Hopperstad, KT

Norwegian University of Science and Technology  
Department of Structural Engineering





## MASTER THESIS 2016

SUBJECT AREA: Computational Mechanics	DATE: June 10, 2016	NO. OF PAGES: 10 + 168 + 16
--	------------------------	--------------------------------

TITLE:

### **Modelling of window glasses exposed to blast loading**

Modellering av vindusglass utsatt for eksplosjonslast

BY:

Kristoffer Aune Brekken  
Petter Tønsberg Ingier



SUMMARY:

Failure of window glasses in buildings subjected to blast loading introduces great potential for casualties and structural damage, primarily by the creation high velocity glass fragments. The application of laminated security glazing mitigates the risk in blast load scenarios by reducing the size and number of glass fragments projected from window panes. Glass is used extensively in building façades, and in order to design safer buildings, an improved understanding of the complex phenomenon of blast loaded window panes is needed.

In the work of this thesis, material tests to determine elastic behaviour and stochastic dispersion of failure strength in monolithic glass, were carried out. Blast tests in the shock tube facility at SIMLab on monolithic and laminated glass panes, have been conducted to study behaviour of glass exposed to blast loading. Point-tracking with DIC was used to determine deflection of glass panes and variations in boundary conditions. In addition, experiments to research boundary conditions in blast experiments were conducted.

Non-linear explicit simulations of material and blast tests have been conducted in the finite element code LS-DYNA. Material models with and without stochastic distribution of failure criteria have been used to model failure response in laminated and monolithic glass by element erosion. Numerical and experimental results have been compared, with emphasis on capturing the stochastic distribution of failure strength and fragmentation found in glass.

Good correlations between numerical simulations and material tests on elastic and failure strength for glass was found. Numerical models of blast tests were able to describe fragmentation and a stochastic distribution in material strength. However, the exact capacity of the tested monolithic and laminated glass were not captured in simulations.

RESPONSIBLE TEACHER:	Professor Tore Børvik
SUPERVISORS:	Professor Tore Børvik, PhD candidate Karoline Osnes, Professor Odd Sture Hopperstad
CARRIED OUT AT:	Department of Structural Engineering, NTNU





## MASTEROPPGAVE 2016

FAGOMRÅDE: Beregningsmekanikk	DATO: 10. juni, 2016	ANTALL SIDER: 10 + 168 + 16
----------------------------------	-------------------------	--------------------------------

TITTEL:

### **Modellering av vindusglass utsatt for eksplosjonslast**

Modelling of window glasses exposed to blast loading

UTFØRT AV:

Kristoffer Aune Brekken  
Petter Tønsberg Ingier



SAMMENDRAG:

Knusning av vindusglass i bygninger utsatt for eksplosjonslast utgjør en stor risiko for skade på mennesker og bygninger. Bruk av laminert sikkerhetsglass reduserer risikoen for skader ved å redusere størrelsen og antallet på fragmentene fra glasset når det knuser. Vindusglass brukes ofte i bygningsfasader, og forståelse av oppførselen til glass utsatt for eksplosjonslast er derfor viktig for å kunne optimere designet av sikre bygninger.

I denne masteroppgaven er det utført materialforsøk for å bestemme den elastiske oppførselen og bruddstyrken til monolittisk glass. Eksplosjonsforsøk er utført i SIMLab sitt sjokkrør på monolittiske og laminerte glassruter for å studere oppførselen til glass utsatt for eksplosjonslast. Punkt-søking med DIC har blitt benyttet for å bestemme glassets forskyvning og variasjoner i randbetingelser. Forsøk for å undersøke randbetingelser i eksplosjonsforsøk har blitt gjort.

Ikke-lineære eksplisitte simuleringer av material- og eksplosjonsforsøk har blitt gjennomført ved bruk av elementmetodeprogrammet LS-DYNA. Materialmodeller med og uten stokastisk fordeling av bruddkriterier har blitt benyttet for å modellere brudd i monolittisk og laminert glass, ved bruk av elementerosjon. Numeriske resultater har blitt sammenlignet med forsøksresultater, med fokus på beskrivelse av stokastisk fordeling av bruddstyrke og fragmentering funnet i glass.

En god numerisk beskrivelse av elastisk oppførsel og bruddstyrke i glass sammenlignet med materialforsøk ble funnet. De numeriske modellene av eksplosjonsforsøkene klarte å beskrive fragmentering og en stokastisk fordeling av bruddstyrken, men den nøyaktige kapasiteten til glasset som ble testet i eksplosjonsforsøk ble ikke gjenskapt på en god måte med numeriske modeller.

FAGLÆRER:	Professor Tore Børvik
VEILEDERE:	Professor Tore Børvik, PhD kandidat Karoline Osnes, Professor Odd Sture Hopperstad
UTFØRT VED:	Institutt for konstruksjonsteknikk, NTNU



## **MASTER'S THESIS 2016**

for

*Kristoffer A. Brekken and Petter T. Ingier*

# **Modelling of window glasses exposed to blast loading**

### **1. INTRODUCTION**

Annealed float glass is often used in windows, but is a brittle material that offers little resistance to the intense blast waves produced by explosions. When the window fails, it breaks into a number of sharp fragments that can travel at high velocities. Laminated glass has been found to mitigate the risk of flying glass fragments by retaining them on a polymer interlayer upon fracture. It is, however, important to fully understand the conditions for and the types of failure mechanisms in both annealed glass and laminated glass to be able to optimise the design of façades against blast loading. The modelling of blast-exposed structural components, including glass, has received considerable attention in recent years. In regards to the new government building complex in Oslo, safety glasses and façades are of major concern in the case of a possible new blast event, and the research on the behaviour of glass is therefore of great interest.

### **2. OBJECTIVES**

The main objective of this research project is to determine how annealed and laminated glass will behave under blast loading. Numerical models will be made to examine the response of annealed and laminated glass exposed to blast loading. Blast experiments will be performed to validate the numerical models and to examine to which extent they can predict the qualitative response of the glasses. Only PVB as polymer layer will be tested.

### **3. A SHORT DESCRIPTION OF THE RESEARCH PROJECT**

The main topics in the research project will be as follows;

1. A literature review should be conducted to understand the blast load phenomenon, blast load design and shock tube test facilities. In addition, constitutive and failure modeling of glass and the polymer materials (PVB) exposed to extreme loadings should be reviewed.
2. Constitutive relations and failure criteria are chosen and calibrated based on material tests and literature results.
3. The SIMLab Shock Tube Facility will be used to expose the glasses to blast loading, as an alternative to explosive detonations. The shock tube experiments will be used to investigate typical dynamic responses and failure modes of the glasses exposed to blast loading.
4. Digital Image Correlation (DIC) will be used in the shock tube experiments.
5. Non-linear FE numerical simulations of the material and shock tube experiments will be performed, and the numerical results shall be compared and discussed based on the experimental findings.

*Supervisors:* Tore Børvik (NTNU), Karoline Osnes (NTNU) and Odd Sture Hopperstad (NTNU).

The thesis must be written according to current requirements and submitted to the Department of Structural Engineering, NTNU, no later than June 10<sup>th</sup>, 2016.

NTNU, January 15<sup>th</sup>, 2016.



Tore Børvik  
Professor





---

# Abstract

Failure of window glasses in buildings subjected to blast loading introduces great potential for casualties and structural damage, primarily by the creation high velocity glass fragments. The application of laminated security glazing mitigates the risk in blast load scenarios by reducing the size and number of glass fragments projected from window panes. Glass is used extensively in building façades, and in order to design safer buildings, an improved understanding of the complex phenomenon of blast loaded window panes is needed.

In the work of this thesis, material tests to determine elastic behaviour and stochastic dispersion of failure strength in monolithic glass, were carried out. Blast tests in the shock tube facility at SIMLab on monolithic and laminated glass panes, have been conducted to study behaviour of glass exposed to blast loading. Point-tracking with DIC was used to determine deflection of glass panes and variations in boundary conditions. In addition, experiments to research boundary conditions in blast experiments were conducted.

Non-linear explicit simulations of material and blast tests have been conducted in the finite element code LS-DYNA. Material models with and without stochastic distribution of failure criteria have been used to model failure response in laminated and monolithic glass by element erosion. Numerical and experimental results have been compared, with emphasis on capturing the stochastic distribution of failure strength and fragmentation found in glass.

Good correlations between numerical simulations and material tests on elastic and failure strength for glass was found. Numerical models of blast tests were able to describe fragmentation and a stochastic distribution in material strength. However, the exact capacity of the tested monolithic and laminated glass were not captured in simulations.

---

---

# Acknowledgements

This MSc thesis is written in the period between 15<sup>th</sup> of January and 10<sup>th</sup> of June 2015 for the research group Structural Impact Laboratory (SIMLab) at the Department of Structural Engineering – Norwegian University of Science and Technology (NTNU). The thesis was initiated by the Centre for Advanced Structural Analysis (CASA) which is a Center for Research-based Innovation (CRI) appointed by the Research Council of Norway.

We would like to express our special thanks to our project supervisors Professor Tore Børvik, PhDc Karoline Osnes and Professor Odd Sture Hopperstad for their invaluable weekly guidance and assistance when needed.

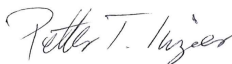
Special appreciation is given to Mr. Trond Auestad and Mr. Tore Wisth from CRI-CASA for their contributions and assistance during the experimental work.

Our sincere thanks go to Dr. Torodd Berstad for truly invaluable assistance in the compiling of several LS-DYNA solvers at our request, to PhDc Vegard Aune for extensive knowledge on the shock tube facility, Dr. Egil Fagerholt for assistance in the use of the DIC software eCorr and John Fredrick Berntsen for an introduction in the use of LS-DYNA.

Additionally we would like express our gratitude to CASA for the extensive funding of this project.

Finally, we would like to thank our fellow students Marcus Løken and Henrik Granum for endless discussions and precious input, and our families who have offered their support, critique and thoughts.

Trondheim, 10<sup>th</sup> June, 2016



Petter Tønsberg Ingier



Kristoffer Aune Brekken

---

# Contents

<b>Abstract</b>	<b>i</b>
<b>Contents</b>	<b>vii</b>
<b>Nomenclature</b>	<b>viii</b>
<b>1 Introduction</b>	<b>1</b>
<b>2 Theoretical background</b>	<b>5</b>
2.1 Blast Mechanics . . . . .	5
2.2 Ideal Shock Tube Theory . . . . .	7
2.3 Fracture mechanics . . . . .	10
2.3.1 Atomistic view of fracture . . . . .	10
2.3.2 Griffith energy balance and energy release rate . . . . .	12
2.3.3 Stress analysis of cracks . . . . .	13
2.4 Statistical treatment of strength in brittle materials . . . . .	15
2.4.1 The Weibull distribution . . . . .	15
2.4.2 Weakest link theory . . . . .	16
2.5 Beam theory . . . . .	17
2.5.1 Euler-Bernoulli beam theory . . . . .	17
2.5.2 Application to bend testing . . . . .	18
2.6 Digital Image Correlation . . . . .	19
<b>3 Materials and material modelling</b>	<b>21</b>
3.1 Materials . . . . .	21
3.1.1 Ceramics . . . . .	21
3.1.2 Glass . . . . .	22
3.1.3 Float glass production . . . . .	23
3.1.4 Laminated glass . . . . .	23
3.2 Material modelling . . . . .	26
3.2.1 LS-DYNA Material Models . . . . .	26

---

3.2.2	SimLab Material Models . . . . .	28
3.3	Stochastic distribution of failure parameters . . . . .	32
3.4	State of the Art . . . . .	35
3.4.1	Material Modelling . . . . .	35
3.4.2	Contact Modelling . . . . .	37
<b>4</b>	<b>Bending tests</b>	<b>39</b>
4.1	Four point bending test . . . . .	39
4.1.1	Setup . . . . .	39
4.1.2	Results . . . . .	42
4.2	Three point bending tests . . . . .	46
4.2.1	Setup . . . . .	46
4.2.2	Results . . . . .	49
<b>5</b>	<b>Blast experiment</b>	<b>53</b>
5.1	The Shock Tube at SIMLab . . . . .	53
5.2	Experimental setup . . . . .	54
5.3	Experimental results . . . . .	58
5.3.1	Monolithic glass . . . . .	58
5.3.2	Laminated glass . . . . .	67
5.3.3	Validation of DIC-measurements . . . . .	75
5.3.4	Boundary conditions . . . . .	77
5.3.5	Design aspects . . . . .	80
<b>6</b>	<b>Numerical modelling: Four point bending test</b>	<b>83</b>
6.1	Numerical model . . . . .	83
6.2	Preliminary study . . . . .	84
6.2.1	Young's modulus . . . . .	84
6.2.2	Loading speed . . . . .	86
6.3	Results with Elastic material with simple erosion criterion . . . . .	87
6.3.1	Effect of mesh size . . . . .	87
6.3.2	Effect of critical stress . . . . .	90
6.3.3	Effect of number of failure integration points . . . . .	90
6.3.4	Solid elements . . . . .	91
6.3.5	Results with Johnson–Holmquist 2 material model . . . . .	95
6.3.6	Effect of mesh size . . . . .	96
6.3.7	Effect of plastic failure strain . . . . .	97
6.4	Results with SIMLab Metal Model . . . . .	98
6.4.1	Comparison with <i>MAT_001</i> . . . . .	98
6.4.2	Effect of number of failure integration points . . . . .	98
6.4.3	Stochastic distribution of failure criterion . . . . .	101
6.4.4	Uncoupled stochastic distribution of failure criterion . . . . .	105
6.5	Results with SIMLab Brittle Materials Model . . . . .	107
6.6	Summary and Discussion . . . . .	109
<b>7</b>	<b>Numerical modelling: Blast tests</b>	<b>111</b>

---

---

7.1	Monolithic Glass . . . . .	111
7.1.1	Numerical Model . . . . .	111
7.1.2	Elastic response . . . . .	112
7.1.3	Failure response . . . . .	118
7.1.4	Summary and Discussion . . . . .	135
7.2	Laminated glass . . . . .	137
7.2.1	Numerical Model . . . . .	137
7.2.2	Elastic response . . . . .	138
7.2.3	Failure response . . . . .	143
7.2.4	Simulation vs Experiment . . . . .	155
7.2.5	Summary and Discussion . . . . .	157
<b>8</b>	<b>Concluding Remarks</b>	<b>159</b>
<b>9</b>	<b>Further work</b>	<b>163</b>
	<b>Bibliography</b>	<b>165</b>
	<b>Appendix A Material tests specimen size</b>	<b>A1</b>
	<b>Appendix B Bending test specimens post-failure</b>	<b>B1</b>
	<b>Appendix C Weibull plots for medium and large specimens</b>	<b>C1</b>
	<b>Appendix D Component test overview</b>	<b>D1</b>
	<b>Appendix E LS-DYNA Keywords</b>	<b>E1</b>

---

# Nomenclature

The following nomenclature list provides a general overview of the notation used throughout the report. Be aware that some symbols are given multiple definitions in order to follow notation established in literature.

## Abbreviations

CPU	Central Processing Unit
DIC	Digital Image Correlation
DOF	Degree(s) of Freedom
FE	Finite Element
FEA	Finite Element Analysis
FEM	Finite Element Method
JH-2	Johnson–Holmquist 2 material model
LEFM	Linear Elastic Fracture Mechanics
LG	Laminated Glass
NCPU	Number of CPUs
NOE	Number of Elements
MG	Monolithic Glass
MS	Material Structure
PVB	Polyvinyl butyral
SIMLab	Structural Impact Laboratory
SBMM	SIMLab Brittle Material Model
SMM	SIMLab Metal Model
3PB	Three point bending
4PB	Four point bending



---

## Latin symbols

A	Cross sectional area
$A_e$	Fracture area
B	Plate thickness
b	Exponential decaying coefficient
D	Damage evolution
E	Youngs's modulus, total energy
$E_b$	Bonding energy
F	Cumulative probability distribution function
f	Probability density function
G	Energy release rate
$G_c$	Critical energy release rate
$G_f$	Fracture energy
I	Second moment of area in beam theory
$i_{r+}$	Specific impulse of the positive phase
$K_{Ic}$	Critical stress intensity factor, mode I
m	Weibull modulus
P	Pressure as a function of time, force needed to separate atoms in a molecule
$P_a$	Driver, firing pressure
$P_{atm}$	Atmospheric pressure
$P_f$	Probability of failure
$P_r$	Peak reflected pressure
$P_{so}$	Peak incident overpressure
q	Applied load
R	Rarefaction waves
s	Cross head speed
$t_+$	Duration of positive phase
$t_-$	Duration of negative phase
$t_a$	Arrival time of shock wave
V	Volume
$V_0$	Reference volume
$V_e$	Element volume
$W_s$	Work required to generate new surfaces
$x_0$	Equilibrium spacing

---

## Greek symbols

$\alpha$	Scale parameter in weibull distribution
$\beta$	Shape parameter in weibull distribution
$\Delta_c$	Deflection at centre of beam
$\Delta t_c$	Critical time interval
$\Delta G_f$	Post-failure fracture energy
$\varepsilon$	Strain
$\varepsilon_D$	Equivalent deformation measure
$\dot{\varepsilon}$	Strain rate
$\gamma_s$	Surface energy required to form one unit area of crack
$\kappa$	Curvature of beam subjected to bending, history variable in SBMM
$\lambda$	Distance to overcome interatomic bonding energy
$\nu$	Poisson's ratio
$\Pi$	Potential energy
$\rho$	Density, curvature at the major axis tip of elliptical hole
$\sigma_A$	Stress at tip of major axis of elliptical hole
$\sigma_I$	Principal stress
$\sigma_0$	Characteristic strength
$\sigma_c$	Cohesive stress, critical stress
$\sigma_f$	Failure stress
$\sigma_n$	Normal stress at interface between PVB and glass
$\sigma_s$	Shear stress at interface between PVB and glass

# Chapter 1

## Introduction

The 22<sup>nd</sup> of July 2011, a terrorist bomb detonated at the Governmental building complex in Oslo. Eight people were killed instantly, ten people were hospitalized with major injuries and at least 200 people received minor injuries. It was later found that one of the main reasons for casualties and injuries was the breakage and fragmentation of ordinary window glass in building façades, and that casualties were prevented in buildings equipped with security glazing [1]. Figure 1.1 shows the Executive Government Building after the attack. Figure 1.2 shows detonation of the car bomb and large amounts of glass fragments falling from one of the adjacent buildings.



**Figure 1.1:** Executive Government Building after the terrorist attack 22<sup>nd</sup> of July 2011 [1].



**Figure 1.2:** Detonation of the car bomb, and glass fragments falling from one of the buildings [1].

Modern buildings utilize glass extensively in façades, and in order to design safer buildings, both for protection against terrorist bombing attacks and accidental explosions, it is essential to understand the behaviour of window glass subjected to blast loading.

The use of a shock tube offers a safe and controllable alternative to blast testing with high-explosives. In the work of this thesis, an extensive experimental programme in order to determine the behaviour of both monolithic and laminated glass panes subjected to blast loading was conducted in the shock tube facility at SIMLab in Trondheim, Norway. Experiments on smaller test specimens were performed to determine the elastic material behaviour and stochastic distribution in failure strength of glass, and investigate how boundary conditions affected blast experiments.

Numerical simulations of both blast and material tests were carried out using the explicit finite element solver LS-DYNA in order to model material behaviour, blast load response and failure of monolithic and laminated glass.

An overview of the chapters in this thesis are briefly described here:

**Chapter 2 - Theoretical background.** In this chapter, an introduction to relevant background theory on blast loading, fracture mechanics and beam theory is given.

**Chapter 3 - Materials and material modelling.** In this chapter, an introduction to the materials of interest to this thesis, and numerical material modelling is presented.

**Chapter 4 - Bending tests.** The procedure for three- and four point bending tests conducted by the authors is presented. Results are presented and interpreted. Stochastic material parameters for glass is calibrated from four point bending tests.

**Chapter 5 - Blast experiment.** A presentation of the experimental set-up and experiments in the shock tube is given. Results are presented and interpreted.

**Chapter 6 - Numerical modelling: Four point bending test.** Numerical simulations of the four point bending tests in LS-DYNA are presented. Material parameters calibrated in chapter 4 are compared with experimental results.

---

**Chapter 7 - Numerical modelling: Blast tests.** In this chapter, numerical simulations in LS-DYNA of monolithic and laminated glass panes subjected to blast loading are presented. Numerical modelling techniques for monolithic and laminated glass are validated and discussed through comparison with experimental results.

**Chapter 8 - Concluding remarks.** The main experiences and conclusions from the experimental and numerical work are presented.

**Chapter 9 - Further Work.** Suggestions on where to focus future research are presented and discussed.



# Theoretical background

## 2.1 Blast Mechanics

In this section, relevant theory on the phenomenon of blast loading is presented. The theory in this subsection is mainly an adaptation from [2].

Explosions are defined as a sudden release of energy from a specific point, or volume of space, which generates a rapid expansion of the medium, usually with the generation of high temperatures and densities. The energy expands rapidly and compresses the sur-

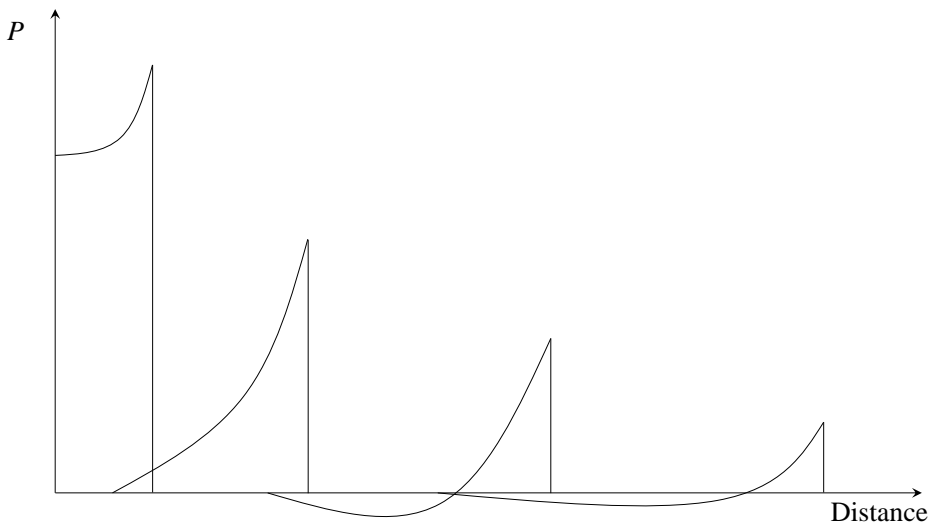


**Figure 2.1:** Influence of distance from the source on the blast pressure

rounding air to produce high velocity propagating waves, i.e. shock waves. The shock wave is a propagating wave having a definite wave front, travelling at supersonic velocities. The shock front is characterised by having a rapid increase of pressure, temperature and density compared to the undisturbed media. As the shock wave expands, a continuous decay in strength is observed, as shown in Figure 2.1.

An instantaneous rise in pressure, from atmospheric pressure  $P_{atm}$  to the peak incident overpressure  $P_{so}$  is produced by the explosive detonation, shown in Figure 2.2. This pressure increase takes place within nanoseconds at time  $t_a$ . A decay back to ambient pressure will occur as the shock front expands. This takes place within a timescale of milliseconds. After the positive phase, lasting a time of  $t_+$ , a negative phase is often generated. The negative phase is produced due to the overexpansion of the fluid creating a suction which serves as a decelerative force on the surroundings, and a reversal of flow back to the explosion center will occur. Ambient pressure is recovered after the negative phase at time  $t_a + t_+ + t_-$ . As the wave expands, the front will impact structures located in its path. The magnitude, duration and distribution of these shock loads are therefore a function of the explosive properties (i.e. weight, shape and type of explosive material), the location of the detonation with respect to the structure, and the alterations of the pressure wave by its interaction with the ground or the structure itself. When an incident shock wave strikes a structure that is not parallel to the travelling direction of the wave, it is reflected and amplified. This is called the reflected pressure  $P_r$ . The reflected pressure,  $P_r$ , is always greater than the incident overpressure,  $P_{so}$ , for the same distance from the detonation. This is shown in Figure 2.2. It is the reflected pressure that depicts the actual

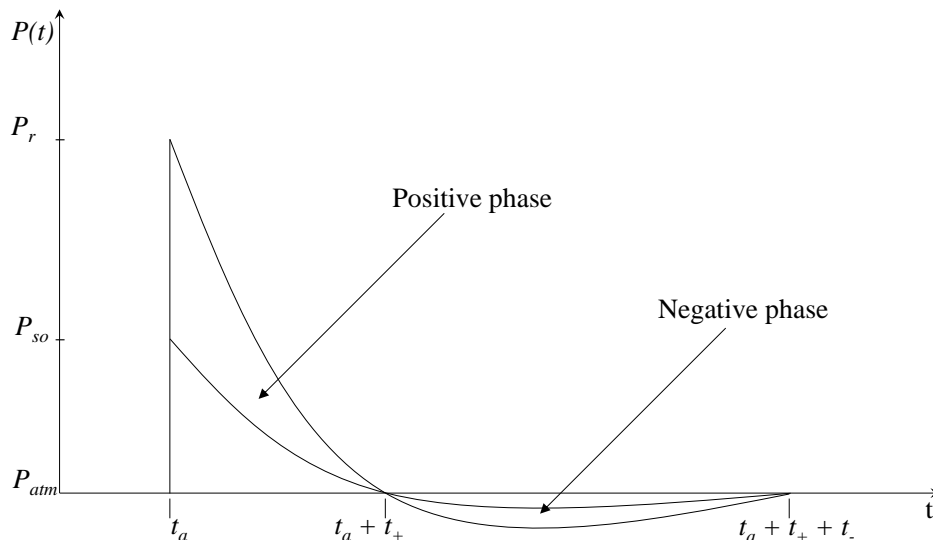


**Figure 2.2:** Ideal curve of incident and reflected blast pressure on an infinitely large surface.

loading on the structure and is used in blast-resistant design of structures. The load can be represented by an exponential pressure-time history such as the Friedlander equation, seen in Equation (2.1.1).



$$P(t) = P_{atm} + P_r \left(1 - \frac{t}{t_+}\right) \exp\left(\frac{-bt}{t_+}\right) \quad (2.1.1)$$

Here,  $P_r$  is the peak reflected pressure and  $b$  is the exponential decaying coefficient. The integrated area under the pressure-time history is defined as the total specific impulse  $i$ , and represents the total energy from an explosion exposed unto a building or structure [2]. The specific impulse of the positive phase is expressed in Equation (2.1.2).

$$i_{r+} = \int_{t_a}^{t_a+t_+} P_r(t) dt \quad (2.1.2)$$

In the case of the Friedlander Equation (2.1.1), the specific impulse of the positive phase has an analytical solution that is given in Equation (2.1.3).

$$i_{r+} = \frac{P_r t_+}{b^2} (b - 1 + \exp(-b)) \quad (2.1.3)$$

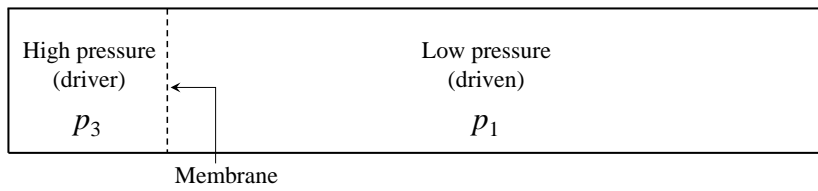
This equation is used to determine the exponential decay coefficient  $b$  iteratively when the other parameters are known. It should also be mentioned that the same expressions are valid for the incident blast pressure when substituting  $P_r$  with  $P_{so}$  in the previous equations.

## 2.2 Ideal Shock Tube Theory

A brief presentation of the basic principle and distinctive features of idealized shock tube theory will be given in this section. The theoretical background is mainly an adaptation from [3, 4].

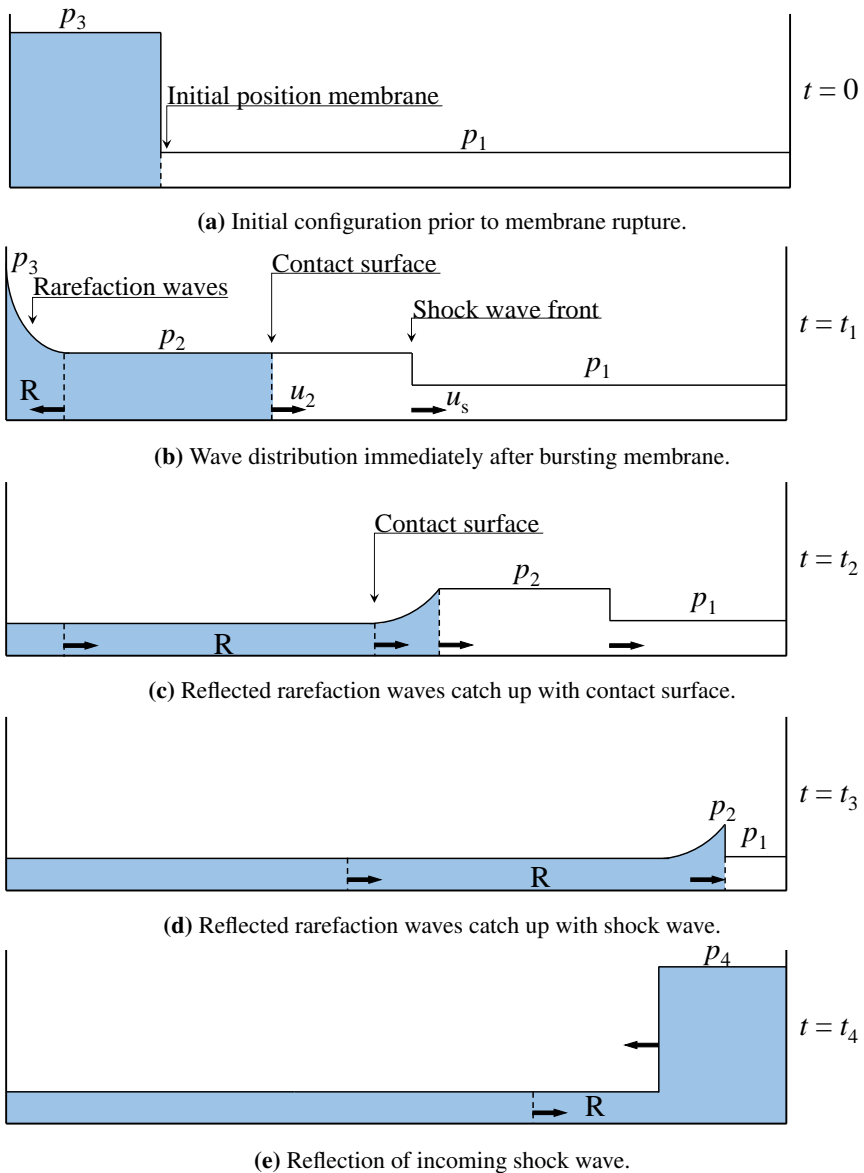
The shock tube consists of a gas-filled tube divided into two main parts, a high pressure chamber known as the *driver*, and a low pressure chamber called the *driven*. The driver and driven sections are separated by a membrane, as shown in Figure 2.3 whereby  $p_4 > p_1$ . A sudden rupture of the membrane generates a compression-wave, i.e. the shock wave, and decompression-waves, denoted rarefaction waves. The membrane is typically ruptured by producing a sufficient pressure difference between the chambers or by puncturing it with a mechanical device.

Figure 2.4 represents the events occurring in a shock tube for blast loading applications, and corresponding pressure distribution along the longitudinal axis of the tube at characteristic times. At  $t = 0$  the membrane bursts and propagating waves are generated, a shock wave moving into the medium of lower pressure and rarefaction waves, R, that expand backwards into the gas at higher pressure. The high pressure gas, with pressure  $p_3$ , previously contained in the driver section works as a piston expanding into the driven section



**Figure 2.3:** The ideal shock tube

generating a shock wave, with a peak pressure of  $p_2$ , moving at supersonic velocity  $u_s$  [4]. The shock wave propagating into the stagnant gas causes a particle motion with velocity  $u_2$  behind the shock wave by compressing, heating, and accelerating the driven gas. The interface between the high pressure and low pressure gases moves from the membrane at this same velocity  $u_2$ , and this interface is called the *contact discontinuity*, or contact surface. Once the target is hit, the shock wave is reflected and a reflected pressure of  $p_4$  occurs. The interested reader is referred to [2, 3, 4] for a more comprehensive review of the ideal shock tube.



**Figure 2.4:** Schematic representation of the events occurring in an idealized shock tube at characteristic times. The figure is adapted from [3].

## 2.3 Fracture mechanics

In the following, an introduction to fundamental theory of fracture mechanics is given, with emphasis on Linear Elastic Fracture Mechanics (LEFM) and brittle fracture. Not all theory presented here is directly used further in the thesis, but is relevant to consider in order to gain an understanding of the fracture process in brittle materials. The theory in this section is mainly an adaptation from [5, 6, 7].

### 2.3.1 Atomistic view of fracture

On an atomic scale, the strength of a material is determined by the attractive forces between molecules. These exist in a state of equilibrium, where attractive and repulsive forces between atoms are equal. This occurs when the potential energy is at a minimum. The distance at minimal potential energy is called equilibrium spacing, which is denoted  $x_0$ . The bonding energy between molecules may be expressed by the force  $P$  needed to separate the atoms.

$$E_b = \int_{x_0}^{\infty} P dx \quad (2.3.1)$$

The cohesive strength for small displacements may be expressed as

$$P = P_c \left( \frac{\pi x}{\lambda} \right) \quad (2.3.2)$$

The cohesive stress in a material may then be expressed as,

$$\sigma_c = \frac{E}{\pi} \quad (2.3.3)$$

when one assumes that  $\lambda$  is approximately equal to the atomic equilibrium spacing. Then the surface energy required to form one unit area of crack may be expressed as

$$\gamma_s = \frac{1}{2} \int_0^{\lambda} \sigma_c \sin \left( \frac{\pi x}{\lambda} \right) dx = \sigma_c \frac{\lambda}{\pi} \quad (2.3.4)$$

and the cohesive stress, may be expressed as:

$$\sigma_c = \sqrt{\frac{E \gamma_s}{x_0}} \quad (2.3.5)$$

In order for a material to fracture, the energy applied in the form of stress and work must be high enough to break intermolecular bonds in the material. Although the theoretical maximum fracture resistance of a material may be found from the result in Equation (2.3.3), the real fracture strength found in experiments is observed to be three to four orders of magnitude lower. The reduction in observed strength on a macroscopic level is caused by the stress concentration observed at a discontinuity, i.e. flaw or crack front, in the material.

In order to explain the difference in theoretical and observed material strength, one must consider the geometrical effects introduced by a discontinuity, such as a crack or surface

flaw in the material. The presence of a flaw acts to concentrate the stress in a structure, as shown in the early work of Inglis [8] on elliptical holes in a flat plate subjected to uniaxial tension. For a plate with infinite area, see Figure 2.5, one may assume that the boundaries do not affect the stresses. In this case the stress at the tip of the major axis of the elliptical hole, point A, may be expressed as

$$\sigma_A = \sigma \left( 1 + 2\sqrt{\frac{a}{\rho}} \right) \quad (2.3.6)$$

where  $\rho$  is the curvature at the major axis tip, given in Equation (2.3.7).

$$\rho = \frac{b^2}{a} \quad (2.3.7)$$

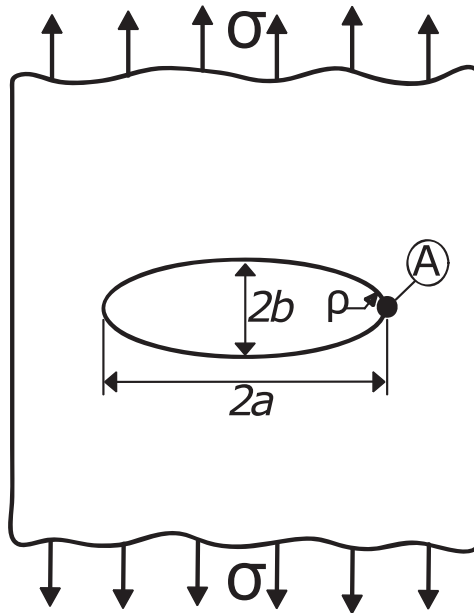


**Figure 2.5:** Elliptical hole in a flat plate subjected to remote stress, adapted from [5].

This may be used in order to calculate the effect of a narrow notch with blunt ends, if one assumes that  $a \gg b$  in Equation (2.3.7). Under this assumption Equation (2.3.6) becomes:

$$\sigma_A = 2\sigma\sqrt{\frac{a}{\rho}} \quad (2.3.8)$$

This implies that, as the notch becomes narrower, as is the case for a crack in a brittle material,  $\rho$  tends towards zero and thus  $\sigma_A$  goes towards infinity. This is of course physically impossible, as this would mean that any material containing a flaw which sharpens will fail for an infinitesimal load. In reality, this effect is counteracted in metals and polymers by plasticity in the form of crack blunting. In brittle materials however, this is counteracted

by the atomic size, which implies that the smallest diameter possible at the crack tip is governed by the diameter of the atoms in the material,  $x_0$ . If one substitutes the curvature  $\rho$  with the atomic size,  $x_0$ , Equation (2.3.8) becomes:

$$\sigma_A = 2\sigma \sqrt{\frac{a}{x_0}} \quad (2.3.9)$$

It is assumed that fracture initiates when the stress at the crack tip is equal to the cohesive stress, and by setting Equation (2.3.9) equal to Equation (2.3.5), the following expression may be used for the applied remote stress at failure:

$$\sigma_f = \left( \frac{E\gamma_s}{4a} \right)^{\frac{1}{2}} \quad (2.3.10)$$

Equation (2.3.10) may be viewed as a more realistic theoretical estimate for the resistance of a material to fracture, which also takes into consideration geometrical effects.

### 2.3.2 Griffith energy balance and energy release rate

Motivated by the paradox of infinite stress at a sharp crack tip in Equation (2.3.8), Griffith [9] formulated a theory for fracture, based on the principles of thermodynamics rather than localized stress. The first law of thermodynamics states that there must be a decrease in energy when a system goes from a state of non-equilibrium to a state of equilibrium. Griffith applied this principle to the case of a growing crack in a structure, and assumed that a crack may only be able to grow when the total energy,  $E$ , is either stationary or decreasing. The energy balance for an incremental increase in crack area,  $dA$ , becomes

$$\frac{dE}{dA} = \frac{d\Pi}{dA} + \frac{dW_s}{dA} = 0 \quad (2.3.11a)$$

or

$$-\frac{d\Pi}{dA} = \frac{dW_s}{dA} \quad (2.3.11b)$$

where  $\Pi$  is the potential energy supplied by the internal strain energy and external forces, and  $W_s$  is the work required to create new surfaces.

For the special case of an elliptical flaw in an infinitely large plate it can be shown that the expression for the potential energy becomes

$$\Pi = \Pi_0 - \frac{\pi\sigma a^2 B}{E} \quad (2.3.12)$$

where  $\Pi_0$  is the potential energy of an uncracked plate, and  $B$  is the plate thickness. Thus  $W_s$  becomes

$$W_s = 4aB\gamma_s \quad (2.3.13)$$

since the formation of a crack implies creation of two new surfaces. And the expressions for the potential energy and work in the energy balance becomes

$$-\frac{d\Pi}{dA} = \frac{\pi\sigma^2 a}{E} \quad (2.3.14a)$$

and

$$\frac{dW_s}{dA} = 2\gamma_s \quad (2.3.14b)$$

Solving the total energy balance for the failure stress, i.e. solving for the fracture strength gives

$$\sigma_f = \left( \frac{2E\gamma_s}{\pi a} \right)^{\frac{1}{2}} \quad (2.3.15)$$

This is a similar result to the one obtained in Equation (2.3.10). However, the Griffith energy approach may also be applied in the same way for any flaw geometry.

Irwin [10], in 1956, proposed an approach similar to Griffith's, more convenient for use in engineering applications. An energy release rate,  $G$  was defined as a measure of the energy available for an increment of crack extension:

$$G = -\frac{d\Pi}{dA} \quad (2.3.16)$$

Combining this definition with the results from Griffith, a critical energy release rate  $G_c$  at which crack extension occurs may be expressed as

$$G_c = \frac{\pi\sigma_c^2}{E} = 2\gamma_s \quad (2.3.17)$$

Thus  $G_c$  may be considered a material property defining the fracture toughness, i.e. the ability of a material to resist fast fracture.

### 2.3.3 Stress analysis of cracks

An alternative to the Irvin and Griffith global energy based approach for determining the fracture toughness of a material, is the analysis of stress concentration at a micro-crack or flaw under stress. In this case, three principal modes of crack opening is defined, illustrated in Figure 2.6. In mode I, the crack is opened by stress perpendicular to the crack, in mode II, the crack is opened by in-plane shear stress, and in mode III, the crack is opened by out-of-plane shear stress. The most detrimental, because the least amount of energy is required in opening the crack, and thus most significant is mode I.

Further, a stress intensity factor,  $K$ , dependent on crack shape, is defined. Here,  $K$  denotes the stress concentration at the crack tip, with subscript I, II, and III for the different loading modes. For a through thickness elliptical hole in an infinitely large plate, Westgaard [11] showed that  $K_I$  takes the form:

$$K_I = \sigma\sqrt{\pi a} \quad (2.3.18)$$

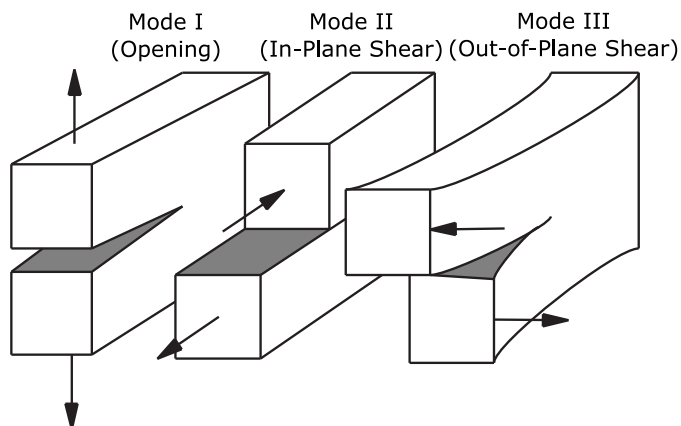


**Figure 2.6:** Loading modes for a crack, adapted from [5].

Analogous to the critical energy release rate  $G_c$ , the crack becomes unstable, and thus propagates at a critical value,  $K_c$ . Here,  $K_c$  is a material property, independent on flaw size and geometry, describing the fracture toughness of the material.

The stress intensity factor  $K$  and energy release rate  $G$  may be related through the relationship:

$$G = \frac{K_I^2}{E'} \quad (2.3.19)$$

where  $E' = E$  for plane stress, and  $E' = \frac{E}{1 - \nu^2}$  for plane strain.

Both the critical stress intensity factor  $K_{Ic}$  and the critical energy release rate  $G_c$  for crack propagation may be found experimentally, e.g. by testing on chevron notched specimens [12]. A typical fracture toughness for soda-lime glass is  $K_{Ic} = 0.7 \text{ MPa m}^{1/2}$  [13].



## 2.4 Statistical treatment of strength in brittle materials

As illustrated in Section 2.3, the ultimate strength of brittle materials is greatly influenced by the size and distribution of flaws. This means that if one were to test a series of identical specimens under the same conditions, there would be a considerable scatter in the results. Thus, in order to gain any meaningful engineering information from test results, one needs a method to incorporate this variation in the design and modelling of the material. A statistical treatment of test data, most commonly by the use of a Weibull distribution [6], is needed. The theory in this section is mainly an adaptation from [6].

### 2.4.1 The Weibull distribution

The Weibull distribution, introduced by Weibull in 1939 [14], is the most commonly used statistical distribution in the treatment of strength in brittle materials. Two forms of the Weibull distribution is most frequently used: the two and three parameter distributions. The probability density function of a two-parameter Weibull distribution with random continuous variable  $x$  is [15]:

$$f(x; \alpha, \beta) = \begin{cases} \alpha \beta x^{\beta-1} e^{-\alpha x^\beta}, & x > 0, \\ 0, & \text{elsewhere} \end{cases} \quad (2.4.1)$$

Where  $\beta > 0$  is called the shape parameter, and  $\alpha$  is a scale parameter. The cumulative probability distribution is given by:

$$F(x) = \int_{-\infty}^x f(t; \alpha, \beta) dt = 1 - e^{-\alpha x^\beta} \quad (2.4.2)$$

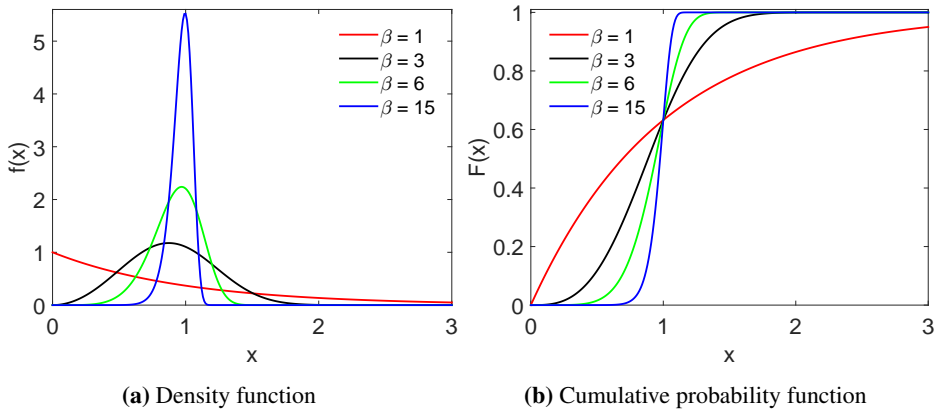


**Figure 2.7:** Weibull density and cumulative probability functions with  $\alpha = 1$ .

In Figure 2.7, the density and cumulative probability distributions for  $\alpha = 1$  with varying values for  $\beta$  is shown. For  $\beta = 1$  the Weibull distribution reduces to the exponential distribution, while for values  $\beta > 1$  the curves resembles the normal distribution, although somewhat skewed.  $\beta$  corresponds to an inverse of the width of the probability density distribution, that is, a high value of  $\beta$  corresponds to a narrow distribution. Additionally, a higher value for  $\beta$  causes the cumulative probability to go from zero to one over a shorter x-interval.

A commonly used representation of the Weibull distribution for interpreting strength testing data is

$$f(\sigma) = \frac{m}{\sigma_0} \left( \frac{\sigma}{\sigma_0} \right)^{m-1} \exp \left[ - \left( \frac{\sigma}{\sigma_0} \right)^m \right] \quad (2.4.3)$$

for the probability density function, and

$$F(\sigma) = 1 - \exp \left[ - \left( \frac{\sigma}{\sigma_0} \right)^m \right] \quad (2.4.4)$$

for the cumulative probability function.

Here  $\beta$  has been replaced by  $m$ , called the Weibull modulus, used for describing the dispersion in fracture strength in a series of tests.  $\alpha$  has been replaced by  $\sigma_0^{-1}$ , called the characteristic strength. In Equation (2.4.3),  $\sigma_0$  represents the 63rd percentile, meaning that the probability of failure occurring at or below a stress of  $\sigma_0$  is 0.63, or 63%.

## 2.4.2 Weakest link theory

The weakest link theory is based on the idea that if failure occurs at any flaw in a specimen, it leads to total failure of the entire specimen, and that the flaws is distributed homogeneously throughout the material. Thus the volume dependence on material strength may be considered by dividing a test specimen in to  $n$  elements of volume  $\delta V$ , where each element is subjected to a stress  $\sigma$ . The probability of failure in each element is equal and denoted  $P_f$ . Thus the probability of survival for the whole specimen may be expressed as

$$1 - P_f(\sigma, V) = [1 - P_f(\sigma, \delta V)]^n = \left[ 1 - \frac{V}{n} \frac{P_f(\sigma, \delta V)}{\delta V} \right]^n = \left[ 1 - \frac{V}{n} \phi(\sigma) \right]^n \quad (2.4.5)$$

where it is assumed that as  $n$  increases,  $\frac{P_f(\sigma, \delta V)}{\delta V}$  approaches a limit  $\phi(\sigma)$ . As the specimen is divided into smaller volumes,  $n$  approaches infinity and  $\delta V$  approaches zero. Then the probability of failure becomes:

$$P_f(\sigma, V) = 1 - \exp [-V\phi(\sigma)] \quad (2.4.6)$$

It was assumed by Weibull [14] that  $\phi(\sigma)$  takes the form

$$\phi(\sigma) = \left( \frac{\sigma}{\Sigma_0} \right)^m \quad (2.4.7)$$

Thus the probability of failure for the whole specimen,  $P_f$  is given by

$$P_f = 1 - \exp \left[ -V \frac{\sigma}{\Sigma_0} \right] \quad (2.4.8)$$

which is the two-parameter Weibull distribution with scale parameter

$$\sigma_0 = \Sigma_0 V^{-1/m} \quad (2.4.9)$$

## 2.5 Beam theory

In the following, a short repetition of fundamental beam theory relevant for the work done in this thesis is given. The theory presented is an adaptation from [16].

### 2.5.1 Euler-Bernoulli beam theory

The Euler-Bernoulli equation, shown in Equation (2.5.1) describes the relationship between an applied load,  $q$ , and the deflection field,  $w(x)$  in the  $z$ -direction, for a static beam.

$$\frac{d^2}{dx^2} \left( EI \frac{d^2}{dx^2} \right) = q \quad (2.5.1)$$

In Equation (2.5.1),  $E$  is the elastic modulus or Young's modulus, and  $I$  is the second moment of inertia of the beam cross section, given by:

$$I = \iiint z^2 dy dx \quad (2.5.2)$$

Which for a uniform cross-section with width  $b$ , and height  $h$  is:

$$I = \frac{bh^3}{12} \quad (2.5.3)$$

The curvature  $\kappa$  of the beam is the second derivative of the deflection:

$$\kappa = \frac{d^2 w}{dx^2} \quad (2.5.4)$$

The relation between the curvature and strain in the longitudinal dimension of the beam is given as:

$$\varepsilon_x = -\kappa z \quad (2.5.5)$$

where  $z$  is the distance from the centreline in the beam cross-section. Assuming linear elastic behaviour, Hooke's law

$$\sigma = E\varepsilon \quad (2.5.6)$$

may be used to determine the stress in the beam cross-section from Equation (2.5.5):

$$\sigma_x = -E\kappa z \quad (2.5.7)$$

Using the result in Equation (2.5.7) together with the definition of  $I$  in Equation (2.5.3),  $\kappa$  may be expressed as a function of the bending moment  $M$  in the beam:

$$\kappa = \frac{M}{EI} \quad (2.5.8)$$

Thus Equations (2.5.5) and (2.5.7) may be written as:

$$\varepsilon_x = -z \frac{M}{EI} \quad (2.5.9)$$

and

$$\sigma_x = z \frac{M}{I} \quad (2.5.10)$$

## 2.5.2 Application to bend testing

The purpose of deriving the expressions for the stress and strain for a beam in the previous section is to apply these relations to the case of clamped (3PBc) and simply supported (3PBss) three point bending, and four point bending (4PB). For the purpose of simplicity, only the case of four point bending is derived here, however similar derivations can be done for simply supported and clamped three point bending. Results for all three cases are given in Table 2.1.

Considering the case of a beam of uniform cross-section,  $b \times h$  loaded in four point bending, the maximum bending moment in the beam is:

$$M = \frac{PL}{8} \quad (2.5.11)$$

The maximum tension stress  $\sigma_{x,max}$  and strain  $\varepsilon_{x,max}$  is found in the bottom of the beam section,  $z = -\frac{h}{2}$ :

$$\sigma_{x,max} = \frac{PL^2}{16I} \quad (2.5.12)$$

and

$$\varepsilon_{x,max} = \frac{PL}{16EI} \quad (2.5.13)$$

The deflection at the centre of the beam  $\Delta_c$  may be found as:

$$\Delta_c = \frac{4PL^2}{768EI} \quad (2.5.14)$$

And Young's modulus is found as:

$$E = \frac{4PL^2}{768\Delta_c I} \quad (2.5.15)$$

Combining Equation (2.5.3) and Equation (2.5.12), the maximum stress in the beam may be expressed as:

$$\sigma_{x,max} = \frac{3PL}{4bh^2} \quad (2.5.16)$$

And similarly combining Equation (2.5.3), (2.5.13) and (2.5.15),  $\varepsilon_{x,max}$  may be expressed as:

$$\varepsilon_{x,max} = \Delta_c \frac{48h}{L^2} \quad (2.5.17)$$

**Table 2.1:** Stress and strain relations for bending tests.

	4PB	3PBss	3PBc
$\sigma_{x,max}$	$P \frac{3L}{4bh^2}$	$P \frac{3L}{2bh^2}$	$P \frac{3L}{4bh^2}$
$\varepsilon_{x,max}$	$\Delta_c \frac{48h}{L^2}$	$\Delta_c \frac{6h}{L^2}$	$\Delta_c \frac{12h}{L^2}$

## 2.6 Digital Image Correlation

Digital Image Correlation (DIC) is a powerful measuring tool used in a vast range of scientific and engineering applications, and can be used for both in-plane displacements (2D-DIC) and out-of-plane displacements (3D-DIC). The basic concept of DIC is that pictures taken during the experiment can be compared to calculate the relative displacement of a sample experiencing deformation. With the use of one camera aligned normally on the surface of interest, a 2D strain field can be calculated, and with the use of two cameras in an angle  $\pm\alpha$  normal of the surface, a 3D strain field can be calculated. DIC measuring can be divided into three parts:

1. Preparation.
2. Image recording.
3. Image processing.

**Preparation.** The specimen preparation is normally done by applying a speckled pattern to the surface of the specimen. This speckled pattern carries the information of displacement and is applied by use of black and white spray paint. The camera preparation is done by calibrating the cameras. This is only necessary in 3D-DIC measurements since it utilizes two cameras to capture the out-of-plane movement. The calibration, i.e., the mathematical relation between three dimensional target coordinates and image coordinates, is found by recording a set of image pairs of a calibration target with known geometry. Calibration targets often used are a cylinder with 80 mm diameter or a flat glass plate both printed with checkerboard pattern.

**Image recording.** During the experiment, the cameras take pictures at a designated recording rate. For dynamic experiments there is often a trigger mechanism to initiate the image recording (shock tube experiments utilize pressure sensors). A bright light source is very important to get satisfactory recordings due to the extremely fast exposure times.

**Image processing.** In order to calculate the displacement of the surface of interest, the camera models, i.e. the calibration has to be processed first. This is done by utilizing software specifically designated to DIC measurements. The corners of the checkerboard pattern on the cylinder are found for each image using a corner detection algorithm, and a least square algorithm is utilised to minimize the difference between the extracted image coordinates and the corresponding image coordinates calculated from known 3D target coordinates. This difference, or residual, determines the accuracy of the camera model.

# Chapter 3

## Materials and material modelling

### 3.1 Materials

This section presents the materials of interest in this thesis. Ceramics, glasses, production of monolithic glass and ultimately laminated glass will be covered. The theory in this part is mainly an adaptation from [17, 18].

#### 3.1.1 Ceramics

Ceramics are compounds consisting of metallic and nonmetallic elements for which the atomic bonding is a combination of ionic and covalent bonds. The nonmetallic elements are most frequently oxides, nitrides and carbides, where common ceramic compounds include aluminium oxide, silicon dioxide, silicon carbide and silicon nitride. In addition to these compounds there are materials that are often referred to as the traditional ceramics, i.e. those composed of clay minerals, as well as cement and glass. The term ceramic comes from the greek word *keramikos* whose original meaning was "burnt earth", indicating that the desired properties of these materials was achieved through heat treatment at high temperatures. Ceramics are in general relatively stiff and strong, i.e. comparable to the stiffness and strength of metals. Additionally they are typically very hard. Ceramics have been known to exhibit extreme brittleness, yielding a low resistance to failure. Ceramics represent a broad class of materials whereof glasses often are considered a subclass [6, 17, 18].

### 3.1.2 Glass

In a molten condition, most inorganic substances are randomly structured and the atoms are in continuous motion. When the substance is cooled down, crystallization occurs at a precisely defined temperature, causing the atoms to arrange in a structured network. In some substances, however, the crystallization proceeds very slowly mainly due to the high viscosity around the crystallization temperature. For a suitable rapid cooling temperature the substance will not be able to attain the rearranged crystalline state and only some atoms will move. As the temperature decreases, it becomes more and more difficult for the atoms to move and eventually they will "freeze" in a disordered state. These substances will act as elastic solids and are called glasses. Glasses are therefore amorphous solids formed by the rapid solidification of a melted substance.

Although there are several ceramics that may form glassy structures, e.g. boron oxide ( $B_2O_3$ ) and germanium oxide ( $GeO_2$ ), the most common inorganic glass that are used for containers and windows are silica glasses. Silica glasses, or noncrystalline silica, has a structure consisting of  $SiO_4^{4-}$  tetrahedrons as a base unit, shown in Figure 3.1a, similar to crystalline silica. However, silica glasses have a considerable amount of disorder compared to crystalline silica, as shown in Figure 3.1. Apart from silica, which is the network former, most silicate glasses contain additional oxides. The metallic ions in these additives are incorporated within and modify the  $SiO_4^{4-}$  network, and are therefore termed network modifiers. These modifiers, e.g. sodium oxide ( $Na_2O$ ) and calcium oxide ( $CaO$ ), are not capable of creating a glassy network by themselves. In modern float glass production, sodium oxide and calcium oxide is supplied as soda ash and limestone, respectively. Stabilizers, or so called intermediates, are also introduced to substitute for silicon and stabilize the structure. Both modifiers and intermediates contribute to a lower melting point and viscosity of the glass, making it easier to produce at lower temperatures.

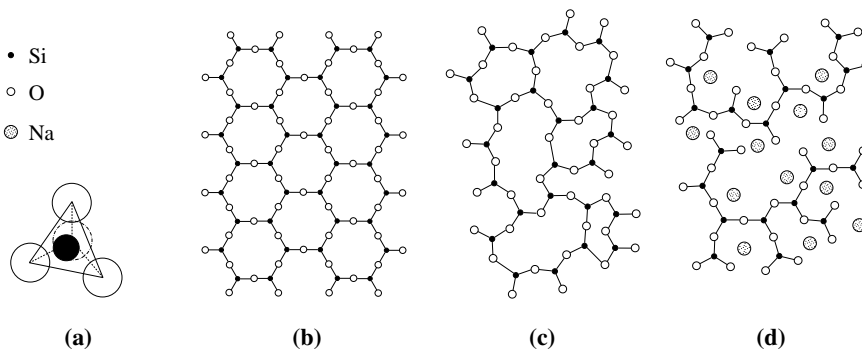


**Figure 3.1:** Characteristic features of the silicate structure. Adapted from [17].

(a) Silicon-oxygen tetrahedron ( $SiO_4$ ) $^{4-}$ , the basic structural unit, (b) Crystalline silica (e.g. quartz), (c) Silica glass, (d) Soda-silica glass

As most ceramics, silica glasses also exhibit brittleness and potential high strength. It has been discovered that carefully manufactured glass fibers can have strengths as high as



14GPa [19]. However, the strength of glass plates vary over a wide range due to surface flaws and microcracks in the microstructure. These flaws are the initiation points for the fracture at a nano scale [20], as described in Section 2.3. This indicates that for a larger glass sample, the probability of an existing critical microcrack increases, and the strength of the sample decreases. Further it is discovered that the compressive and tensile strengths of float glass are very sensitive to strain rate, while the Young's modulus is found to be rather insensitive to strain rate [21].

### 3.1.3 Float glass production

While flat glass was previously produced through a rolling process, it has since the late 1950s mainly been made as float glass [18]. Unlike float glass, rolled glass breaks up the transparency of the glass due to the lines produced by the pressure roller, creating an undesired effect when used in façades. Float glass is made by letting molten glass solidify on a liquid tin bath. Sand, whose main constituent is silicon dioxide, is mixed with the aforementioned modifiers and intermediates, and heated for several days in order to take a liquid form. The glass is then poured in the tin bath, and since glass float on liquid tin (like oil on water), the glass will take a uniform thickness. As the temperature is reduced the glass will harden and ultimately solidify while floating on the tin, since glass hardens at a higher temperature than tin. To obtain glass of a thinner thickness than that determined by the surface tension, the glass is stretched while floating on the tin. Thicker glass is made by holding the glass back, not permitting it to expand before it cools.

Since the glass is produced in long strips it has to be cut into the desirable size and the cut edge is usually grinded and polished [22]. The cutting process is often done by scratching the glass with a glazier's diamond producing a cut in the upper surface, as shown in Figure 3.2. The plate is then bent slightly, as shown by the arrows, generating tension at the cut resulting in an unstable crack-cut propagating down through the thickness cutting the glass into two parts. This cutting process creates damages such as crumbled arrises and cross micro-cracks on the edges of both glass parts. The depth of these specific cross micro-cracks may be larger than those of the initial surface micro-cracks. Their sizes may be so large that the deepest of them may remain partially or fully after grinding and polishing the glass edges. This edge-effect phenomenon indicates that these cross micro-cracks may reduce the strength of the glass even further and ultimately causing the glass to fail from the edge. It is observed that the side of the glass that is scratched to create the cut is on average 20% weaker in bending than the other side. The interested reader is referred to [22] for a more comprehensive review of this study.

### 3.1.4 Laminated glass

Laminated glass consists of two or more layers of glass panes sandwiching one or multiple interlayers of polymer sheeting. In case of failure, the interlayer's adhesive properties holds the glass fragments together preventing high velocity glass shards. Another purpose of the laminated glass pane is to dissipate blast energy through the breakage of glass plies

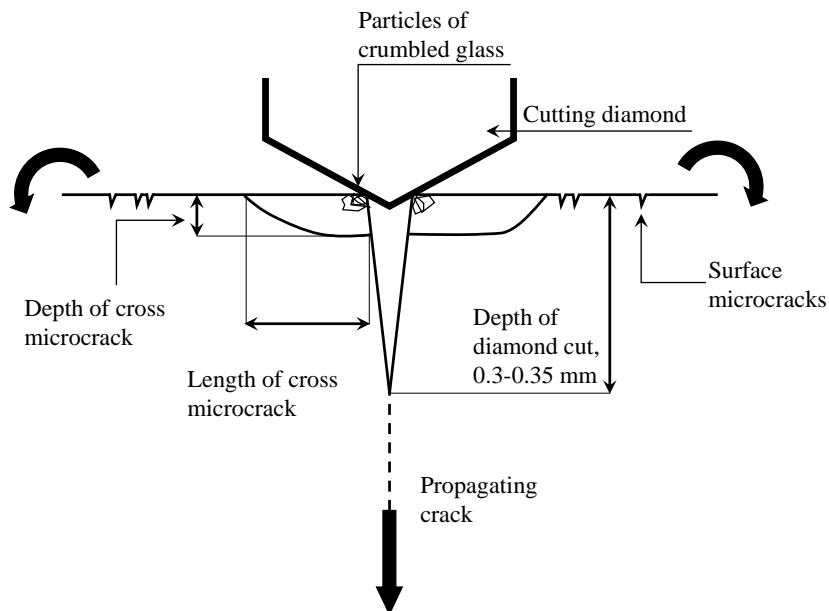


**Figure 3.2:** Diamond cutting and the existence of micro-cracks in cut glass panes.

and the large deformation of the polymer interlayer. Several types of laminated glass have been manufactured with different combinations of glass and interlayer types, yet the one analysed in this thesis consists of two float glass panes interlayered by polyvinyl butyral (PVB), shown in Figure 3.3.

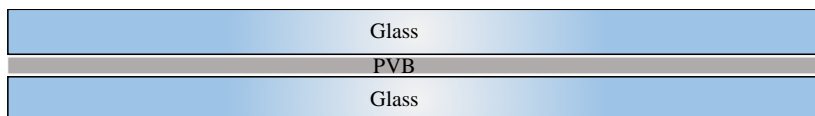


**Figure 3.3:** General cross section of laminated glass.

PVB is a polymer that has the chemical formula  $(C_8H_{14}O_2)_n$ . Experiments have shown that the behaviour of PVB is strain rate dependent [23]. For low strain rates, the PVB is rather viscoelastic, while for higher strain rates, the PVB behaves elastoplastic or even brittle at very high strain rates [24]. This is clearly shown in Figure 3.4, taken from [25]. In this thesis the PVB is treated as linear elastic and the material properties are taken from literature [25] and shown in Table 3.1.

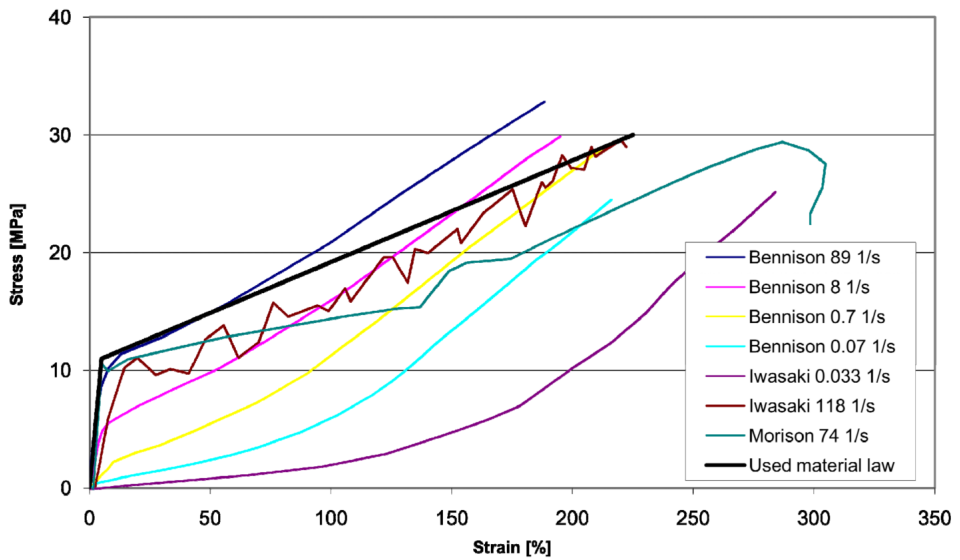


**Figure 3.4:** Material behaviour of PVB at different strain rates. Taken from [25].

**Table 3.1:** Material parameters for PVB. Taken from [25].

Initial Young's modulus	220 MPa
Poisson ratio	0.4
Density	1100 kg/m <sup>3</sup>
Elastic limit	11 MPa
Failure strain	2
Failure stress	28 MPa

The lamination of glass and PVB is done by applying heat and pressure. The process is initiated with a careful rinse of the glass panes, before it is being pre-laminated. This is done by heating the glass and interlayer to remove any bumps and uneven features in the interlayer. After pre-lamination the glass is sent to the autoclave where any air trapped between interlayer and glass is squeezed out to give a tight, stable product. This is done by applying both heat and pressure in a stepwise process. The laminated glass used in this thesis was produced at approximately 13 bar and 120 °C.

The failure of laminated glass can be idealized and distinguished into five phases according to Larcher et al. [26], shown in Figure 3.5.

1. Elastic behaviour of both glass panels.
2. The first glass panel fails, the other glass panel is still intact, interlayer is not damaged.
3. The second glass panel fails. The interlayer reacts elastically.

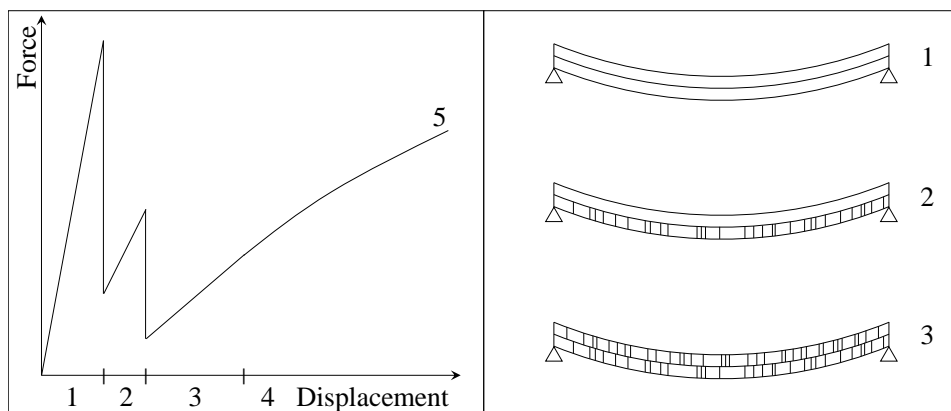


**Figure 3.5:** Idealized force–displacement curve and the different failure mechanisms of laminated glass. Adapted from [26].

4. The interlayer deforms plastically.
5. The interlayer fails. Failure can occur due to reaching of the failure limit or when the glass shards cut the interlayer.

## 3.2 Material modelling

### 3.2.1 LS-DYNA Material Models

The primary numerical tool used in this project is the explicit finite element solver LS-DYNA version R8.0 [27]. A brief introduction to material models which may be suitable in the modelling of glass, adapted from [27], is presented in the following sections. For a more comprehensive description of material models available in LS-DYNA, see [27].

#### Elastic material with simple erosion criterion

For the modelling of the elastic response in glass, *\*MAT\_001* (*\*MAT\_ELASTIC*) may be used. This is an isotropic linearly-hypoelastic material model, available for beam, shell and solid elements. It is easily calibrated, requiring only material density,  $\rho$ , Young's modulus,  $E$ , and Poisson's ratio,  $\nu$ .

In the elastic material, stresses,  $\sigma$ , and strains,  $\varepsilon$ , are related by Hooke's law, i.e:

$$\sigma = E\varepsilon \quad (3.2.1)$$

for the simple 1D case, and

$$\sigma_{ij} = C_{ijkl}\varepsilon_{kl} \quad (3.2.2)$$

for the general case, where  $C_{ijkl}$  is the 4<sup>th</sup> order tensor of elastic constants.

In order to model fracture and fragmentation of glass with *\*MAT\_001*, the failure routine *\*MAT\_ADD\_EROSION* may be used. This offers a large variety of failure and damage routines which may be coupled with many of the constitutive models available in LS-DYNA. When one or more of the failure criteria chosen is reached in a specified number of integration points, the element is eroded.

For the application in glass modelling, the failure criterion *SIGPI* may be used. This specifies a maximum allowable first principal stress,  $\sigma_{I,max}$ , in the element. When the stress in a specified number of integration points, *NUMFIP*, equals or exceeds  $\sigma_{I,max}$ , the stress in the element is set to zero, and the element is eroded.

### **Johnson–Holmquist 2 material model**

The Johnson–Holmquist 2 (JH-2) material model is specifically developed for use in modelling brittle materials, such as ceramics, subjected to large pressures, shear strain and high strain rates.

In simple terms the JH-2 model can be described as an elastoplastic material model which attempts to include phenomena observed in brittle materials subjected to high speed loading and damage. The model is based on two sets of curves that plot the yield stress against pressure. This is intended to simulate the increased strength observed at elevated hydrostatic pressure, as well as the reduced strength observed in damaged ceramics. A detailed description of the model can be found in the paper by Johnson and Holmquist [28], and a description of its implementation in LS-DYNA in [29].

In LS-DYNA the JH-2 material model is implemented as *\*MAT\_110* (*\*MAT\_JOHNSON\_HOLMQUIST\_CERAMICS*), and is only available for use with solid elements.

### **Laminated Glass Model**

*\*MAT\_32* (*\*MAT\_LAMINATED\_GLASS*) is a layered shell model made for efficient modelling of laminated glass. In this model, one shell element is used to model the entire thickness of the laminated glass pane. Parameters for two materials, i.e. glass and PVB, is input, and each integration point through the thickness is given either of the two material properties. Thus each integration point represents the middle of a thin material layer. A typical cross-section of a LG shell element, indicating integration points and material layers is shown in Figure 3.6. *\*MAT\_32* allows for defining failure criteria for the glass based on the failure strain, where the stress in an integration point is set to zero when the failure strain is reached.

The position and relative thickness of each layer is determined by a custom integration rule. In LS-DYNA *\*INTEGRATION\_SHELL* is used. This allows full control of the number and position of integration points over the shell thickness.

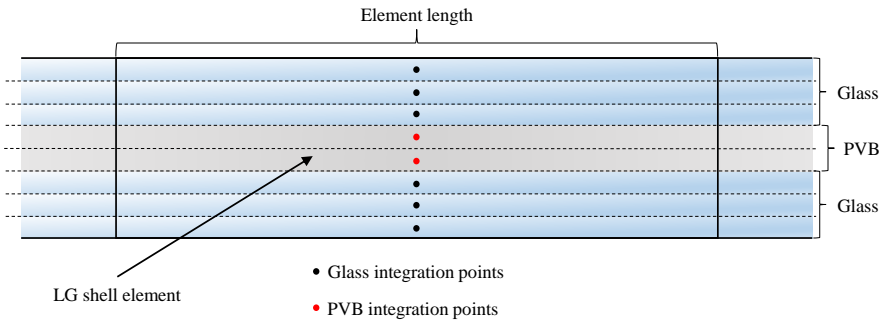


**Figure 3.6:** Cross-section of layered LG-model, adapted from [30].

### 3.2.2 SimLab Material Models

In addition to the commercially available material models in LS-DYNA, material models developed at SIMLab, NTNU, may be of interest in the modelling of brittle materials. A brief introduction to the relevant components of these models will be given in the following sections. For a comprehensive theoretical description, and user guides for the models, see [31] and [32].

#### SIMLab Metal Model

The SIMLab Metal Model (SMM) is developed at SIMLab, NTNU, primarily for the use in modelling metal behaviour. SMM offers a variety of material behaviours, including, linear hypoelasticity, viscoplasticity, anisotropic yield criteria, kinematic hardening, strain ageing, and a variety of damage and failure criteria. The model also has the opportunity of stochastic distribution of failure criteria.

Most of the features included in this model, e.g. plasticity and isotropic hardening, has no application in the modelling of glass, and only the elastic material behaviour is applicable. But, in particular, the ability for stochastic distribution of material parameters is interesting in the modelling of brittle materials. Thus the model is applied with material parameters chosen in order to attempt to model the behaviour of glass.

#### Elastic response

For the application of glass, the elastic response is modelled by Young's modulus and Poisson's ratio, while the yield stress is set to a high value, in order to avoid the plastic material routine. The material will thus be modelled as isotropic elastic, in a similar manner to *\*MAT\_001*.

#### Failure criteria

In SMM, failure is described by element erosion, as in the commercially available mate-

rial models in LS-DYNA. As the failure criterion is reached in an integration point in an element, the stress tensor in the integration point is set to zero, and thus it may no longer carry load.

In the modelling of glass, a stress based failure criterion is most appropriate [5]. A critical stress  $\sigma_c$  is introduced as a material variable in each integration point. If the maximum principal stress  $\hat{\sigma}_I$  stays larger than the critical stress during a critical time interval  $\Delta t_c$ , it is assumed that fracture occurs:

$$\hat{\sigma}_I \geq \sigma_c \quad \text{for} \quad \Delta t \geq \Delta t_c \quad \Rightarrow \quad \hat{\boldsymbol{\sigma}} = \mathbf{0} \quad (3.2.3)$$

Where the critical time interval  $\Delta t_c$  is used to avoid spurious fracture due to short duration stress waves.

### Stochastic distribution of failure criteria

The critical stress,  $\sigma_c$ , in each element may be distributed as a random variable by a Weibull distribution.

In SMM the probability density function as a function of the random variable  $x$ , takes the form:

$$f(x) = \frac{m_w}{x_0} \left( \frac{V}{V_0} \right)^{\mu_w} \left( \frac{x}{x_0} \right)^{m_w-1} \exp \left[ - \left( \frac{V}{V_0} \right)^{\mu_w} \left( \frac{x}{x_0} \right)^{m_w} \right] \quad (3.2.4)$$

Which is a similar but somewhat modified version of the standard two-parameter Weibull distribution in Equation (2.4.1). In Equation (3.2.4),  $m_w$  is the Weibull modulus,  $0 \leq \mu_w \leq 1$  defines the volume dependence of the distribution,  $x_0$  is a scale parameter,  $V_0$  is a reference volume and  $V$  is the volume associated with an element. In order to eliminate unrealistically high or low values for  $x$ , the distribution may be truncated by setting an allowable range for  $x$ . The range of  $x$  is then defined as

$$x_{min} \leq x \leq x_{max} \quad (3.2.5)$$

where  $x_{min} \geq 0$  and  $x_{max} \geq x_{min}$  is user defined variables.

### SIMLab Brittle Materials Model

The SIMLab Brittle Materials Model (SBMM) is developed for modelling failure and fracture in brittle materials. It offers isotropic or anisotropic linear elasticity, or linear viscoelasticity together with coupled brittle damage and failure by element erosion.

The formulation of elastic or viscoelastic behavior is broadly similar to SMM, and thus only the brittle damage and fracture formulation will be presented in this section.

### Brittle damage and fracture

The damage and failure rule in SBMM is largely based on a model proposed by Ritchie, Knott and Rice [33], further developed by Soong et al. [34]. A brief explanation of the theoretical background for this damage model is given in the following.

In modelling damage for brittle materials, an equivalent deformation measure  $\bar{\varepsilon}_D$  is defined as:

$$\bar{\varepsilon}_D = \sqrt[a_f]{\sum_{i=1}^3 \langle \hat{\varepsilon}_i \rangle^{a_f}} \quad (3.2.6)$$

where  $a_f$  is a model constant and  $\hat{\varepsilon}_i$  ( $i=1,2,3$ ) are the principal values of the corotational deformation tensor  $\hat{\mathbf{D}}$ .

In Kuhn-Tucker form, the loading/unloading conditions for damage may be expressed as:

$$f_D = \bar{\varepsilon}_D - \kappa \leq 0, \quad \dot{\kappa} \geq 0, \quad \dot{\kappa} f_D = 0 \quad (3.2.7)$$

where  $\kappa$  is a history variable. A damage threshold may be introduced by giving  $\kappa$  an initial positive value  $\kappa_0$ , i.e. for  $\kappa \leq \kappa_0$  there is no damage evolution. It thus follows that  $\kappa$  is equal to the maximum value of  $\bar{\varepsilon}_D$  reached during the straining history, that the material "remembers" the most critical state, and the damage only increases when this is exceeded.

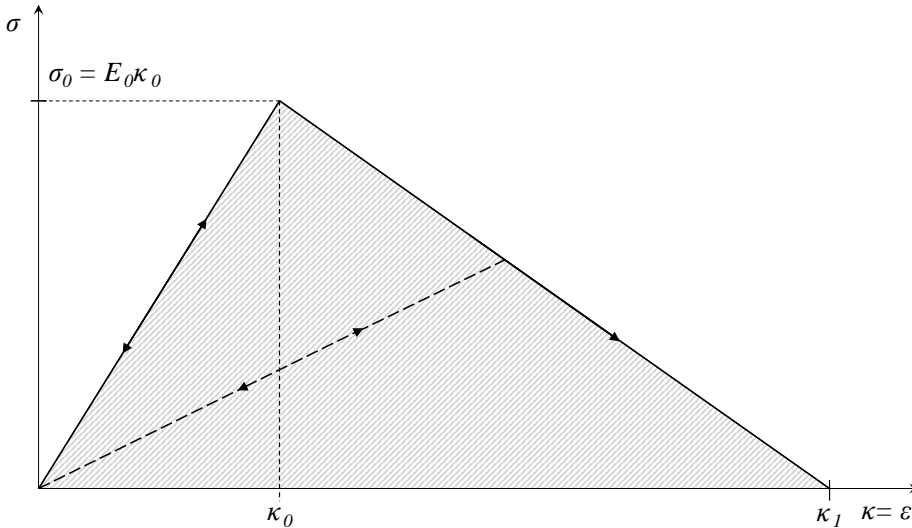


**Figure 3.7:** Stress–strain curve in uniaxial tension in the reference direction

The damage evolution law for the material is then defined as:

$$D(\kappa) = 1 - \frac{\kappa_0}{\kappa_0 - \kappa_1} \left( \frac{\kappa_1}{\kappa} - 1 \right) \quad (3.2.8)$$

where  $\kappa_1$  is a material parameter.

The damage evolution law may be visualised by considering a monotonic uniaxial tension test, in which case the strain,  $\varepsilon$ , is equal to both  $\bar{\varepsilon}_D$ , and  $\kappa$ . For a material with characteristic stiffness  $E_0$ , the response described by the brittle damage evolution law is shown in Figure 3.7.



The shaded area in Figure 3.7 represents the dissipated energy at fracture. For a cubic element of volume  $V_e = h_e^3$ , this energy is  $\frac{1}{2}E_0\kappa_0\kappa_1V_e$ . It is desirable that the energy dissipation is invariant to the element size. Thus a fracture energy  $G_f$  is introduced, defined as:

$$G_f A_e = \frac{1}{2}E_0\kappa_0\kappa_1V_e \quad (3.2.9)$$

Here  $G_f$  is assumed to be a material property, not dissimilar to the fracture energy introduced in Section 2.3.3.  $A_e$  is the fracture area of the cubic element shown in Figure 3.8. Solving for  $\kappa_1$  Equation (3.2.9) becomes:

$$\kappa_1 = \frac{2G_f}{E_0\kappa_0 h_e} \quad (3.2.10)$$

Thus  $\kappa_1$  may be inserted as a parameter which depends on the fracture energy of the material, and the mesh sensitivity of the finite element solution is greatly reduced.

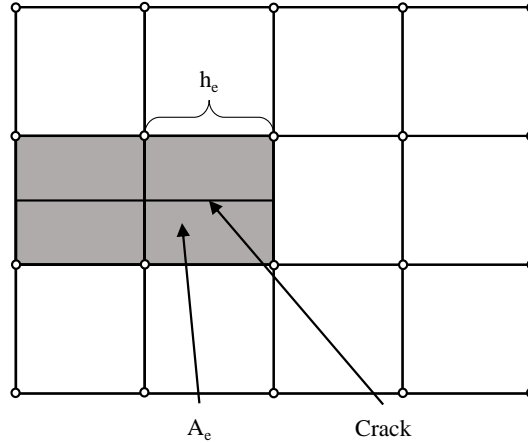


**Figure 3.8:** Crack propagation by deletion of elements

The result obtained in Equation 3.2.10 leads to the following restriction on the element size to ensure that  $\kappa_1 \geq \kappa_0$ , i.e. ensuring that  $D(\kappa) \geq 0$  in Equation 3.2.8:

$$h_e \leq \frac{2G_f}{E_0\kappa_0^2} \quad (3.2.11)$$

If the material has low toughness, this criterion leads to a minute element size, making the model extremely impractical for use in engineering applications.

In such cases, the regularization method is modified by assuming that the energy dissipated after passing the peak stress is given by

$$\Delta G_f A_e = \frac{1}{2}E_0\kappa_0(\kappa_1 - \kappa_0)V_e \quad (3.2.12)$$

where  $\Delta G_f$  is denoted the post-failure fracture energy.  $\Delta G_f$  is assumed to be a material characteristic, and is thus independent of element size. For the cubical element with characteristic size  $h_e$ , this becomes

$$\kappa_1 = \kappa_0 + \frac{2\Delta G_f}{E_0\kappa_0 h_e} \quad (3.2.13)$$

so that  $\kappa_1 \rightarrow \kappa_0$  for  $h_e \rightarrow \infty$ , and  $\kappa_1 \rightarrow \infty$  for  $h_e \rightarrow 0$ . With this approach, the mesh size may be chosen freely. But the energy released per unit area of crack during erosion of an element will be dependent on element size:

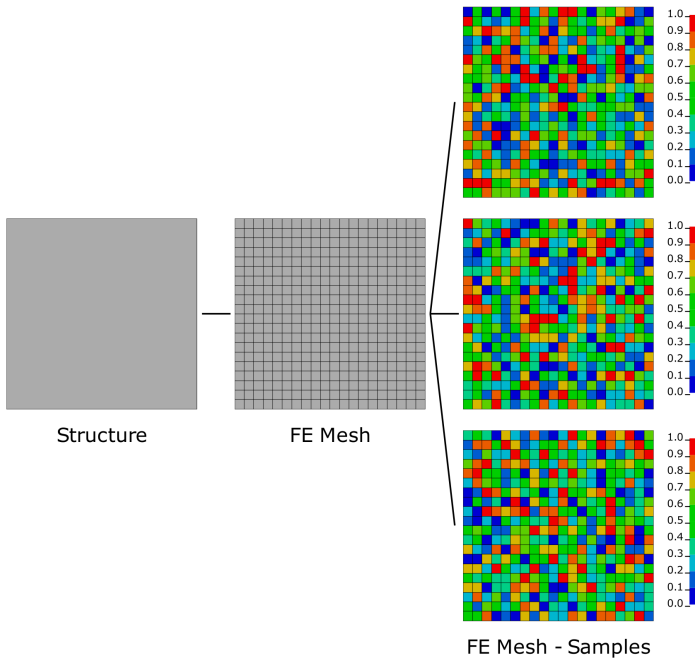
$$G_f = \frac{1}{2}E_0\kappa_0^2 h_e + \Delta G_f \quad (3.2.14)$$

In the same manner as in SMM the parameter  $\kappa_0$  is a material variable, and may be defined by a Weibull distribution in order to capture the stochastic variation in material strength.

### 3.3 Stochastic distribution of failure parameters

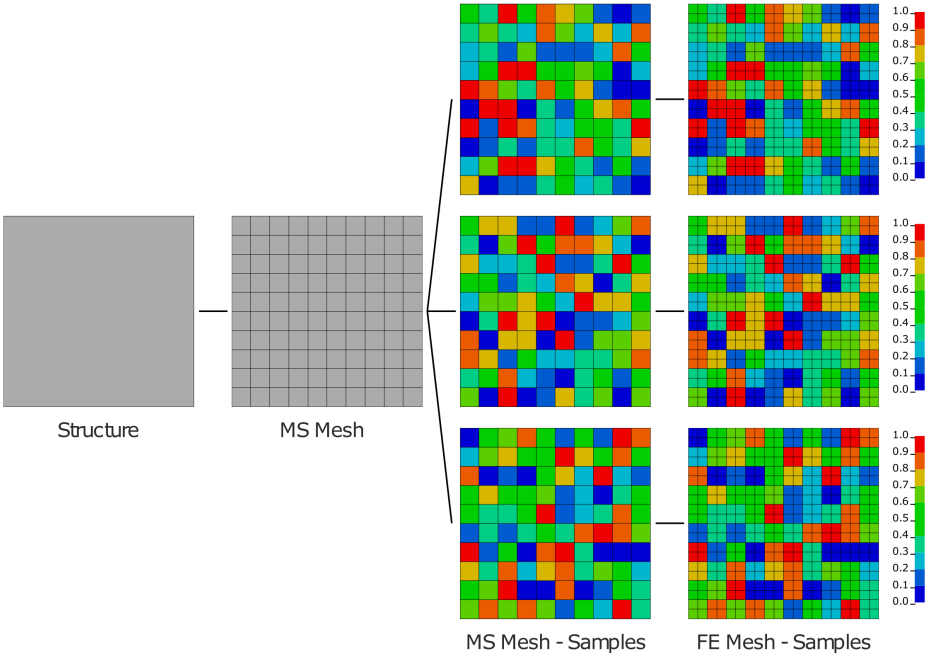
Glass contains microcracks and surface flaws controlling the strength of the material, as described in Section 3.1. Due to this, it is of interest to introduce a randomly distributed failure parameter that would be able to represent these damaged regions. The following section is adapted from [35].

Figure 3.9 shows a graphical representation of the finite element modelling of a structure with a stochastic distributed critical failure value,  $f_c$  that takes a value between 0 and 1. The failure parameter is scaled to fit the desired failure criteria in the Finite Element code. Firstly, the structure is discretised into a square mesh. Then,  $f_c$ , is distributed within the mesh according to the weakest-link approach, described in Section 2.4.2. Figure 3.9 shows three samples of the stochastic model. It is observed that the structure obtain strong and weak regions based on the stochastic distributed failure parameter. It should be noted that the sample range is influenced by the initial volume of the elements, or rather the number of elements (if they are all the same size). The probability of drawing a critical failure value  $f_c$  which exceeds a certain value increases when the number of elements increases. This is due to the fact that a sample from a finely discretised model is drawn from a wider range than a sample of a coarsely discretised model. Hence, a mesh sensitivity analysis is not possible using this modelling approach, since the material structure is defined by the mesh and changes with each mesh refinement. A mesh insensitive model is desired in order to compare element erosion and global behaviour in two models with stochastic distribution of the failure parameter; one finely discretised and the other coarsely discretised. In order to do this, a Material Structure (MS) mesh is introduced for which the material properties are distributed. In Figure 3.9 it is seen that the Finite Element (FE) mesh and the MS mesh coincides, it is said that they are congruent or coupled. This leads to an alternative modelling approach where the FE mesh and the MS mesh are uncoupled. This uncoupled modelling approach is presented in Figure 3.10. Here, the structure is discretised into a mesh of MS elements, where this mesh forms the basis to scatter the critical value  $f_c$



**Figure 3.9:** Randomly distributed failure parameters. The failure parameter is randomly distributed within the FE mesh.

according to the weakest link approach. Then, the critical value  $f_c$  is distributed within the MS mesh, before the MS mesh is discretised into FE mesh. This uncoupled modelling approach enables to perform a FE mesh sensitivity analysis without changing the mesh of the material structure for a model with stochastic distribution of the failure parameters, given that the MS mesh is coarser than the FE mesh.



**Figure 3.10:** Stochastic distributed failure parameter. The failure parameter is distributed within the MS mesh, before the MS mesh is discretised into a FE mesh.

## 3.4 State of the Art

Several approaches in the modelling of glass panes subjected to blast loading have been tried in the past. Of the most important differences in conducted literature studies is the type of material model used and element configuration used. The following section will cover the findings in this area.

### 3.4.1 Material Modelling

A single shell element through the thickness of the laminated glass pane, employing a user defined integration rule, with different material laws for the integration points through the thickness have been tried in several studies, [25, 30, 36], modelled in LS-DYNA. Larcher et al.'s model [25] in the study of laminated glass subjected to blast loading, yielded good results compared to non-failing experiments for larger blast loads, while the model was experienced to be inaccurate for smaller blast loads. The plastic strain limit (PSL) for the glass was found to have a strong influence on the global response, even though a plastic part is not evident from a physical point of view.

A combined model, consisting of two shell elements and one solid element through the thickness was proposed by Sun et al. [37] in 2005 in the study of safety windscreens. The two shell elements represented the outside and inside glass layers, while a single solid element for the PVB interlayer. The PVB was modelled utilising both a linear elastic model and a hyperelastic model. For the glass, three different material models was tested: A brittle cracking material model (ABAQUS), a linear elastic material model with element erosion for principal stress above a critical stress (ABAQUS), and an elasto plastic material model with element erosion for principal strain above a given critical strain (LS-DYNA). For the different material models of PVB, it was observed that the PVB interlayer shows different global response in the loading phase after rupture of the glass layers.

Laminated glass is also being modelled as solid elements. Wei and Dharani [38, 39, 40] modelled laminated glass subjected to blast loading with solid elements, whereby the glass layers were treated as linearly elastic and the PVB was modelled as both viscoelastic and elastic. It was concluded that the treatment of PVB as linearly elastic was justifiable as the response for the two material models was seen to be almost identical for a typical blast wave, up until failure of the glass. Ten elements over the entire thickness was utilised, four in both glass layers and two in the PVB. Wei et al. [40] also indicated that the change in the shear modulus of PVB is negligible under short duration loads, approximately 100 ms. Thus the viscoelasticity of PVB could be neglected when analysing the short-term behaviour of laminated glass subjected to blast loading.

Wu et al. [41] analysed the dynamic failure of nanomaterial enhanced laminated glass under impact using solid elements. Two solid elements described each of the three layers in the laminated glass pane. The Johnson-Holmquist Ceramic model, only available for solid elements in LS-DYNA, was used to model the glass layers while the PVB was treated as piecewise linear plastic. The results from the numerical simulation provided useful information in the understanding of the dynamic performance of the enhanced laminated

glass panes, and was also partly able to describe the delamination phenomenon utilising LS-DYNA's tiebreak contact type.

Hidallana-Gamage et al. [30, 42, 43, 44] have studied laminated glass subjected to blast load for both failing plates, and non-failing plates. Hidallana-Gamage et al. employed ten solid elements over the thickness of the laminated glass, four for each glass layer and two for the PVB. The glass was modelled with the Johnson-Holmquist Ceramic model, while the PVB was modelled with a piecewise linear plastic material model. The results showed that the behaviour of the laminated glass is influenced largely by the tensile strength of glass. The stiffness of the interlayer has a major influence on the response of the glass pane only for larger blast loads. The modelling techniques used could be applied to study the post-crack behaviour of laminated glass. By reducing the stiffness of the sealant joints, it was found that the flexibility at the support increased and reduced the stresses and damage to the glass panes, while this had little impact for larger deflections and larger loading.

A comparison between different element formulations of laminated glass was studied by Larcher et al. [26] in 2012. It was seen that the layered model only can represent a linear in-plane strain distribution through the thickness. Thus, the layered model is not able to represent the case when only one glass layer fails and the other withstand failure. It was concluded that the solid element model can give very detailed results, however the computational power required is rather large, while the layered model should be used for design studies where the interlayer fails. Delamination was not considered in this study.

In Zhang et al.'s [24] model it is seen that the glass pane deflection varies negligibly for any element size smaller than 5 mm. Three 8 noded fully integrated elements through the thickness was used, one element for each layer. The glass layers were modelled using the Johnson-Holmquist Ceramic material model, and the material constants were revised to better fit the experiments. A strain rate dependent material model was used for the PVB. A tiebreak type of contact was utilised and delamination was clearly seen in the resulting simulation.

All of the studies mentioned in this section have modelled the failure of laminated glass using erosion of elements. In order to keep erosion to a bare minimum, the glass pane have to be extremely finely discretised. An alternative approach to element erosion is the node splitting technique. Node splitting, described by Olovsson et al. [45], is an algorithm of introducing fragmentation to a material and still maintaining a good energy conservation, i.e. no loss of mass. The algorithm locates the two integration points with the largest damage surrounding the node that is to be split. A vector is then established between these two integration points, before the node is split such that the propagating crack plane has its normal as close to the direction of this vector as possible.

Larcher and Solomos [46] proposed that node splitting can be a reasonable approach to describe brittle failure in glass, however few studies have been conducted on this topic.

### 3.4.2 Contact Modelling

An important property of laminated glass is the adhesive bonding between glass and interlayer. This complex bonding mechanism is influenced by several factors; autoclave temperature and pressure, processing time and storage humidity of PVB [47]. Froli and Lani [48] conducted compression and shear tests, and found that the shear bonding strength between PVB and glass is around 10 MPa, and that the tensile strength lies between 5 MPa to 10 MPa. Wu et al. [41] and Zhang et al. [24] obtained reasonable results utilising *\*CONTACT\_AUTOMATIC\_SURFACE\_TO\_SURFACE\_TIEBREAK* to simulate the potential debonding phenomenon between glass and interlayer. This LS-DYNA implemented type of contact, is used to simulate the adhesive contact between glass and PVB interlayer. The glass and PVB elements are connected until a prescribed failure criterion, shown in Equation (3.4.1), is fulfilled.

$$\left(\frac{|\sigma_n|}{\text{NFLS}}\right)^2 + \left(\frac{|\sigma_s|}{\text{SFLS}}\right)^2 \leq 1 \quad (3.4.1)$$

Here,  $\sigma_n$  and  $\sigma_s$  are the normal and shear stresses at the interface, respectively, while NFLS and SFLS are the corresponding tensile and shear bonding strength. For a more comprehensive description of this contact type, see [27].





# Bending tests

Two different bending experiments were carried out in this project:

1. Four point bending tests on three different sizes of monolithic glass specimens in order to determine fracture strength and stiffness.
2. Three point bending tests performed with the fixture used in blast experiments to investigate the influence of boundary conditions.

## 4.1 Four point bending test

In order to determine fracture strength and stiffness, four point bending tests on three different sizes of monolithic glass specimens were done. The tests were conducted by the authors under supervision of Mr. Trond Auestad and PhDC Karoline Osnes in the laboratory at the Department of Structural Engineering at NTNU. The following sections will give an overview of the set-up, and presentation of the results for four point bending tests on monolithic glass.

### 4.1.1 Setup

The ASTM standard test method for flexural strength of advanced ceramics (ASTM C1161) [49] was used as a basis for the four point bending tests. Three different sized testing fixtures were manufactured by NOMEK AS, according to specifications in ASTM C1161. A schematic of the fixture with a specimen is shown in Figure 4.1, and the fixture used for small specimens is shown in Figure 4.2.

Testing fixtures consisting of a loading member and a support member were used. The loading and support members supported four cylinders with a diameter,  $d$ , of 6 mm, that

was free to rotate and restricted from excessive in-plane movement by four rubber bands. The support length  $L$  of the fixture was 80mm, 180mm and 280mm for the small, medium and large test specimens, respectively. The loading span was half the length of the support length. An INSTRON 5985 testing system with a 5kN load cell was used to generate the load and an optoNCDT 2310-50 laser at a data logging rate of 50 kHz, was used to capture the displacement of the centre-point at the underside of the specimens. During testing of the large specimens, it was found that the fixture for the largest test specimen size was too shallow. Thus the support member of the large testing fixture was milled approximately 5 mm, by staff at the laboratory at the Department of Structural Engineering, NTNU.

Two different devices were used for fastening the 5kN load cell to the loading member. One where the loading member was not allowed to rotate relatively to the load cell, i.e. fixed, and one where some rotation was allowed. The fixed fastening mechanism was used in all small specimen tests except the first one, and the three first tests on the medium specimens. The fixture which allowed rotation was used for all other tests. The fixed fastening mechanism was subject to adjustment in the first five tests for the small specimens.

ATSM C1161 specifies a desired loading strain rate of  $\dot{\epsilon} = 1.0 \times 10^{-4} s^{-1}$ . Thus the cross-head speed for each specimen size was determined through the relation [49]:

$$\dot{\epsilon} = \frac{6hs}{L^2} \quad (4.1.1)$$

Where  $h$  denotes specimen thickness,  $s$  the cross-head speed and  $L$  the outer support span. In order to test all specimens at the specified strain rate, the cross-head speed was set to 1.6 mm/min for the small specimens, 8.1 mm/min for medium specimens, and 19.6 mm/min for large specimens.

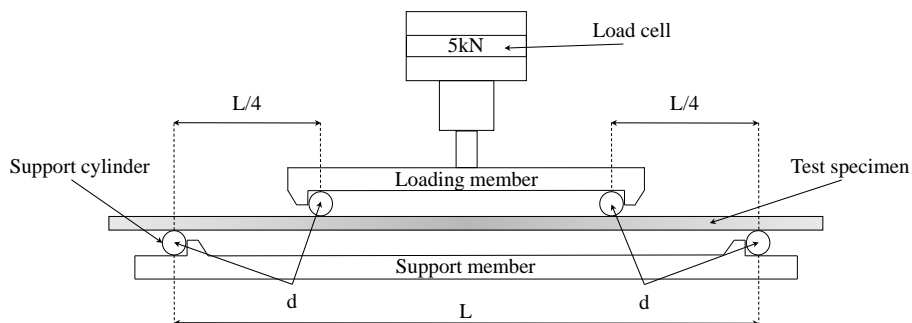


**Figure 4.1:** Schematic of four point bending test (not to scale).

### Test specimens

All glass specimens was delivered by Modum Glassindustri AS. The three sizes of interest were  $100 \times 20$  mm,  $200 \times 40$  mm and  $300 \times 60$  mm, all with a thickness of 4 mm.

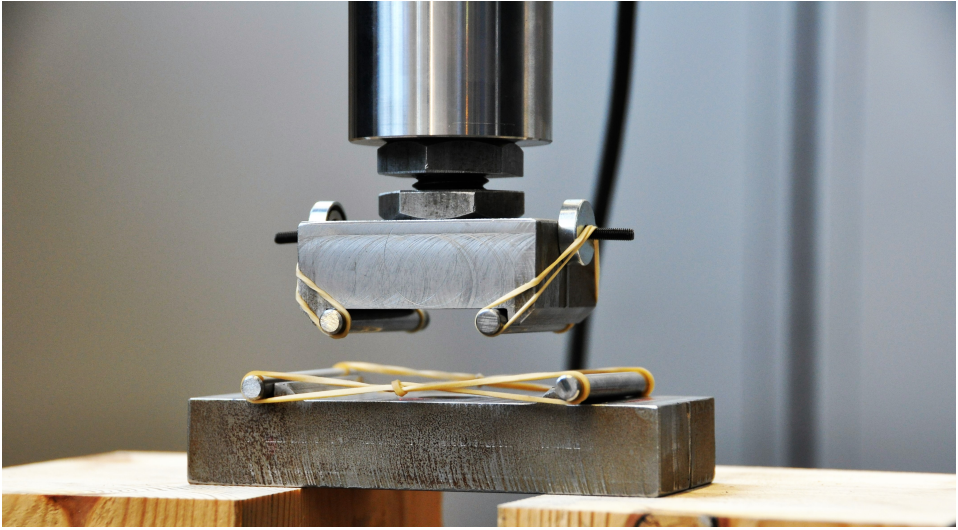


**Figure 4.2:** Testing fixture for small specimens.

In order to obtain a reliable Weibull distribution of failure strength, a sufficient number of specimens should be tested. As values in literature varies from five [17], to 60 tests [13], 30 tests for each size was chosen in this study. Therefore 35 specimens of each aforementioned size was ordered from the manufacturer. Some cracks and dents along the edges were visible to the naked eye in the received specimens, yet the overall finish was fairly good. It is also worth mentioning that both the small and the large specimens had a noticeably better edge finish than that of the medium sized specimens.

Specimen dimensions were measured before testing by the use of a slide gauge. Key dimensions for all three specimen sizes are presented in Table 4.1, and a full list of measurements are given in Tables A.1 to A.3 in Appendix A.

**Table 4.1:** Overview of specimen dimensions. Full list is given in Appendix A. All dimensions in mm.

Specimens Dimension	Small			Medium			Large		
	$L$	$w$	$h$	$L$	$w$	$h$	$L$	$w$	$h$
Mean	100.03	20.06	4.02	199.97	40.04	4.01	300.05	60.07	3.95
Max	100.41	20.19	4.05	200.12	40.18	4.05	300.13	60.20	3.97
Min	99.90	19.97	3.99	199.90	39.89	3.98	299.92	59.95	3.92

## 4.1.2 Results

### Force–displacement

Figure 4.3 shows the resulting force–displacement curves found from all 94 four point bending tests, 32 tests on small specimens, 31 tests on medium specimens, and 31 tests on large specimens. The displacement was measured by laser, at the midpoint on the underside of the specimens. Force and displacement data has been filtered by a 10 point moving average, without altering the last data point. As some inconsistencies were experienced regarding the displacement at zero force, this has been moved in order for the first data point in each series to start at the origin.

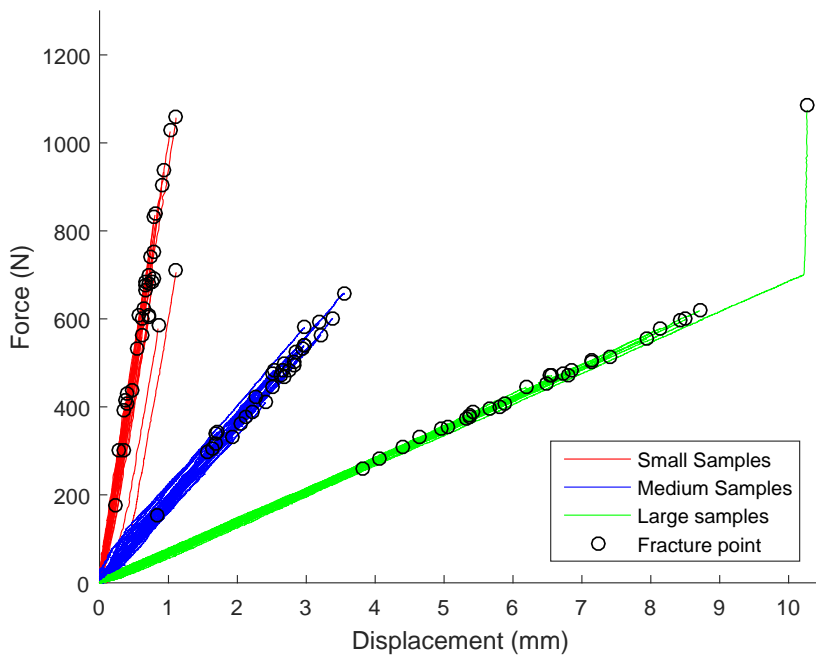


**Figure 4.3:** Force–displacement data for all four point bending tests.

For the small,  $100 \times 20$  mm, specimens the results are generally as expected with linear elastic behaviour until fracture. There are however three exceptions which shows non-linear behaviour at low force and displacement. For these tests, the adjustments of the fastening mechanism for the upper part of the testing jig is suspected to be the cause. These results are disregarded in the further data analysis.

For the medium,  $200 \times 40$  mm, specimens all results exhibit linear elastic behaviour until fracture, and thus all are included in further analysis. The dispersion of measured bending stiffness is greater than for small and large sample series. The reason for this is not exactly

known and no obvious explanation was found at the time.

For the large,  $300 \times 60$  mm, specimens all but one result exhibits the expected linear behaviour until fracture. One result has a clear kink at a force of approximately 700 N, this is most likely due to the specimen bottom surface touching the jig at this point, preventing further displacement. As this specimen exhibits linear behaviour prior to this point, the result up until 700 N is included in calculating the average Young's modulus, the fracture strength found in this test is excluded in further calculations.

Pictures of a selected number of small and medium test specimens showing typical fracture patterns, are given in Figures B.1 to B.3 in Appendix B. Similar patterns were seen for large specimens.

### Young's modulus and fracture stress

Beam theory was assumed valid for the four point bending tests, and Young's modulus,  $E$ , and fracture stress,  $\sigma_f$  for monolithic glass was calculated using Equations (2.5.15) and (2.5.16), in Section 2.5. 50% of data points were used in calculating Young's modulus in order to exclude non-linear effects at extremes of the force–displacement curve. Maximum force and displacement measured was used for the calculation of the fracture stress. A contracted representation of calculated results for all 94 specimens are listed in Table 4.2.

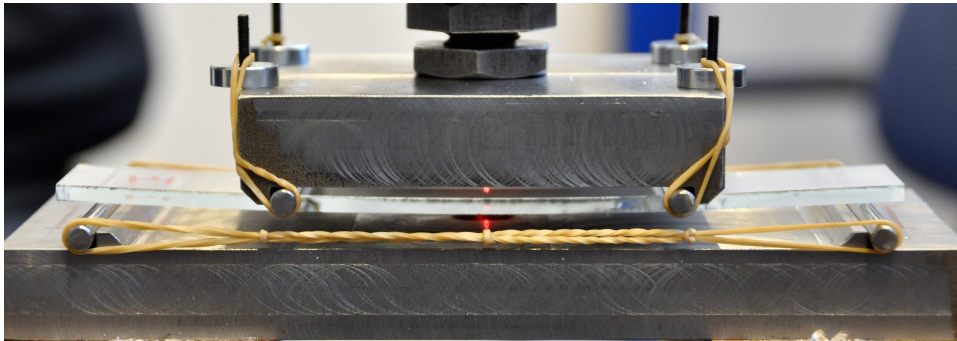


**Figure 4.4:** Medium sized test sample during bending test.

**Table 4.2:** Resulting material parameters calculated from test results

Specimen size	Small		Medium		Large	
	E [GPa]	$\sigma_f$ [MPa]	E [GPa]	$\sigma_f$ [MPa]	E [GPa]	$\sigma_f$ [MPa]
Mean	64.8	116.0	71.8	94.1	70.5	103.1
Max	75.7	197.2	88.1	136.8	75.5	157.7
Min	49.1	32.1	63.2	30.3	65.0	57.5

For the medium and large specimens, the calculated mean Young's modulus was consistent with the expected value of between 70 and 74 GPa [17, 6] for monolithic float glass, and the variation between extreme values were within a reasonable extent.

For the small specimens, the calculated mean Young's modulus was lower than the expected value. While some of the results are within or above the expected range, the general trend is that results were in the range of 65 to 70 MPa. The reason for this is not entirely clear, but it is believed that the fastening mechanism used in the small experiments is the main reason.

The mean fracture stress for all samples are all within or close to the values found in literature, e.g. in [6], and fairly consistent for different specimen sizes. The highest mean and maximum fracture strength are found in the small specimens. This is expected, as these are less likely to contain a dominating micro-crack, and thus are less likely to fail at a low stress. Contrary to this prediction, the lowest mean and minimum fracture stresses are found in the medium size specimens, rather than the large ones. This seems counter-intuitive as it is expected that a bigger specimen would have a higher probability of containing critical micro-cracks. This inconsistency may be explained by the fact that the edges of the medium samples was visibly less smooth, i.e. probably having greater probability of containing critical micro-cracks, than the small and large specimens.

### Weibull analysis

In order to calibrate a Weibull distribution of the fracture strength for use in numerical modelling, the approach specified in ASTM C1239 [50] was used. The Weibull analysis was applied separately for each sample size series.

In the following, a brief explanation of the procedure recommended in ASTM C1239, and used here, for calibrating Weibull parameters from a series of tests is given.

First, the fracture stress for all tests in a series is ranked in ascending order. The probability for failure in each test is then calculated by

$$P_f(\sigma_i) = \frac{i - 0.5}{N} \quad (4.1.2)$$

where  $\sigma_i$  is the failure stress found in test  $i$  in the ranked series, and  $N$  is the number of test specimens in the series. Then a linear regression is done on  $\ln(\sigma_i)$  versus  $\ln(\ln[1 - (1 - P_f)])$  in order to obtain Weibull parameters  $\hat{\sigma}_0$  and  $\hat{m}_w$ . In this thesis, a MATLAB [51] script has been used in order to perform the linear regression. Note that the Weibull parameters calibrated from tests are signified with the hat in order to emphasize that these are approximate and not real values, as an infinite amount of tests is needed in order to find the real distribution values.

For small test specimens, all of the 32 test results obtained were used in calibrating Weibull parameters. The two that used a different fastening mechanism for the testing fixture were used because the fracture stress in these tests were within a reasonable range from the other tests. For medium test samples, all 31 test results obtained were used, as no outliers were found. For large test samples, 30 of 31 test results obtained were used. The one excluded is the one where contact is suspected to have happened between the testing fixture and the test specimen.

Resulting Weibull parameters found for all specimen sizes are presented in Table 4.3. The linear regression fit of results for small test samples is presented in Figure 4.5, with corresponding figures for medium and large samples in Figure C.1 and Figure C.2, respectively, in Appendix C.

Comparison between probability density and cumulative probability density curves for calibrated Weibull parameters and experimental results, for small samples, are presented in Figure 4.6. Corresponding figures for medium and large samples are presented in Figure C.3 and Figure C.4, respectively, in Appendix C.

**Table 4.3:** Weibull parameters calibrated from four-point bending tests

	Small specimens	Medium specimens	Large specimens	Average
$\hat{m}_w$	3.20	4.10	5.09	4.13
$\hat{\sigma}_0$	129.58	103.93	108.24	113.8

From the comparisons between calibrated Weibull distribution and experimental results, it seems that the correlations between calibrated distributions and experimental results are sufficient. And it is further assumed that the distributions found for each sample size are representative for the experimental results.

A trend that the Weibull modulus increases for larger sample sizes is observed. Characteristic strength,  $\hat{\sigma}_0$ , for all sample sizes follows the trend found when analysing the mean fracture strength, i.e. a relatively high  $\hat{\sigma}_0$  for the smallest samples, and the lowest  $\hat{\sigma}_0$  found in medium samples with  $\hat{\sigma}_0$  for large samples slightly higher than for medium samples.

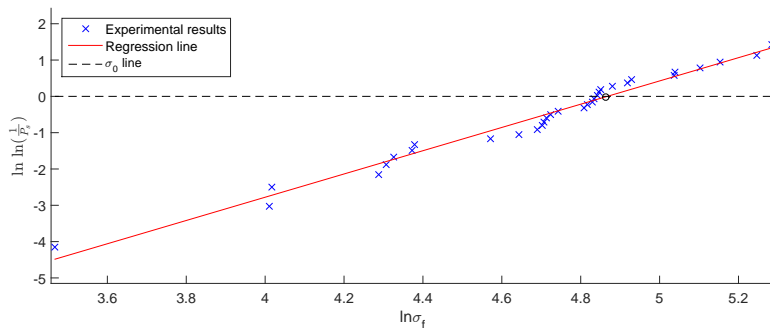


**Figure 4.5:** Regression fit of Weibull parameters, small samples

The correlation between Weibull modulus and sample size is likely to be caused by edge effects. That is, the length of specimen edge divided by specimen volume is approximately three times higher for small versus large specimens. As mentioned in Section 3.1.3, critical micro cracks are more likely to be apparent on the edges, causing a larger variation in strength for the small specimens.

Paradoxically, it is believed that edge effects should lower specimen strength, supposed to be the cause for a lower strength in the medium compared to large specimens. However

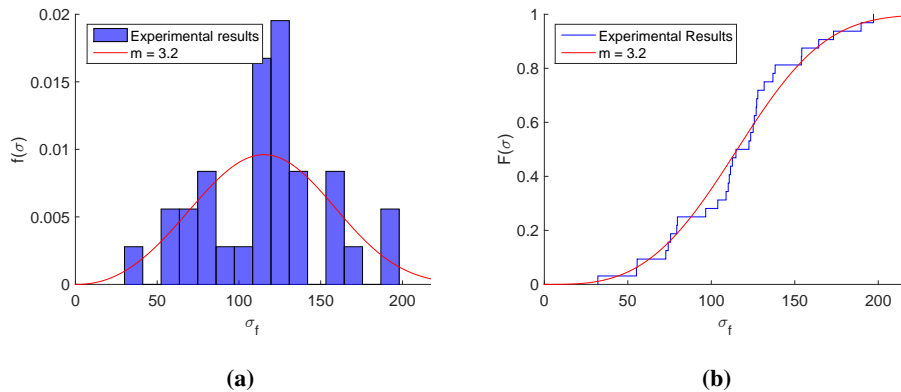


**Figure 4.6:** (a) Probability density, and (b) cumulative probability density compared with experimental results, small samples

the lowered strength is not found in the small specimens, as would be the case if this assumption was true. The reason for this discrepancy is not entirely clear, and underlines the difficulties of predicting behaviour in materials which are stochastic in nature.

## 4.2 Three point bending tests

Three point bending tests were conducted in order to investigate effects of boundary conditions in the shock tube tests. The following sections will give an overview of the setup and a presentation of the results for three point bending tests. Influence of the results found in tree point bending tests on experiments in the shock tube, is discussed.

### 4.2.1 Setup

Three point bending tests were performed at the laboratory at the Department of Structural Engineering, NTNU, using an INSTRON 5985 testing system equipped with a 5kN load cell. Cross-head loading speed for all tests was 5 mm/min. Displacement of the centre point on the underside of the test specimens was measured by an optoNCDT 2310-50 laser at a data logging rate of 50kHz, in the same manner as in the four point bending tests.

Test specimens were fixed in the same frame as used in shock tube tests. In order to apply the required clamping force on the frame, two bolts, one on either side of the glass specimen were fastened to the desired torque with a BAHCO torque wrench, as shown in Figure 4.8a. The frame was placed on two I-beams such that a rounded punch with diameter 20 mm loaded the specimens in the centre.

The three following boundary conditions were investigated:



**Rubber** Rubber strips, made of neoprene, 50 mm wide and 4 mm thick, were taped to the frame, as in the shock tube tests. Bolts were fastened with a torque of 5, 10, and 20 Nm.

**Teflon** In place of rubber strips, 50 mm wide and 4 mm thick Teflon strips were used. Bolts were fastened with a torque of 10Nm.

**Bare aluminium** Rubber/teflon strips were removed, such that there was direct contact between the aluminium frame and glass specimens. Bolts were fastened with a torque of 10Nm.

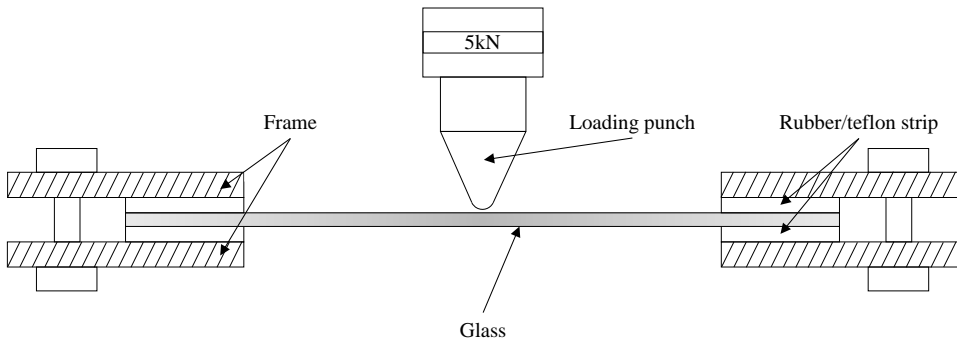
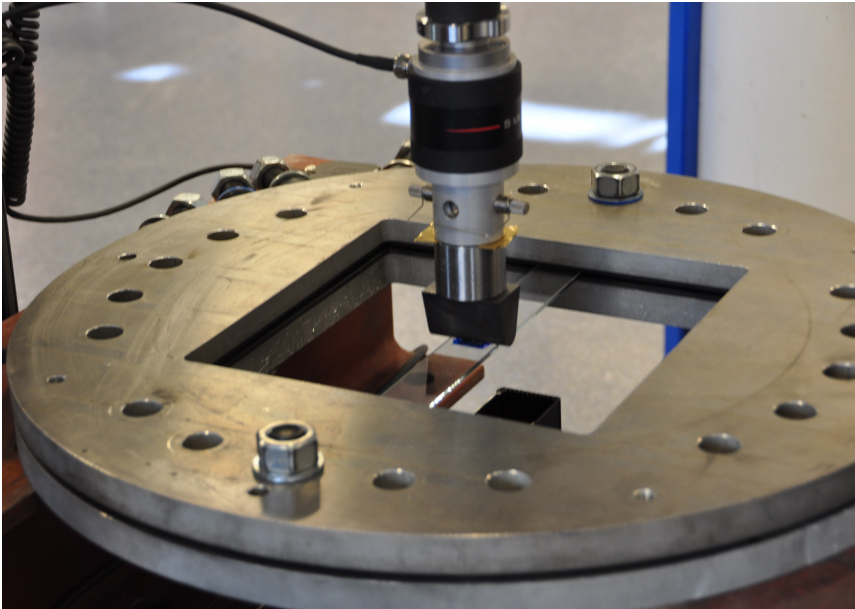


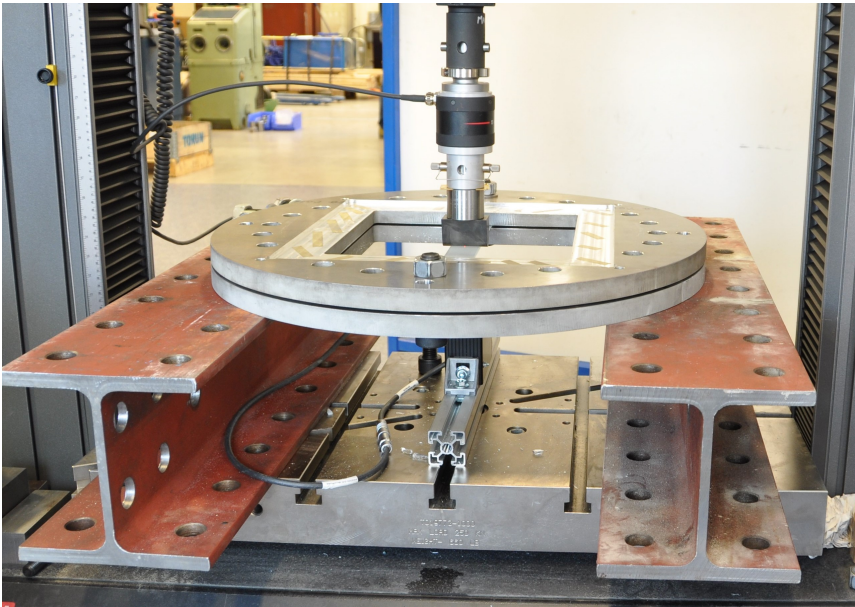
**Figure 4.7:** Schematic showing side view of three point bending test (not to scale).

### Test specimens

Test specimens were made by cutting glass panes made for shock tube testing into ten equal test specimens. This resulted in test specimens of size  $400 \times 10\text{mm}$ , with a thickness of 4mm. The rough edges left after the cutting process were polished, contrary to the samples used in four point bending. But as the results of interest was not variations of the fracture strength within the test series, this difference was regarded as non-important. As the thickness measured on test specimens for four point bending was consistent, and test specimens used in three point bending were made by the same manufacturer, no thickness measurements were taken.



(a) Three point bending test detail.



(b) Three point bending test overview.

**Figure 4.8:** Test setup for three point bending.

## 4.2.2 Results

A total of 21 specimens were tested using different supporting strips along the boundary. 14 tests were done using rubber strips between the specimen and the frame. Of the tests with rubber strips, one was done with grease between the rubber and glass, one was done without fastening the top plate with grease between the rubber and glass, and one test was done without the top plate with grease between the glass and rubber. Three tests were done using teflon strips instead of rubber strips. Four samples were tested without any intermittent strips, such that the glass specimen was in direct contact with the aluminium frame. An overview of the three point bending tests is presented in Table D.1 in Appendix D.

### Force – displacement

Of the 14 experiments conducted using rubber, two were deemed invalid due to the fact that cracks were clearly visible in the specimens prior to the experiments. Figure 4.9 shows the resulting force–displacement curves for all valid tests done with rubber strips and a clamped frame. The displacement data used is the deflection of the specimen's mid point, as measured by laser. As some inconsistencies were experienced related to the

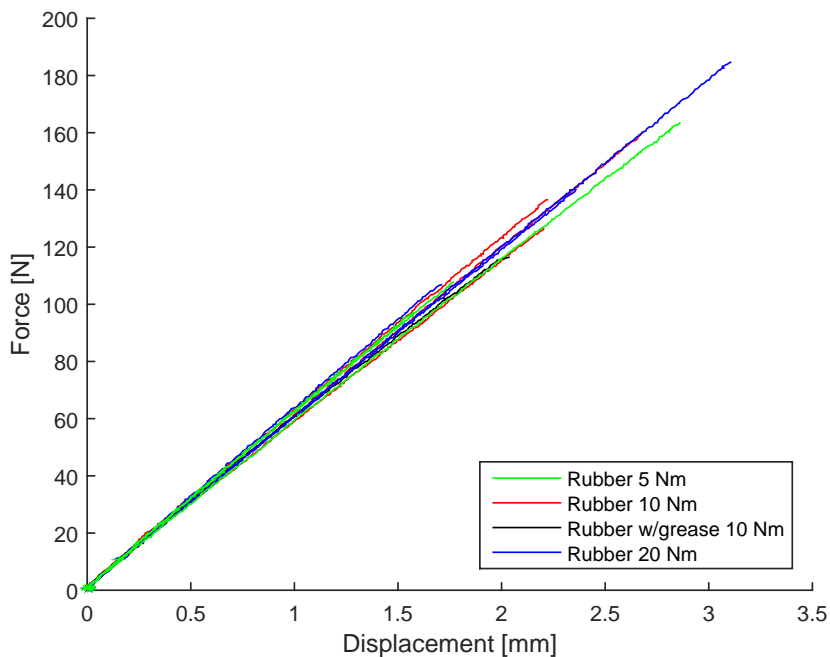


**Figure 4.9:** Force displacement data for different clamping pressures.

displacement at zero force, the results were moved in order for the first data point in each series to start at the origin.

The results with rubber strips were consistent regardless of the fastening torque of the bolts. A linear elastic response with small variations in the slope of the force–displacement curves until fracture was observed for all tests done with rubber strips. It was also observed that the effect of grease between the glass specimen and rubber strip is negligible in the matter of the slope on the force–displacement curve. These results indicate that the fastening torque used has a small influence on the stiffness of the specimen in quasi-static loading.

Although all tests with rubber strips showed a similar force–displacement history, the failure mode was not the same. For increasing fastening torque on the bolts, it was observed that the point of failure moved closer to the supports. The reason for this is not entirely known, but is suspected to be influenced by the rotational angle allowed at the frame, which is suspected to be smaller for a higher fastening torque.

Figure 4.10 shows the force–displacement curves for tests done with teflon strips and bare aluminium, along with a typical test with rubber strips. The results show a consistent slope in the force–displacement curve for each individual support material. In the tests where teflon was used, a higher incline than in tests with rubber is observed. This may be explained by the higher stiffness of teflon compared to the rubber. For the tests where the glass was in direct contact with the aluminium frame, at first a non-linear behaviour is seen which stabilizes to a linear force–displacement relationship with a higher incline than with rubber or teflon strips. The reason for the non-linear behaviour is not entirely known, but it is believed that it may be due to friction between the glass and aluminium, and inconsistencies in the aluminium surface. This may cause the specimen to shift or slide a small distance before it stabilizes.

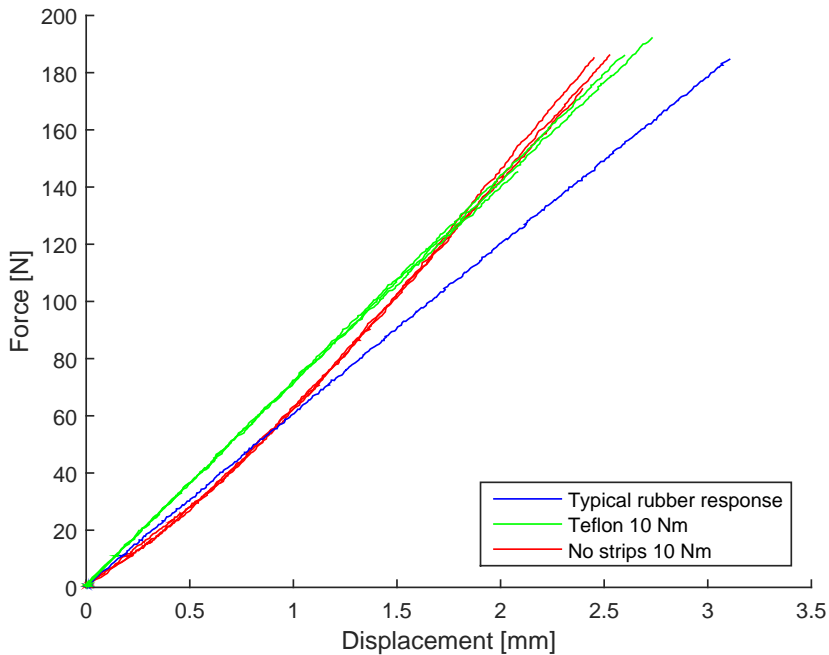


**Figure 4.10:** Force–displacement curves for three different support materials.

### Analytical study of boundary conditions

The relations, found by beam theory, given in Table 2.1 in Section 2.5, were applied in order to gain an indication of whether the three point bending tests could be considered clamped or simply supported. One of the test results with rubber and a fastening torque of 10 Nm was used, and stress and strain was calculated, first assuming the conditions in the test to be simply supported, and then assuming the test to be clamped. As both calculations are linear relationships, these two results give two different slopes on a stress–strain curve.

The test which was done without the top plate was assumed to be simply supported, and used as a reference. The stress and strain in this test was calculated using the relations for a simply supported beam in three point bending. This comparison between the test with and without a top plate is presented in Figure 4.11. The red line is the test which is assumed to be simply supported, and the dashed and solid black lines are results from the test with the top plate, calculated assuming clamped and simply supported boundary conditions respectively.

All test pieces are made from the same material, i.e. have the same elastic modulus and the same cross-section. Thus the red and either of the two black lines should coincide if the assumption that the fastened frame provides either a clamped or simply supported boundary is correct.

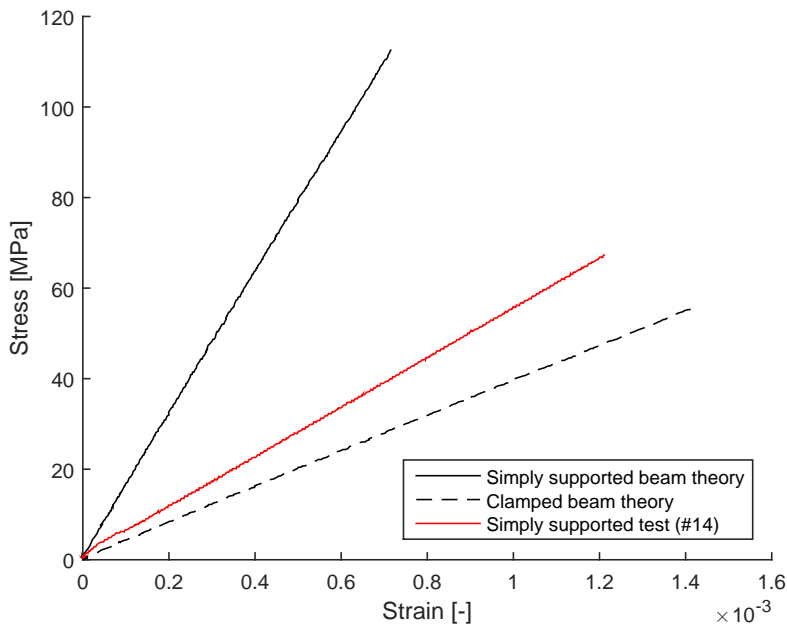


**Figure 4.11:** Stress–strain curves computed assuming the test as both clamped and simply supported, compared to test without top plate.

The result calculated assuming the test with the frame fastened to be clamped, is closest to the results from the test which is assumed to be simply supported, i.e. the dashed black line is closest to the red line. This indicates that the frame fastened with a torque of 10 Nm and rubber strips provides a boundary which is closer to clamped than simply supported. It should be noted that the results found in this section are not sufficient in order to come to a definite conclusion on the boundary conditions, neither in the three point bending tests, nor in the shock tube experiments. There are numerous assumptions which may not be correct, and thus invalidates the results, e.g. that the test without the top plate is simply supported or that beam theory applies in these tests.

# Chapter 5

## Blast experiment

Blast tests on monolithic and laminated glass panes were performed at the SIMLab shock tube facility. A shock tube, rather than explosives was used because it provides a safe alternative, with better possibilities for controlling the environment and data collection. In this chapter, first a general introduction to the shock tube at SIMLab is given, followed by the test setup and experimental results.

### 5.1 The Shock Tube at SIMLab

The blast tests were performed at the SIMLab shock tube facility. The shock tube consists of a high pressure chamber, called the driver, a firing section and a driven section, where the test specimen is located at the end of the driven section as shown in Figure 5.1. The firing section consists of two intermediate pressure chambers, between the driver and driven, that can be separated by membranes which enables the total pressure difference between the driver and driven sections to be achieved stepwise. A test starts by filling the driver and firing section with pressurized air, and the pressure in the intermediate chambers is operated such that the desired pressure is obtained in the driver. The rupture of the membranes is initiated by controlled venting of the intermediate pressure closest to the driver. This ensures a controlled rupture of the membranes, and the sudden release of the high pressure generates a shock wave propagating down the driven section. For further details on the SIMLab shock tube facility, see [4].

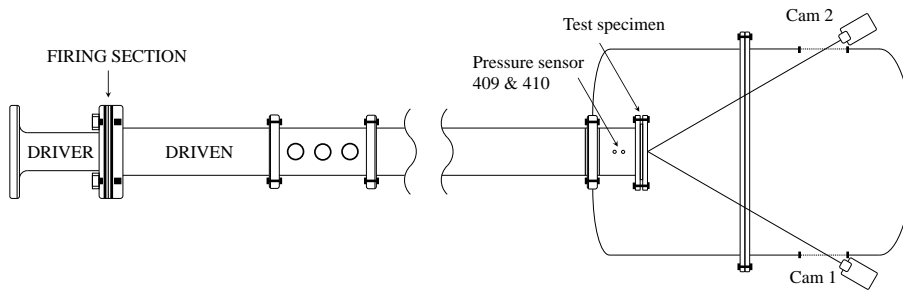


**Figure 5.1:** Schematic illustration of the SIMLab shock tube facility, adapted form [4].

## 5.2 Experimental setup

The blast tests were performed, to the extent possible, in accordance to the European Standard EN 13541 [52]. Some modifications were done, due to limitations in the testing facility. Thus the dimensions of glass panes tested were limited by the shock tube size to  $400 \times 400$  mm instead of the specified  $1100 \times 900$  mm.

Glass panes were fastened in the desired position by clamping between two aluminium plates. Between the aluminium plates and glass panes, neophrene strips of 50 mm width and 4 mm thickness with a hardness of approximately 50 on the International Rubber Hardness Degree (50 IRHD). The aluminium plates were held together over the glass panes using bolts with a measured torque of 10 Nm, applied with a BAHCO torque wrench. Bolts were tightened in the sequence indicated in Figure 5.2b, starting with bolts 1 trough 6 in ascending order, then tightening bolts L1 trough L4 in ascending order, to attach the laser rig.

The tests were monitored using two Phantom v1610 high-speed cameras with 100 mm Nikon lenses recording at 24000 frames per second. Cameras were positioned as indicated in Figure 5.1, in order to utilize DIC-technology for measuring deflection of the glass panes. A previous study done by PhDc Karoline Osnes and Dr. Egil Fagerholt showed that point-tracking, rather than a continuous 3D-field produced better results for measurements on glass. Thus, the glass panes were painted with tracking dots, (1) in Figure 5.3, in a pattern of  $5 \times 5$  dots covering the are of the glass panes. Chequered stickers, (2) in Figure 5.3 were fastened to the aluminium frame, in order to obtain displacements relative to the cameras. The axes inserted in the middle of Figure 5.3 indicates the axis-system utilized when displacements from DIC was extracted. The DIC-software was calibrated using a cylinder with 80 mm diameter equipped with a checkerboard pattern with squares of size  $6.527 \times 6.527$  mm. This should result in a difference in results of approximately 0.07 mm compared to a perfect plane, according to Aune et al. [3].

In order to verify displacement fields calculated with DIC, an optoNCDT 2310-50 laser was attached to the testing rig as shown in Figure 5.2a. Unfortunately, the laser did not suit the stringent conditions in the shock tube well, and failed after only nine tests on monolithic glass.



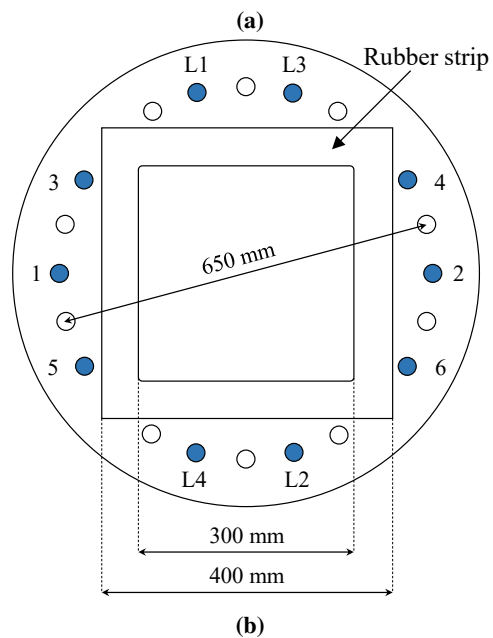
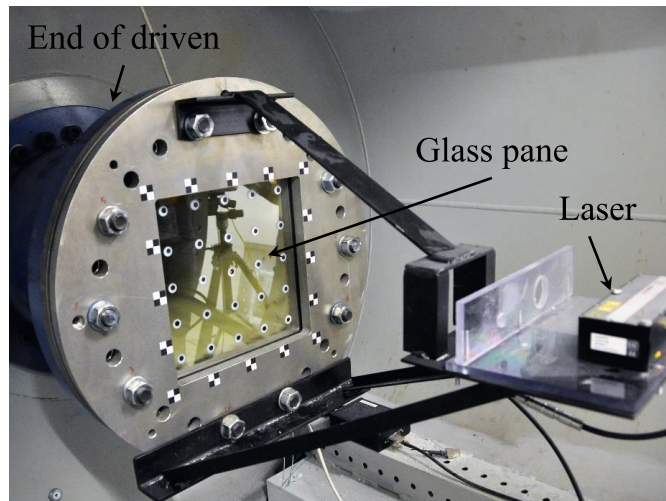


**Figure 5.2:** Test setup in shock tube, (a) glass pane in testing rig with laser attached, and (b) schematic representation of dimensions and bolt tightening pattern.

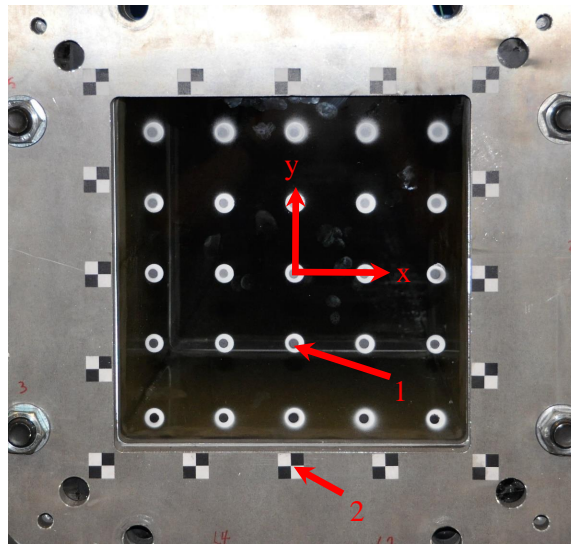


**Figure 5.3:** DIC-tracking dots on glass pane (1), and frame tracking stickers (2).

Friedlander curve fits for all tests were found by using pressures measured at sensor 409, and 410 in the shock tube and using the Curve Fitting Tool in MATLAB [51]. This provided estimates for the peak reflected pressure,  $P_r$ , by extrapolation of the Friedlander curve to the arrival time, and the time of the positive phase,  $t_+$ . The exponential decay coefficient  $b$  was found iteratively, as described in Section 2.1. Constants for the fitted Friedlander curve were further used in the numerical studies.

### Test specimens

Monolithic and single-laminated glass panes, produced by Modum Glassindustri AS, were tested in the shock tube at SIMLab. Monolithic glass panes had dimensions  $400 \times 400$  mm, and a thickness of 4 mm. Laminated glass panes had dimensions  $400 \times 400$  mm, with a 1.52 mm thick PVB interlayer, produced by Eastman Chemical Company, between two 4 mm thick monolithic glass panes. A schematic of the layout of laminated glass panes is shown in Figure 5.4.

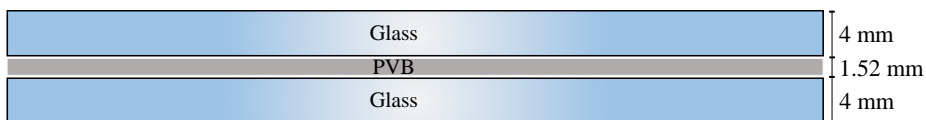


**Figure 5.4:** Layout of the laminated glass tested in this thesis.

No measurements were made of specimen thickness for the monolithic or laminated glass panes as the manufacturer was the same as for the samples used in four point bending, and

these showed a consistent thickness, measurements were deemed unnecessary.

## 5.3 Experimental results

In this Section, results from experiments conducted on monolithic and laminated glass panes in the shock tube at SIMLab are presented and discussed.

### 5.3.1 Monolithic glass

A total of 12 monolithic glass panes were tested at different firing pressures in the shock tube facility. A full list of all tests and key results on monolithic glass panes are provided in Table D.2, Appendix D. Tests are divided into five distinct series based on the firing pressure. All tests were performed under ambient conditions of 20-21 °C and humidity between 33-34%.

#### Series one

The first series was conducted with a desired firing overpressure,  $P_a$ , of 5.7 bar, resulting in a peak reflected pressure,  $P_r$ , of between 1.88 and 1.92 bar, on a total of three glass panes. An overview of the tests in series one is presented in Table 5.1.

**Table 5.1:** Overview of test series one on monolithic glass panes.

Test	Pane number	$P_a$ [bar]	$P_r$ [bar]
MG-5.7-01	1	5.7	-
MG-5.7-02	2	5.7	1.92
MG-5.7-03	3	5.7	1.88

All panes showed total failure in a similar manner. Fracture initiated at or close to the centre with radial crack pattern, which in a short time propagated over the whole pane. Figure 5.5 and 5.6 shows the fracture development of test MG-5.7-03. The pane is almost completely fractured only 0.17 milliseconds after failure initiates, and approximately 0.8 milliseconds after the blast wave reaches the structure. All three tests in the series showed a similar fracture pattern, and time from initial fracture to full failure of the pane.

An indication of how violent the failure of the glass panes was, may be the size of glass fragments found in the dump tank after the test. As the fragments from the test specimen is projected at the back wall, they shatter. For higher impact speeds, smaller fragments is expected. For this test series, the fragments left in the tank were very small, indicating a high impact speed against the back wall.

Pressure loading data was lost in test MG-5.7-01, and thus it is not possible to determine the exact load on the pane in this test. Firing pressure data was recovered, and found to be between the second and third test. As the correlation between firing pressures and reflected pressure was consistent over all tests, the load in the first test is assumed to be within what was observed in test MG-5.7-02 and test MG-5.7-03.

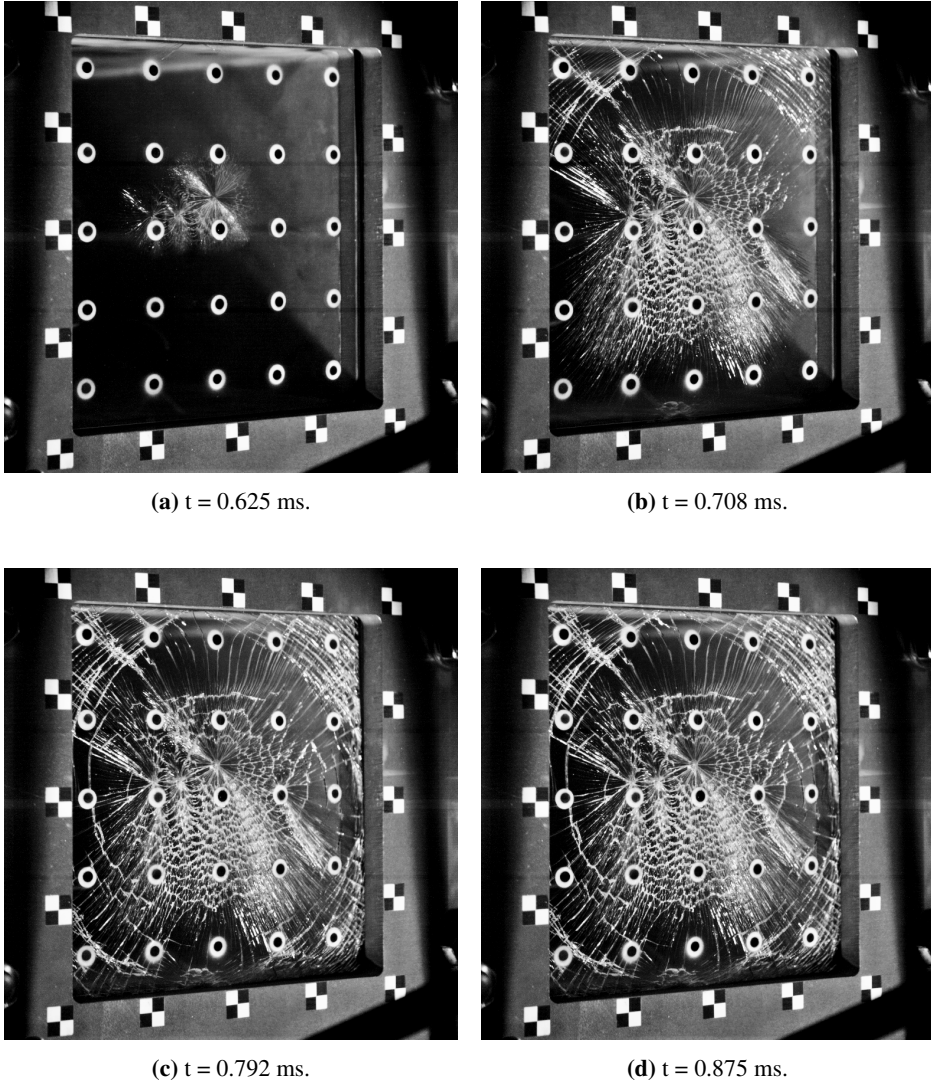
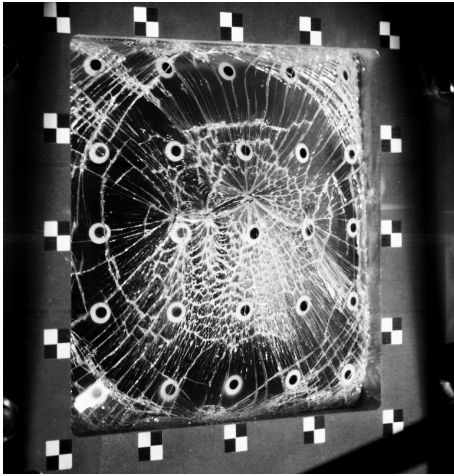
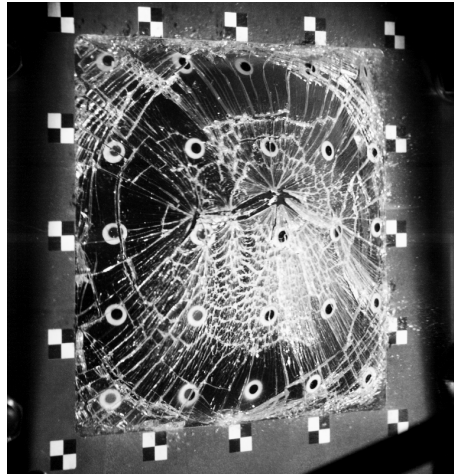


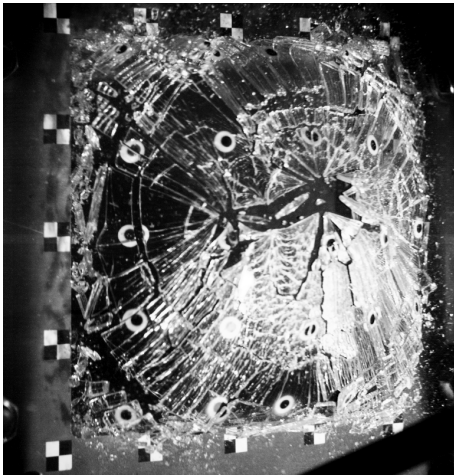
**Figure 5.5:** Fracture progress for test MG-5.7-03.



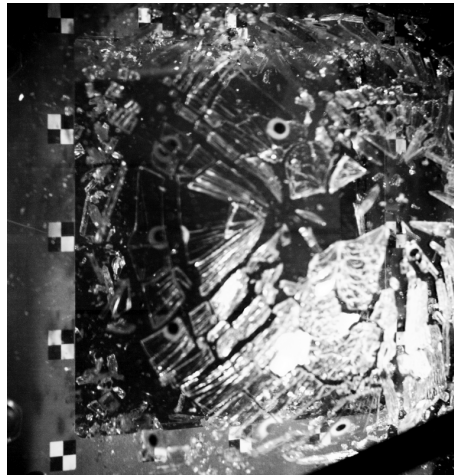
(a)  $t = 2.25$  ms.



(b)  $t = 2.95$  ms.



(c)  $t = 4.25$  ms.



(d)  $t = 5.83$  ms.

**Figure 5.6:** Fracture progress for test MG-5.7-03.

### Series two

As the results from series one showed that the firing pressure chosen was high compared to the capacity of the glass panes. It was decided to do a study to determine an estimate of the range for the capacity of the glass panes. A single pane was chosen, and tested at increasing firing pressures until failure was obtained. An overview of the tests in series two is presented in Table 5.2.

**Table 5.2:** Overview of test series two on monolithic glass panes.

Test	Pane number	$P_a$ [bar]	$P_r$ [bar]
MG-1.6-01	4	1.6	0.64
MG-2.1-01	4	2.1	0.78
MG-2.6-01	4	2.6	0.98
MG-3.6-01	4	3.6	1.25

The firing pressures used in this test ranged from the lowest possible with the membranes available, 1.6 bar, and increasing with the smallest increments possible, until failure of the pane was obtained at a firing pressure of 3.6 bar. This resulted in reflected pressures ranging from 0.64 to 1.25 bar.

The use of a single pane for several tests is not advised. The pane may suffer damage from the tests in the form of propagating micro-cracks, which then invalidates subsequent test results in terms of absolute accuracy. In order to minimize the effect of this, the pane was visually inspected between tests in order to detect damage which may have been inflicted. Although no damage visible with the naked eye was observed, there is no certainty that the pane would have failed at the same pressure, had it only been tested once at this pressure.

### Series three

Based on the results obtained in series two, it was decided to investigate response at a firing pressure of 2.6 bar, a lower pressure than what caused failure for test MG-3.6-01. Three different glass panes were tested at this pressure, discarding panes after one test, regardless of whether it failed or not. Reflected pressures for the three tests was between 0.93 and 0.98 bar, i.e. consistent with a variation of less than 5%. An overview of the tests in series three is presented in Table 5.3.

**Table 5.3:** Overview of test series three on monolithic glass panes.

Test	Pane number	$P_a$ [bar]	$P_r$ [bar]
MG-2.6-02	5	2.6	0.93
MG-2.6-03	6	2.6	0.97
MG-2.6-04	7	2.6	0.98

One of the three panes tested did not fail, and this pane did not show any signs of damage visible to the naked eye. The panes which failed, did so completely, but slightly less violent

than the panes in series 1. Failure occurred in a similar manner to what was observed in series 1, with fracture initiating at or close to the centre, with cracks propagating radially outwards. For the panes which failed there was larger fragments scattered in the dump tank, than what was observed in series 1. This indicated a lower fragment velocity.

### Series four

For the fourth series, the firing pressure was increased to the pressure at which the pane in test MG-3.6-01 failed, i.e. 3.6 bar. This was done to investigate if the failure of the pane in test MG-3.6-01 was influenced by previous tests in series two. Three panes were tested, at a desired firing pressure of 3.6 bar, resulting in a peak reflected pressure ranging from 1.16 to 1.56 bar. An overview of the tests in series four is presented in Table 5.4.

**Table 5.4:** Overview of test series four on monolithic glass panes.

Test	Pane number	$P_a$ [bar]	$P_r$ [bar]
MG-3.6-02	8	3.6	1.16
MG-3.6-03	9	3.6	1.23
MG-3.6-04	10	3.6	1.56

All panes tested failed, with the failure initiating close to the centre in two panes, i.e. similar to the panes tested in series one. Failure in two of the tests, MG-3.6-01 and MG-3.6-02, initiated behind the fastening rubber strip, at the top in the middle.

### Series five

The response in series three and four was dominated by failure of the glass panes. Thus, a series consisting of two tests was done with a firing pressure of 2.1 bar, resulting in a reflected pressure of 0.75 and 0.74 bar. An overview of the tests in series five is presented in Table 5.5.

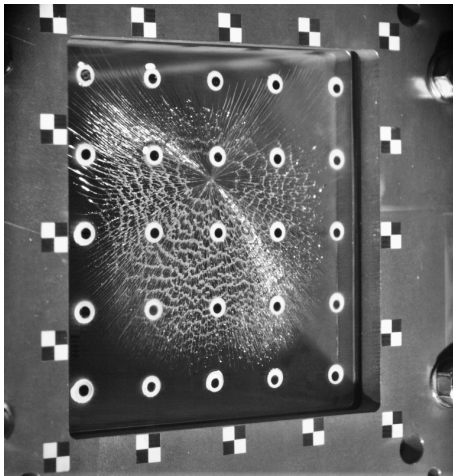
**Table 5.5:** Overview of test series five on monolithic glass panes.

Test	Pane number	$P_a$ [bar]	$P_r$ [bar]
MG-2.1-02	11	2.1	0.75
MG-2.1-03	12	2.1	0.74

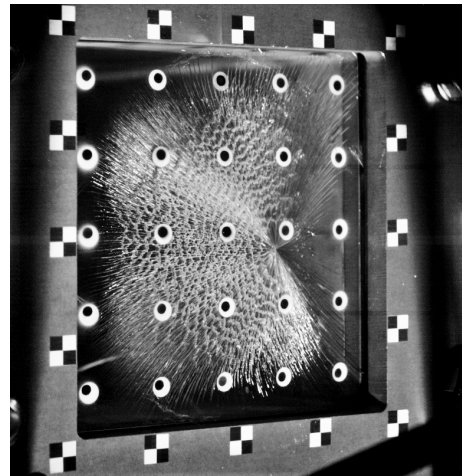
Neither of the two panes tested failed or showed any sign of damage after the tests.

Figure 5.7 shows fracture patterns in four of the eight monolithic panes which failed. Pictures are taken two frames after, i.e. approximately 0.083 ms, the first frame in which fracture is first visible.

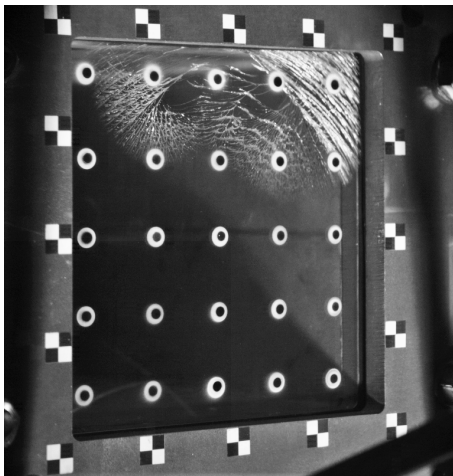




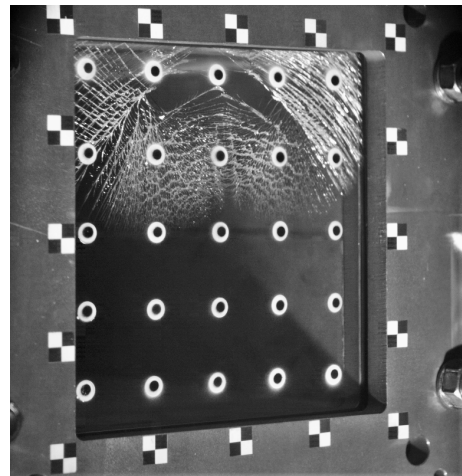
(a) Test MG-2.6-04,  $P_a = 2.6$  bar.



(b) Test MG-5.7-02,  $P_a = 5.7$  bar.



(c) Test MG-3.6-01,  $P_a = 3.6$  bar.



(d) Test MG-3.6-02,  $P_a = 2.6$  bar.

**Figure 5.7:** Fracture patterns in four tests from series one to four on monolithic glass, at  $t = 0.083$  ms after fracture is first visible.

## Pressure and displacement

Figures 5.8 to 5.10 show the centre point displacement, as measured with DIC point-tracking, the pressure measured in sensor 409 and the Friedlander curve fit for all test done on monolithic glass panes, except MG-5.7-01. Note that axes have been scaled in order for the data to utilize the whole figure.

The centre point displacement for all panes which did not fail reached a maximum at approximately 1.9 ms after the blast wave reached the panes. The panes oscillated, and the oscillations decay towards zero over time. The centre point displacement for the panes which failed are cut off at 10 mm, as no meaningful information is shown by plotting these for larger displacements. It should however be noted that tracking was possible after failure occurred, discussed further in Section 5.3.3.

The positive phase of the pressure curve is much shorter in the tests where the glass failed. Believed to be caused by the fact that as the glass fails, there was nothing for the blast wave to be reflected by. This is discussed further in Section 5.3.5. It is worth noting that this effect results in a less than optimal Friedlander curve fit, and thus uncertainty in peak reflected pressures calculated for these tests are higher.

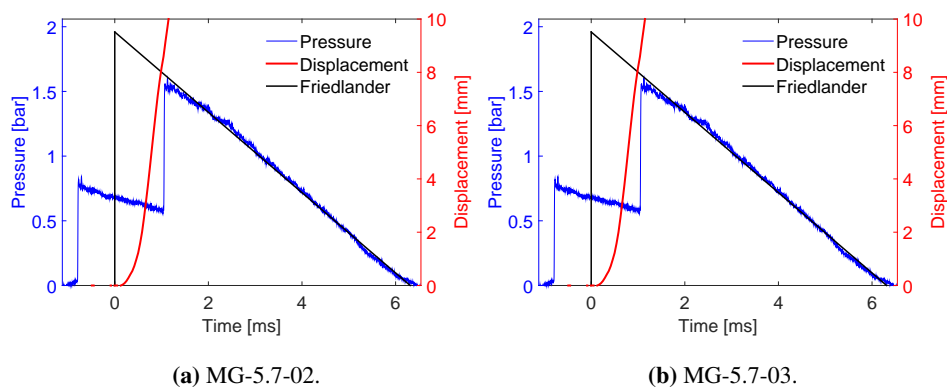


**Figure 5.8:** Pressure and displacement for tests on monolithic glass panes.

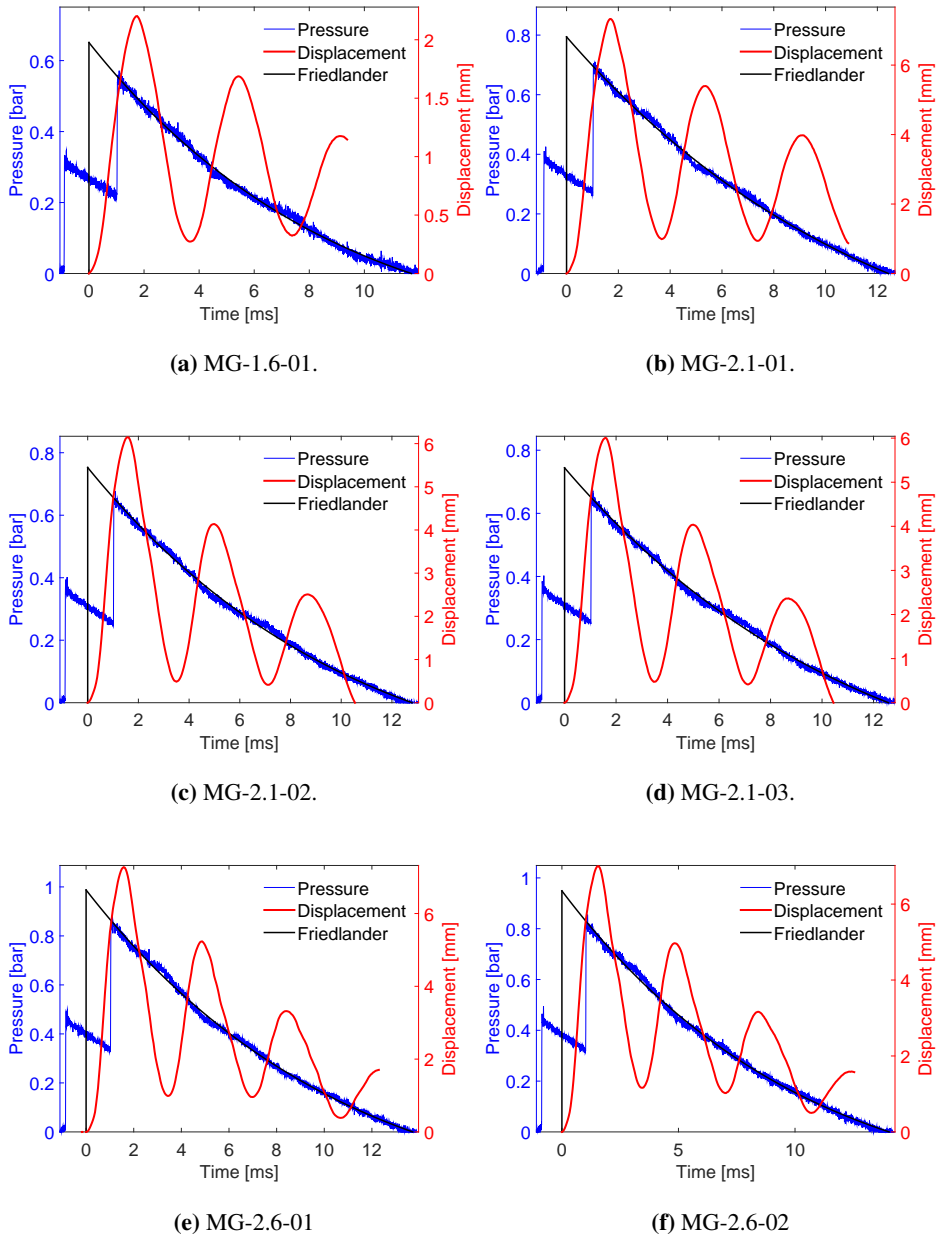


**Figure 5.9:** Pressure and displacement for tests on monolithic glass panes.

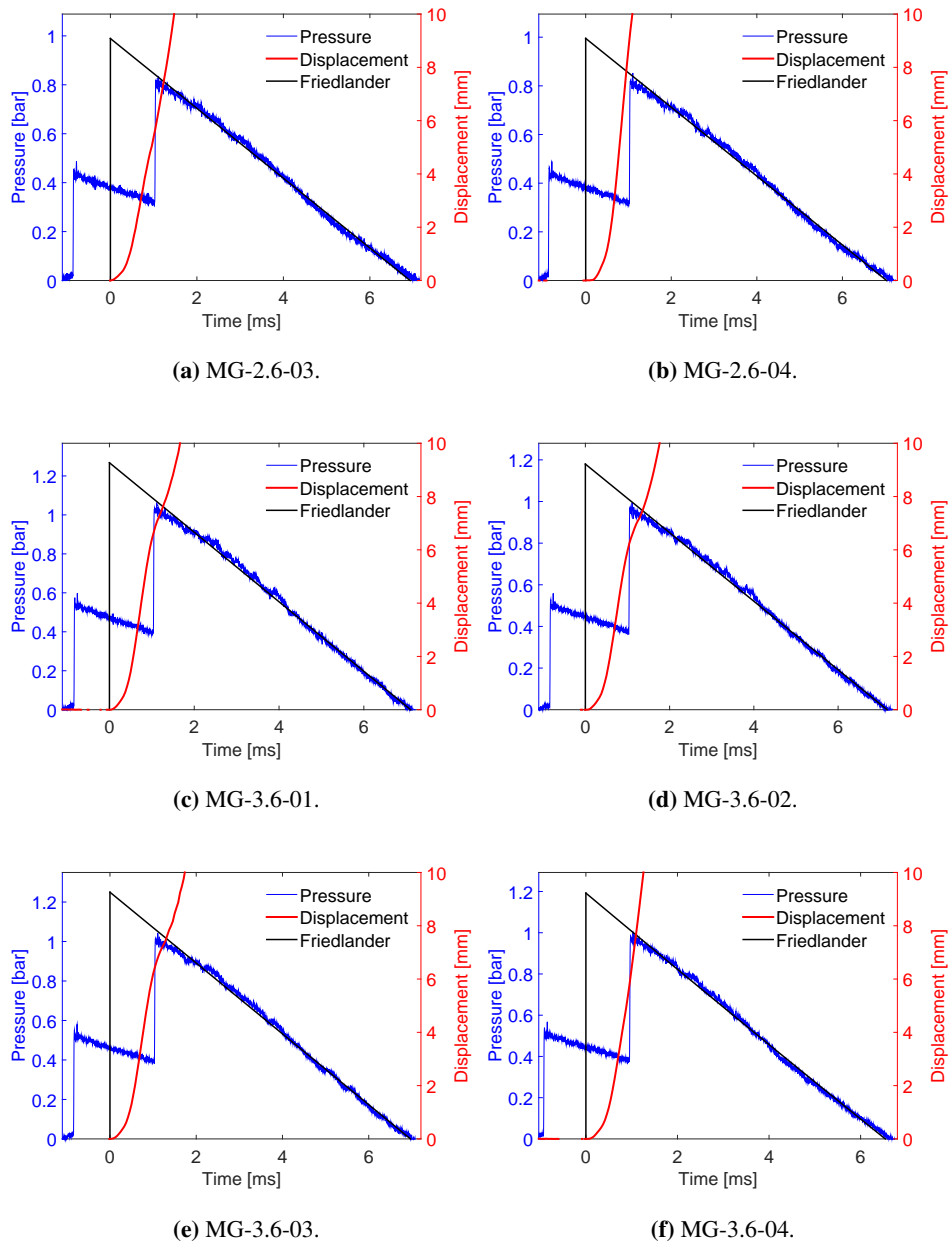


Figure 5.10: Pressure and displacement for tests on monolithic glass panes.

### 5.3.2 Laminated glass

A total of 9 laminated glass panes were tested at different firing pressures in the shock tube facility. A full list of all tests and key results on laminated glass panes are provided in Table D.2, Appendix D. Tests are divided into four distinct series based on the firing pressure. All tests were performed under ambient conditions of 20-21 °C and humidity between 33-34%.

#### Series one

As for the monolithic glass panes in Section 5.3.1, a series of tests in order to determine a preliminary capacity estimate of the panes were done. A single laminated glass pane was tested at increasing firing pressures until failure was observed. The test specimen was visually inspected after each test in order to detect damage. Based on a previous unpublished study done on similar laminated glass panes by PhDc Karoline Osnes at NTNU, it was decided to start with a firing pressure of 5.7 bar, increasing in small increments to a final firing pressure of 10.3 bar. An overview of the tests in series one is presented in Table 5.6.

**Table 5.6:** Overview of test series one on laminated glass panes.

Test	Pane number	$P_a$ [bar]	$P_r$ [bar]
LG-5.7-01	13	3.6	1.77
LG-6.7-01	13	3.6	1.89
LG-7.7-01	13	7.7	2.00
LG-8.5-01	13	8.5	2.33
LG-10.3-01	13	10.3	2.76

No damage was visible after the first four tests, reaching a firing pressure of 8.5 bar. It was thus decided, in order to make use of the limited time in the testing facility, to increase the firing pressure by two times the smallest increment to 10.3 bar.

At a firing pressure of 10.3 bar complete failure of both glass panes and the intermittent PVB-interlayer was observed after the test. It was found that the PVB-interlayer did not fail under loading by the initial blast wave, only the glass panes did. The PVB-interlayer failed during a second, reflected blast wave. The second loading is outside the scope of this thesis, and is thus disregarded.

#### Series two

A firing pressure of 10.3 bar caused complete failure of the laminated glass pane in test LG-10.3-01. Thus, for series two, a firing pressure of 9.6 bar was decided, as this was omitted in series one. Resulting reflected pressures was consistent, between 2.37 and 2.38 bar.

Four panes were tested in series two, continuing the practice of tests on monolithic glass panes. Testing a pane once, visually inspecting it for damage after each test, and discarding the pane before a new pane was tested. An overview of the tests in series two is presented in Table 5.7.

**Table 5.7:** Overview of test series two on laminated glass panes.

Test	Pane number	$P_a$ [bar]	$P_r$ [bar]
LG-9.6-01	14	9.6	2.37
LG-9.6-02	15	9.6	2.38
LG-9.6-03	16	8.8	-
LG-9.6-04	17	9.6	2.37

Of the four panes tested in series two, three of these failed. In tests LG-9.6-03 and -04, only one glass pane failed, and in test LG-9.6-02, both of the glass pane failed. None of the panes tested in this series showed signs of rupturing of the PVB-interlayer.

In test LG-9.6-02, both the front and back glass panes failed. The front pane failed first, with failure initiating close to the centre, and fracture propagating radially, shown in Figure 5.11. After complete fracture of the front pane, the back pane failed, with fracture initiating at the top left corner propagating diagonally towards the bottom left right, shown in Figure 5.12. Figure 5.13 shows the deformation after both glass panes failed completely.

In tests LG-9.6-03 and LG-9.6-04, only the front pane failed. This did so in a similar manner to the front pane in test LG-9.6-02, but without failure of the back pane. Subsequent inspection of the laminated glass panes revealed no visible damage to the back pane.

In test LG-9.6-03, the membranes regulating the firing pressure failed prematurely. This means that for this test, the firing pressure was 8.8 bar, about 0.8 bar lower than desired. As data logging and high-speed camera recording is initiated when firing is manually triggered, no data was available except driver filling pressures, and thus recorded firing pressure.

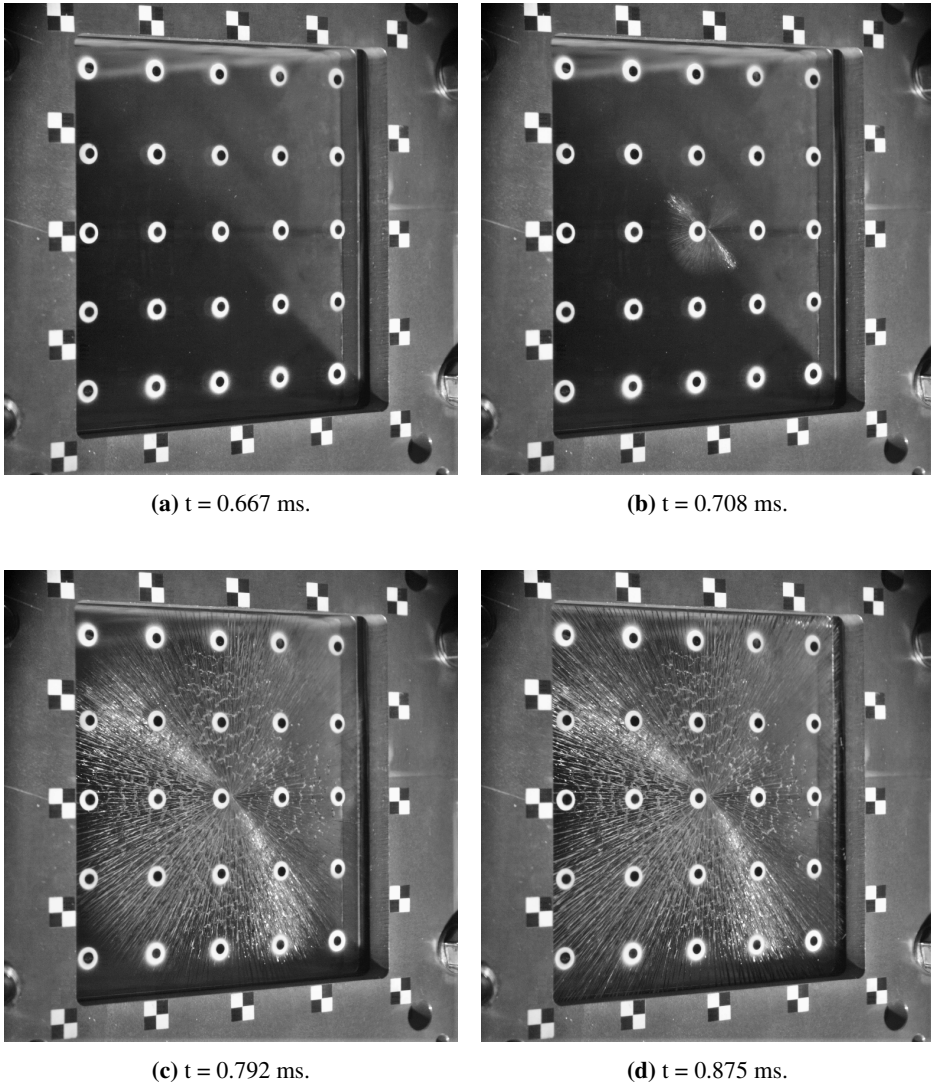
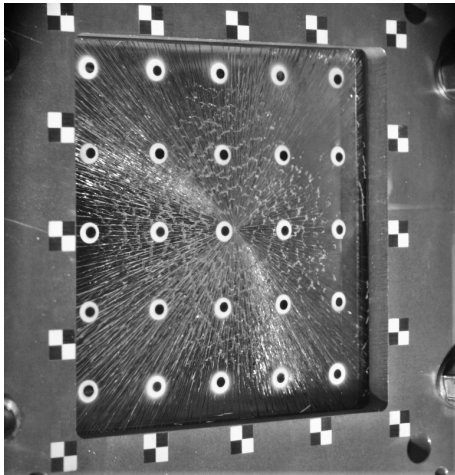
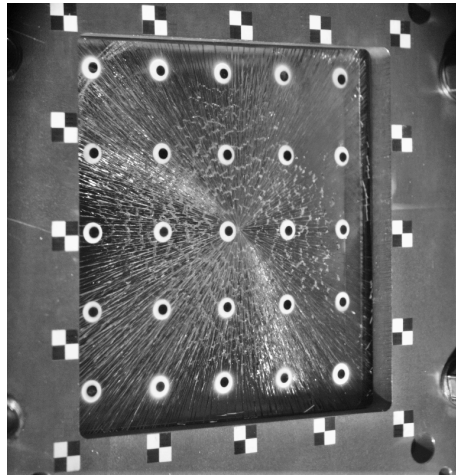


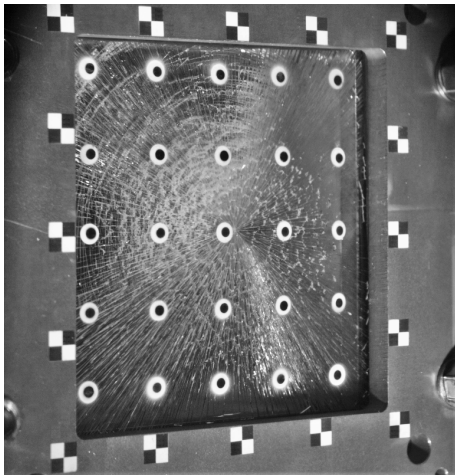
**Figure 5.11:** Fracture progress of the front pane in test LG-9.6-02.



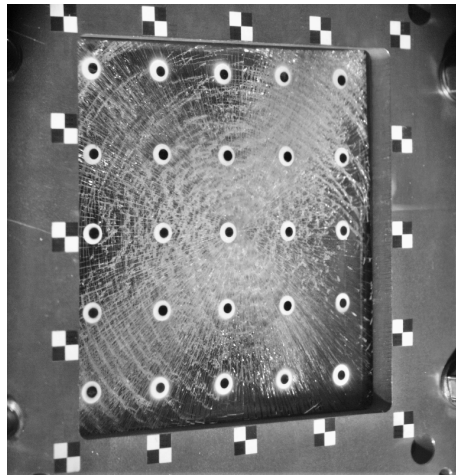
(a)  $t = 1.584$  ms.



(b)  $t = 1.625$  ms.



(c)  $t = 1.708$  ms.



(d)  $t = 1.792$  ms.

**Figure 5.12:** Fracture progress of the back pane in test LG-9.6-02.



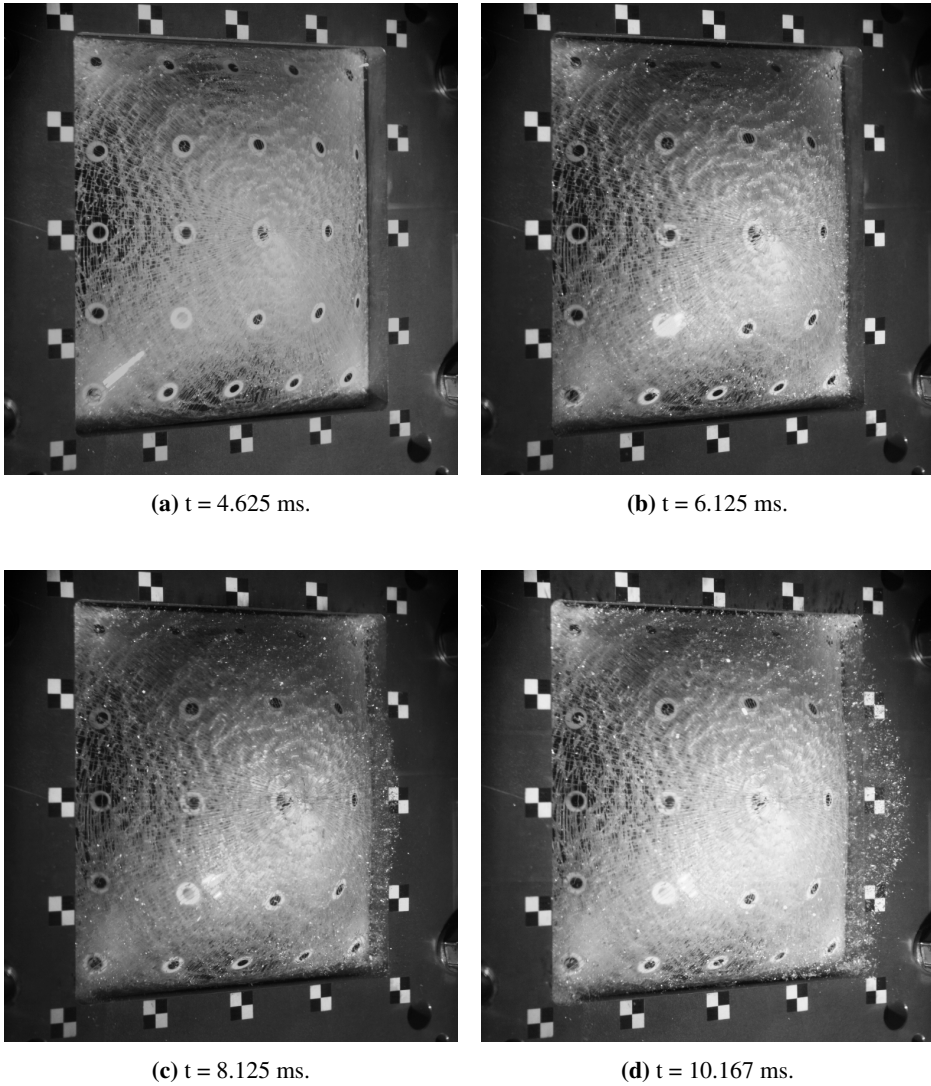


**Figure 5.13:** Test LG-9.6-02 after failure in both panes.

### Series three

For the third test series, the firing pressure was reduced to 8.6 bar, as the pane in test LG-9.6-03 failed at a firing pressure of 8.8 bar. Reflected pressures were 2.32 and 2.42 bar for the first and second test respectively. Due to restricted time in the testing facility, only two panes was tested in this series. An overview of the tests in series three is presented in Table 5.8.

**Table 5.8:** Overview of test series three on laminated glass panes.

Test	Pane number	$P_a$ [bar]	$P_r$ [bar]
LG-8.6-01	18	8.6	2.32
LG-8.6-02	19	8.6	2.42

Neither of the tested panes failed or showed any signs of damage after the tests.

### Series four

For the fourth and last series, the firing pressure was again increased to 10.3, the pressure at which the pane in test LG-10.3-01 failed. Reflected pressures was 2.68 and 2.76 bar for the first and second test respectively. An overview of the tests in series four is presented in Table 5.9.

**Table 5.9:** Overview of test series four on laminated glass panes.

Test	Pane number	$P_a$ [bar]	$P_r$ [bar]
LG-10.3-01	20	10.3	2.68
LG-8.6-02	21	10.3	2.76

In both tests in series four, both the front and back glass panes failed, with the PVB-interlayer staying intact. Failure in both front panes initiated close to the centre propagating radially, with the back panes failing in a similar manner.

### Pressure and displacement

Figures 5.14 and 5.15 show the centre point displacement, as measured with point-tracking using DIC, the pressure measured in sensor 409 and the Friedlander curve fit for all test done on laminated glass panes, except LG-9.6-03. Note that axes have been scaled in order for the curves to utilise the entire designated space.

In tests were neither of the glass panes failed, the trend in displacement is the same as for monolithic panes. In test LG-9.6-04, where one pane failed, shown in Figure 5.15c, the maximum displacement is higher, and oscillations are smaller and damped faster. When both glass panes failed,

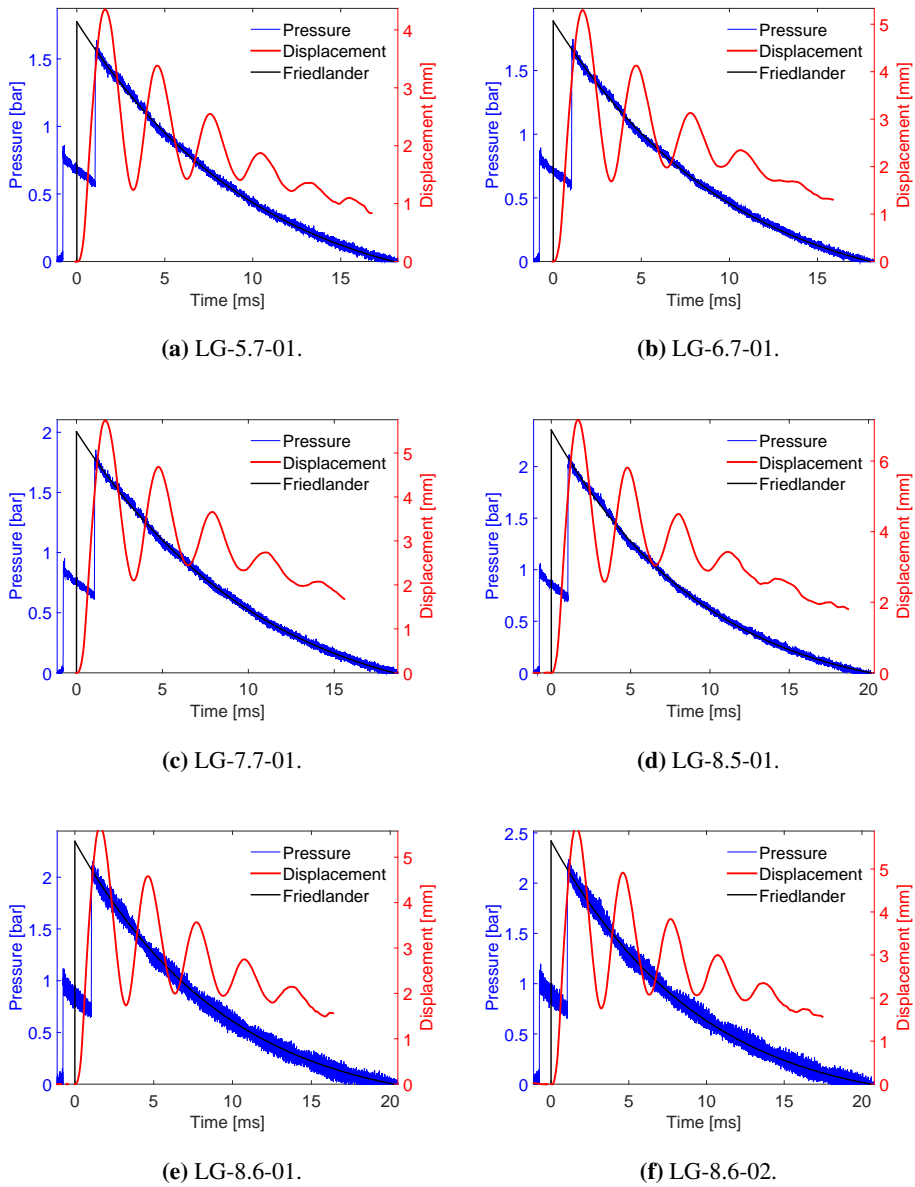


**Figure 5.14:** Pressure and displacement for tests on laminated glass panes.

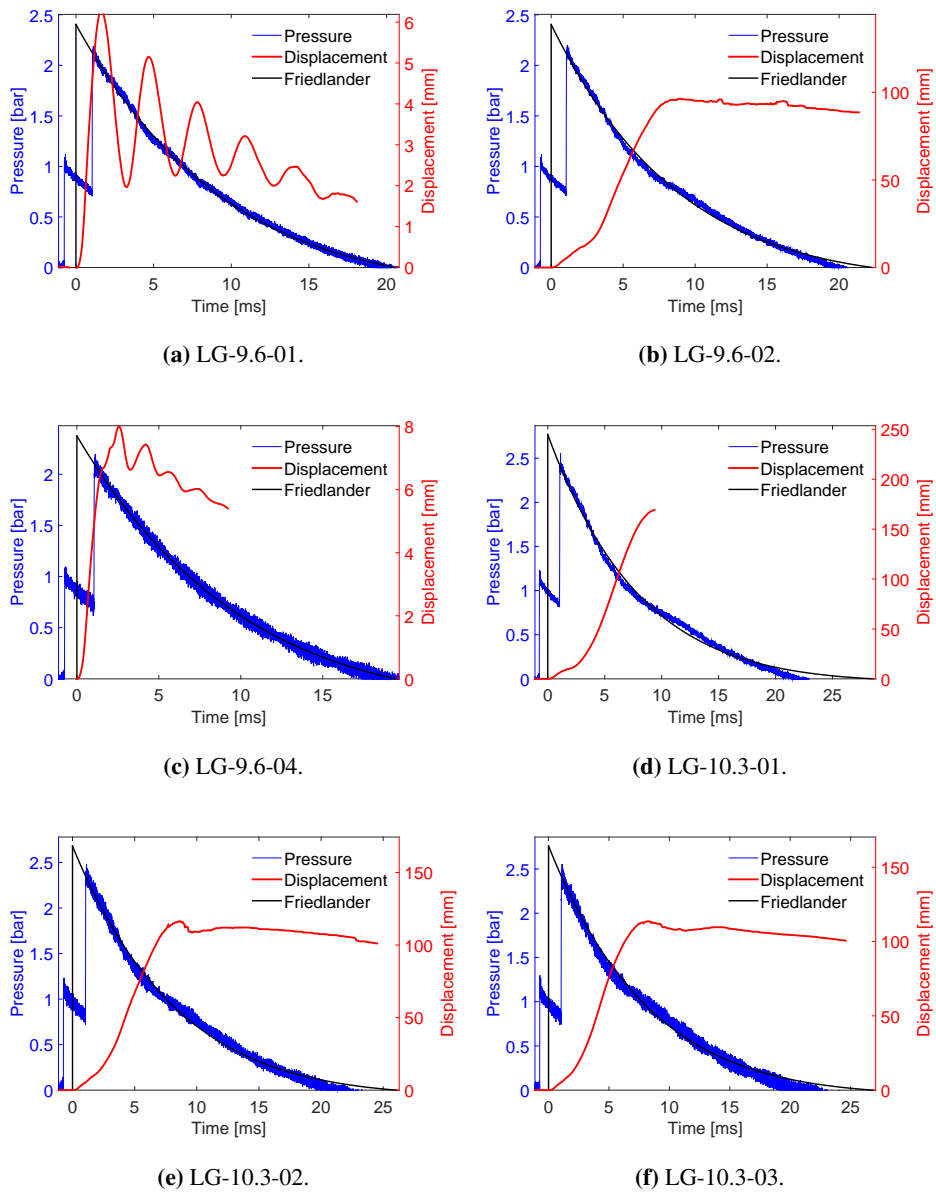
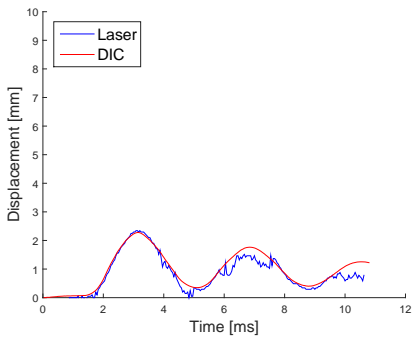


Figure 5.15: Pressure and displacement for tests on laminated glass panes.

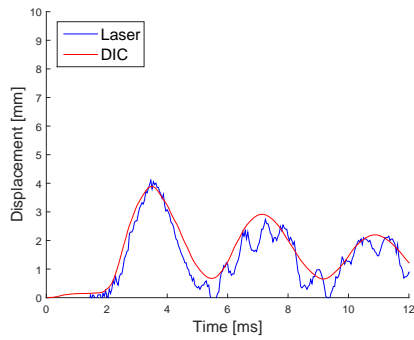
### 5.3.3 Validation of DIC-measurements

In the first nine tests on monolithic glass, the centre-point deflection of the glass panes was measured using both DIC and laser. After nine tests, the laser failed because of insufficient protection against high-velocity glass fragments. As a result of this failure, a verification is important in order to determine if results from DIC-measurements are reliable. Figure 5.16 shows a comparison between centre-point displacements measured with DIC and laser, for six of the nine tests where the laser was operational. The comparison gives an indication of the accuracy of DIC measurements, as the performance of DIC in this application is not tested as thoroughly as the laser. Note that the relative displacement between the testing rig and the high speed cameras, caused by the recoil when firing, is omitted here. The effect of this rig-displacement was found to be small compared to the displacement of the glass.

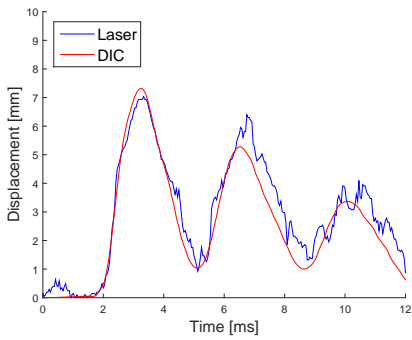
It is observed that displacements measured using DIC and laser coincide well, not only for the panes where no failure occurred, shown in Figures 5.16a to 5.16d, but also where the panes failed, shown in Figures 5.16e and 5.16f. This should be emphasized as this information can be utilized in further studies, as in the calculation of fragment velocities, presented in Section 5.3.5. It should however be noted that uncertainties are present in both the laser and DIC-measurements. The laser is subjected to vibrations in the rig connected to the frame that also experiences displacement, while the DIC-measurements are very sensitive to software calibration. For further studies where no data from laser measurements was available, it was assumed that the DIC measurements provided sufficient results.



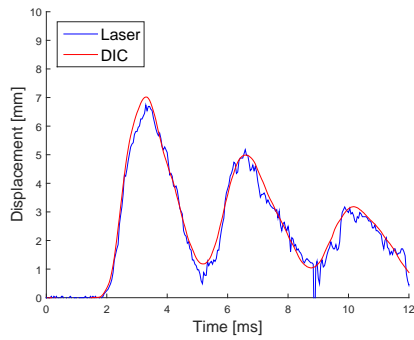
(a) MG-1.6-01.



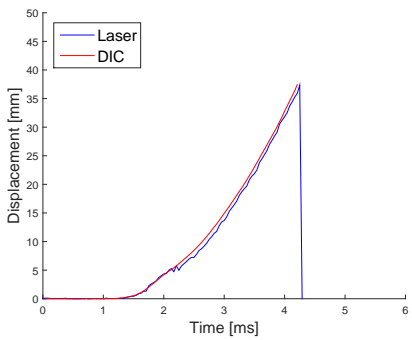
(b) MG-2.1-01.



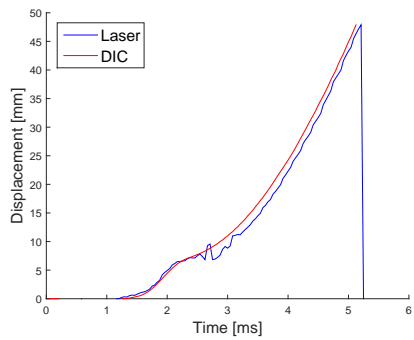
(c) MG-2.6-01.



(d) MG-2.6-02.



(e) MG-2.6-03.



(f) MG-3.6-01.

Figure 5.16: Validation of the DIC measurements.

### 5.3.4 Boundary conditions

In order to determine the variation in boundary conditions during blast loading of the glass panes, displacement of the clamping frame was determined with DIC-measurements from point-tracking the chequered stickers fastened to the frame.

Figure 5.17 shows the frame displacement relative to the high-speed cameras at three times during the test LG-10.3-03, the test where maximum displacement of the frame was found. Here  $t = 0$  ms is the time at which the shock wave reaches the glass pane, and  $t = 1.4167$  ms is the time at which displacement of the frame midpoints is at a maximum.

The frame has a uniform, negative displacement, i.e. in the opposite direction of the propagating shock wave, before the shock wave impacts the glass pane. This is likely caused by the test rig recoil when it is firing. As the shock wave impacts the glass pane, the frame has a uniform displacement at a maximum of approximately 0.5 mm. In addition, the frame bends, causing a relatively uniform curvature of each side. The average maximum difference in displacement, i.e. the difference between corners and midpoints on all four sides, is 0.8 mm.

In all tests the frame showed similar behaviour, both a uniform displacement of the testing rig relative to the high-speed cameras, and bending of the frame. Maximum displacement and curvature of the frame showed an overall trend to depend on the peak reflected pressure, i.e. load magnitude. The largest displacements was found for the greatest pressure, and the smallest displacements for the lowest pressure. Although for some tests, this is not the case. This is especially noticeable in tests MG-2.6-01, -02 and -03.

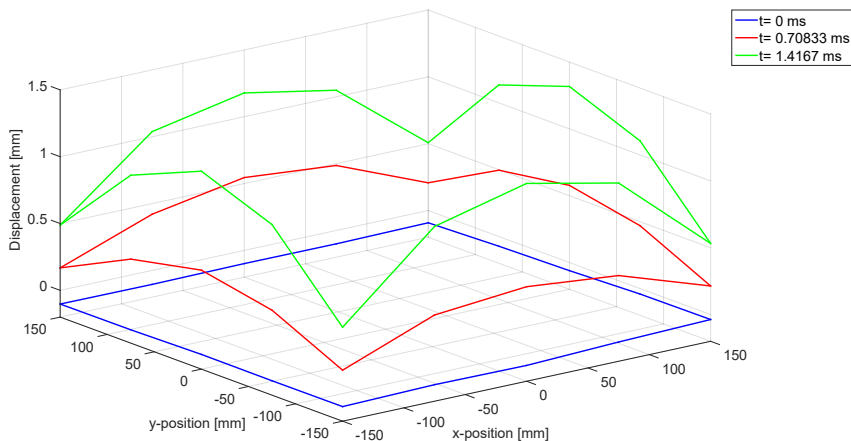


**Figure 5.17:** Displacement of clamping frame in test LG-10.3-03.

The variations in elastic response of the glass panes is especially noticeable in tests MG-2.1-01, -02 and -03. The displacement of the glass centre point in the first three mil-

liseconds after the blast wave impacts the glass in these tests, as measured with DIC, is presented in Figure 5.18.

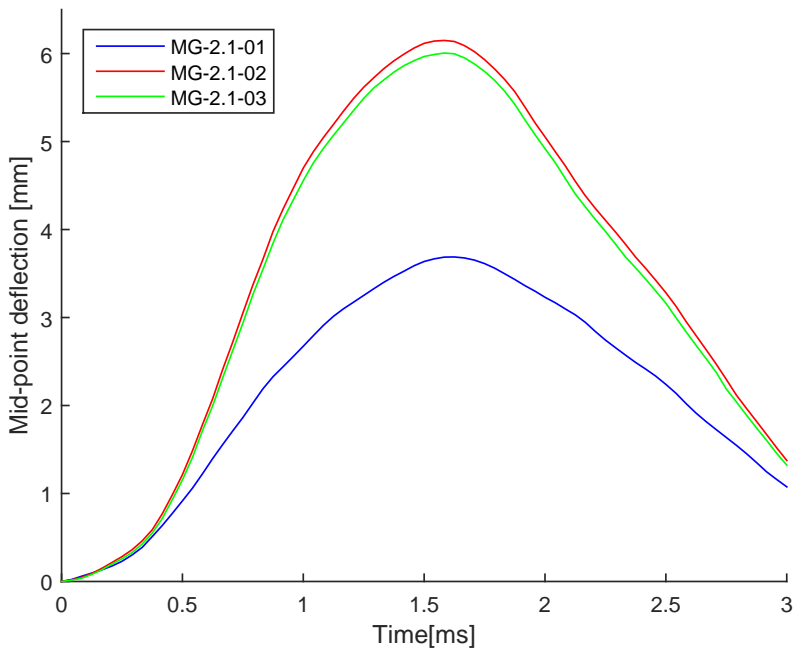


**Figure 5.18:** Centre-point displacement from tests MG-2.1-01, -02 and -03

The displacement of the frame and glass panes in these tests are shown in Figures 5.19 to 5.21. Here, both the frame and glass displacement profile is shown at the time of maximum mid-point deflection of the glass, approximately 1.9 ms after impact of the shock wave. The glass pane displacement profile is extracted from the five points at  $y = 0$ , i.e. the points horizontally across the centre of the pane.

For MG-2.1-01, the maximum mid-point displacement is 3.90 mm. For MG-2.1-02 and -03, the maximum mid-point displacement is approximately 6.1 mm. The difference in reflected pressure, see Table D.2 in Appendix D, is not excessive and was not expected to result in such a differing displacement response.

These results indicate that there probably is a correlation between frame and glass displacement, although two separate results is insufficient for a clear conclusion. It is believed that the difference in mid-point displacements in tests MG-2.1-01, -02 and -03 may be caused by a different fastening torque used at test setup. Even though care was taken in order to apply a consistent torque to the bolts, the accuracy of the torque wrench used was limited and only a small difference may have resulted in the variation seen.



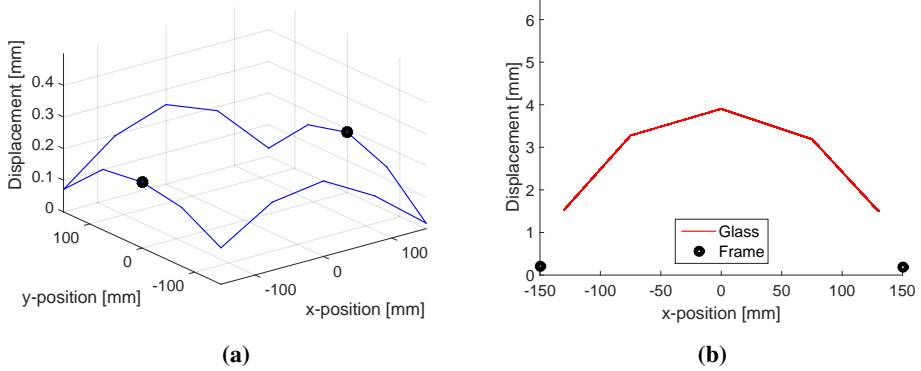


**Figure 5.19:** Maximum displacement of frame (a) and glass (b), in test MG-2.1-01

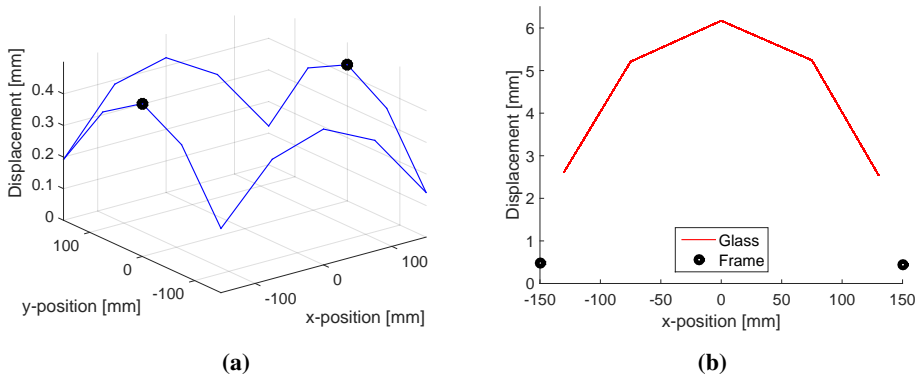


**Figure 5.20:** Maximum displacement of frame (a) and glass (b), in test MG-2.1-02

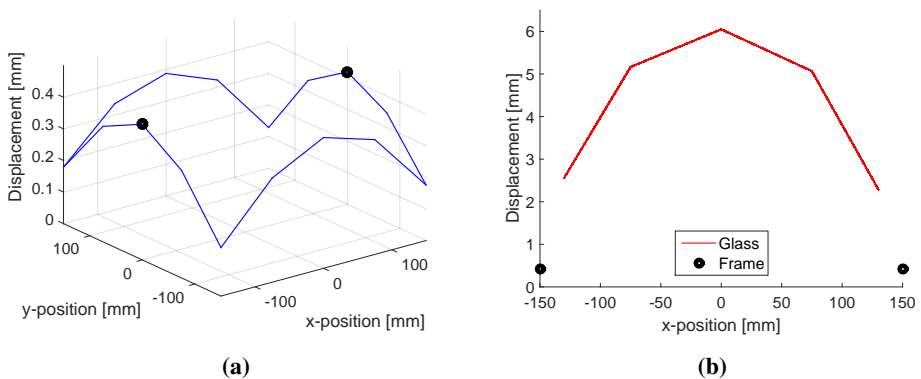


**Figure 5.21:** Maximum displacement of frame (a) and glass (b), in test MG-2.1-02

### 5.3.5 Design aspects

#### Fragment velocity

The creation of high velocity glass fragments is a highly detrimental mechanism resulting from fracture in a blast loaded monolithic glass pane. Thus, the relationship between the velocity of the incident blast wave, and glass fragments are of interest when considering damage caused by blast loading. Figure 5.22 shows the fragment velocity compared to shock wave velocity in the tests on monolithic glass where failure occurred. The fragment velocity data is calculated from the last DIC measurement of each series, due to the constant acceleration within the dataset. The shock wave velocity is calculated assuming a uniform and constant shock front, and using distance between sensor 409 and 410 in the shock tube, shown in Figure 5.1. The time of arrival at each sensor enables the calculation of the average velocity of the shock wave across this distance.

There seems to be a trend showing that higher shock wave velocity yields higher fragment velocities. There also seems to be a relationship between fracture pattern and fragment velocity, a fracture pattern that initiates at the boundary seems to lead to a lower fragment velocity than if fracture initiates at the centre of the pane. Different fracture patterns are shown in Figure 5.7. It is believed that the reason for this may be that when the glass panes break along the boundary, the glass will absorb more energy before being pushed out of the frame, leading to a lower fragment velocity.

#### Intact versus fractured glass

Upon fracture of glass panes in a blast loaded building, the energy that enters a room may cause severe damage. Ceiling plates may drop, and interior may be thrown around inside the room, causing possible fatalities. In the experiments conducted it was found that for the same incident blast pressure, one pane fractured and another remained intact, see Table D.2 in Appendix D.

By comparing results from tests at the same firing pressure, it is possible to find an indication of the impulse travelling through the window pane when fracture occurs. Figures 5.23a and 5.23b show two reflected pressure curves, where one curve represents a pane that fractured and the other represents a pane that remained intact. In figure 5.23a it is observed that the pressure–time histories from the two experiments with monolithic glass is starting to deviate from each other approximately 2 ms after peak reflected pressure. This is when the effect of the glass pane fracturing first reaches the pressure sensor, and a lower pressure is measured. Integrating each of the pressure–time histories gives the amount of energy, or rather impulse per area, that penetrates the pane. This value is 40% lower for the case where the glass pane fails, symbolised by the area between the red and blue curve. It is observed that for the laminated glass, as shown in Figure 5.23b, the two pressure–time histories coincide and the impulse per area are equal in both experiments. This means that all incident pressure is reflected for both panes. This indicates that the use of laminated glass panes, in addition to reducing the size and number of glass fragments,

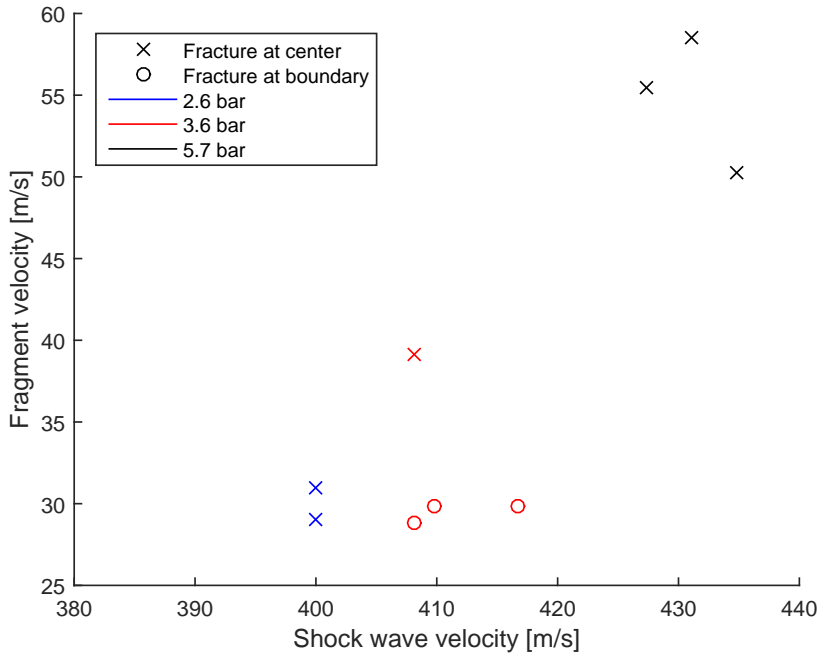


**Figure 5.22:** Fragment velocity versus shock wave velocity for the monolithic panes that fractured.

may prevent some of the energy carried by the shock wave from entering the space behind the glass when it fails.

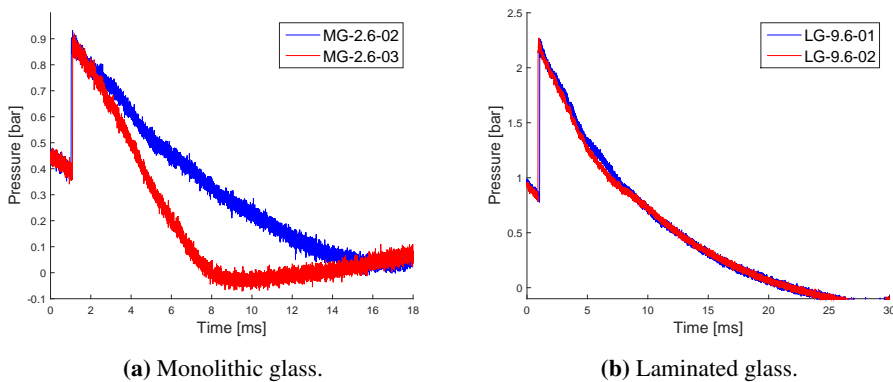


**Figure 5.23:** Pressure–time history of the reflected pressure at sensor 409 in the shock tube, displaying the difference between fracture and no-fracture.



# Numerical modelling: Four point bending test

In order to get an understanding of what is possible to achieve with the different material models presented in Section 3.2, a study of material and failure modelling techniques was conducted by doing analyses based on the four point bending tests.

## 6.1 Numerical model

A general representation of the model used for simulation of the small,  $100 \times 20$  mm, four point bending tests is shown in Figure 6.1. Here the glass is modelled by shell elements, with an element size of  $1 \times 1$  mm. Since modelling of failure was of interest, no use of symmetry was applied. It should be noted that the small element length compared to element height in the shell elements is not a problem in this model, as the model's loading span is large compared to the thickness of the glass pane.

The loading cylinders were modelled as analytical rigid parts (*\*RIGIDWALL\_GEOMETRIC\_CYLINDER\_(MOTION)*). The bottom cylinders were fixed in all 6 degrees of freedom (DOF). The loading cylinders were fixed in all DOF, except translational movement in the z-direction. Contact between the cylinders and glass specimen is modelled without friction.

In order to calculate contact between the analytical surface and the model, material properties for the analytical surface is required. These were chosen as,  $E = 210$  GPa,  $\nu = 0.3$ , and  $\rho = 7850$  kg/m<sup>3</sup>, generic elastic parameters for steel [16].

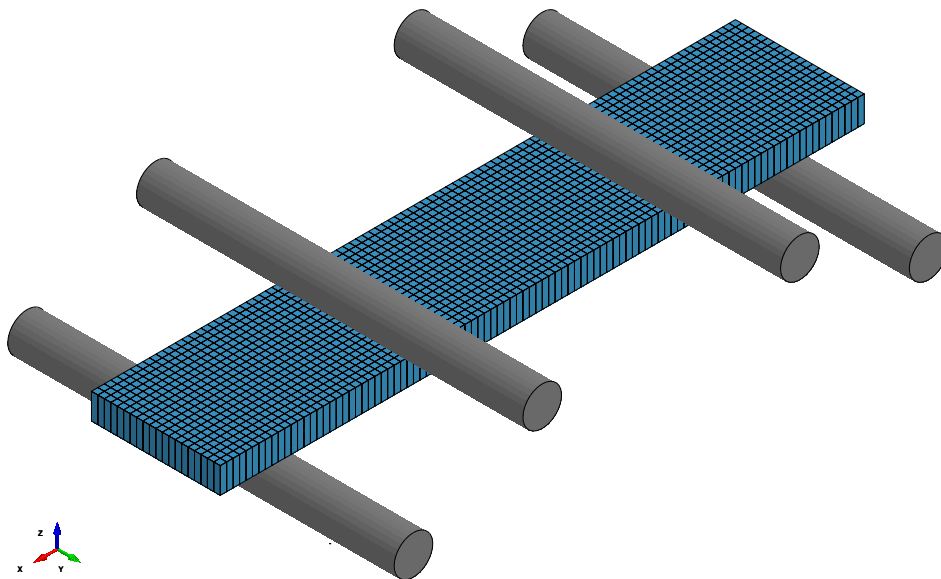


**Figure 6.1:** Numerical model used for simulation of material tests.

## 6.2 Preliminary study

In order to obtain a good numerical foundation for comparison of the material models, a preliminary study was performed using *MAT\_001*, without modelling failure. The relevant results from this study is presented in the following.

### 6.2.1 Young's modulus

Until fracture, the characteristic response in glass is linearly elastic characterised by Young's modulus,  $E$ . The results from the conducted material tests were somewhat inconsistent, between 65 and 72 GPa for all sample sizes. Especially the small samples were in the lower end of expected results, between 65 and 75 GPa [17]. A correlation study between Young's modulus used in the numerical analysis, and thus the modelled elastic response, and the material test results was performed.

Young's moduli of 65, 70, 72, and 80 GPa were applied with *\*MAT\_001*, no erosion criteria were used. Resulting force–displacement curves from the analysis are presented in Figure 6.2.

Here, the test results on small glass specimens are represented by the fracture strength, i.e. each black circle is the force and displacement for one test sample at fracture. Note that for the experimental results presented in Figure 6.2 and subsequent figures, results from three tests have been removed, this is explained in Section 4.1.2.

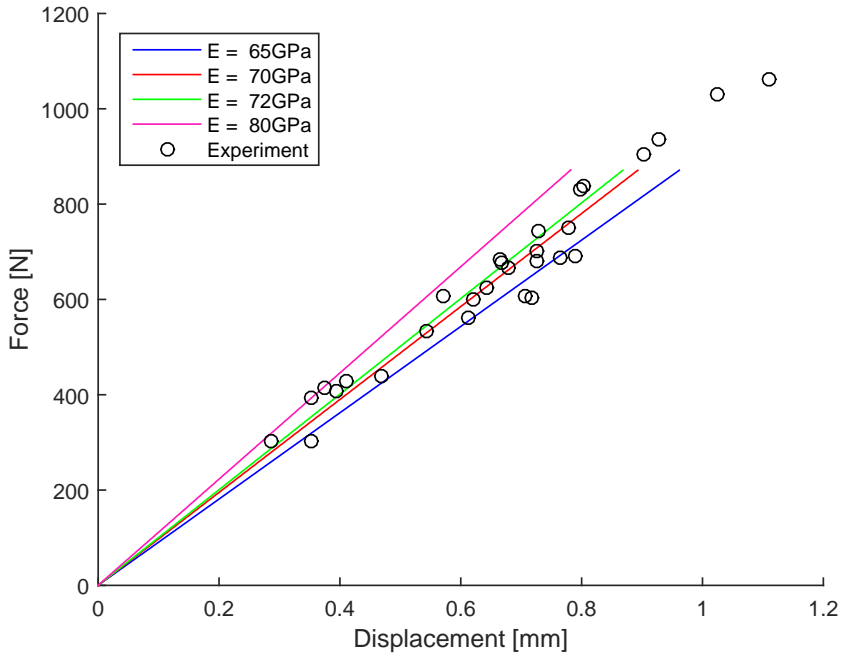


**Figure 6.2:** Force–Displacement for varying Young’s moduli.

Results are as expected, meaning that a higher Young’s modulus yields a greater incline in force versus displacement, which indicates that the numerical and material model exhibits the expected behaviour. Results for all four Young’s moduli used is within the interval found experimentally. This is also expected, as the calculated values from the tests also are within this range.

As the experimental results were somewhat inconsistent, no exact value was clearly correct. After accounting for the medium and large experimental results, and consulting with literature [19], a value of 72 GPa was chosen for Young’s modulus in the further work.

The material parameters used for modelling the elastic behaviour of float glass is presented in Table 6.1. Where the density and Poisson’s ratio are taken from literature [17].

**Table 6.1:** Elastic material constants for soda-lime glass [17].

Density [ $kg/m^3$ ]	2500
Young’s modulus [GPa]	72
Poisson’s ratio [-]	0.22

## 6.2.2 Loading speed

In the quasi-static material tests, the speed of the loading cylinders were 1.6 mm/min. With shell elements of size of  $1 \times 1$  mm, the critical time step is approximately  $1.64 \times 10^{-7}$  s<sup>1</sup>, indicating that a cylinder displacement of 1 mm would require more than 3.8 million time steps. The need for time scaling of the problem is evident.

In order to find a time scaling factor which provides a stable and accurate solution, five different cylinder speeds, ranging from 5 mm/s to 300 mm/s, were investigated.

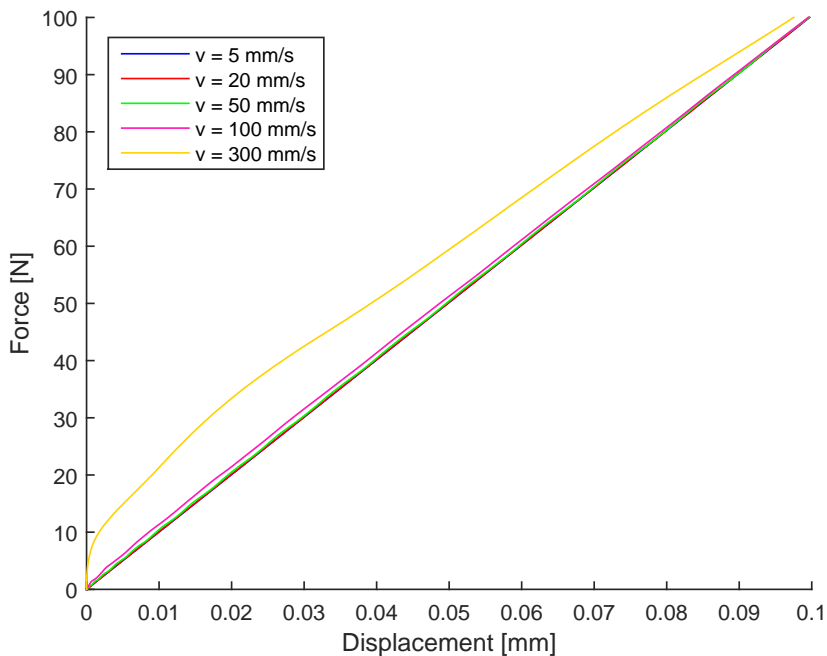


**Figure 6.3:** Force–Displacement for different loading speeds.

Results from the study are presented in Figure 6.3. At a cylinder velocity of 300 mm/s inertia effects are clearly visible, and the force–displacement curve deviates significantly from the other analyses. With a velocity of 100 mm/s, the inertia effect is greatly reduced, but still present to a small degree. For velocities of 50, 20, and 5 mm/s, the results are for all practical purposes identical. It is thus fair to assume that for all loading velocities at or below 50 mm/s the conditions are quasi-static, as in the experiments. For further studies a loading velocity was chosen as 50 mm/s, as this showed to be a good compromise between computational cost<sup>2</sup> and accuracy. It should be noted that the energy balance for

<sup>1</sup> From resulting LS-DYNA files.

<sup>2</sup> At a loading speed of 5 mm/s the computation took  $\approx$  1 hour and 12 minutes minutes on 12 CPU's, with  $\approx$  950000 time steps. While with a loading speed of 300 mm/s the computation took 71 seconds on 8 CPU's,



all simulations done in this study have been checked, and no numerical instabilities were found.

## 6.3 Results with Elastic material with simple erosion criterion

The elastic material model described in Section 3.2 (*\*MAT\_001*) with a stress based failure criterion was applied to the four-point bending model, with elastic material constants given in Table 6.1.

In order to determine how input parameters influences the failure response of this material model, a parametric study was conducted for shell and solid elements. Results are presented in the following sections.

### 6.3.1 Effect of mesh size

Four different mesh sizes for the model with shell elements were investigated,  $0.5 \times 0.5$ ,  $1 \times 1$ ,  $2 \times 2$ , and  $5 \times 5$  mm. All models used had five integration points over the element thickness, a critical stress,  $\sigma_c$ , of 116 MPa, the average found from bending tests on small samples, in Table 4.2. One failure integration point, as described in Section 3.2, was used.

The resulting force–displacement curves are presented in Figure 6.4, and the fracture patterns are presented in Figure 6.5.

The fracture strength and bending stiffness found in simulations do not vary significantly for different mesh sizes. But a trend showing slightly decreased bending stiffness and slightly increased fracture strength for smaller element sizes emerges. Both the stiffness and fracture strength is within the limits of the experiments, indicating that the model is able to represent material strength and stiffness in an adequate manner.

Fracture patterns, i.e. eroded elements for all mesh sizes is presented in Figure 6.5. It is observed that the failure pattern is highly dependent on element size, with a finer and more intricate pattern appearing for a finer mesh. Strictly transverse lines of eroded elements are observed for the largest element size, and more diagonal lines for the smallest element size. For all mesh sizes approximately 90% of element erosion occurs during 0.15 ms.

The results presented in Table 6.2 emphasizes one of the inherent problems with modelling brittle fracture with element erosion, the large fraction of eroded elements. Approximately one third of the material is eroded in order to form cracks, which is clearly non-physical behaviour. In particular, this problem is magnified when all elements have the same strength, because the critical stress is reached in a large number of elements simultaneously. Instead of a crack propagating from a weak point, the model instantly fails across the specimen width.

---

with  $\approx 15000$  time steps.

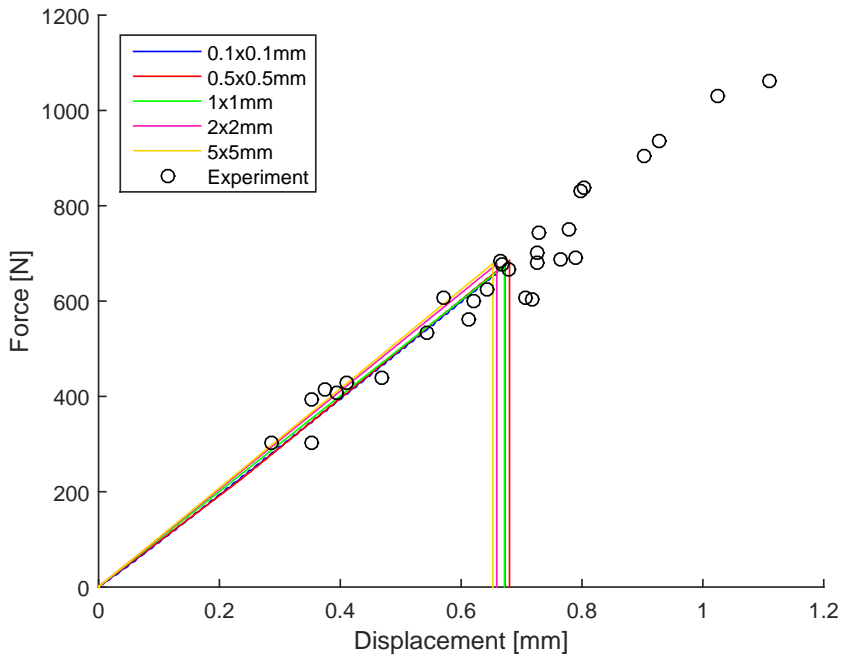
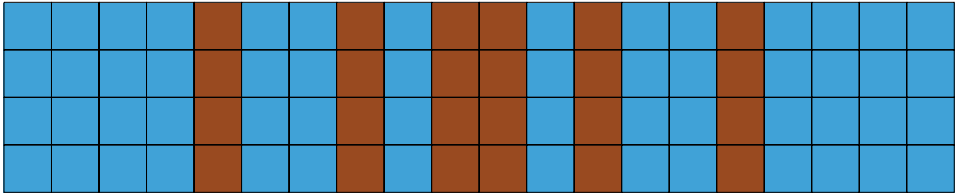


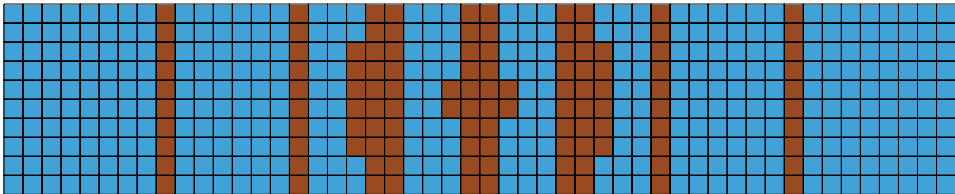
**Figure 6.4:** Force–displacement for varying mesh size with elastic material model.

**Table 6.2:** Eroded mass for different mesh sizes.

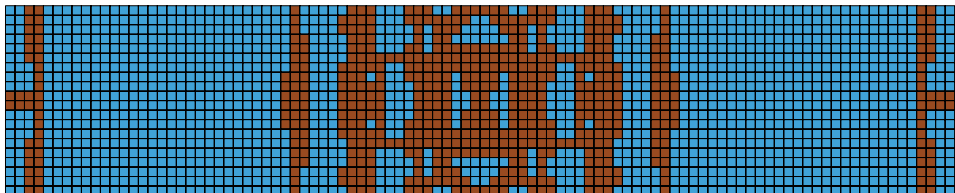
Element size [mm]	NOE	Eroded elements	Eroded mass [%]
0.1x0.1	200000	44870	22.4
0.5x0.5	8000	2616	32.7
1x1	800	568	28.4
2x2	500	116	23.2
5x5	80	24	30.0



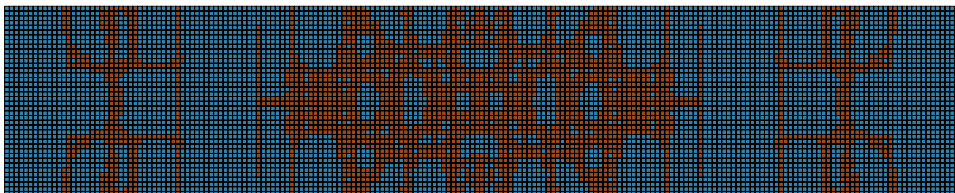
(a)  $5 \times 5$  mm mesh size.



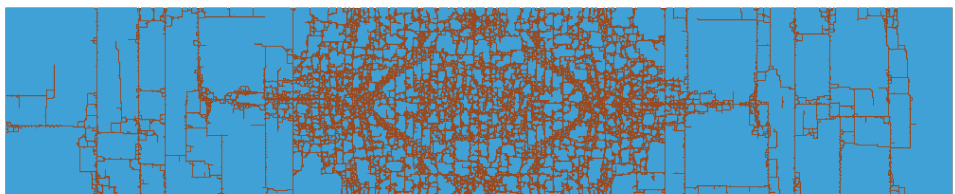
(b)  $2 \times 2$  mm mesh size.



(c)  $1 \times 1$  mm mesh size.



(d)  $0.5 \times 0.5$  mm mesh size.



(e)  $0.1 \times 0.1$  mm mesh size.

**Figure 6.5:** Eroded elements (brown) for varying mesh sizes.

### 6.3.2 Effect of critical stress

Five different values for the critical stress were investigated, ranging from 50 MPa to 170 MPa. The model with shell elements, a mesh size of  $1 \times 1$  mm, five integration points over the element thickness, and one failure integration point was used.

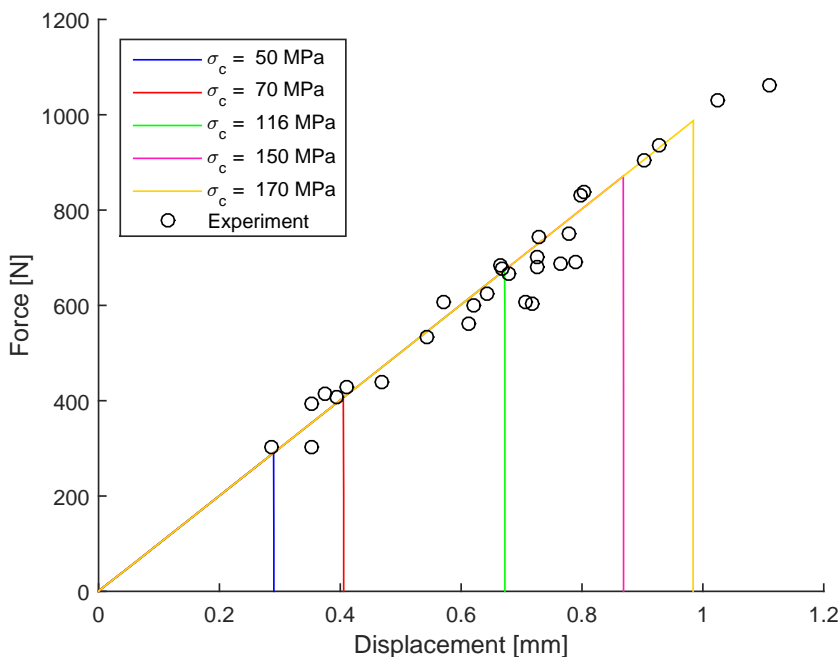


Figure 6.6: Force–displacement for varying critical stress.

As seen in Figure 6.6, the failure strength is highly influenced by the critical stress. With the range chosen, the model is able to represent nearly the whole dispersion in fracture strength found experimentally.

The fracture pattern and eroded mass were nearly identical, and very similar to Figure 6.5c, for all five simulations. Indicating that the only difference achieved by changing the critical stress, is the stress level at which failure occurs.

### 6.3.3 Effect of number of failure integration points

The number of failure integration points (NFIP) over element thickness, that is, the number of integration points where the erosion criterion is reached before an element is eroded, is used in order to model through thickness fracture in the shells. In order to investigate the effect of NFIP, simulations with models using one to five NFIP were carried out. Shell

elements with a mesh size of  $1 \times 1$  mm, five integration points over the element thickness, and a critical stress of 116 MPa was used.

Resultant force–displacement curves are presented in Figure 6.7. The failure strength is approximately equal for one to four NFIP, with a distinct increase for five NFIP. The reason for this is not entirely known, and no explanation was found during the work on this thesis. Failure patterns are all essentially identical to the one shown in Figure 6.5c.

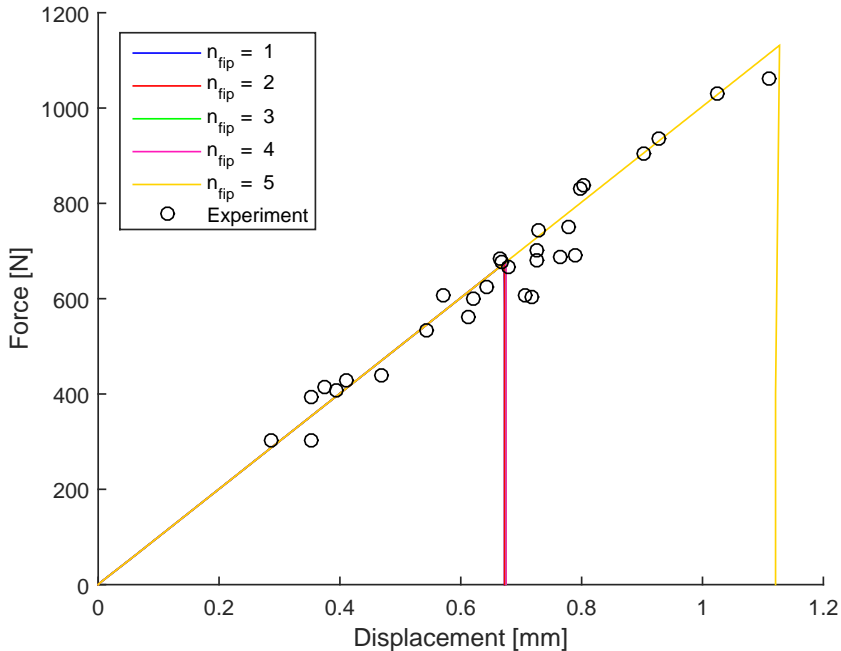


**Figure 6.7:** Force–displacement for varying number of failure integration points.

### 6.3.4 Solid elements

As mentioned in Section 3.2, *\*MAT\_001* with erosion criteria is also applicable with solid elements. A short study to determine material response with solid elements was conducted. Four different cubic element sizes were investigated,  $0.2 \times 0.2 \times 0.2$ ,  $0.5 \times 0.5 \times 0.5$ ,  $1 \times 1 \times 1$  and  $2 \times 2 \times 2$  mm. Element formulation number 3 for solid elements in LS-Dyna was used. That is, 8 node fully integrated quadratic elements with nodal rotations, resulting in a total of 48 degrees of freedom. Elastic material parameters were taken from Table 6.1, and a critical stress of 116 MPa with one failure integration point was used.

The resulting force–displacement curves are presented in Figure 6.8. When solid rather than shell elements was used, the force and displacement at failure is clearly mesh de-

pendent. A coarser mesh results in a significantly higher failure strength. This is likely caused by the number of integration points across model thickness, which will increase as the mesh size is reduced when using solid elements. The first principal stress,  $\sigma_I$ , just before failure in the model with element size  $0.5 \times 0.5 \times 0.5$  mm is shown in Figure 6.9. Consistent with beam theory, the stress varies from tension at the bottom, to compression at the top. If one considers two element sizes, one where the model thickness is represented by two elements, and one where the thickness is represented by four elements, it is clearly seen that the model with two elements over the thickness yields a lower stress in the integration point closest to the surface.

The bending stiffness is slightly less affected by element size for solid rather than shell elements. The reason for this is not entirely known, but may be caused by a difference in contact modelling of shell thickness versus solid elements with analytical rigid surfaces. Solid elements also does not show the same tendency for spurious vibrations when mesh size becomes very small.

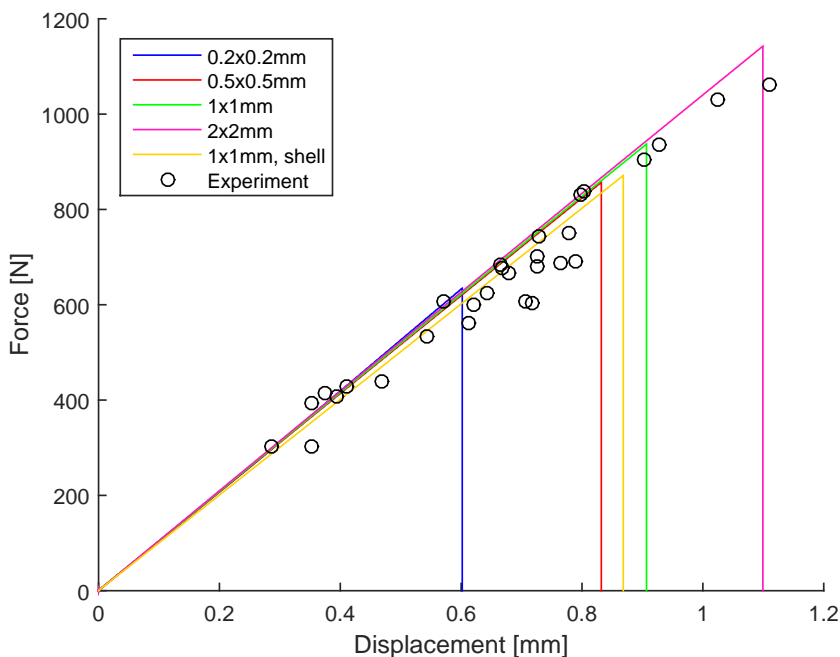


**Figure 6.8:** Force–Displacement for varying mesh size with solid elements, compared to shell elements.

The number of eroded elements for each mesh size is presented in Table 6.3. The percentage of eroded mass is much more consistent for various mesh sizes than for shell elements. As mesh size becomes too coarse, the eroded mass increases drastically.

The significant reduction in eroded mass is likely caused by unsymmetrical erosion of

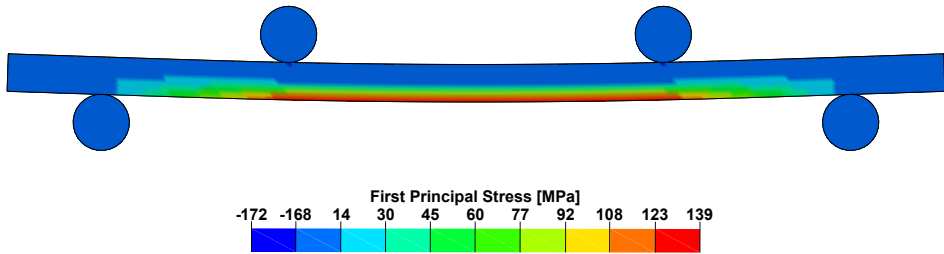


**Figure 6.9:** Stress through thickness of solid element four-point bending model.

elements through the model thickness. In Figure 6.10, the eroded elements in the model with the finest mesh are shown. It is evident that the eroded elements does not follow a straight line through model thickness. With shell elements, the entire thickness is eroded as the erosion criterion is reached.

**Table 6.3:** Eroded mass for different mesh sizes.

Element size [mm]	Number of elements	Eroded elements	Eroded mass [%]
$0.2 \times 0.2 \times 0.2$	1000000	51515	5.2
$0.5 \times 0.5 \times 0.5$	64000	2829	4.4
$1 \times 1 \times 1$	8000	378	4.7
$2 \times 2 \times 2$	1000	102	10.2

In comparison with the shell element model, the solid element model is much more computationally expensive. The computational time with different mesh sizes in the four point bending model, with solid and shell elements is presented in Table 6.4. Especially the rate at which the solid element model's computational time increases with mesh refinement is important. From  $1 \times 1 \times 1$  mm elements to  $0.5 \times 0.5 \times 0.5$  mm elements the computational time increases by a factor of 14.

**Table 6.4:** Computational cost for solid versus shell elements.

Element length [mm]	Computational time [NCPU]	
	Shell	Solid
0.1	9h 11min [24]	-
0.2	-	16h 54min [24]
0.5	17min 11sec [12]	3h 44min [12]
1	8min 14sec [8]	15min 58sec [12]
2	4min 7sec [8]	3min 16sec [4]
5	31sec [8]	-

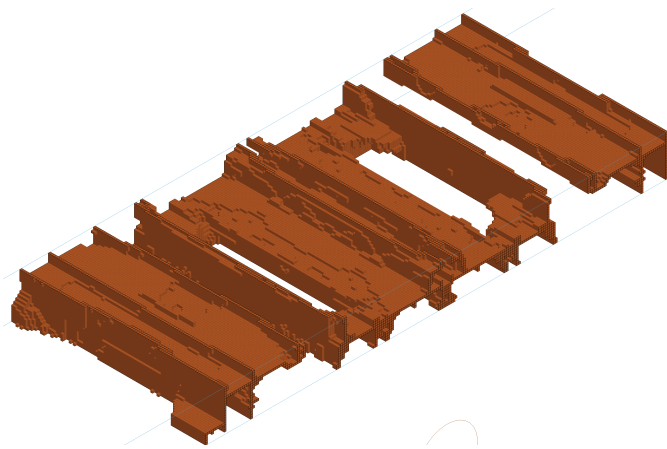


**Figure 6.10:** Eroded elements (brown) for  $0.2 \times 0.2 \times 0.2$  mm element size.



### 6.3.5 Results with Johnson–Holmquist 2 material model

Zhang et al. [53] have shown promising results in modelling monolithic and laminated glass panes subjected to dynamic loading, including blast loading by use of the Johnson–Holmquist 2 (JH-2) material model for ceramics, introduced in Section 3.2.1.

**Table 6.5:** Material constants for JH2 material model, [53].

Density [kg/m <sup>3</sup> ]	2530
Strength constants	
A	0.95
B	0.2
C	0.01
M	1.0
N	0.64
Tensile strength [GPa]	0.15
HEL [GPa]	5.95
Normalized fracture strength	0.5
HEL strength [GPa]	4.5
Shear modulus [GPa]	30.4
Damage constants	
D1	0.043
D2	0.85
Equation of state	
K1 [GPa]	45.4
K2 [GPa]	-138.0
K3 [GPa]	290.0
Bulk	1.0

As this material model is implemented and easily available in LS-DYNA, it was compared to the other material models under quasi-static loading in four point bending. Material parameters were taken from [53], repeated for clarity in Table 6.5. It should be noted that the JH-2 material model is developed for dynamic loading, and thus results obtained in quasi-static simulations may not be representative for model performance in dynamic loading.

As the JH-2 material model is only available for use with solid elements, the solid element model used in the previous section was used without alterations other than the material card.

The failure criterion used for this model is effective plastic strain at failure  $\varepsilon_{pc}$  which is not consistent with the material behaviour assumed for glass presented in Chapter 3, i.e. elastic until brittle failure.

### 6.3.6 Effect of mesh size

The mesh size dependence of the JH-2 model was investigated for three different solid element sizes; 0.5x0.5x0.5, 1x1x1 and 2x2x2 mm. As with material model \*MAT\_001, element formulation 3 was used. Material constants for the JH-2 model given in Table 6.5 was used. The plastic failure strain was set to 0.03, as recommended by Zhang et al. [53].

The resulting force–displacement curves are presented in Figure 6.11. All mesh sizes initially show the expected linear elastic behaviour. The bending stiffness for all mesh sizes with the JH-2 model is also in agreement both with the bending stiffness obtained with *MAT\_001*, and the experiments. The JH-2 shows a little higher stiffness than with *MAT\_001*, but is within the upper limit found experimentally. As no work was done in order to calibrate material constants, a small difference in elastic material response was expected.

The characteristic difference in response of the JH-2 model from the other material models used is clearly seen at large force and displacement. As the material strength limit is reached, the force–displacement curves shows three distinct kinks consistent with weakening of the damaged material in the JH-2 model.

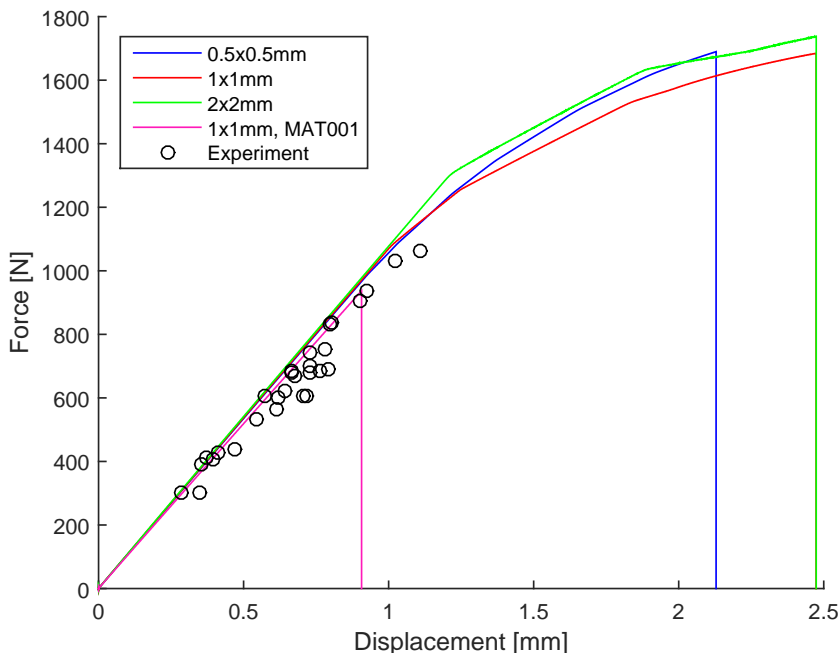


**Figure 6.11:** Force–displacement curves for the JH-2 material model with varying mesh size, compared to *MAT\_001*.

### 6.3.7 Effect of plastic failure strain

From the results on mesh dependence (Figure 6.11) it was found that a plastic failure strain of  $\varepsilon_{pc} = 0.03$  was too high for a physical response in quasi-static loading. As no generally accepted value for this parameter could be found in the literature, a study investigating the influence of  $\varepsilon_{pc}$  was done. The model using elements of size  $1 \times 1 \times 1$  mm in the previous section was used. Four different values for the plastic strain at failure, ranging from  $\varepsilon_{pc} = 0.03$  to  $\varepsilon_{pc} = 0.0001$ , were used. Other material constants were from Table 6.5.

The resulting force–displacement curves are presented in Figure 6.12. As was expected the plastic strain at failure,  $\varepsilon_{pc}$ , did not alter material response before failure. The point at which elements started to erode was completely governed by the plastic strain at failure. The most appropriate value for  $\varepsilon_{pc}$  for this case seems to be a value that is as low as possible. But even with a very low value for  $\varepsilon_{pc}$  the material strength is at the highest end of the range found experimentally.

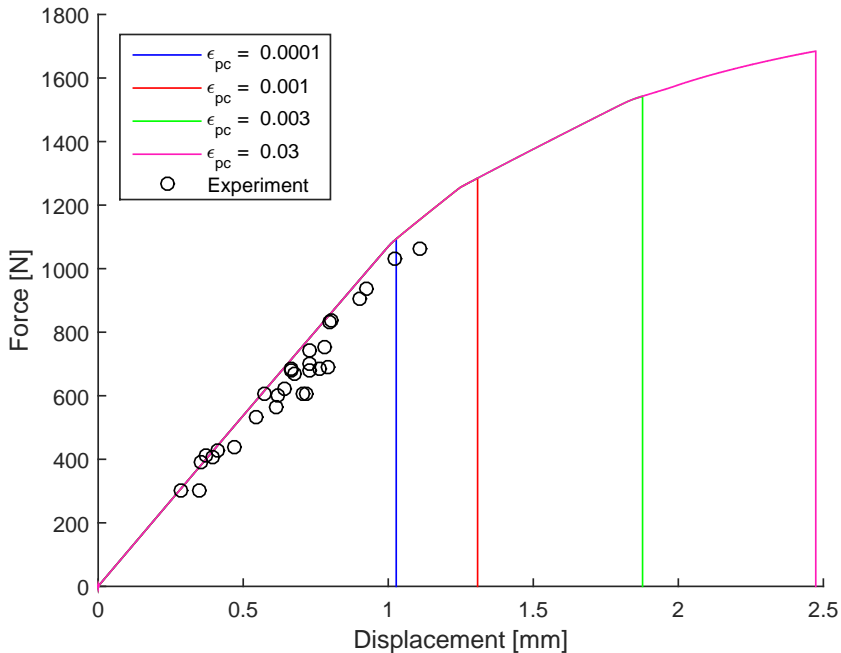


**Figure 6.12:** Force–displacement curves for JH-2 material model with varying plastic failure strain.

This material model was not the focus of the thesis, and no further work was done in order to find strength values which provided a more conservative estimate of material strength. In addition, it is emphasised that the JH-2 material model is developed for dynamic, and especially impact loading of ceramics, and thus a less than optimal performance in quasi-static loading was not unexpected.

## 6.4 Results with SIMLab Metal Model

As indicated in Section 2.4.2 and 3.1.2, the strength of a series of material tests is not uniform, but rather distributed in a manner which may be described statistically with a sufficient amount of tests. In order to include the stochastic distribution of strength described in literature and observed in the material tests, the SIMLab Metal Model (SMM), introduced in Section 3.2.2, was employed in the numerical model of the four point bending test.

The SMM is primarily used for modelling metals, and is thus developed with emphasis on plastic deformation. In this application, the plastic material routine is avoided by specifying an arbitrary, high yield strength of the material. In this study, the yield strength,  $\sigma_y$ , is set to  $1 \times 10^9$  MPa. Elastic material constants are the same as for *MAT\_001*, i.e. constants in Table 6.1.

In the modelling of failure, the stress based criterion, as introduced in Section 3.2.2 was used. That is, a critical first principal stress,  $\sigma_c$ , is specified, and as this stress is reached in a given number of integration points through element thickness, the element is eroded.

### 6.4.1 Comparison with *MAT\_001*

In order to verify elastic and fracture response of the SMM, the model with shell elements of size  $1 \times 1$  mm, described in Section 6.3, was used. A failure criterion of  $\sigma_c = 116$  MPa was chosen for the same reason as in Section 6.3. No stochastic distribution of failure strength was employed in this study. In Figure 6.13, the results for both material models are presented. The elastic response of the SMM is identical to *MAT\_001*, indicating that the plastic material routine of the SMM has in fact been avoided without complications. It was thus further assumed that using SMM in this manner did provide the expected elastic material response.

Note that the failure strength was slightly different for the two material models, despite the fact that the same value for  $\sigma_c$  was used. As the difference was very small, no further investigation was done.

### 6.4.2 Effect of number of failure integration points

The SMM offers the possibility of modelling through-thickness failure of shell elements. As mentioned in Section 3.2.2, this is achieved by specifying a number of failure integration points through element thickness,  $n_{fip}$ , and the elements are not eroded until the required number of integration points in an element has reached this criterion.

In order to determine the appropriate number of failure integration points for a good representation of strength in the material, the effect of number of failure integration points was reviewed. The shell element model with five integration points over element thickness was used. SMM with a critical stress of 116 MPa, and one to five failure integration points

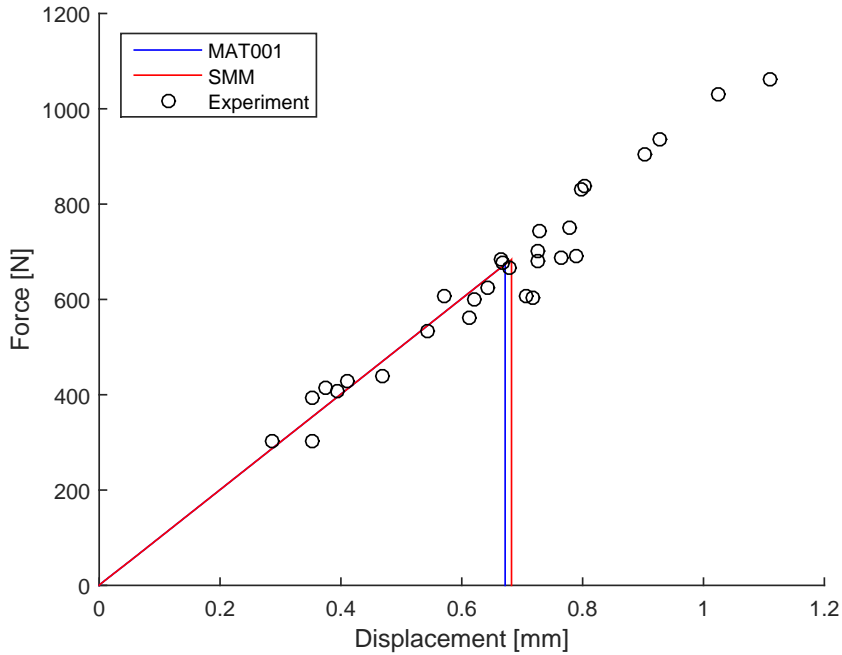


**Figure 6.13:** Comparison between SMM and *MAT\_001*.

were used. No stochastic distribution of failure strength was employed in this study. The resulting force–displacement curves are presented in Figure 6.14.

In contrast to *MAT\_001*, see Figure 6.7, the SMM exhibits a high dependence on the number of failure integration points. Where the stress at failure varies from 77 MPa for  $n_{fip} = 1$ , to 133 MPa for  $n_{fip} = 5$ , as calculated by beam theory. The fracture strength specified, 116 MPa, is obtained with four failure integration points over element thickness.

It is not exactly clear why these models exhibit such a different behaviour, but it is believed to be caused by the treatment of failed integration points. It is known that the SMM removes the stress in each failed integration point as the failure criterion is reached. And it may seem likely that *MAT\_ADD\_EROSION* retains the stress in each integration point, until the required number of points fail, although this was not found in either the LS-DYNA user’s manual or the LS-DYNA theory manual.

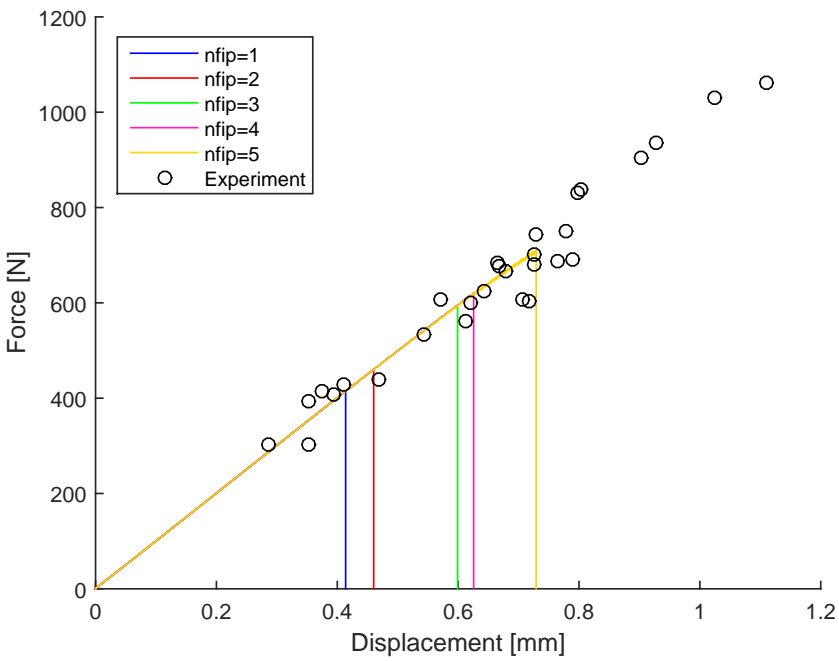


**Figure 6.14:** Force–displacement for varying number of failure integration points.

### 6.4.3 Stochastic distribution of failure criterion

Stochastic distribution of the stress based failure criterion in the SMM was investigated using the shell element model with  $1 \times 1$  mm mesh size. For all models, shell elements with five integration points over element thickness, and four failure integration points were used.

The critical stress,  $\sigma_c$ , failure criterion was distributed individually on each finite element by Equation (3.2.4), using parameters given in Table 6.6. The values for the stochastic distribution were chosen based on results from four point bending tests.  $\sigma_c$  and  $m_w$  were chosen as the average values obtained from all tests, shown in Table 4.3. Although this is not the preferred procedure for choosing the stochastic distribution, and the parameters should ideally be calculated using weakest link theory, described in Section 2.4.2. The primary objective was to determine trends obtained with a model which was not primarily made for modelling failure in brittle materials, and this was considered a sufficient approach. Truncation values,  $\sigma_{c,min}$  and  $\sigma_{c,max}$ , were chosen as approximately the highest and lowest fracture strength found in tests on large material samples, as these tests were less prone to be influenced by edge effects. The reference volume,  $V_0$  was chosen as the volume subject to tensile stress in the model, i.e.  $80 \times 20 \times 2$  mm.  $\mu_w$  was chosen based on discussion with Professor Odd Sture Hopperstad.

A coinciding MS and FE mesh, i.e. a coupled modelling approach, as described in Section 3.3, was used. Each time a new simulation was started, a new pseudo-random distribution of the failure parameter was generated.

**Table 6.6:** Weibull parameters for SMM

$\sigma_0$	113 MPa
$m_w$	4.13
$\mu_w$	0.3
$V_0$	3200 mm <sup>3</sup>
$\sigma_{c,min}$	57.5 MPa
$\sigma_{c,max}$	157.7 MPa

The distribution of  $\sigma_c$  in three different simulations using the same input file is presented in Figure 6.15. Elements with a low  $\sigma_c$  are coloured red, and elements with a high  $\sigma_c$  are coloured blue. The high number of high-strength elements, relative to low-strength elements, is due to the distribution shift caused by the volume dependence parameters,  $\mu_w$  and  $V_0$ .

Corresponding patterns of eroded elements for each distribution of  $\sigma_c$  are presented in Figure 6.16. The influence of stochastic distribution of  $\sigma_c$  is clearly seen, as each simulation exhibits diverse failure patterns at different positions along the specimen section subjected to stress. Failure initiated at or close to elements with a particularly low  $\sigma_c$ , and propagated over the model width, mostly through elements with a lower failure strength. Note the single eroded elements in Figure 6.16b and 6.16c, which is caused by the sparsity of low-strength elements, compared to high-strength elements. As a low-strength element

fails, if it is surrounded by high-strength elements, a crack does not propagate.

Failure with stochastic distribution of  $\sigma_c$  in the SMM differed significantly compared to failure with the uniform failure strength  $\sigma_c$  in *MAT\_001*. The fraction of eroded mass, i.e. the number of eroded elements, was greatly reduced, from approximately 30% with *MAT\_001*, shown in Table 6.3, to between 1.3 and 2.1% in the three simulations with equal material input shown in Figure 6.15. Additionally, the eroded elements were in a narrow band across model width, contrary to results with *MAT\_001* where elements failed across the entire loaded model area.



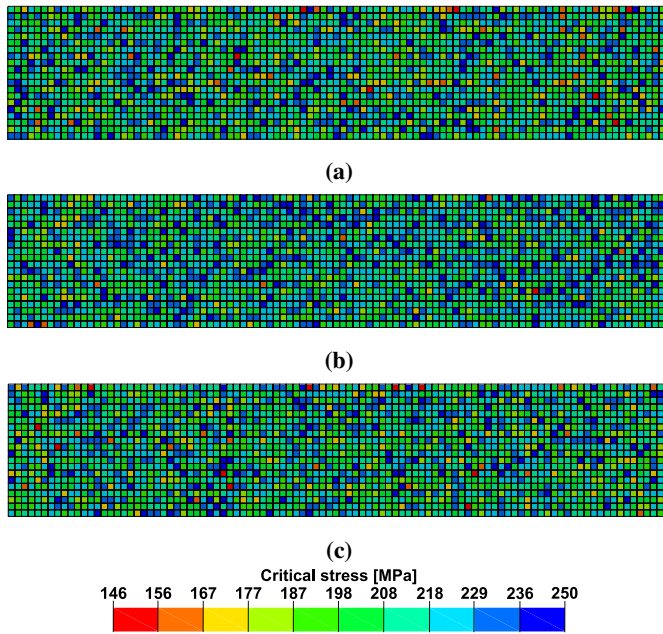


Figure 6.15: Stochastic distribution of  $\sigma_c$ .

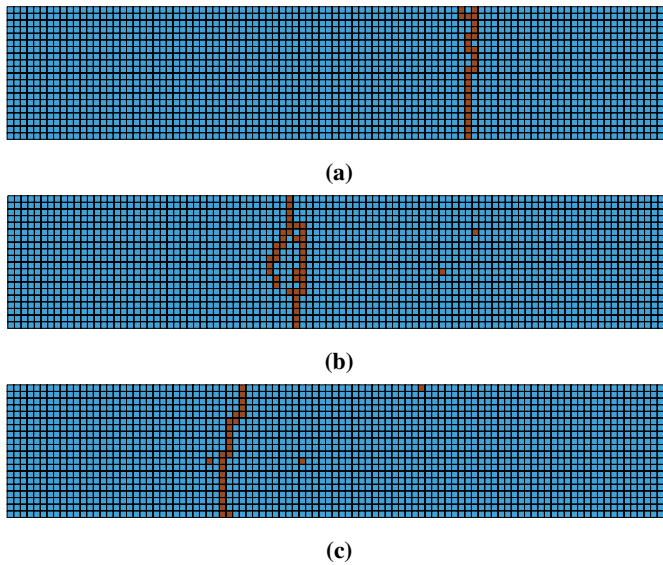
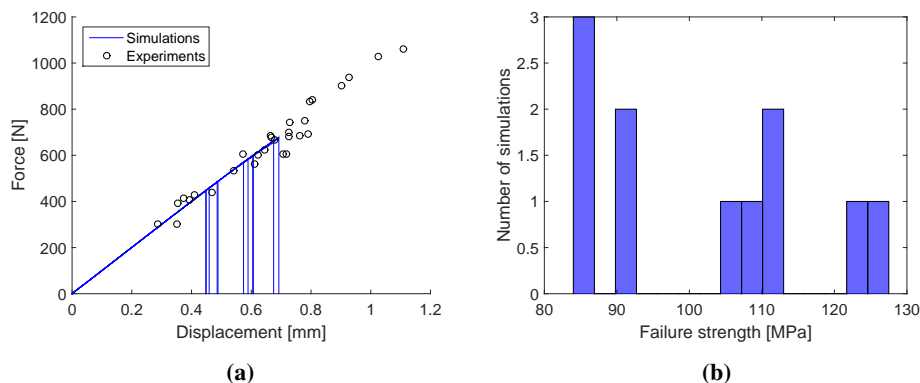


Figure 6.16: Eroded elements (brown) with stochastic distribution of  $\sigma_c$ .

Resulting force–displacement curves and distribution of failure strength for eleven different simulations with the same material input as the three shown in Figure 6.15 are presented in Figure 6.17. Note that the failure strength is calculated by taking the force and displacement when the first element is eroded, and calculating the stress in the part by the relationship for four point bending Table 2.1. In Figure 6.17b each bar in the histogram represents a span of 5 MPa.



**Figure 6.17:** Force–displacement (a), and resulting failure strength distribution (b) with coupled stochastic distribution of  $\sigma_c$ .

It is observed that the stochastic distribution of critical stress to some degree captures the dispersion in component strength found experimentally. The failure stress found in simulations range from  $\sigma_f = 83.9$  MPa to  $\sigma_f = 127.1$  MPa, while the experimental results range from  $\sigma_f = 75.7$  MPa to  $\sigma_f = 197.2$  MPa. A larger dispersion in modelled failure strength is expected if more simulations are conducted.

### 6.4.4 Uncoupled stochastic distribution of failure criterion

In the previous section, the MS-mesh and FE-mesh was coinciding. That is, if the element size was changed, the distribution of critical stress change accordingly. The uncoupled approach, where the FE-mesh is independent of the distribution parameters, may be preferable in some cases. For example, it is observed that with the coupled approach, occasionally single elements are eroded without failure propagating. In these cases, an uncoupled distribution of failure parameters may cause failure to propagate by clustering lower-strength elements, thus reducing probability of eroding single elements.

The influence of an uncoupled stochastic distribution of material strength was investigated by using a simple MS-meshing tool developed for SMM, based on the theory in Section 3.3. Figure 6.18 shows an example of an MS-, and corresponding FE-mesh for a shell element four-point bending model with FE-mesh size of  $1 \times 1$  mm, and MS-mesh size  $5 \times 5$  mm. Material input is the same as for the coupled model, the parameters given in Table 6.6.

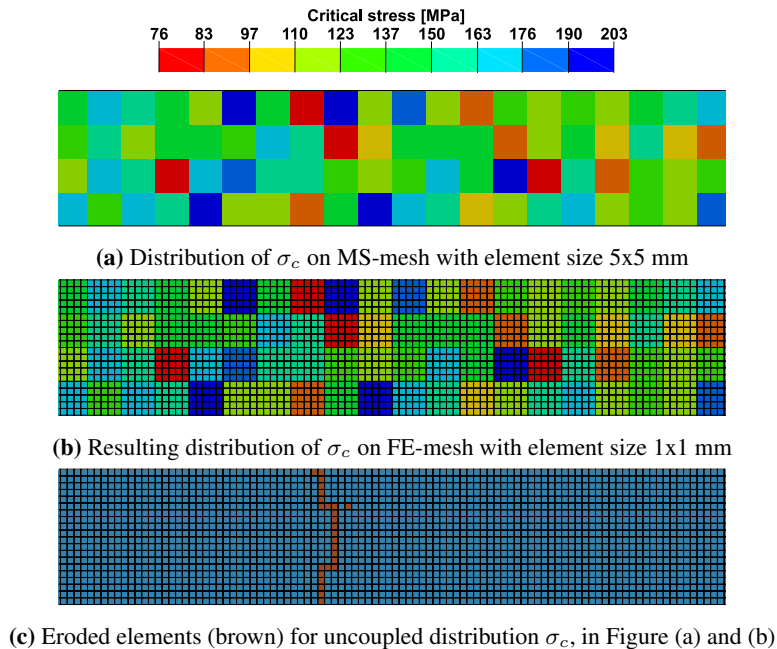


**Figure 6.18**

The distribution of  $\sigma_c$  in Figure 6.18a and 6.18b has a much lower maximum and minimum value than with the coupled approach, Figure 6.15. This is caused by the change in reference volume,  $V$ , in the Weibull distribution used for distributing material parameters. With the uncoupled approach  $V$  is given by the element size of the MS-mesh, and thus this value becomes higher compared to the reference volume,  $V_0$ , which is equal in both cases.

The failure pattern with the uncoupled strength distribution, shown in Figure 6.18c, is

similar to the failure pattern for the coupled strength distribution. But tends to propagate through MS-elements of low strength. The spurious erosion of elements without propagation is much less evident with the uncoupled distribution of the failure criterion.

Figure 6.19 shows force–displacement curves and distribution of failure strength for 25 simulations with the same material input parameters as in Figure 6.18.

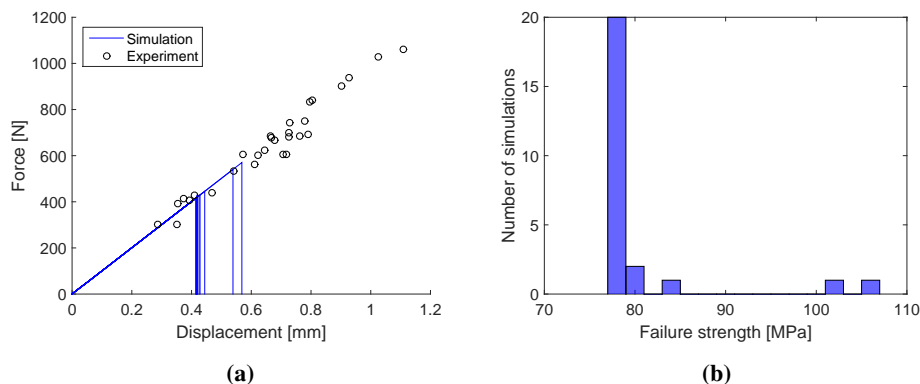


**Figure 6.19:** Force–displacement (a), and resulting failure strength distribution (b) with uncoupled stochastic distribution of  $\sigma_c$ .

The dispersion in failure strength is very low with the uncoupled distribution chosen, and much lower than what was achieved with the coupled approach and in found experimentally. There may be several reasons that this is the case, but it is believed to mainly be caused by the change in reference volume, and thus a shift towards the lower limit of the stochastic distribution of the failure criterion. Thus a higher probability of seeding low-strength elements, which lowers the overall model strength as failure is most likely to occur at these elements.

It is suspected that the low dispersion of ultimate failure strength found in simulations, both with the coupled, and especially with the uncoupled distribution of material strength, may be caused by the presence of elements of low strength in all models. Thus a series of 15 simulations where the MS-mesh covered the entire FE-model, i.e. seeding the same strength in all FE-elements, was conducted. Investigating if a global distribution of  $\sigma_c$  was able to capture the distribution of fracture strength found experimentally.

Figure 6.20 shows force–displacement curves and distribution of failure strength for 15 simulations with a global seed of  $\sigma_c$ . All simulations used the same material input parameters, given in Table 6.6. Here the reference volume,  $V_0$  is approximately equal to the model volume,  $V$ , and thus the Weibull distribution is not much affected by volume dependency.

It is evident that the global distribution of failure parameters results in a dispersion in modelled failure strength which is closer to the experimental distribution. The range between the highest and lowest obtained fracture strengths are also wider than in other simulation series, and closer to the range found experimentally.

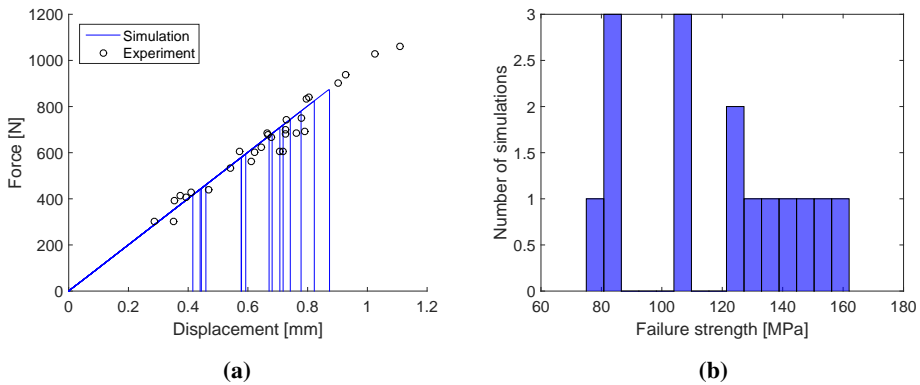


**Figure 6.20:** Force–displacement (a), and resulting failure strength distribution (b) with uncoupled global stochastic distribution of  $\sigma_c$ .

## 6.5 Results with SIMLab Brittle Materials Model

The SIMLab Brittle Materials Model (SBMM) is developed in order to model fracture in brittle materials, and is thus of interest. Due to the model being under development at the time of writing this thesis, and only available for practical use during the latter part, the material model behaviour in four-point bending was not investigated as thoroughly as the previously discussed models. Only a short validation study of elastic behaviour and fracture strength with shell elements was done, in order to focus on using the model for numerical simulation of the blast tests.

The validation study used the same shell element model previously used, with a mesh size of  $1 \times 1$  mm, and elastic material constants given in Table 6.1. Fracture parameters used are presented in Table 6.7. No viscoelasticity was applied.

**Table 6.7:** Failure constants used in four-point bending with the SBMM

$a_f$	2
$G_f$	0.01 J/mm <sup>2</sup>
$\Delta G_f$	0.01 J/mm <sup>2</sup>
$\kappa_0$	0.001157
$D_c$	0.99

A comparison between the force–displacement curves for the SBMM, SMM and *MAT\_001* is presented in Figure 6.21. It is evident that elastic material response is equal to what was found with *MAT\_001* and the SMM.

Failure strength is lower for the SBMM, than for the other material models, but is within the range found experimentally.

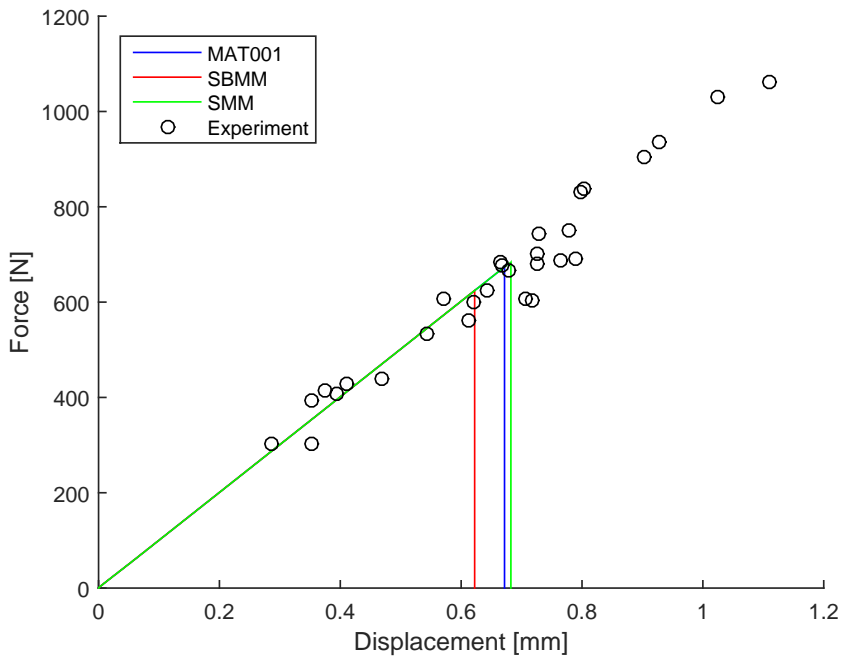


**Figure 6.21:** Force–displacement for SBMM, SMM and *MAT\_001*.

## 6.6 Summary and Discussion

In this chapter, the numerical performance of four material models in quasi-static, four-point bending, have been investigated in the Finite Element software LS-DYNA, and compared to each other and experimental results.

Material models investigated were:

**\*MAT.001 with a simple, stress based, failure criterion** An elastic material model, with a generic stress based failure criterion, commercially available in LS-DYNA.

**Johnson–Holmquist 2 material model** A material model developed for modelling dynamic material response and failure in ceramics.

**The SIMLab Metal Model** A material model developed at SIMLab, NTNU, primarily for modelling metals. With the ability for stochastic distribution of failure criteria.

**The SIMLab Brittle Materials Model** A material model developed at SIMLab, NTNU, for modelling elastic response and brittle fracture in ceramics.

All material models were able to capture the linear elastic response observed experimentally in a consistent and satisfactory manner. Slight variations in bending stiffness were found between the use of solid and shell elements, and for variations in mesh size, although all simulations were within the variations found experimentally.

### Failure response

With the use of *\*MAT.001*, initial failure in simulations within the range found experimentally was obtained, both for shell and solid elements. It was observed that with shell elements of varying element size, the fraction of eroded elements was excessive. An improvement on this problem was observed with the use of solid elements, at a significant increase in computational cost. Stochastic distribution of the failure criterion was not a possibility with this model, but it is noted that for the use in design, where the stochastic nature of ceramics is non-important, the model may provide sufficient results provided the failure stress is properly chosen.

The JH-2 material model did not provide good results in the modelling of failure, with plastic deformation rather than the desired brittle fracture behaviour. It is already mentioned that this material model is primarily designed for modelling dynamic behaviour of ceramics, and it was confirmed that the application of this model in quasi-static loading does not provide satisfactory results.

The SIMLab metal model was used in order to stochastically distribute, by the use of a Weibull distribution, a stress based failure criterion. Both a coupled and uncoupled distribution of the failure criterion were investigated. Coupled distribution of the failure criterion greatly reduced the fraction of eroded elements, although with some spurious erosion of elements, while providing a fracture strength in accordance with experimental results. For four-point bending, the uncoupled distribution of the failure criterion did not significantly improve results obtained with the coupled approach, in terms of reflecting distribution in fracture strength observed experimentally. The amount of spurious erosion

of elements was reduced. A global uncoupled distribution of the failure criterion provided a good approximation of distribution in failure strength observed experimentally, at a cost of worse approximation of fracture patterns.

The SIMLab brittle materials model was not investigated as thoroughly in four-point bending as would have been desired in order to determine the failure criterion properly. A single simulation in order to verify that failure strength was in the correct range compared to other models and experiments was conducted.

**Three point bending tests** Numerical work was done modelling the three point bending tests, in order to obtain information on boundary conditions for use in simulations of blast tests. Due to limited time and unreliable results the three point bending simulations have been omitted from the thesis. It is however believed that good and usable results may have been obtained provided more time.



# Numerical modelling: Blast tests

Along with the numerical study on four point bending tests, a study was conducted on the blast scenario. Both failing and non-failing scenarios with monolithic glass and laminated glass were studied. Attempts were made to recreate the qualitative failure behaviour found experimentally in the shock tube. To get an understanding of what is possible to achieve with different approaches discussed in previous sections, simulations were conducted with and without a failure criterion such that the elastic response also could be compared to the experimental results. Due to the complexity of fast transient loading, sensitivity studies on boundary conditions have also been conducted. Relevant LS-DYNA input files are presented in Appendix E.

## 7.1 Monolithic Glass

### 7.1.1 Numerical Model

A general representation of the model used for simulation of the blast experiment is shown in Figure 7.1. Since an investigation of failure was desired, no use of symmetry was applied. The blast experiment model includes only a part of the frame and the entire rubber sealant. This simplification omit the description of the bolts clamping the frame in order to reduce complexity. As the effect of clamping bolts was assumed to be negligible, this was deemed satisfactory. The  $400 \times 400$  mm glass pane was modelled both with solid and shell elements. Glass modelled with shell elements utilized fully integrated shell elements with five integration points over the thickness and Gauss integration rule. Glass modelled with solid elements utilized fully integrated quadratic 8 node solid elements with nodal rotations, resulting in a total of 48 Degrees of Freedom (DOF). The rubber sealant, in addition to a portion of the frame was modelled with solid elements. The aluminium frame was modelled with reduced integration solid elements, whereby the back frame where fixed in

all 6 DOF, and the front frame was free to move in the z-direction. The rubber sealant was modelled using fully integrated solid elements. Both the frame and the rubber was modelled with a linear elastic material model (*\*MAT\_001*), as described in Section 3.2.1, with a Young's modulus of 70 GPa and 3 MPa<sup>1</sup> respectively. A thoroughly developed material model for the rubber was not obtained, and the rubber used was not tested within the work of this thesis. For small strains, the rubber may be assumed to exhibit a linear elastic behaviour. The Young's modulus of 3 MPa is only valid for quasi-static behaviour, while for higher strain rates this may not be the case. Thus material parameters for the rubber in simulations were considered an uncertainty. In order to represent the clamping pressure applied by the bolts, a small initial gap of 0.01 mm between every part in the numerical model was included, before a prescribed motion of 0.1 mm was applied to the front frame, compressing the rubber and generating the desired clamping pressure effect. The clamping force was observed to be approximately 2 kN, which is low compared to the values in [52], yet it was deemed satisfactory. The blast loading was applied by a Friedlander curve obtained from the experiments. The segment subjected to the blast loading was defined as the nodes of the top surface of the glass pane facing the incident blast wave. Note that with this approach, the load is removed when elements are eroded.

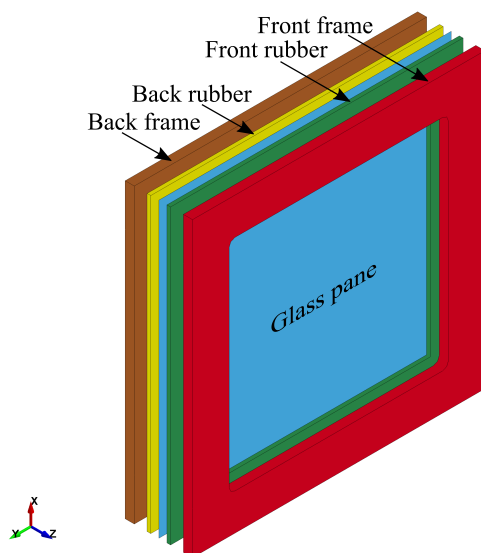


**Figure 7.1:** Exploded view of the general numerical model for blast experiment, seen from front. Incident blast wave propagates in the negative z-direction.

### 7.1.2 Elastic response

As a preliminary study, the elastic response was examined to determine if it was within reasonable limits of the experimental results. The simulations utilized the load determined

<sup>1</sup> Obtained from the rubber product description; *Semperit CR-SBR N9581*

from the experiments where the glass panes did not fail, shown in Section 5. A basic general model was made with elements with area  $5 \times 5$  mm, where the solid model utilized one element over the thickness. The following sections examines the effect of different decisive parameters.

### Rubber sealant

The fact that elastomers have a high strain rate dependency [54], makes the rubber material a natural parameter to examine further. Even if Young's modulus of the rubber was given as 3 MPa this might not be the case for higher strain rates, as in the shock tube experiments. As experiments were not conducted specifically to determine the characteristics of the rubber, little knowledge is acquired about this matter. Therefore it is of interest to analyse the effects of its stiffness. Figure 7.2 shows the effect of different degrees rubber stiffness on the mid-point deflection of the glass pane. The basic shell model was used

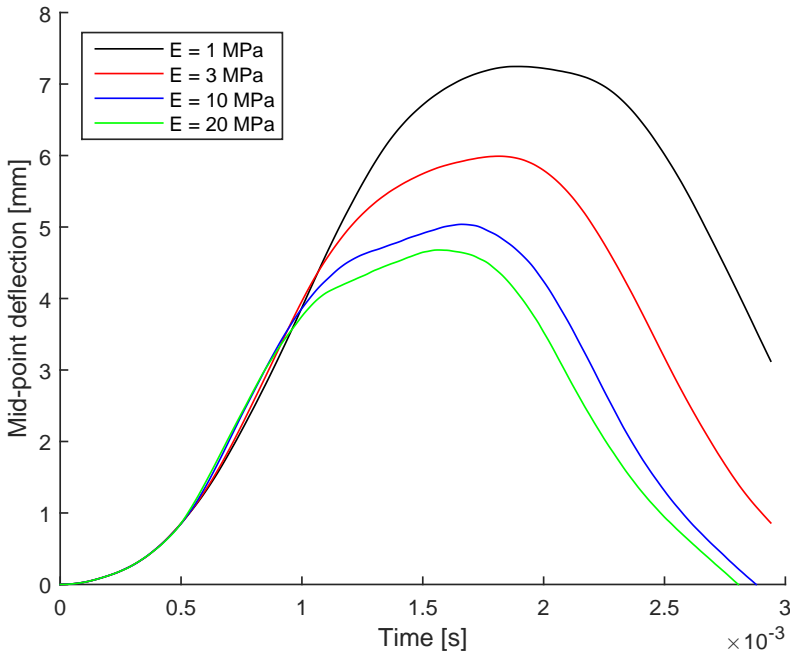


**Figure 7.2:** Effect of different rubber stiffness on the mid-point deflection.  $P_r = 0.64$  bar.

for this study. As expected it is observed that for higher Young's modulus, the mid-point deflection decreases. This follows from the fact that when the stiffness of the rubber increases, the pane will experience a more clamped state, and the global geometric stiffness will increase. The mid-point deflection experiences an increase of more than 55% when Young's modulus of the rubber is decreased from 20 MPa to 1 MPa, indicating that the rubber stiffness controls the problem to some degree. It should be noted that these mod-

els was loaded with the lowest pressure found experimentally,  $P_r = 0.64$ , and it may be speculated that the effect of rubber stiffness may increase in events with higher loading pressure.

### Shell glass elements

In order to ensure satisfactory results with the shell model, the number of integration points over element thickness were examined to study the influence on model response. Figure 7.3 shows the resulting mid-point deflection as a function of the simulation time. It is observed that the number of integration points has a minor influence on the numerical shell model. It is obvious that a single integration point never will be able to describe this problem which is also clear from figure 7.3.

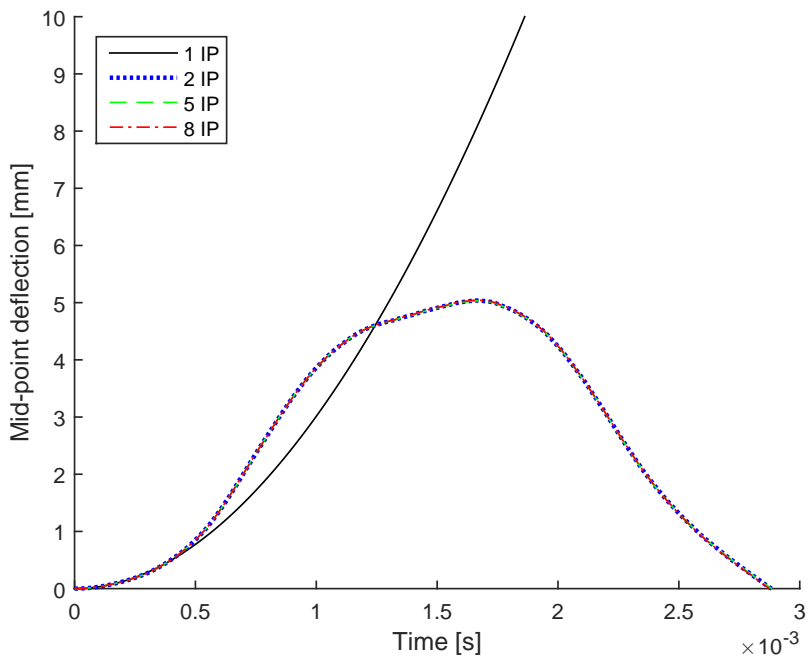


Figure 7.3: Effect of number of integration points.  $P_r = 0.64$  bar.

### Solid glass elements

To validate the accuracy of the basic solid model with one element over the thickness, a mesh sensitivity study was conducted. The aspect ratio was kept constant at 5 : 5 : 4, except for the coarsest mesh, for an increasing number of elements (NOE) over the thickness.

Name	NOE over thickness	Size of element [mm]	Total NOE
<i>A</i>	1	$10 \times 10 \times 4$	1600
<i>B</i>	1	$5 \times 5 \times 4$	6400
<i>C</i>	2	$2.5 \times 2.5 \times 2$	51200
<i>D</i>	4	$1.25 \times 1.25 \times 1$	409600

**Table 7.1:** Different mesh sizes for the sensitivity study.

The deflection–time histories for the different simulations are shown in Figure 7.4. It is clear that the elastic response is close to independent of the number of elements. A reason for this is the choice of element formulation. A fully integrated quadratic 8 node element with nodal rotations, will capture the bending behaviour rather well, and mesh refinement will be of little significance as is seen. Table 7.1 shows the total number of elements and emphasizes the fact that for 64 times as many elements, the change in maximum response was less than 1%. It is clear that the trade-off between accuracy and computational cost<sup>2</sup> is important in such a study, and considering the low mesh dependency in the model, a rather coarse mesh can be utilized.

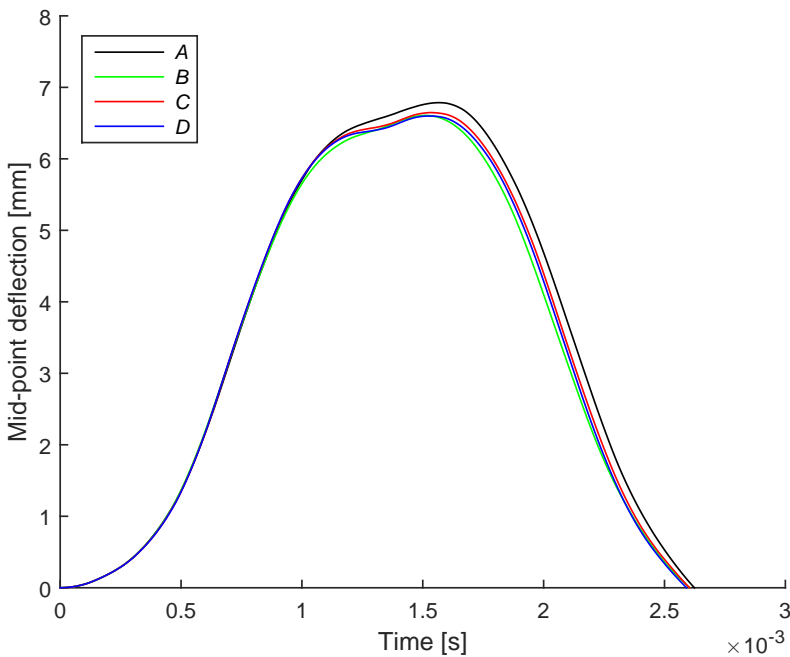


**Figure 7.4:** Effect of number of elements over the thickness.  $P_r = 0.98$  bar.

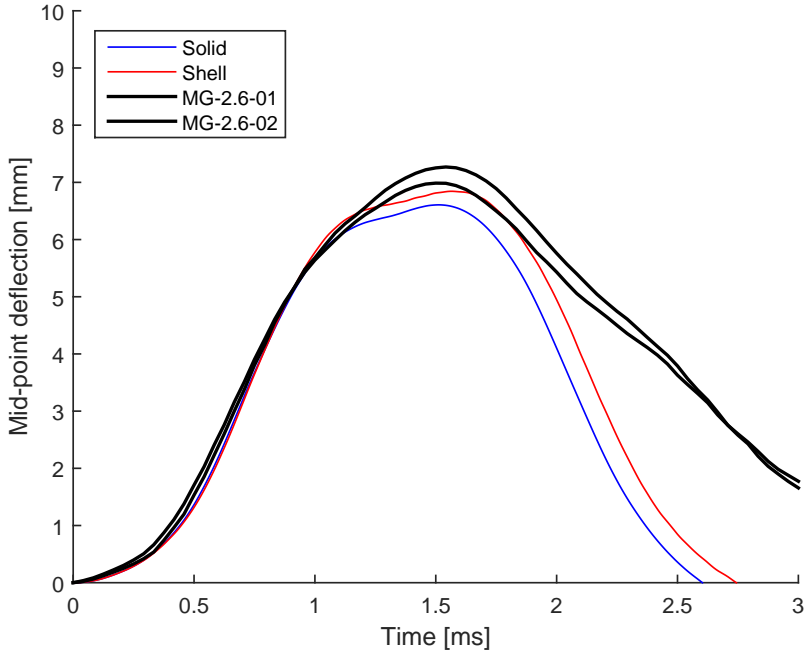
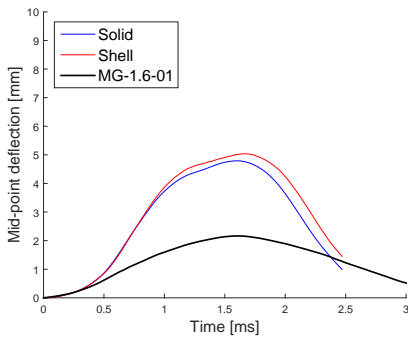
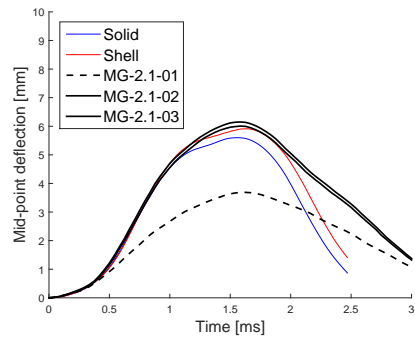
<sup>2</sup> Computational time with the cluster computer at SIMLab using 12 CPU's for the mesh sensitivity study was *A* - 54s, *B* - 1m 50s, *C* - 22m 44s, *D* - 3h 26m 53s

### Simulation vs experiment

Figure 7.5 shows the mid-point deflection for non-fracturing experiments for three different pressures along with the mid-point deflection of two numerical simulations. One of which is modelled with shell elements with five integration points over element thickness, while the other represents the deflection of a model with solid elements, utilizing mesh *B*, see Table 7.1. Assuming a strain rate dependent rubber sealant, the stiffness is set to a value higher than that of the quasi-static value, here  $E = 10$  MPa. It is observed that the simulations are in fairly good accordance with the experiments up until maximum deflection. However, after maximum deflection it is observed that the displacement–time history starts to deviate from the experiments. There may be several reasons for this:

- The arbitrary frame properties. In the experiments, the frame was clamped with a measured torque of 10 Nm each time, but due to the material properties of the rubber, the exact torque applied to the bolts would vary. Additionally, the rubber is not as thoroughly modelled as would be desired.
- Rigid body motion of the test rig. It is known from previous tests in the shock tube facility that the rig usually have an exponentially increasing rigid body motion during experiments, however this was checked and was not the case for these experiments, due to low firing pressures used.
- Simplified blast loading applied in the simulations. The loading used is not able to capture the complex physics, and fluid–structure interaction of the shock tube. However, the pressure used here is so low that this hypothesis is probably not a reason for the deviation.

Further is it worth noting the difference between the experimental results shown in Figure 7.5c, which is discussed in detail in Section 5.3.4. The difference between simulation and experiment shown in Figure 7.5b is also believed to be caused by the same reason, however only a single experiment was conducted for this pressure.

(a)  $P_r = 0.98$  bar.(b)  $P_r = 0.64$  bar.(c)  $P_r = 0.75$  bar.**Figure 7.5:** Mid-span deflection comparison between numerical and experimental values.

### 7.1.3 Failure response

Numerical simulations of fracturing glass subjected to blast loading is no doubt an advancing field, and a general accepted approach is yet to be developed. In order to understand how the different approaches recreate the failure response of the glass pane, a thorough study of the material models presented in Section 3.2 have been conducted.

The following sections cover the material models from Section 3.2, discussing their effect on failure pattern, eroded mass and displacement by varying input parameters. The goal with this study is not to recreate the exact failure capacity of the glass panes, but rather give an indication of possibilities in the qualitative modelling of failure and fragmentation. It is noted that the mesh is omitted in most figures for clarity and illustrative reasons.

#### Elastic material with simple erosion criterion

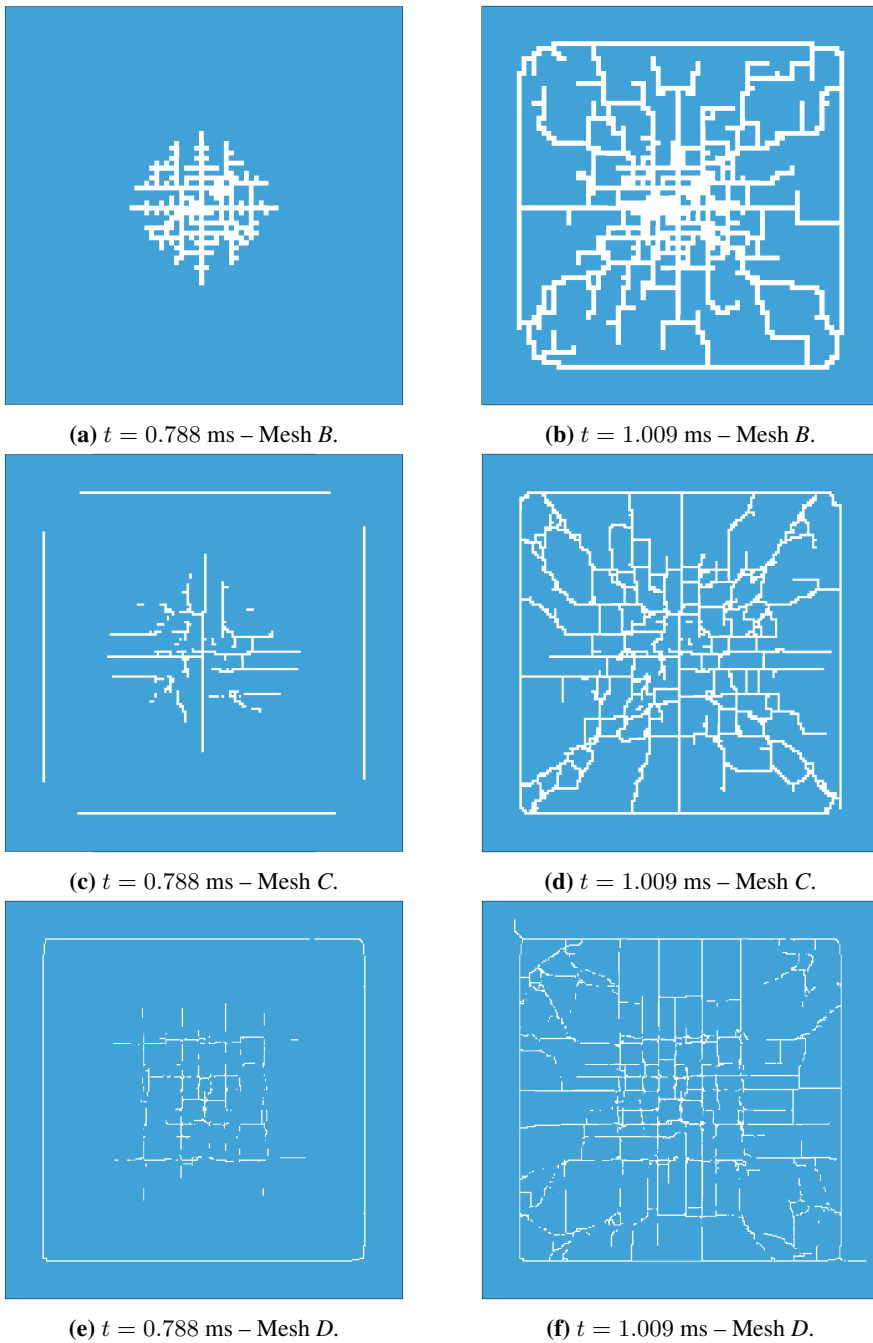
The elastic material model used in the four point bending tests was employed in the modelling of the blast experiments. The material constants used are given in Table 6.1. It was expected that these simulations would emphasize the drawbacks with such a material model. Since all the elements have the same strength, elements will erode in large quantities as soon as the critical principal stress is reached. Three models with different mesh, *B*, *C* and *D* from Table 7.1, and with glass modelled with solid elements, were loaded with the corresponding Friedlander equation found from experiment MG-3.6-02.

Figure 7.6 shows the failure patterns for the three models at two specific times. As can be seen in Figure 7.6a, which shows the first timestep after failure for mesh *B*, a large quantity of elements is removed. The case with mesh *C* and *D*, observed in Figure 7.6c and Figure 7.6e, shows that a finer mesh erodes less mass, however a large quantity of elements is still eroded.

That being said, the material model gives a relatively good representation of the fracture pattern after first failure for all three mesh sizes. Figure 7.6b, 7.6d and 7.6f shows the formation of radial cracks propagating, and the initiation of propagating cracks in the circumferential direction. When compared to the failure pattern seen in the experiments, in Figure 5.5, it is observed that the time from first visible failure to initiation of circumferential crack propagation is about 0.22 ms in the simulations, and 0.08 ms in the experiments. This, along with the excessive element erosion indicates that the elastic material model with a simple erosion criterion does not capture the physical properties of failure in the glass pane. The same behaviour is found for simulations with shell elements.

In order to represent the erosion development graphically, an eroded internal energy–time history graph, shown in Figure 7.7 will be used frequently in the following sections. The graph shows the eroded internal energy (EIE) of the model as a function of time. This method makes it easy to determine the point of first eroded element,  $EIE > 0$ , and a figurative way of determining the total eroded mass in one simulation, relative to another. Figure 7.7 compares the three models shown in Figure 7.6. As can be observed, mesh *D* has its first eroded element before mesh *B* and *C*, however a through-thickness crack is generated at approximately the same time. The mid-point displacement at failure is observed to be





**Figure 7.6:** Fracture progress using an elastic material model with simple erosion criterion. Mesh types *B-D* from Table 7.1 was utilized.  $P_r = 1.16$  bar.

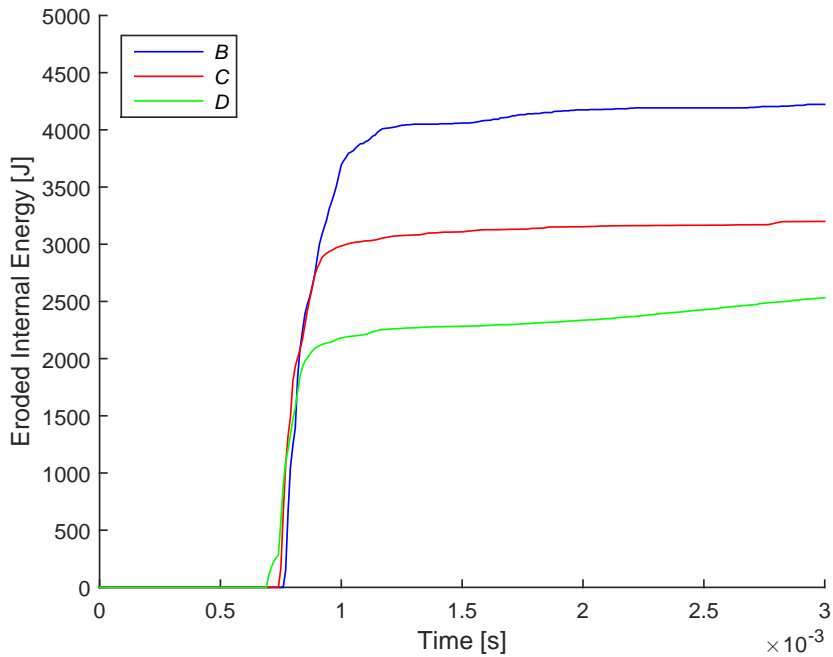


**Figure 7.7:** Eroded internal energy–time history for the three different meshes.

the same for the three meshes. Also note the significant difference in eroded energy for the different mesh sizes.

The excessive element erosion connected with this material model is accentuated even further for higher loading pressures. For a reflected pressure of 2 bar the material model's lack of ability to model glass subjected to blast loading becomes evident, as shown in Figure 7.8. The figure shows that a glass pane model consisting of elements with identical strength will erode an unphysical amount of elements when subjected to a large blast load. This indicates that some kind of stochastic distribution of material parameters might be needed in order to properly describe glass failure characteristics.

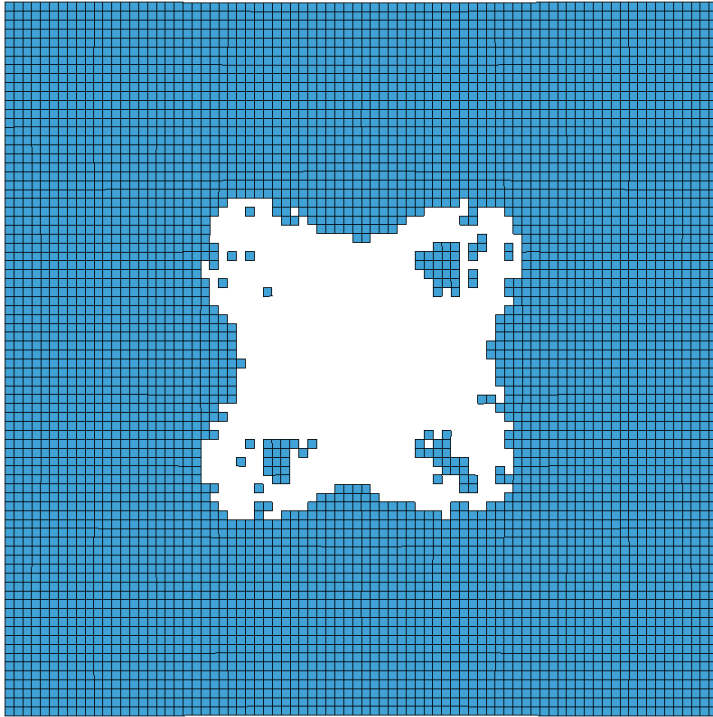


**Figure 7.8:** Fracture of a glass pane with an elastic material model with simple erosion criterion modelled with mesh  $B$ .  $P_r = 2$  bar.

### Johnson – Holmquist 2 material model

The JH-2 material model was used with material parameters taken from [53], provided in Table 6.5, and solid elements with mesh *C*.

As the JH-2 material model is specifically developed for use in modelling of brittle metals, it naturally represents the glass pane subjected to blast loading better than the elastic material model with a simple erosion criterion. However, the differences are smaller than what should be expected. Figure 7.9 shows the fracture pattern of a simulation utilising the JH-2 material model. Although the amount of eroded elements is higher for the JH-2 model, it describes the failure pattern in a fairly well with clearly propagating cracks. However, the JH-2 material model is somewhat cumbersome to calibrate, and several experiments is often needed in order to obtain proper material parameters.

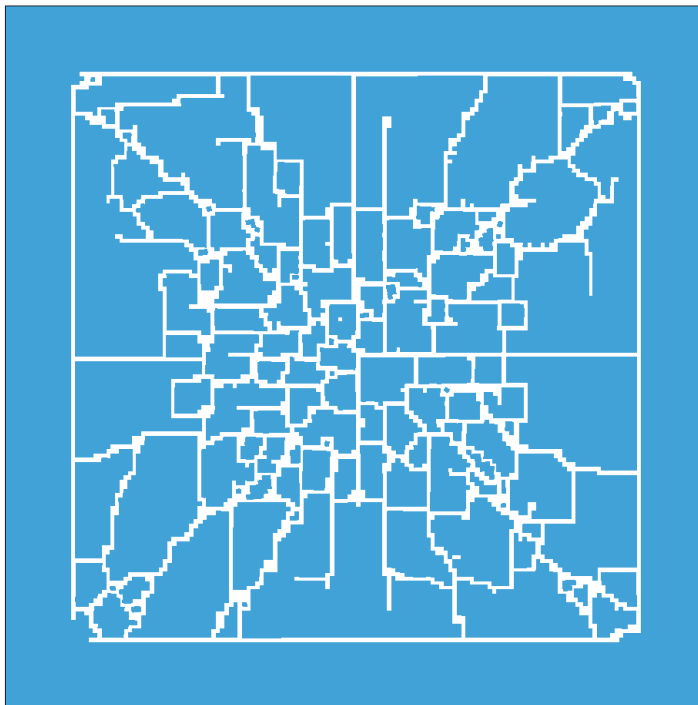


**Figure 7.9:** Fracture progress using the JH-2 material model with mesh *C* and corresponding pressure as in MG-3.6-02.

### SIMLab Metal Model

**Coupled approach:** As mentioned in Section 3.2.2, the SMM introduces the possibility of distributed material parameters, which may avoid excessive element erosion and may generate cracks in the most prone areas of the pane. This also enables the feature of producing different failure patterns and capacities. Six identical inputs, containing the basic shell model subjected to a blast load with a peak reflected pressure of  $P_r = 0.5$  bar, was run with LS-DYNA. The material parameters were taken from Section 6.4, stated in Table 7.2. As no sufficient way of converting the weibull parameters to the case of blast loading was found at the time, the same values as used in four point bending was employed. Note that this is not the ideal procedure, but in order to analyse the trends of the material model it was deemed sufficient.  $V_o$  is the volume in the model assumed under tensile stress. Note that the value for this volume is simplified. Figure 7.10 shows the resulting failure patterns after a simulation time of 3 ms. The initial crack propagation is different in every case creating six unique failure patterns. Fracture initiates in the middle

**Table 7.2:** Weibull parameters for SMM in blast simulations

$\sigma_0$	113 MPa
$m_w$	4.13
$\mu_w$	0.3
$V_0$	180 000 mm <sup>3</sup>
$\sigma_{c,min}$	57.5 MPa
$\sigma_{c,max}$	157.7 MPa

of the pane and propagates towards the corners of the pane before circumferential cracks appear. It is observed that the upper truncation limit is reached in all of the simulations, yet it is the seeded lower limit value that is of interest since it often determines first failure.

The variation in the seeded  $\sigma_{c,min}$  values in the various simulations indicate that the failure response should differ largely from one another. However, this is not the case due to the fact that low strength elements are too few and scattered. A low strength element may be eroded but a propagating crack may be prohibited due to the strong surrounding elements. This phenomenon is clearly seen in Figure 7.10 as a spurious erosion of single elements. Figure 7.11 graphically describes the small variation in response. It is observed that all simulations fail at approximately the same time and that the variation in deflection profile at failure is smaller than anticipated. A indication that the distribution of material parameters capture the crack propagation fairly well compared to the implemented material models in LS-DYNA is also observed. However, the influence on the global response is detained by the lack of larger regions of fragile elements.

**Uncoupled approach, 1 MS element:** A possible solution to capture the distribution in global strength, found experimentally, is to utilise the weibull distribution globally instead of applying it to each element individually, similarly to what was done in the four point bending simulation, described in Section 3.3. Employing only 1 MS element, all of the elements within a simulation will have the same strength, however each simulation will have a different strength. Six identical simulations like this was performed, yielding the

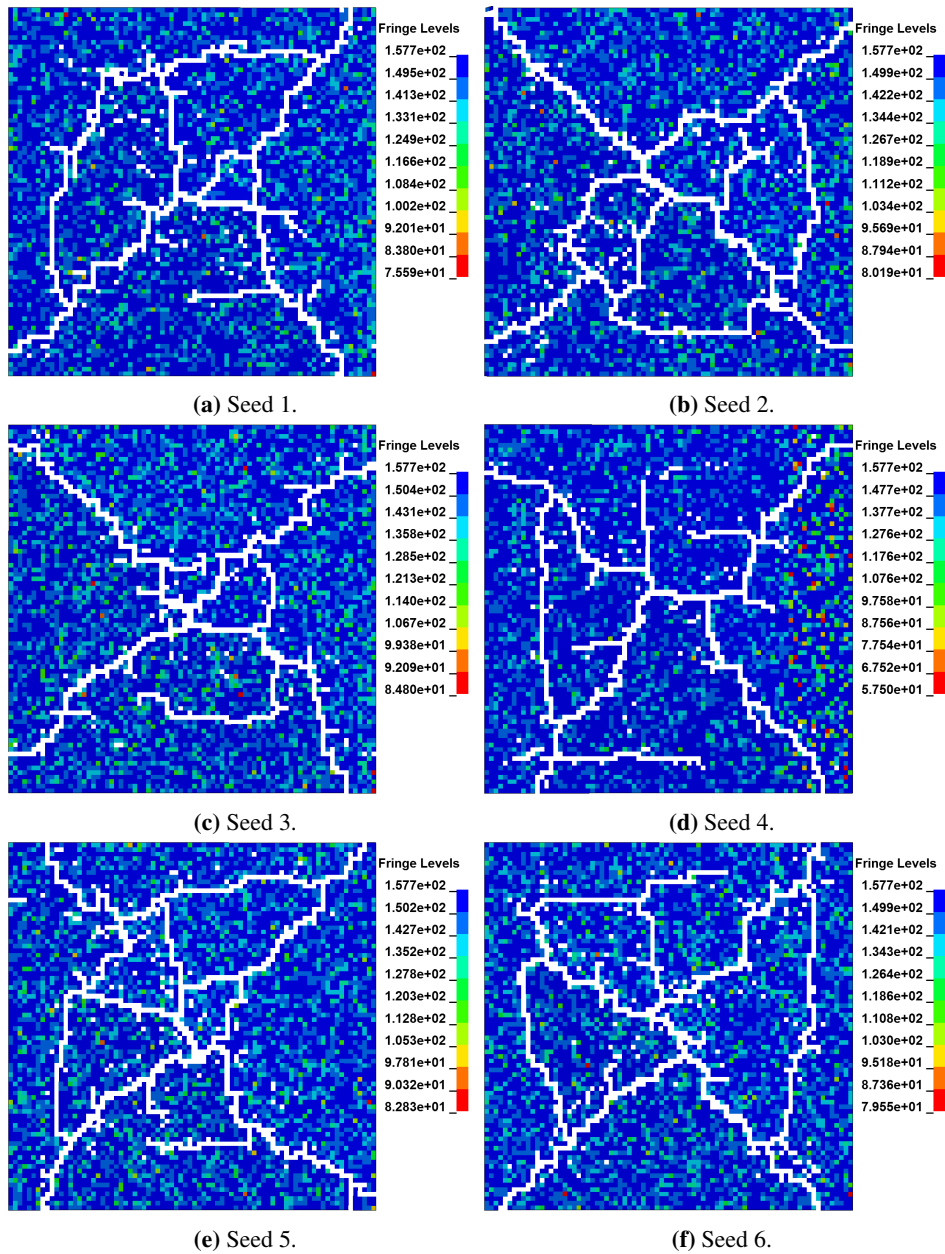


**Figure 7.10:** Fracture pattern in six identical simulations with a distributed material parameter  $\sigma_c$  as described in Section 3.2.2.  $P_r = 0.5$  bar.

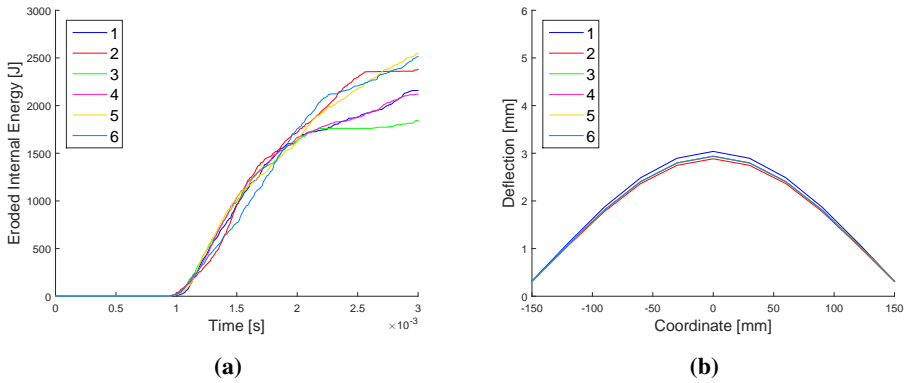


**Figure 7.11:** (a) Eroded internal energy–time history and (b) deflection profiles (11 points across the pane in the  $y$ -direction) at failure for the six identical tests with the SMM.

results shown in Figure 7.12. It is observed that failure occur at different times, shown in Figure 7.12a, for different strengths, shown in Table 7.3, yielding a different displacement at failure, shown in 7.12b. It should be noted that the amount of eroded elements is not represented in Figure 7.12a, since the glass panes fail at different times, meaning that the eroded energies do not correspond to one another.

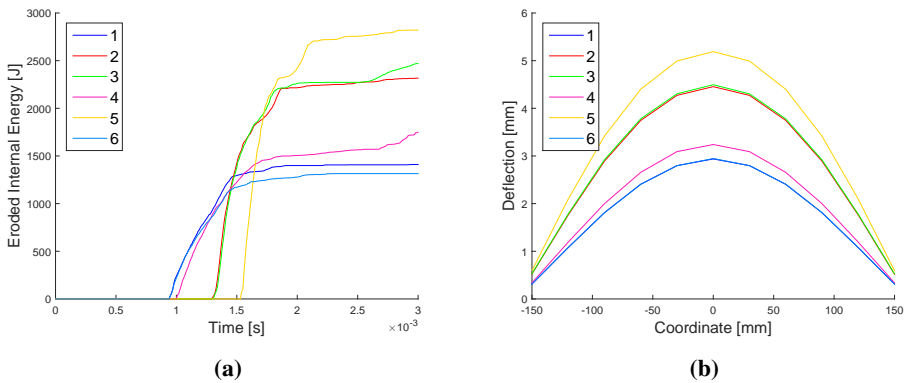


**Figure 7.12:** (a) Eroded internal energy–time history and (b) deflection profiles (11 points across the pane in the  $y$ -direction) at failure for the six identical tests with the SMM. Uncoupled approach where 1 MS element was used.

A summary of the six simulations along with its corresponding seeded critical principal stress and number of elements eroded, is provided in Table 7.3. The trend is that more elements are eroded for a weaker pane, the reason for this is that when the panes fail at an earlier time, more time is available for element erosion. Also note that the panes with the highest seeded  $\sigma_{c,min}$  also have the largest deflection at the time of failure.

**Table 7.3:** Critical first principle stress in the identical models for which only one weibull value was extracted for the entire pane, i.e. one MS element for the entire glass pane.

Plate [#]	$\sigma_c$ [MPa]	NOE eroded
1	57.5	924
2	83.4	810
3	84.0	843
4	64.5	924
5	94.3	810
6	57.5	876

**Uncoupled approach:** Another solution, aiming at capturing both the different global responses and the random propagation of cracks, is to refine the MS mesh on the glass pane, similar to the one proposed in Section 3.3. Although this will not yield a physically correct behaviour, the uncoupled approach is employed as a numerical tool to attempt capturing the initial damage in glass panes. A numerical shell model was created with an MS mesh consisting of  $21 \times 21$  elements, covering the entire glass pane. The failure parameter was distributed within this MS mesh, and projected onto the FE discretisation. Figure 7.13 shows the distributed failure parameter within the MS mesh. Volume dependency and the larger volume of each MS element compared to the coupled approach, cause the probability density function to shift lower, capturing an overall lower range when extracting the failure values. It is observed that the entire span of the weibull distribution is covered, similarly to some of the cases seen in Figure 7.10. Here however, the MS mesh is coarser than in the coupled approach, i.e. approximately  $20 \times 20$  mm, meaning that a unique weibull distributed failure value represents a larger area of the pane, minimizing the possibility of crack propagation being prevented by stronger surrounding elements.

**Table 7.4:** Summary of mesh sensitivity study for the uncoupled approach.

Mesh name	Element size	NOE	NOE eroded	Eroded mass	$w_{failure}$
-	mm	-	-	%	mm
<i>ShA</i>	$5 \times 5$	6400	633	9.89	3.828
<i>ShB</i>	$2 \times 2$	40000	1995	4.99	3.822
<i>ShC</i>	$1 \times 1$	160000	5926	3.70	3.768

A mesh sensitivity study was performed with this numerical model and the specific MS mesh shown in Figure 7.13. The different sizes of mesh and a summary of the results are shown in Table 7.4. The failure pattern for the different meshes can be seen in Figure 7.14. It is observed that the different mesh sizes produce surprisingly similar failure patterns. The most fragile regions in the centre of the pane fail first, and it is observed that all mesh sizes fail at the same time at more than one single point, also seen in some of the experiments, e.g. MG-5.7-03 in Figure 5.5a. It is obvious that the propagating cracks avoid the stronger regions, implying that the MS mesh and the stochastic distributed failure values,  $\sigma_c$ , control the failure pattern to a larger degree than what was the case for a coupled FE and MS mesh. Comparing the coarsest mesh in Figure 7.14a to the simulations in Figure



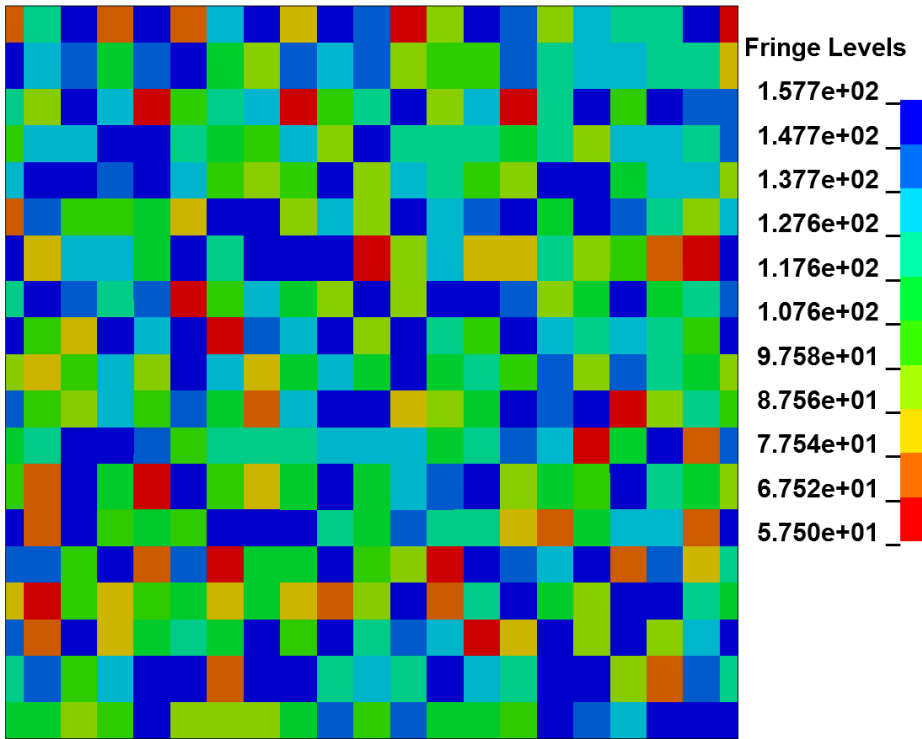


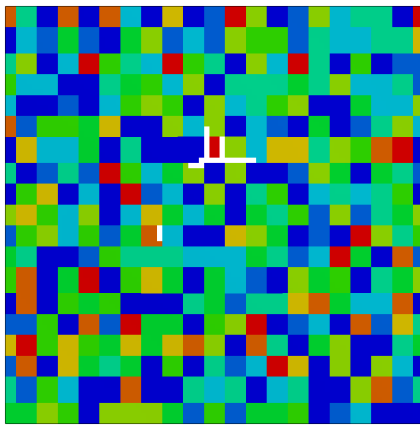
**Figure 7.13:** MS mesh for a numerical model with the SMM.

7.10, it is seen that the problem with single eroded elements due to strong surrounding elements has been greatly reduced, even though approximately the same number of elements are eroded<sup>3</sup>. Table 7.4 summarises the results from the three simulations and shows that the ratio of eroded elements decreases for increased refinement of the FE mesh. However, the global response is similar and there is not much difference in the maximum deflection at failure  $w_{failure}$  of the pane. The  $5 \times 5$  element size is therefore reasonable to use due to both accuracy and computational time<sup>4</sup>.

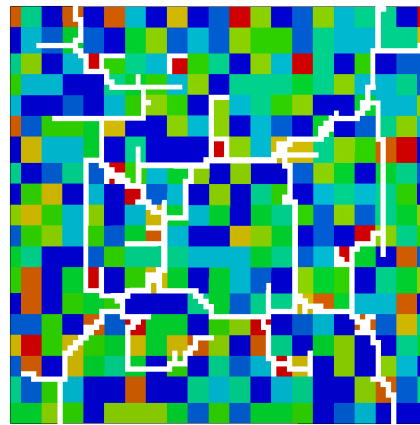
Six identical simulations were performed with the uncoupled approach in order to compare them with the coupled approach and the 1 MS element uncoupled approach. The same loading pressure and FE mesh was utilized as in the simulations with the coupled approach, and the entire distribution range within the truncation limits was present for all of the simulations. Figure 7.16 shows the failure patterns of the six simulations with identical inputs. It is observed that six unique fracture patterns are obtained. Further, it is observed that the problem with single eroded elements almost vanishes. The reason for this is the

<sup>3</sup> Average NOE eroded in the six identical coupled approach tests is 612 while it is 633 in the uncoupled approach.

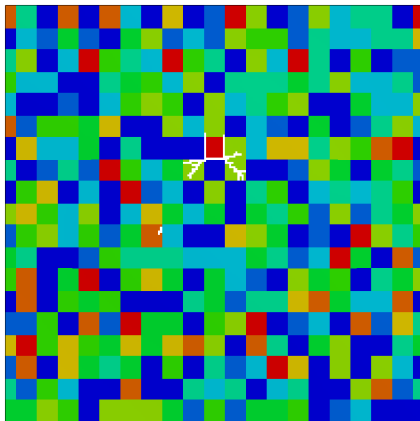
<sup>4</sup> Computational time with the cluster computer at SIMLab using 12 CPU's for the mesh sensitivity study.  $5 \times 5$  – 1m 48s,  $2 \times 2$  – 25m 41s,  $1 \times 1$  – 3h 40m 56s.



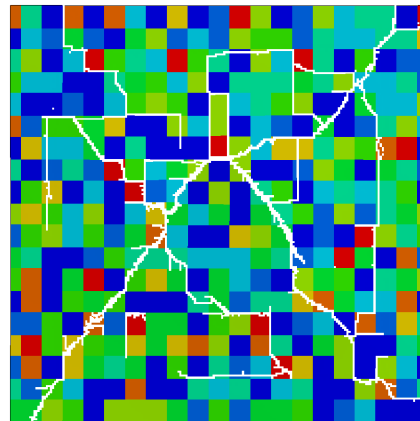
(a)  $t = 1.21$  ms – Mesh *ShA*.



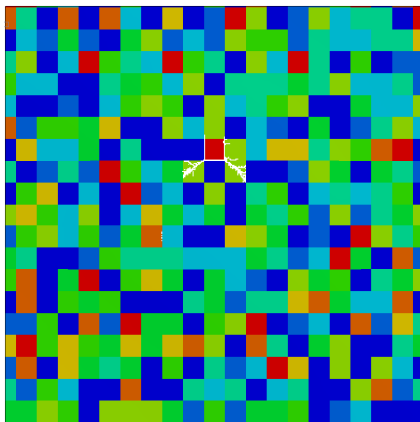
(b)  $t = 3.00$  ms – Mesh *ShA*.



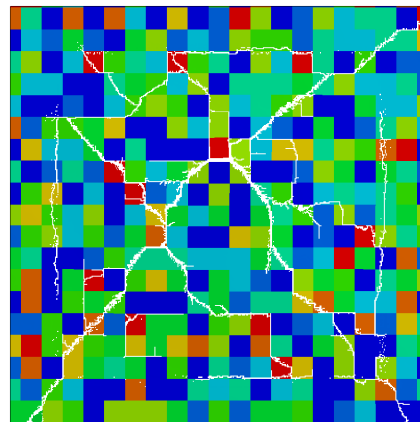
(c)  $t = 1.21$  ms – Mesh *ShB*.



(d)  $t = 3.00$  ms – Mesh *ShB*.



(e)  $t = 1.21$  ms – Mesh *ShC*.



(f)  $t = 3.00$  ms – Mesh *ShC*.

**Figure 7.14:** Fracture pattern for three different FE meshes with identical MS mesh.

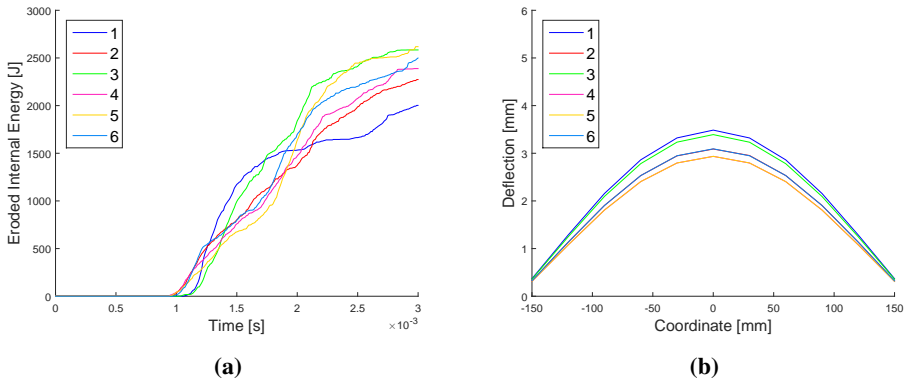


**Figure 7.15:** (a) Eroded internal energy–time history and (b) deflection profiles (11 points across the pane in the y-direction) at failure for the six identical tests with the SMM. The stochastic material failure parameter was distributed utilizing the uncoupled approach.

uncoupled FE and MS mesh, generating several coincident elements that have the same strength causing them either to fracture or withstand fracture. It is clear from Figure 7.16 that the stochastically distributed failure parameter determines the fracture pattern. Cracks propagate through or along the edges of low strength regions of the pane and propagates away from and around stronger elements. Figure 7.15b illustrates how the uncoupled approach of distributing the failure parameter controls the global response.

It is seen that the deflection profile and the maximum deflection is different for the six simulations, indicating that the uncoupled approach is able to describe variations in material strength in addition to crack propagation.

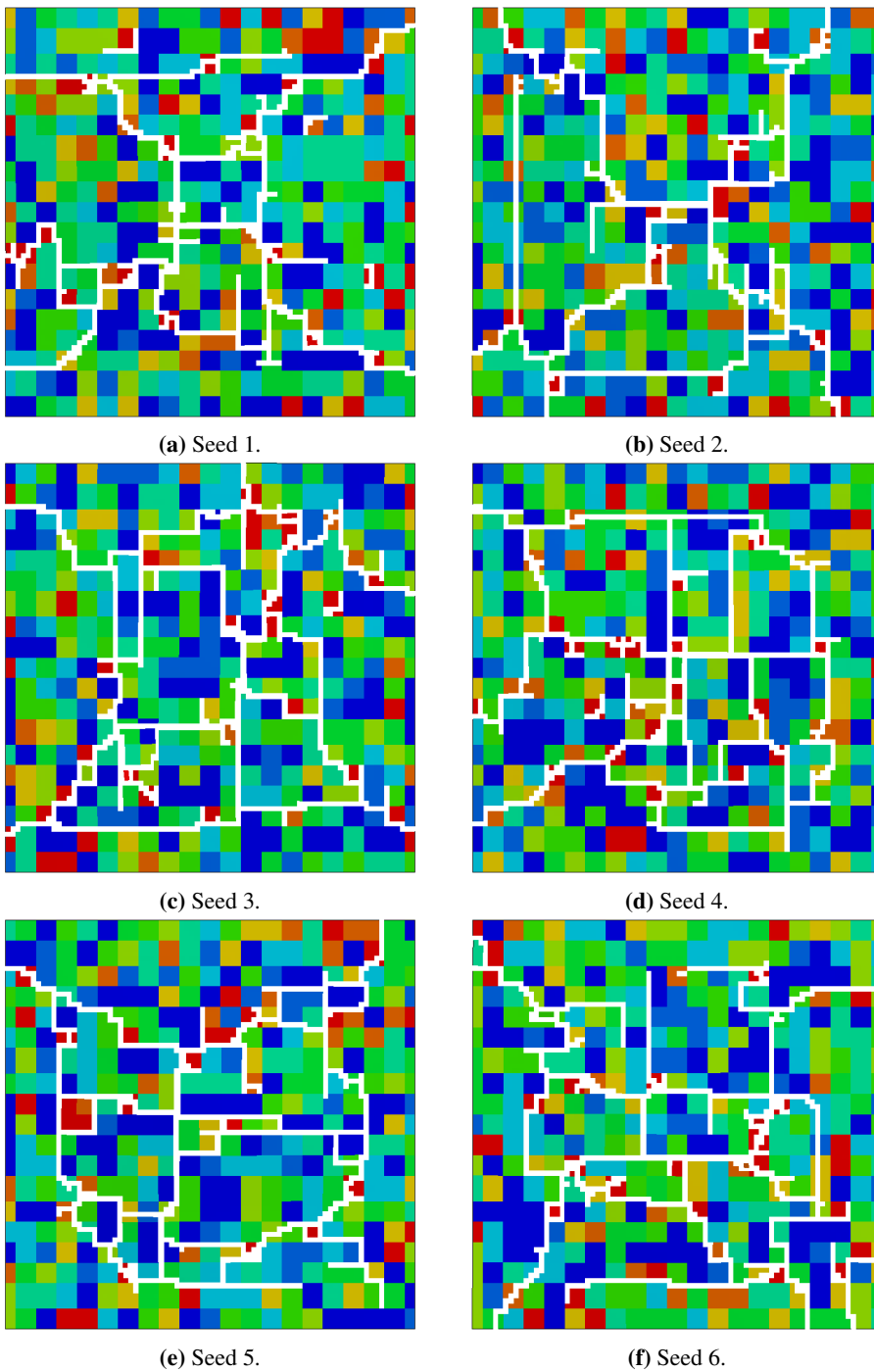


**Figure 7.16:** Fracture pattern for six identical numerical simulations with a distributed material parameter  $\sigma_c$  using the uncoupled approach, described in Section 3.3.

---

### SIMLab Brittle Materials Model

The SIMLab Brittle Materials Model is especially intended for brittle materials. This material model was under development during the work with this thesis, and therefore a thorough study with this material model, was not conducted. However, some studies utilizing the SBMM were conducted.

As the fracture energy  $G_f$  and post-failure fracture energy  $\Delta G_f$  are difficult to determine, a sensitivity study was conducted analysing the effect of these two parameters. The peak reflected pressure was  $P_r = 1.16$  bar representing the pressure in experiment MG-3.6-02, and the mesh used was *ShB*, see Table 7.4. Unless stated otherwise, material parameters from Table 6.7 were used.

As earlier indicated the fracture energy and post-failure fracture energy determines the history variable  $\kappa_1$ , meaning that they control the maximum strain at element deletion, ultimately leading to the fact that these parameters control the brittleness of the material. Therefore, for higher values of  $G_f$  and  $\Delta G_f$  a less brittle response would be expected. For the simplicity of the study,  $\Delta G_f$  is set equal to  $G_f$ . Table 7.5 gives a brief summary of the simulations. It was observed, as expected, that the behaviour became less brittle for higher values of the fracture energy. Additionally, higher values of the fracture energy, generates a failure pattern not observed experimentally, shown in Figure 7.17.

**Table 7.5:** Summary of fracture energy study for the coupled approach using the SBMM.

Fracture energy $J/mm^2$	NOE eroded -	Eroded mass %	$w_{fracture}$ mm
0.00001	12964	32.4	0.53
0.1	8190	20.5	2.06
1	2980	7.5	7.06
10	665	1.7	10.31

Similar behaviour was found for in corresponding study when the glass was modelled with solid elements. It is noted that the amount of eroded elements connected with this model is larger than what was found for the SMM model when distributing the failure parameter with the uncoupled approach.

The effect of mesh size is of interest to see how different mesh sizes affect the global response. Therefore three numerical models consisting of the same mesh as the ones used with SMM, see Table 7.4, was studied. The peak reflected pressure was  $P_r = 0.5$  bar, and the fracture energy and post-failure fracture energy used was,  $G_f = 0.1 J/mm^2$  and  $\Delta G_f = 0.1 J/mm^2$ . No LS-DYNA solver utilizing the uncoupled meshing approach was available at the time of working with the thesis and thus the sensitivity study had to be performed with different distributions. Consequently, referring to Section 3.3, this will only provide a representation of the mesh refinement effect. Figure 7.18 shows the failure history of the three different models at three characteristic times: at first fracture, when there are clearly propagating cracks, and when circumferential cracks become present. Firstly, it is evident that this material model produces a different failure pattern than what

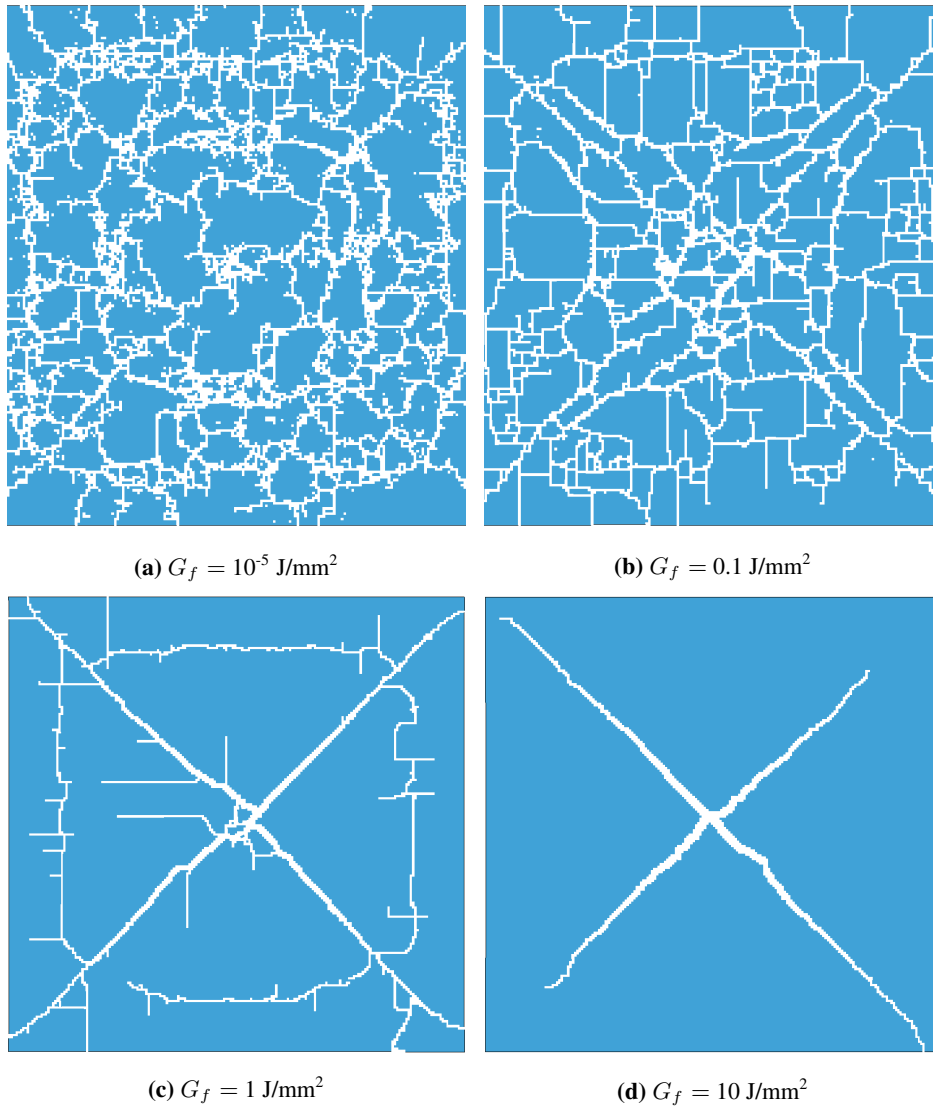


**Figure 7.17:** Failure pattern for different values of  $G_f$  and  $\Delta G_f$  using the SBMM.

was seen with the other material models that have been tried. Similar to the experiments and more highlighted than in the simulations using other material models, the propagation of radial cracks occur first, before circumferential crack propagation initiate. The time from first fracture to established circumferential cracks is consistent for all three mesh sizes (0.26 ms – 0.24 ms – 0.24 ms). When compared to the experiments it is observed that the speed of crack propagation is almost identical, 0.25 ms for test MG-5.7-03, shown in Figure 5.5. Even though it is observed that the crack initiation is at the boundary for the

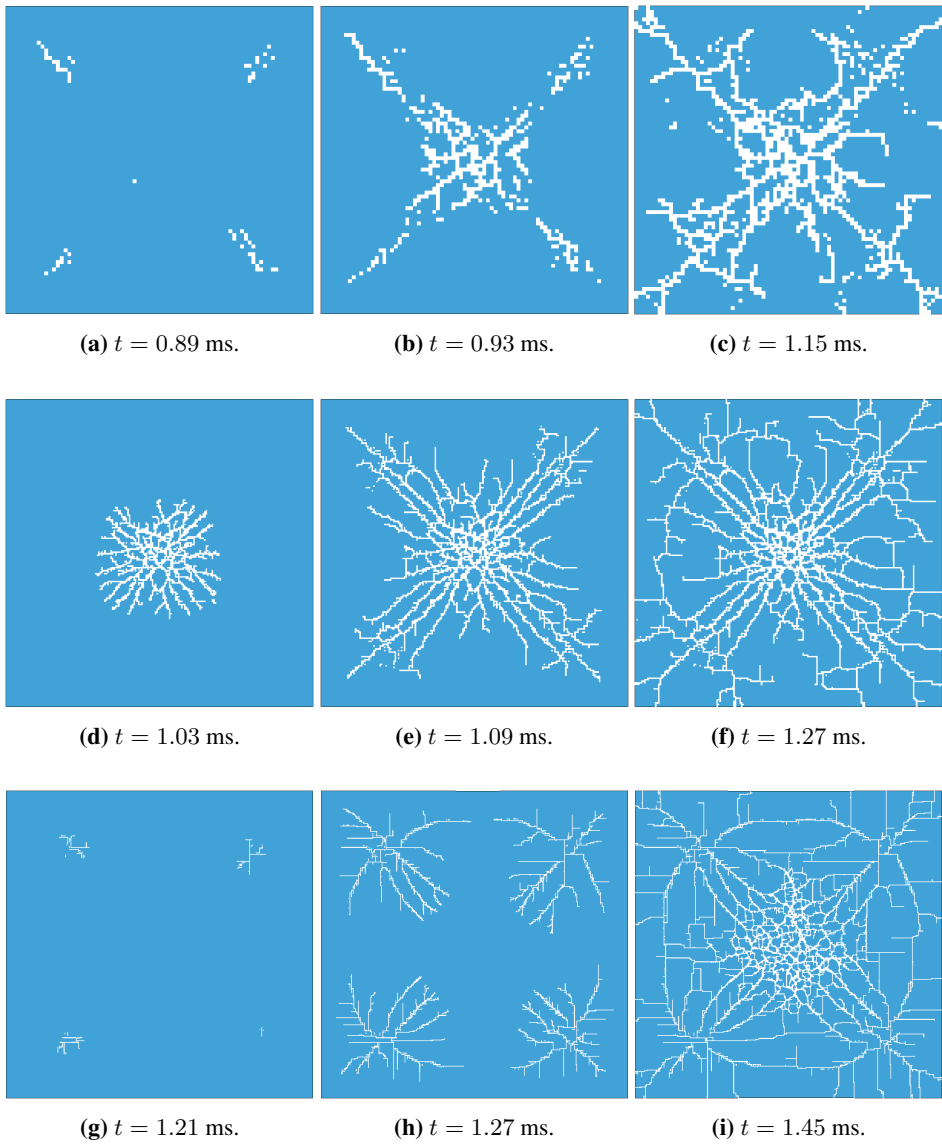


**Figure 7.18:** Fracture history for the three numerical simulations with different mesh size using the SBMM, with a distributed material parameter  $\kappa_0$  using the coupled approach, described in Section 3.3. Mesh: (a)-(c)  $5 \times 5$ , (d)-(f)  $2 \times 2$ , (g)-(i)  $1 \times 1$ .

*ShA* and *ShC* mesh, this was also seen in some experiments. If studying experiment MG-5.7-03 in Figure 5.5 it is seen that the fracture history can be described as a combination of Figures 7.18d–7.18i. Table 7.6 summarises the mesh sensitivity study, and shows that the amount of erosion is drastically higher for the SBMM compared to the SMM.

**Table 7.6:** Summary of mesh sensitivity study for the coupled approach using SBMM.

Mesh name	Element size	NOE	NOE eroded	Eroded mass	$w_{fracture}$
-	mm	-	-	%	mm
<i>ShA</i>	$5 \times 5$	6400	1818	28.41	2.26
<i>ShB</i>	$2 \times 2$	40000	7066	17.67	3.18
<i>ShC</i>	$1 \times 1$	160000	18678	11.67	4.06

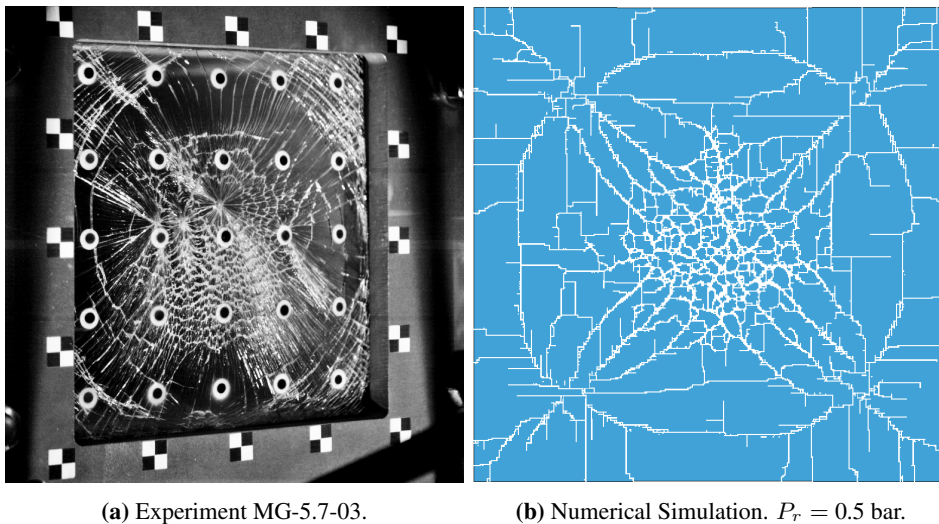


**Figure 7.19:** Comparison between the failure pattern of a sample experiment and a numerical simulation utilising the SBMM.



### 7.1.4 Summary and Discussion

In the previous sections results several simulations, modelling float glass subjected to blast loading have been presented. The chapter addresses the elastic response, i.e. response without failure, and failure response separately. For elastic response without failure, parameters controlling the global behaviour were determined and their effect was studied. Here, the effect of rubber sealant stiffness, number of integration points in shell elements, and mesh size in solid elements was studied. For failure response, simulations were carried out with different material models for the glass pane. Results were studied and analysed to clarify and identify possible advantages and disadvantages with the different material models. The material models that have been studied are the elastic material model with simple erosion criterion, the Johnson–Holmquist 2 material model, the SIMLab Metal Model, and the SIMLab Brittle Materials Model. A reference model was established with a simplified setup, modelling only a part of the clamping frame. It is emphasised that the energy balance was controlled in all models, in order to detect numerical instabilities, and no such instabilities were found.

#### Elastic response

The influence of rubber sealant stiffness was found to be of great importance, and a greater mid-point deflection history was seen for a less stiff rubber sealant. This follows from the argument that a stiff rubber will tend to hold the glass pane in a more clamped state increasing the geometrical stiffness. Although no material tests were performed on the rubber, it is safe to assume that the rubber is not linearly elastic in reality, and in order to capture the global response in a better manner, a thorough material model is needed for the rubber sealant.

It was found that the number of integration points over element thickness in the shell model had a negligible influence on the global response. The same mid-point deflection history was seen for two to five integration points over element thickness, while a single integration point, as expected, was not enough to describe the response.

Effect of mesh size in the solid model was also of minor importance. This due to the choice of element formulation. The quadratic fully integrated elements used managed to capture the global response even for one element over the model thickness. And in order to minimise computational cost it was sufficient to use a rather coarse mesh.

When compared to the experimental results, the numerical simulations were able to capture the mid-point deflection acceptably until maximum deflection. After this point the deflection–time histories in simulations and experiments started to deviate from each other. The main reason for this is believed to be the unknown and arbitrary boundary conditions in the experiments. Although the bolts were tightened with the same torque and in the same

sequence for every experiment, there is no certainty that the clamping pressure applied to the glass pane in the experiments is equal each time due to the rubber sealant.

### **Failure response**

The elastic material model with a simple erosion criterion was able to describe failure in the monolithic glass pane subjected to blast loading fairly good. However, an excessive amount of elements is eroded due to uniform strength throughout the pane. This became more pronounced for higher loading pressures.

Similar behaviour was found for the JH-2 material model as with the elastic model with a simple erosion criterion; a probable failure pattern along with excessive element erosion.

For the SIMLab metal model three different approaches to distribute the failure parameter stochastically was demonstrated. Firstly, where the FE and MS mesh were coupled. This approach yielded little variation in results due to the few and scattered low strength elements. This caused spurious erosion of single elements without crack propagation. However, unique failure patterns were generated for each simulation and probable crack propagation was achieved. Secondly, an approach with only one MS element over the entire glass pane was used. This resulted in a larger variation in global response, however since all FE elements had the same strength, the failure pattern was seen to be somewhat unlikely, with excessive element erosion. Finally, a regular uncoupled approach with MS elements of approximately  $20 \times 20$  mm was carried out. It was seen that with this approach cracks propagated on accord of the weak and strong regions in the pane. In addition, the spurious single element erosion phenomenon seen in the uncoupled approach was greatly reduced. It is worth noting that the glass pane fractured for 0.5 bar in the simulations while the lowest peak pressure the experiments failed for was 0.97 bar. As trends and qualitative behaviour was primarily analysed, the same weibull parameters was used for blast loading as in the four point bending tests. For better quantitative results, a more thorough conversion of distribution parameters, found in four point bending, to blast loading should be conducted.

The SIMLab brittle materials model depicted failure of the glass pane in a good manner. The failure pattern was similar to that observed experimentally, and the crack propagation velocity is within a reasonable extent of experimental values. Figure 7.19 compares the failure pattern of an experiment and a simulation. The formation of radial cracks propagating toward the corners of the pane and then the formation of circumferential cracks are similar in both Figures 7.19a and 7.19b. The effect of the fracture energy and post-failure fracture energy was found to have a large influence on results in the numerical model. For increasing value of the fracture energies, a less brittle behaviour in the glass pane was observed.

It is observed that for the numerical simulations, the capacity is underestimated. This may indicate that the material data obtained from the material tests, may have been implemented incorrectly for usage in simulations of the blast tests.

## 7.2 Laminated glass

### 7.2.1 Numerical Model

As already indicated, there is no general approach in the modelling of laminated glass. However, as stated in Section 3.4 effort have been made to obtain such an approach. A general representation of the numerical model used for simulations of the response of laminated glass subjected to blast loading is shown in Figure 7.20. The model is similar to the one employed in the modelling of monolithic glass, however two glass panes separated by a PVB interlayer were used in this model. The glass was modelled edge to edge against the PVB. A gap of 0.01 mm was present between the outer glass panes and rubber, similar to the model used for monolithic glass. The rubber seal, the frame, the boundary conditions and the pressure loading was applied in the same manner as described in Section 7.1.1. The glass and PVB was modelled with both shell and solid elements. The interface between the PVB and glass pane was modelled utilising the contact keyword *\*\_TIEBREAK* in accordance with [24], described in Section 3.4. This contact type, which enables the simulation of the potential delamination phenomenon between glass and PVB, is used to simulate the adhesive contact between the two materials.

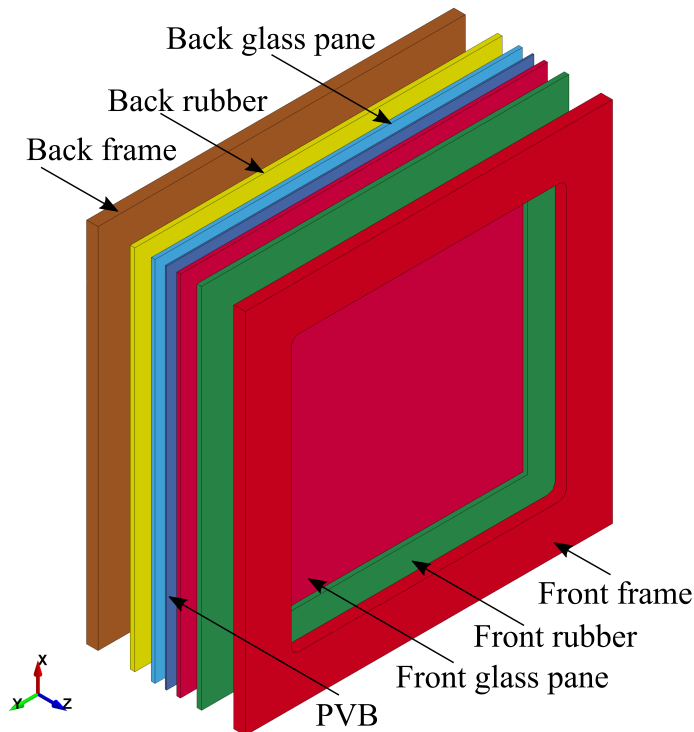


**Figure 7.20:** Exploded view of the general numerical model for blast experiment of laminated glass. Incident blast wave propagates in negative z-direction. Seen from front.

## 7.2.2 Elastic response

As with monolithic glass, an initial study focusing on the elastic response of the laminated glass panes was conducted. The simulations utilized the Friedlander curve fits from the experiment LG-8.6-02 where the glass pane did not fail. The following sections examines the elastic behaviour of a laminated glass pane subjected to blast loading for different numerical simulation techniques. Unless otherwise stated the PVB is modelled with solid elements and material properties stated in Table 3.1. As accurate modelling of the PVB behaviour was not within the scope of this thesis, the PVB was treated as a linear elastic material in order to reduce complexity. The rubber sealant's stiffness is known to control the deflection history, here  $E = 20$  MPa is used, since this value was seen to yield decent results.

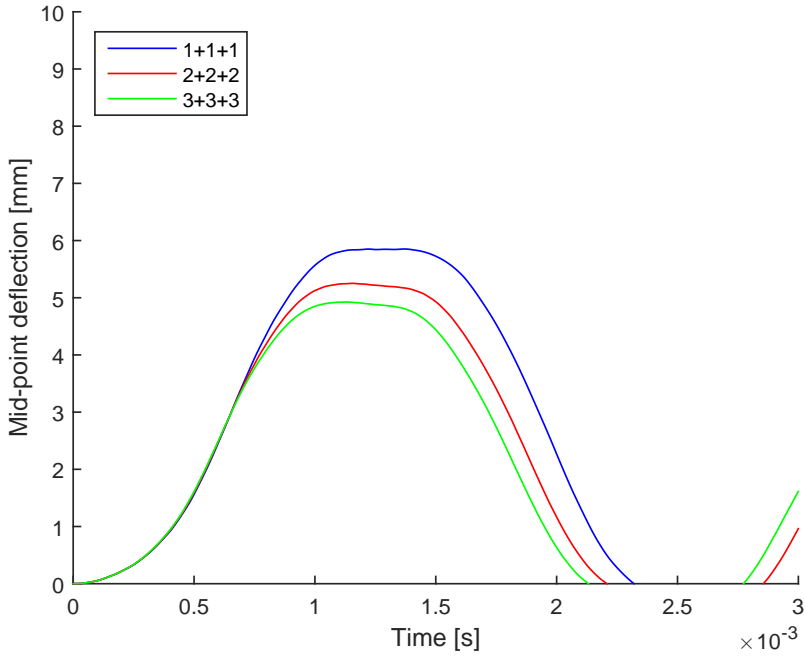
### Solid glass elements

The effect of mesh size is of interest, and therefore a mesh sensitivity study was conducted. Since only the elastic response was to be analysed, no failure criterion was implemented. Seven numerical models, each with a different mesh size, stated in Table 7.7, was generated to examine the effect of mesh size. The computational time,  $t_{clock}$ , along with number of CPU's, NCPU, are also listed. It is worth noting that the aspect ratio for glass and PVB were  $5 \times 5 \times 4$  and  $5 \times 5 \times 1.52$ , respectively. The mesh naming is based on the number of elements through the thickness of each individual layer in the laminated glass pane; NOE in front glass pane + NOE in PVB + NOE in back glass pane. Figure 7.21 shows

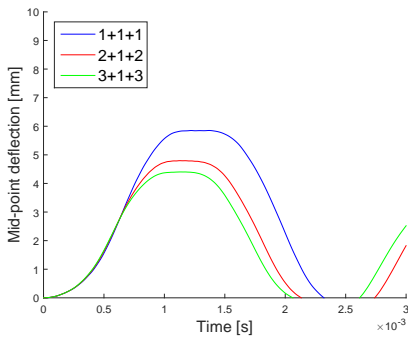
**Table 7.7:** Summary of the different meshes utilised in the mesh sensitivity study.

Mesh name	Glass element size	PVB element size	NOE in LG	$t_{clock}$ [NCPU]
1+1+1	$5 \times 5 \times 4$	$5 \times 5 \times 1.52$	19200	9m 49s [8]
1+2+1	$5 \times 5 \times 4$	$2.5 \times 2.5 \times 0.76$	64000	NA
1+3+1	$5 \times 5 \times 4$	$1.66 \times 1.66 \times 0.51$	185600	47m 34s [8]
2+2+2	$2.5 \times 2.5 \times 2$	$2.5 \times 2.5 \times 0.76$	153600	2h 20m 36s [8]
2+1+2	$2.5 \times 2.5 \times 2$	$5 \times 5 \times 1.52$	108800	2h 8m 59s [8]
3+3+3	$1.66 \times 1.66 \times 1.33$	$1.66 \times 1.66 \times 0.51$	518400	5h 44m 7s [12]
3+1+3	$1.66 \times 1.66 \times 1.33$	$5 \times 5 \times 1.52$	396800	4h 29m 46s [12]

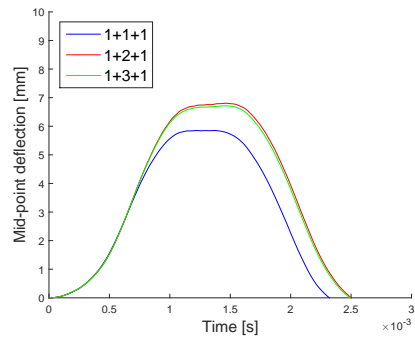
the resulting mid-point deflection history for the different meshes. It is observed that the maximum deflection decreases for an increasing number of elements over the thickness in the glass layers. Contrary, it is seen that for an increasing amount of elements over thickness in the PVB layer, the maximum deflection increases. The overall response when increasing the number of elements over the thickness in all layers is that the mid-point deflection decreases. Without further study, it is difficult to determine the exact reason for this. However, it is believed that the reason for this behaviour is the contact between PVB and glass, whereby the shear stress is not represented correctly.



(a) Same number of elements over thickness for all three layers.



(b) Single element in PVB layer.



(c) Single element for both glass layers.

**Figure 7.21:** Mid-point deflection history for different meshes.

### Shell–solid–shell behaviour

A cost-effective way of modelling laminated glass is to model the glass layers with shell elements, while the PVB is modelled with solid elements, termed a combined model in this thesis. It was found in Section 7.1 that the modelling of glass with shell elements provided good results for both elastic and failure response. The 8 node fully integrated solid elements with nodal rotations are well suited for connections with shells, [55], making this approach an appropriate way of modelling laminated glass. The front and back glass was modelled coincident with the solid PVB and an offset was employed with the NLOC parameter in the keyword *\*SECTION\_SHELL*. A thorough study of this approach of modelling laminated glass was not performed. However, Figure 7.23 shows a typical representation of the response seen for such a simulation. It was experienced that the modelling of the two glass layers in such a close proximity to each other along with the connectivity between shell and solid led to poor results. In order to obtain satisfactory results from a laminated glass model using a shell – solid – shell configuration, more work is needed.

### Single layered shell

As described in Section 3.2.1 *\*MAT\_LAMINATED\_GLASS* is a commercially available LS-DYNA material model that efficiently models laminated glass behaviour. This material model along with *\*INTEGRATION\_SHELL* was used in order to describe the different layers of the laminated glass pane. This section will cover the effect of integration points used with this material model. Table 7.8 shows the different configurations used.

**Table 7.8:** Summary of the integration point configurations employed in the sensitivity study of the layered shell model.

NIP	Layer distribution
6	2+2+2
8	2+4+2
10	4+2+4
13	5+3+5
14	5+4+5

Figure 7.22 shows the resulting mid-point deflection for the different configurations of integration rules. An increased mid-point deflection is found for a higher number of integration points in the PVB layer, and a decreased mid-point deflection for more integration points in the glass layers. This is similar behaviour to what was seen in the solid mesh sensitivity study. The reason for this is unknown, but it is worth noting that the difference in response is rather large, meaning that the material model should be employed with care.

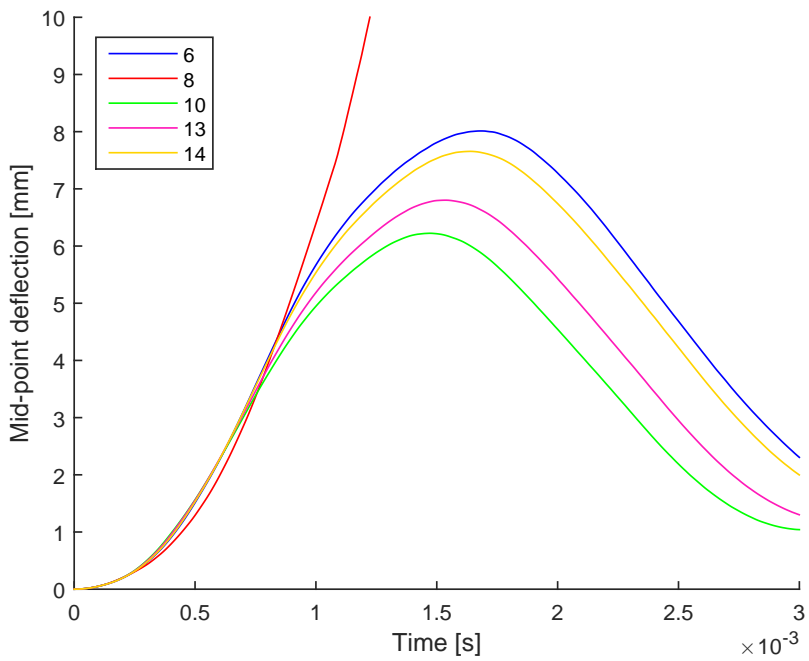


**Figure 7.22:** Mid-point deflection history for different configurations of integration points with layered shell model.

### Simulation vs Experiment

Figure 7.23 shows the mid-point deflection history for two experiments, LG-8.6-01 and -02, along with the mid-point deflection history for three numerical simulations; a solid model with the 3+3+3 mesh configuration, a layered shell with the 14 integration point configuration, and a combined model. It is observed that neither of the models are able to describe the global response in a satisfying manner. The displacement history of the simulations is seen to coincide with the experiments for the first 0.5 ms, but after this point the simulations deviate from the experiments. It is clear that the behaviour of the combined model is too flexible while the solid and layered shell model is too stiff. The solid and layered shell model is seen to have qualitatively similar behaviour, however the combined model is far off from recreating what was observed in the experiments. It is worth noting that the rubber sealant stiffness has been set to 20 MPa for these simulations. It is highly unlikely that the rubber stiffness is higher than this even when accounting for strain rate sensitivity. As found in Section 7.1, an increased rubber sealant stiffness will increase the overall stiffness of the system. These remarks indicate that the combined model does have some practical errors. In order for the combined model to represent experimental results accurately, a more comprehensive study of it is in order.

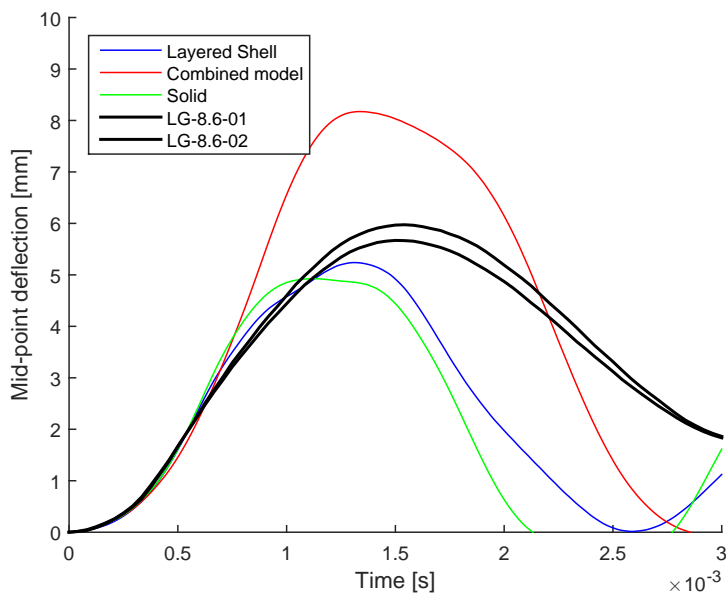


**Figure 7.23:** Comparison of the mid-point deflection history between the experiments and the simulations.



### 7.2.3 Failure response

In this section, the results from numerical modelling of failure response in laminated glass panes subjected to blast loading, is presented. Failure in the layered shell model was not be studied, as it is not able to represent the failure pattern and delamination phenomenon found in laminated glass. In Chapter 6 and in Section 7.1 it has been observed that simulation of glass subjected to blast loading can be described fairly good utilising an LS-DYNA implemented material model and shell elements. Due to this, a combined model as de-

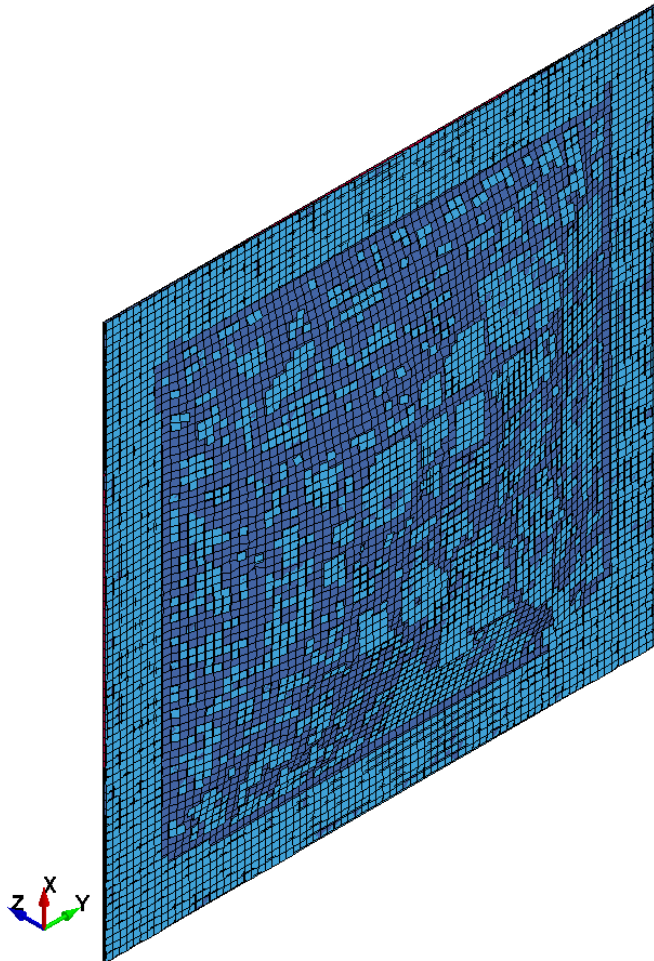


**Figure 7.24:** Failure pattern of the combined model, seen from back.

scribed in Section 7.2.2, was analysed as an introductory study. The model utilised shell elements of size  $ShA$ , see Table 7.4, for the glass, and was modelled with the elastic material model with simple erosion criterion as described in Chapter 6. It is clearly seen in

Figure 7.24 that the element erosion is excessive; more than 38% of the total mass of the glass layers is eroded. Along with the excessive erosion, some problems was found with this numerical model regarding elements with negative volume. This was believed to be caused by a discrepancy in the shell – solid interaction yet the matter is still unresolved.

It was experienced in Chapter 6 and Section 7.1 that solid elements, as with shell elements, managed to describe the failure response of the glass pane in a satisfactory manner, however the computational cost was much higher. The poor results and problems with the combined model and the good results employing solid elements modelling monolithic glass, encouraged the further use of solid elements. An introductory study was performed

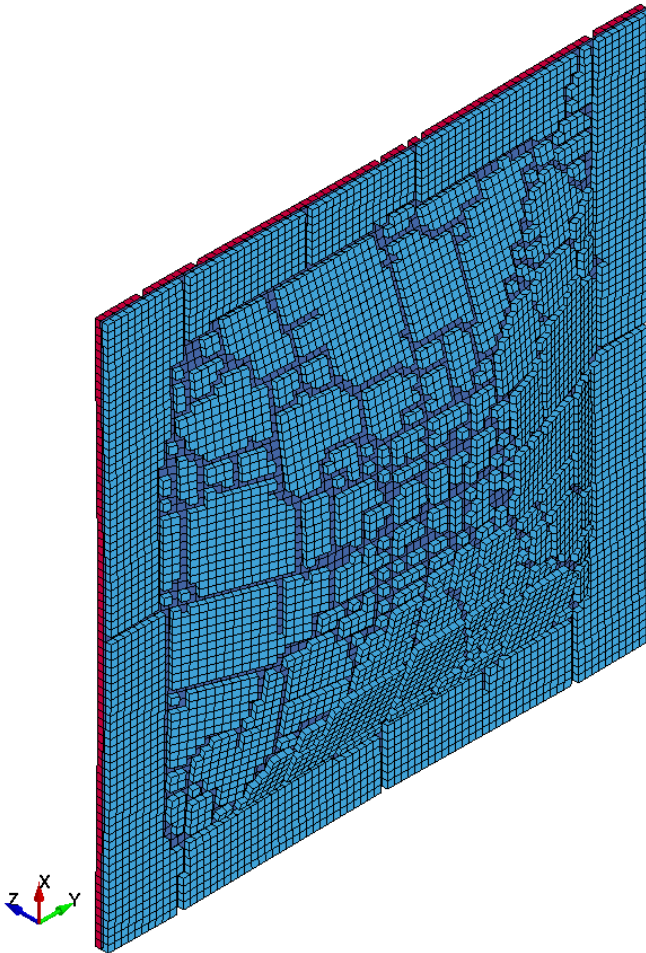


**Figure 7.25:** Failure pattern of the solid model, seen from back.

in order to analyse the global behaviour utilising solid elements. A solid element model was established with the elastic material model with simple a erosion criterion, described

in Section 3.2.1. The mesh size corresponded to the 1+1+1 configuration given in Table 7.7. Figure 7.25 shows the resulting failure pattern. The erosion is seen to be drastically reduced compared to the combined model, approximately 25% of the total mass of the glass layers was eroded. The rather coarse mesh yielded a computational time of 6m 17s, and when compared to the time of the combined model, 4m 42s, this is not a high price to pay regarding the accuracy of the models.

The model managed to recreate several phenomena observed experimentally. The typical behaviour when laminated glass subjected to blast loading fails, is that the back glass pane fractures first, while the front glass pane fractures later, shown in Figure 3.5. This was described well in the model, as shown in Figure 7.26. It is seen that the back glass panel fractures about 0.06 ms before the front pane. Comparing this to what was seen in the experiments, e.g. Figure 5.11 and 5.12. Note that the difference in times of fracture is much larger in the experiments, around 0.9 ms. However, the propagation of cracks in the back pane is well-established when the front pane fails, which is similar to the experiments. Another interesting result is the delamination of the glass and PVB in the numerical model. The use of the *\*TIEBREAK* contact as described in Section 3.4 enabled the delamination of the laminated glass.

Considering that the solid element model yielded rather good results, it was also employed with a finer mesh, and different material models, described further in subsequent sections. Note that all subsequent models utilise the 3+3+3 mesh configuration in Table 7.7.

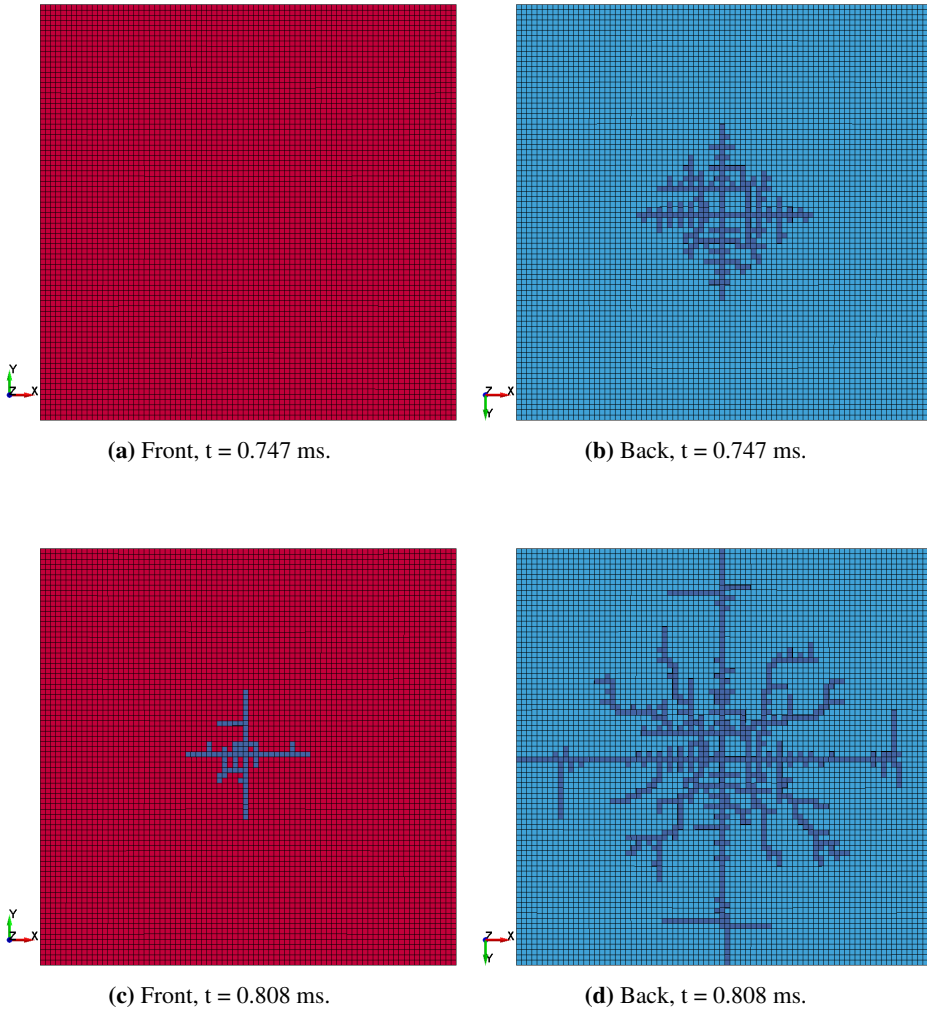


**Figure 7.26:** Fracture progress for the front and back glass layer using elastic material with simple erosion criterion.

### Elastic material with simple erosion criterion

The elastic material with simple erosion criterion was further studied using the refined mesh. The applied pressure history was the Friedlander fit from experiment LG-9.6-02, shown in figure 5.15b. Figure 7.27 shows a detailed view of the failure pattern for the model. As with the model in the introductory study, the qualitative description of the laminated glass pane is satisfactory. The time interval between fracture of back pane and

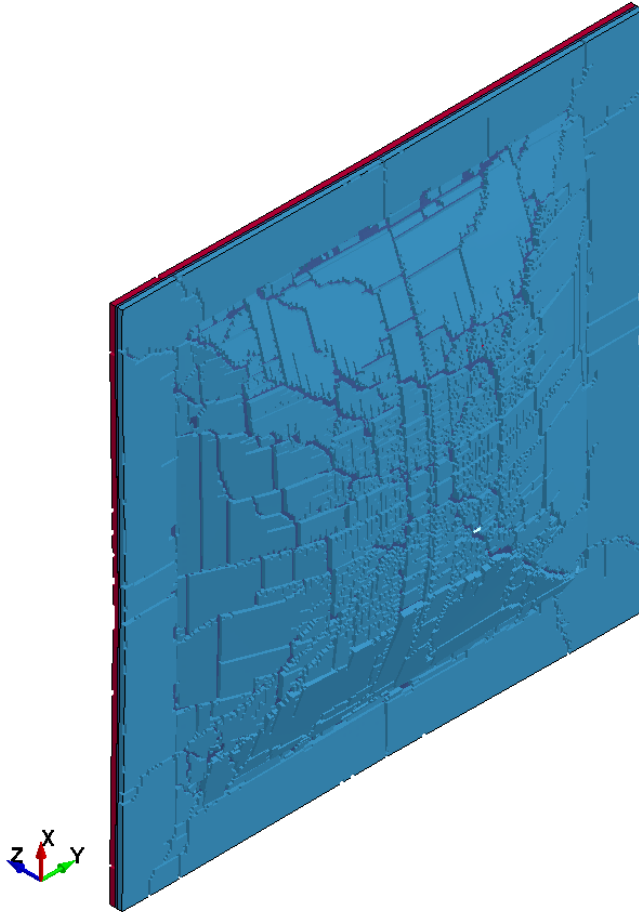
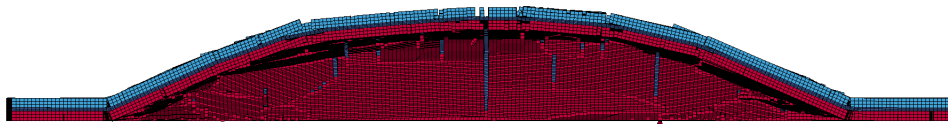


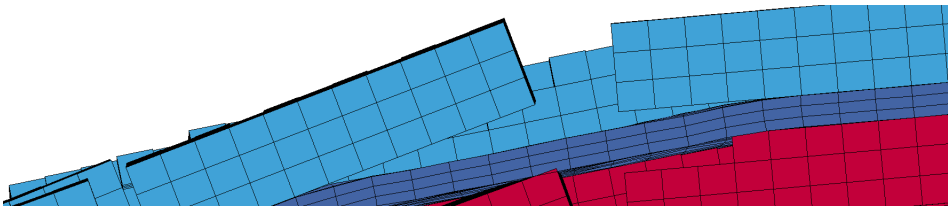
**Figure 7.27:** Failure pattern of the solid model, seen from back using elastic material with simple erosion criterion.

front pane was observed to be similar to the introductory study, see Figure 7.26, about 0.06 ms. it was found that less mass was eroded compared to the introductory study, less than 17% for the refined mesh. Figure 7.28a shows a sectioned view, the  $yz$ -plane cut at  $x = 0$ , giving a representation of the deflection profile for the laminated glass

pane, and Figure 7.28b shows a detail of the sectioned view. Figure 7.28a provides an indication of the adhesion properties of the *\*TIEBREAK* contact. It is observed that the glass cracks up while following the deflection profile of the PVB until the glass fails. Figure 7.28b highlights the delamination phenomenon modelled using the *\*TIEBREAK* contact. It is evident that the failure criterion, described in 3.4, is fulfilled and it is seen that the back glass pane has debonded from the PVB. It is also seen that once the failure criterion is reached, all contact for the current part is neglected, illustrated by the front glass penetrating the PVB in Figure 7.28b.



(a) Section view of the deflection profile.



(b) Detail of section view of the deflection profile.

**Figure 7.28:** Section view of the deflection profile with elastic material with simple erosion criterion.

### SIMLab Metal Model

The SMM yielded good results in the modelling of monolithic glass in Section 7.1.3. The material model together with the uncoupled approach of distributing the failure parameter managed to create weak and strong regions in the pane that determined the fracture of the monolithic glass. It was observed that the capacity was dependent on the distribution of the failure parameter. The SMM was also applied for the laminated glass model with refined mesh. The stochastic distribution parameters used were the same as in Section 7.1.3, given in Table 7.2.

Figure 7.29 shows the failure pattern the SMM on laminated glass. The fracture is seen to

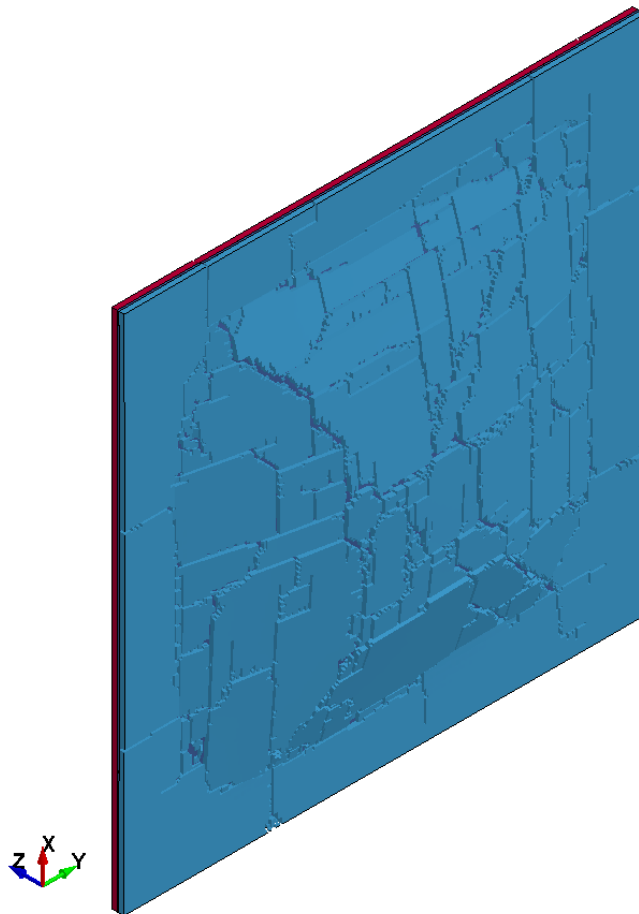


**Figure 7.29:** Failure pattern of the solid SMM model, seen from back.

be more distributed compared to the elastic material model with simple failure criterion, seen in Figure 7.27. It is also noted that the eroded mass was only 11%. Figure 7.30 shows

the distribution of the failure parameter  $\sigma_c$  for the front and back glass layers.

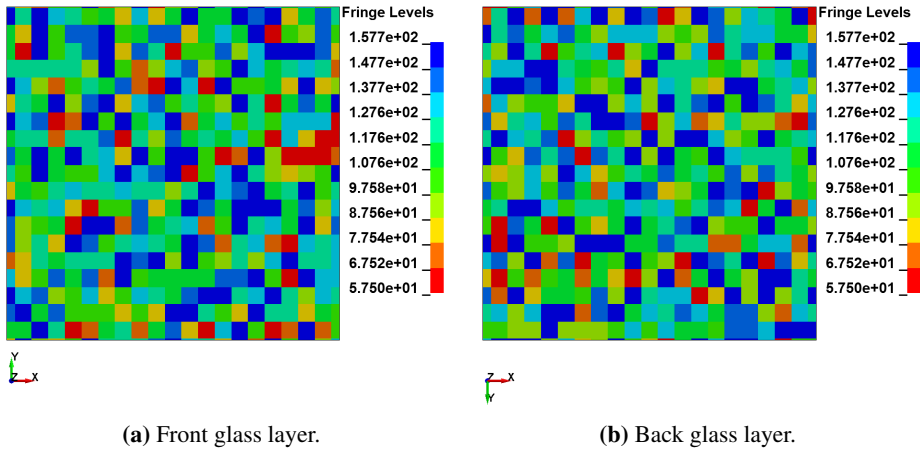


**Figure 7.30:** Distributed failure parameter  $\sigma_c$  in both glass layers of the laminated glass pane.

Figure 7.31 shows the corresponding failure history of the individual glass layers in the laminated glass pane. It is seen that there is a time interval between fracture in the back and front glass layer. While this difference in time, 0.12 ms, is slightly larger than that of the results with the elastic material model, it is still too small compared to the experiments. From Figures 7.30 and 7.31 it is observed that the failure parameter determines the failure pattern. The weakest regions of the pane fracture first, and the cracks propagate through weak regions and around stronger regions.



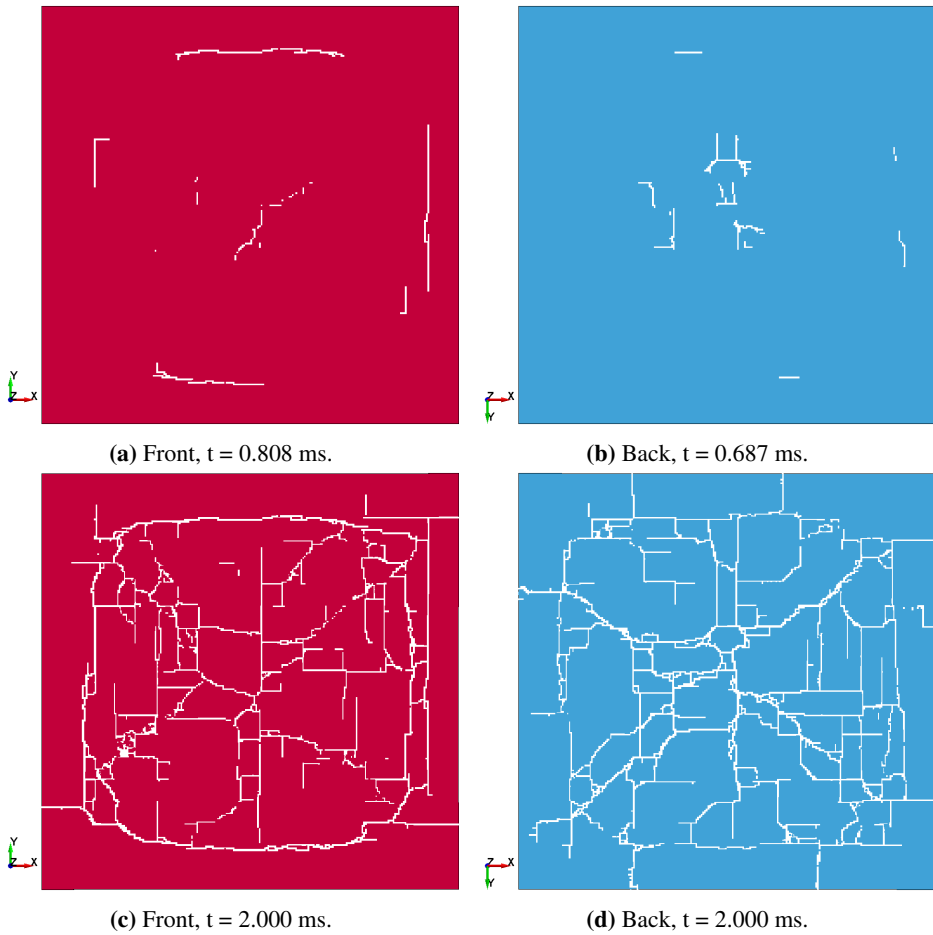


**Figure 7.31:** Fracture progress for the front and back glass layer.

### SIMLab Brittle Materials Model

The SBMM was found to provide a physically reasonable failure response of the monolithic glass, compared to experimental results, shown in Section 7.1.3. The laminated glass model with this material model was established using the general model described in preceding sections, only changing the material input. Figure 7.32 shows the resulting failure pattern of the laminated glass pane. Even if the eroded mass of the glass layers is higher than that of the material model with a simple erosion criterion, approximately 20% for SBMM, it is evident that the failure pattern is more physically representative with the SBMM. This is highlighted with irregular crack propagation and distinct circumferential cracks indicating that the brittle fracture is well described with this material model. Figure

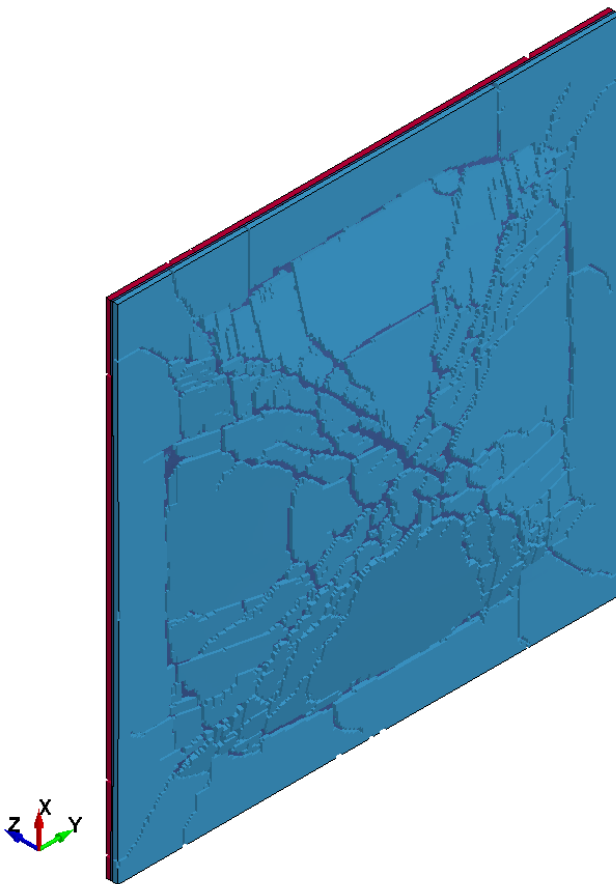
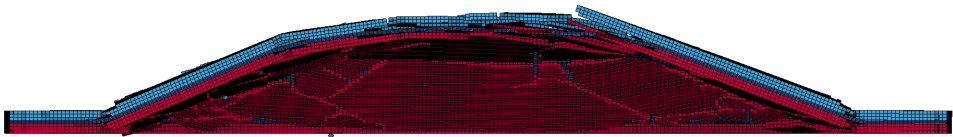


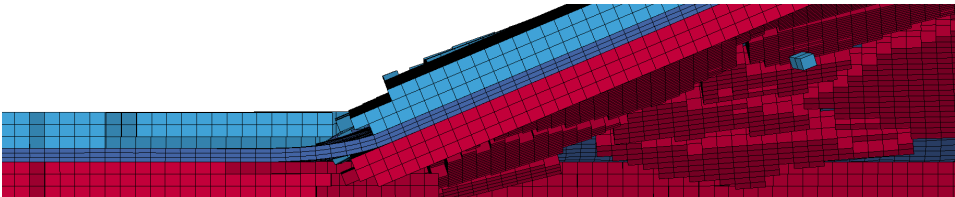
**Figure 7.32:** Failure pattern of the solid SBMM model, seen from back.

7.33a shows a sectioned view of the deflection profile of the laminated glass pane, the  $yz$ -plane cut at  $x = 0$ . It is observed that after the *\*TIEBREAK* failure criterion is reached, described in Section 3.4, contact is neglected. This is seen here as the front pane pene-

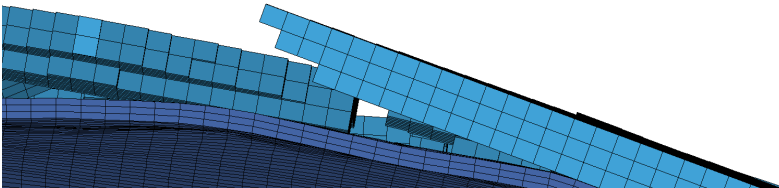
trating the PVB. Figure 7.33b emphasize the models ability to recreate the behaviour of the PVB. At the boundary, it is observed that there are adhesive forces bonding the glass and PVB together. The glass breaks and sticks to the PVB, while the PVB undertakes the bending. Figure 7.33c shows a detailed view of the delamination phenomenon. For illustrative reasons the front glass pane is not shown in Figure 7.33c. The PVB and glass elements will stay in contact until the normal and shear stresses at the interface fulfils the criterion given in Section 3.4. It is evident that the failure criterion is achieved in Figure 7.33c and a region of the glass layer has debonded from the PVB. It is also observed that after delamination, the PVB no longer has restricted motion by the glass layers, and is free to take an irregular profile.



(a) Section view of the deflection profile.



(b) Detailed section view of the deflection profile.



(c) Detailed section view of the deflection profile.

**Figure 7.33:** Section view of the deflection profile.

Figure 7.34 shows the failure history of the laminated glass pane modelled with the SBMM. As was seen utilising the elastic material model with a simple erosion criterion, the back glass pane fractures prior to the front pane. The time interval between the fracture of the two layers is similar to what was seen for the elastic material model with a simple erosion criterion, see Figure 7.25, approximately 0.06 ms.

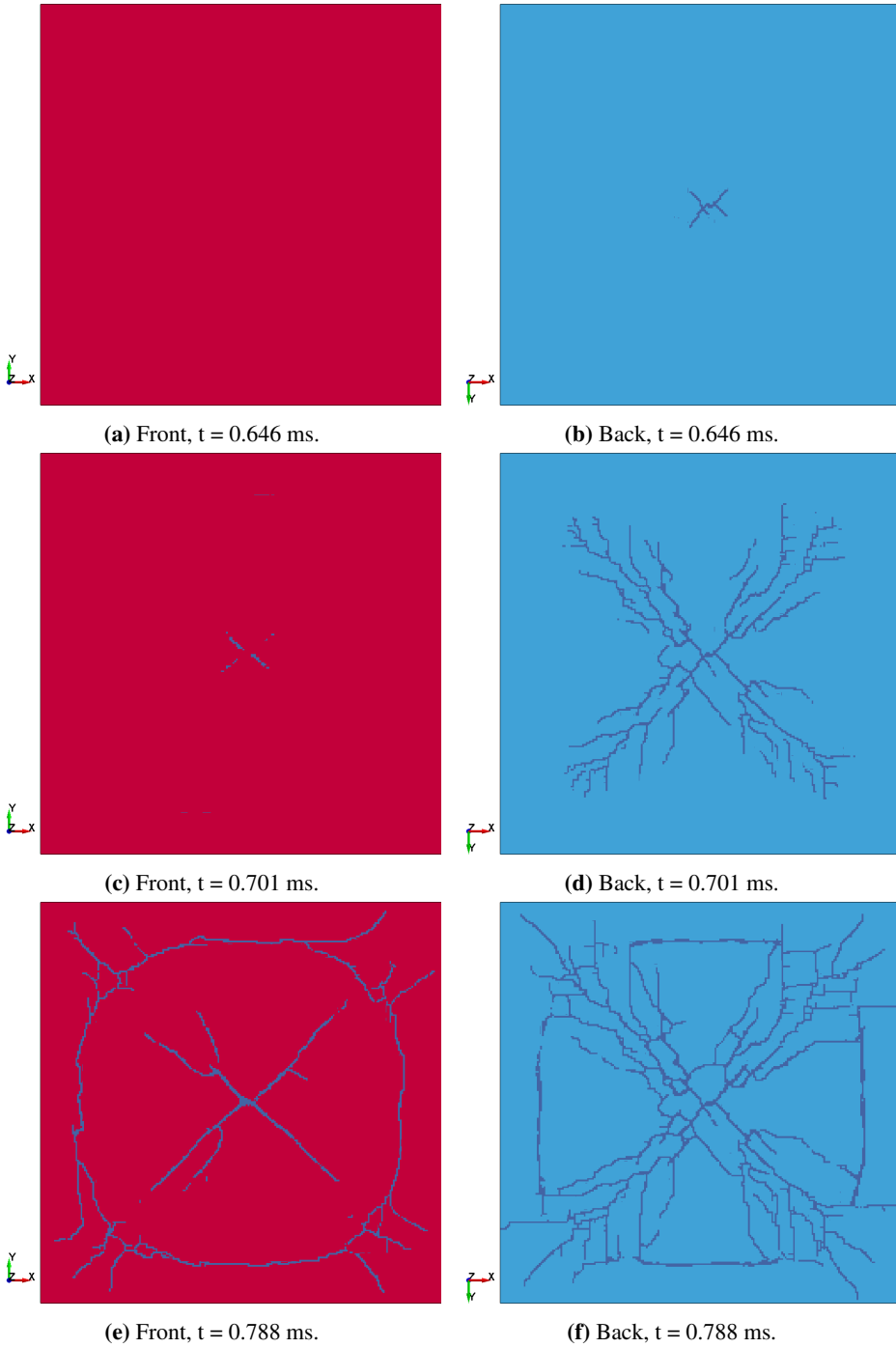


**Figure 7.34:** Fracture progress for the front and back glass layer.

### 7.2.4 Simulation vs Experiment

This section compares numerical results with the experiments. The laminated glass model utilising the SBMM yielded quantitatively the most similar results to the experiments, and therefore these are the simulations that were used in this comparison. Figure 7.35 shows the comparison between the post-fracture pattern of experiment LG-9.6-03 where only the back glass pane failed and a simulation utilising SBMM. There are clear similarities between the two failure patterns. The crack pattern that initiates at the centre of the pane and propagates radially towards the corners is similar in both cases. The initiation of circumferential crack propagation along the boundary and circumferential cracks closer to the centre of the pane is similar in both cases. It is emphasized that Figure 7.35a is the post-fracture pattern of the experiment, i.e. the picture was taken after the laminated glass pane was removed from the shock tube frame. Further, it is noted that both glass panes fractured in the simulation. However, Figure 7.35 gives a good comparison between the general failure of laminated glass subjected to blast loading.

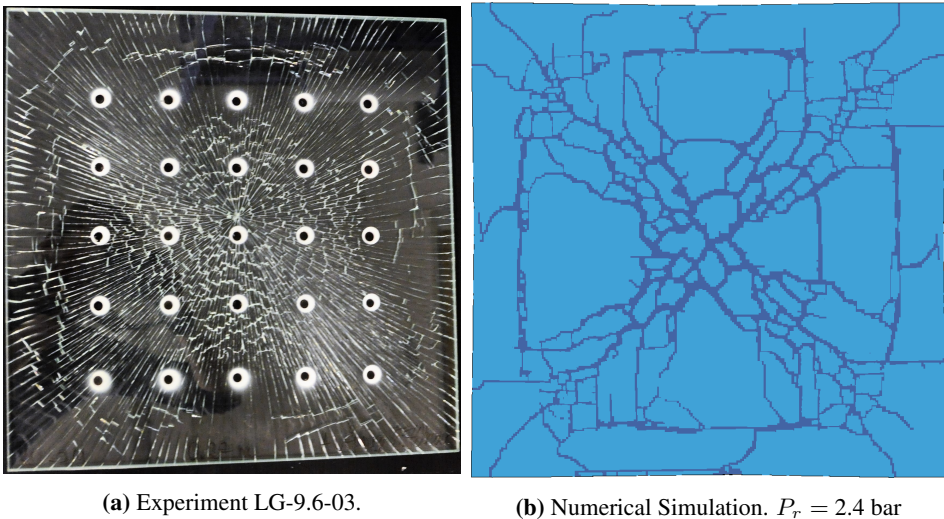
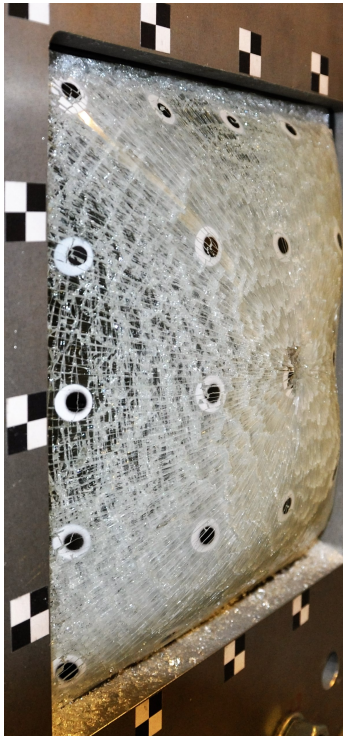
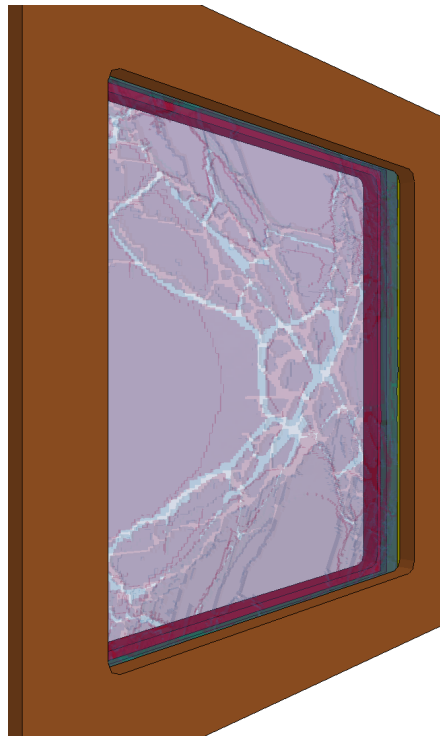


**Figure 7.35:** Comparison between the failure pattern of a sample experiment and a numerical simulation utilising the SBMM.

Figure 7.36 shows experiment LG-9.6-02 and a simulation utilising the SBMM. The picture of the experiment was taken after the experiment was conducted, showing the post-failure fracture pattern and deformation of the PVB-interlayer. The simulation was, due to computational cost, run for 3 ms and therefore not fully fractured. Similarities between experiment and simulation is seen, however a longer simulation time is needed in order to compare the post-failure fracture pattern. This was not done in the work of this thesis, as it was deemed unnecessary.



(a) Experiment LG-9.6-02.



(b) Numerical Simulation.  $P_r = 2.4$  bar.

**Figure 7.36:** Comparison between the failure pattern of a sample experiment and a numerical simulation utilising the SBMM.

### 7.2.5 Summary and Discussion

In the previous sections, several simulations have been conducted, modelling laminated glass subjected to blast loading. The sections address the response with and without failure. In the modelling without failure, three configurations were studied. PVB and glass modelled with solid elements, PVB modelled with solid elements and glass modelled with shell elements and the laminated glass modelled as a layered shell. In the modelling of failure, an introductory study was conducted to review the behaviour of the monolithic glass and PVB interaction. Further, simulations were run with different material models to identify possible advantages and disadvantages in the modelling of failure with the respective material models. The material models for glass that have been studied are; the elastic material model with simple erosion criterion, the SIMLab Metal Model, and the SIMLab Brittle Materials Model. The PVB interlayer was modelled using a linear elastic material model. It is emphasised that the energy balance was controlled in all models, in order to detect numerical instabilities, and no such instabilities were found.

#### Elastic response

The configuration with solid elements for all layers was found to be the most expensive way of modelling laminated glass. A mesh sensitivity study was conducted and the following was found.

1. Global stiffness increased for an increased amount of elements over the thickness in the glass layers.
2. Global stiffness decreased for an increased amount of elements over the thickness in the PVB layer.
3. Global stiffness increased for an increased amount of elements over the thickness in all layers.

The reason for these results is believed to be the contact between PVB and glass, whereby the transfer of shear stress between layers is not represented correctly. For an increasing number of elements, a drastic increase in computational time,  $t_{clock}$ , was found.

The combined configuration, or the shell–solid–shell configuration, is a potential cost-effective way of modelling laminated glass subjected to blast loading. However, the model was found to have a lower stiffness than what was expected and produced generally poor results compared to experiments. In order for this configuration to be truly cost-effective while providing good results, further work with it is needed.

The single layered shell configuration is a way to bypass the complex interaction between PVB and glass layers. An integration rule study was conducted analysing the effect of different integration point configurations. A stiffer response was found for an increased amount of integration points in the glass layers, while a less stiff response was found for an increased amount of integration points in the PVB layer.

When compared to the experimental results, the numerical simulations did not capture the elastic behaviour very well. The rubber sealant stiffness may control the global behaviour to some degree as seen in Section 7.1. It is however unlikely that the combined model used in this thesis will be able to describe the elastic behaviour of laminated glass panes subjected to blast loading. The combined model is therefore deemed inaccurate.

### **Failure response**

The introductory study on the modelling of failure in laminated glass panes subjected to blast loading was performed with the combined model and with a solid element model. Both models utilised the elastic material model with a simple erosion criterion. It was observed that the mass erosion for the combined and solid element model was approximately 38% and 25%, respectively. The combined model exhibited some problems with negative volume in the PVB elements, yet unresolved. The solid element model managed to give a decent description of the failure pattern and was able to describe the time interval in glass layer fracture along with the phenomenon of delamination. A more thorough study was therefore conducted with solid elements and other material models.

The elastic material model with a simple erosion criterion and refined mesh, yielded improved results compared to the introductory study. Debonding and fracture at different times for the glass layers were more pronounced in this model. A fraction of eroded mass of around 17% was observed.

The model with the SMM and refined mesh was able to represent the variation in capacity of laminated panes by distribution of material strength. The simulation was seen to fracture first in a weak region of the pane, where crack propagation avoided stronger regions. The model exhibited good erosion characteristics compared to the other simulations, as only 11% of the mass was removed for this model.

The model with the SBMM and a refined mesh was able to describe the failure behaviour found experimentally in a fairly good manner. The SBMM recreated a physically probable failure pattern that propagated randomly from the centre of the pane and out towards the corners, before circumferential crack propagation initiated at the boundary, similar to the experiments, see Section 5. The failure pattern in both glass layers individually gave a good representation of what was seen in the experiments. The model was also able to give a good representation of the adhesion and delamination effects between glass and the PVB interlayer in the laminated glass pane.

When compared qualitatively to the experiments it was found that the SBMM yielded the best results. However, it should be noted that the SMM better managed to represent the variation in strength of individual laminated glass panes.



## Concluding Remarks

In the work of this thesis, an experimental programme and numerical modelling have been done in order to gain an understanding of the behaviour of monolithic and laminated glass subjected to blast loading. The main experiences and knowledge gained are presented and discussed in this chapter.

### **Bending tests**

- In the four point bending tests, material properties including stiffness and failure strength for monolithic glass were found. The stochastic distribution of failure strength was calibrated to a two-parameter Weibull distribution.
- In the three point bending tests, the influence of boundary conditions on blast experiments was investigated. It was found that force–displacement relationship was independent of the fastening torque. However, it was observed that for higher fastening torque, the specimens failed closer to the support. The difficulties in predicting boundary conditions were highlighted by these tests.

### **Blast tests**

- In the tests on monolithic glass panes, it was found that the panes either stayed intact with no signs of damage, or that the panes showed total failure and fragmentation.
- Test results indicated a capacity of between 0.97 and 0.98 bar peak reflected pressure, for the glass panes tested.
- When failure of monolithic glass panes occurred, a large number of glass fragments were projected at a high speed. This illustrates the potential damage to the surroundings when failure in blast loaded monolithic glass windows occurs.
- In the tests on laminated glass panes, it was found that when failure of the glass panes occurred, it did so in three distinct modes. One of the glass panes failed, with the other glass pane and the PVB-interlayer staying intact. Both glass panes

failed, with the PVB-interlayer staying intact. Or both glass panes failed, and the PVB-interlayer ruptured.

- Test results indicated a capacity of between 2.37 and 2.42 bar peak reflected pressure, for the panes tested.
- The advantage of laminated glass panes compared to monolithic glass panes in protection against blast loading was observed. The PVB-interlayer retained glass fragments from projecting from the glass pane as failure occurred, greatly reducing the potential damage.

#### **Numerical modelling: Four point bending**

- A good representation of elastic material behaviour in four point bending was found for all material models used.
- The elastic material with a stress based failure criterion was able to represent material failure within the range observed experimentally, although excessive element erosion was observed, especially with the use of shell elements. No stochastic distribution of failure strength was possible with this material model.
- The Johnson–Holmquist 2 material model was not well suited for use in the quasi-static model, and failure was at the higher end of the experimental range.
- The SIMLab Metal Model with stochastic distribution of failure criteria was able to describe a variation in material strength, within the range found experimentally. An exact distribution in material strength compared to experimental results was not found.
- The SIMLab Brittle Materials Model was able to capture failure within the range found experimentally.

#### **Numerical modelling: Blast**

- The simulations were able to give a good representation of the non-failing monolithic glass experiments for both shell and solid elements.
- The 8 noded fully integrated element formulation managed to give a good description of the monolithic glass panes even for a single element over the thickness.
- A deviation between the experiment and simulation was seen for the non-failing monolithic panes after maximum deflection. This is believed to be related to the uncertainties regarding the boundary conditions of the glass pane.
- A strong influence of the rubber sealant's stiffness on the global response was observed for all numerical blast simulations.
- All of the material models managed to recreate probable failure patterns in the fracturing monolithic glass panes. However, excessive element erosion was observed for the elastic material with a stress based failure criterion and for the JH-2 material model, especially for larger blast loads.

- 
- For monolithic glass, by utilising the uncoupled approach in the distribution of the failure parameter, the SMM managed to determine the failure pattern by generating larger areas of damage in the pane. This approach gave a good representation of different capacities for individual glass panes.
  - The SBMM was able to create a good qualitative representation of the failure history seen in the experiments with monolithic glass.
  - It is noted that for all simulations with monolithic glass, the capacity of the glass panes was underestimated compared to experimental results.
  - For non-failing laminated glass, the simulations were observed to capture the elastic response poorly. This is believed to be caused by the uncertainties related to the boundary conditions of the laminated glass pane, and the contact description between PVB and glass layers.
  - The mesh sensitivity study showed that the laminated glass model was dependent on the number of elements through the thickness, even when the 8 noded fully integrated element was used.
  - The qualitative failure patterns found in simulations were seen to yield good results for all material models utilising solid elements.
  - By using the uncoupled approach together with the SMM the least amount of elements were eroded. It was observed that the brittle fracture with the SBMM produced the failure patterns most similar to the experiments.

This thesis has emphasised that glass is stochastic in nature and thus prediction of its material behaviour is complicated using simple methods. However, simplified approaches may provide good results that can be utilised in the design of blast loaded structures.



## Further work

Blast loading on window glass has proven to be a complex problem. This chapter presents the challenges that the authors believe should be subject for further research in order to improve both understanding of the phenomenon of blast loading on glass and numerical modelling of this problem.

### Experimental work

- Further studies should be performed in order to understand the effect of boundary conditions in shock tube tests on window panes. Special attention should be given to the material properties of the rubber sealant used. The authors believe that removing the rubber seal in shock tube tests may reduce the complexity of the problem.
- The DIC-software's point-tracking tool should be further developed, as the authors have struggled with its lack of development considering this feature.
- Studies on the behaviour and influence of the PVB-interlayer should be conducted in order to better describe the behaviour of laminated glass subjected to blast loading. The development of a thoroughly calibrated material model is essential in order to describe the long term behaviour of laminated glass subjected to blast loading.
- Quasi-static experiments on full-sized window panes clamped in the shock tube frame, may provide additional insight to the behaviour and influence of boundary conditions.
- The conversion of weibull parameters from uniaxial tension (4PB) to biaxial tension (blast loading) should be studied in further detail. A possible approach is given in [56].

### **Numerical work**

- The SIMLab Brittle Materials Model should be further investigated for a better qualitative description of the capacity, of monolithic and laminated glass panes subjected to blast loading.
- In order to better describe the complex boundary conditions, a numerical model consisting of the entire clamping frame and fastening bolts should be considered.
- A thorough numerical study should be conducted on the brittle fracture of glass utilising the node splitting failure algorithm, and comparing the results to the blast tests in this thesis.
- Numerical studies modelling the fluid-structure interactions in the blast tests should be conducted.

# Bibliography

- [1] NOU 2012: Rapport fra 22. Juli kommmisjonen. Report from terror attacks 22 July 2011 in norway.
- [2] V. Aune, T. Børvik, and M. Langseth. Lecture Notes in TKT4128, Impact Mechanics: An Introduction to Blast Mechanics. *Structural Impact Laboratory (SIMLab), Department of Structural Engineering, NTNU*, 2015.
- [3] V. Aune, E. Fagerholt, M. Langseth, and T. Børvik. A Shock Tube Facility to Generate Blast Loading on Structures. *International Journal of Protective Structures*, Special Issue on Blast Load Characterisation, 2016.
- [4] V. Aune. Fluid-Structure Interaction in Compressible flow. *DIXIL Report, SIMLab NTNU*, 2015.
- [5] T.L. Anderson. *Fracture Mechanics, Fundamentals and Applications*, volume 3. Tylor and Francis, 2005.
- [6] J.B. Wachtman, W. R Cannon, and Matthewson M.J. *Mechanical Properties of Ceramics*, volume 2. Wiley, 2009.
- [7] Ashby M.F. and D.R.H. Jones. *Engineering Materials I: An introduction to Properties, Applications and Design*, volume 4. Elsevier.
- [8] C.E. Inglis. Stresses in a Plate Due to the Presence of Cracks and Sharp Corners. *Transactions of the Institute of Naval Architects*, 55:219–241, 1913.
- [9] A.A. Griffith. The Phenomena of Rupture and Flow in Solids. *Philisophical Transactions of the Royal Society of London*, 221:163–198, 1921.
- [10] G.R. Irwin. Onset of Fast Fracture Propagation in High Strength Steel and Aluminum Alloys. *Sagamore Research Conference Proceedings*, 2:289–305, 1956.
- [11] H.M. Westergaard. Bearing Pressures and Cracks. *Journal of Applied Mechanics*, 6:49–53, 1939.

- 
- [12] ASTM International. *ASTM C1421: Standard Test Methods for Determination of Fracture Toughness of Advanced Ceramics at Ambient Temperature*, 2016.
- [13] M. Bengisu. *Engineering Ceramics*. Springer Science and Business Media, 2013.
- [14] W. Weibull. A Statistical Theory of the Strength of Materials. *Ingenjörsvetenskapsakademiens handlingar*, 151:1–45, 1939.
- [15] R. Walpole, R. Myers, S. Myers, and K. Ye. *Probability and Statistics for Engineers and Scientists*, volume 9. Pearson Education, 2012.
- [16] J.M. Gere. *Mechanics of Materials*, volume 6. Thomson Learning.
- [17] J. Menčík. Strength and Fracture of Glass and Ceramics. *Glass Science and Technology*, 12, 1992.
- [18] W.D. Callister and D.G. Rethwisch. *Materials Science and Engineering*, volume 8. Wiley, 2011.
- [19] C.R. Kurkjian. Mechanical Stability of Oxide Glasses. *Journal of Non-Crystalline Solids*, 102(1):71–81, 1988.
- [20] M. Larcher. Simulation of Several Glass Types Loaded by Air Blast Waves. *European Commission, Joint Research Centre, Institute for the Protection and Security of the Citizen*, 2008.
- [21] X. Zhang, Y. Zou, H. Hao, X. Li, G. Ma, and K. Liu. Laboratory Test on Dynamic Material Properties of Annealed Float Glass. *International Journal of Protective Structures*, 3(4):407–430, 2012.
- [22] F.A. Veer and Yu. M. Rodichev. The Structural Strength of Glass: Hidden Damage. *Strength of Materials*, 43(3):302–315, 2011.
- [23] C. Morison. *The Resistance of Laminated Glass to Blast Pressure Loading and the Coefficients for Single Degree of Freedom Analysis of Laminated Glass*. PhD Thesis, Cranfield University, Defence College of Management and Technology, 2007.
- [24] X. Zhang, H. Hong, and M. Guowei. Parametric study of laminated glass window response to blast loads. *Engineering Structures*, 56:1707–1717, 2013.
- [25] M. Larcher, M. Teich, N. Gebbeken, G. Solomos, F. Casadei, G. A. Falcon, and S. L. Sarmiento. Simulation of Laminated Glass Loaded by Air Blast Waves. In *Applied Mechanics and Materials*, volume 82, pages 69–74. Trans Tech Publications Inc., 2011.
- [26] M. Larcher, G. Solomos, F. Casadei, and N. Gebbeken. Experimental and Numerical Investigations of Laminated Glass Subjected to Blast Loading. *International Journal of Impact Engineering*, 39(1):42–50, 2012.
- [27] J. O. Hallquist. *LS-DYNA - Keyword User's Manual, version R8.0*. Livermore Software Technology Corporation, 2015.
-



- 
- [28] G.R. Johnson and T.J. Holmquist. An improved computational constitutive model for brittle materials. In *High-pressure science and technology*, volume 309, pages 981–984. AIP Publishing, 1994.
- [29] D.S. Cronin, K. Bui, C. Kaufmann, G. McIntosh, T. Berstad, and D. Cronin. Implementation and Validation of the Johnson–Holmquist Ceramic Material Model in LS-DYNA. In *Proc. 4th Eur. LS-DYNA Users Conf*, volume 1, pages 47–60, 2003.
- [30] H.D. Hidallana-Gamage, Thambiratnam D.P., and Perera N.J. Computational Analysis of Laminated Glass Panels Under Blast Loads: A Comparison of Two Dimensional and Three Dimensional Modelling Approaches. *The International Journal of Engineering and Science*, 2:69–79, 2013.
- [31] Structural Impact Laboray (SIMLab), NTNU. *SIMLab Metal Model (SMM), Theory, user’s and example manual*, 2015.
- [32] Structural Impact Laboratory (SIMLab), NTNU. *SIMLab Brittle Materials Model (SBMM), Theory and user’s manual*, 2016.
- [33] R.O. Ritchie, J.F. Knott, and J.R. Rice. On the Relationship Between Critical Tensile Stress and Fracture Toughness in Mild Steel. *J. Mech. Phys. Solids*, 21(6):395–410, 1973.
- [34] J.H. Song, H. Wang, and T. Belytschko. A Comparative Study on Finite Element Methods for Dynamic Fracture. *Comput. Mech.*, 42:239–250, 2008.
- [35] O. Knoll. *A Probabilistic Approach in Failure Modelling of Aluminium High Pressure Die-Castings*. PhD thesis, Department of Structural Engineering, NTNU.
- [36] M. Nawar, H. Salim, B. Lusk, and S. Kiger. Modelling and Shock Tube Testing of Architectural Glazing Systems for Blast Resistance. *Journal of Structural Engineering*, 141(7):04014174: 1–9, 2014.
- [37] D.Z. Sun, F. Andrieux, A. Ockewitz, H. Klamser, and J. Hogenmüller. Modelling of the Failure Behaviour of Windscreens and Component Tests. In *5th European LS-DYNA Users Conference*, volume 25, page 26, 2005.
- [38] J. Wei and L.R. Dharani. Dynamic Response of Laminated Glass Under Blast Loading: Effect of Negative Phase. *Structures under Shock and Impact*, 8, 2004.
- [39] J. Wei and L.R. Dharani. Fracture Mechanics of Laminated Glass Subjected to Blast Loading. *Theoretical and Applied Fracture Mechanics*, 44(2):157–167, 2005.
- [40] J. Wei and L.R. Dharani. Response of Laminated Architectural Glazing Subjected to Blast Loading. *International Journal of Impact Engineering*, 32(12):2032–2047, 2006.
- [41] C.D. Wu, X.Q. Yan, and L.M. Shen. A Numerical Study on Dynamic Failure of Nanomaterial Enhanced Laminated Glass Under Impact. In *IOP Conference Series: Materials Science and Engineering*, volume 10, page 012176. IOP Publishing, 2010.
-

- 
- [42] H.D. Hidallana-Gamage, D.P. Thambiratnam, and N.J. Perera. Numerical Modelling and Analysis of the Blast Performance of Laminated Glass Panels and the Influence of Material Parameters. *Engineering Failure Analysis*, 45:65–84, 2014.
- [43] H.D. Hidallana-Gamage, D.P. Thambiratnam, and N.J. Perera. Failure Analysis of Laminated Glass Panels Subjected to Blast Loads. *Engineering Failure Analysis*, 36:14–29, 2014.
- [44] H.D. Hidallana-Gamage, D.P. Thambiratnam, and N.J. Perera. Influence of Interlayer Properties on the Blast Performance of Laminated Glass Panels. *Construction and Building Materials*, 98:502–518, 2015.
- [45] L. Olovsson, J. Limido, J.-L. Lacombe, A. Grønsund Hanssen, and J. Petit. Modeling Fragmentation With New High Order Finite Element Technology and Node Splitting. In *European Physical Journal Web of Conferences*, volume 94 of *European Physical Journal Web of Conferences*, 2015.
- [46] M. Larcher and G. Solomos. Laminated Glass Loaded by Air Blast Waves - Experiments and Numerical Simulations. *European Commission, Joint Research Centre, Institute for the Protection and Security of the Citizen*, 2010.
- [47] M. Froli and L. Lani. Adhesion and Viscoelasticity Properties of PVB in Laminated Safety Glass. In *International Symposium on the Application of Architectural Glass 2010*, pages 75–81, 2010.
- [48] M. Froli and L. Lani. Adhesion, Creep and Relaxation Properties of PVB in Laminated Safety Glass. *Glass performance days, Tampere (Finland)*, 2011.
- [49] ASTM International. *ASTM C1161: Standard Test Method for Flexural Strength of Advanced Ceramics at Ambient Temperatures*, 2013.
- [50] ASTM International. *C1239: Standard Practice for Reporting Uniaxial Strength Data and Estimating Weibull Distribution Parameters for Advance Ceramics*, 2013.
- [51] Mathworks Inc. Matlab: R2014a. <http://www.mathworks.com/products/matlab/>, 2014.
- [52] European Committee for Standardization CEN. NS-EN 13541: Glass in building – Security glazing – Testing and classification of resistance against explosion pressure. 2012.
- [53] X. Zhang, H. Hong, and M. Guowei. Dynamic material model of annealed soda–lime glass. *International Journal of Impact Engineering*, 77(1):108–119, 2015.
- [54] C.M. Roland. Mechanical Behavior of Rubber at High Strain Rates. *Rubber Chemistry and Technology*, 79(3):429–459, 2006.
- [55] T. Erhart. Review of Solid Element Formulations in LS-DYNA: Properties, Limits, Advantages and Disadvantages. In *2011 LS-DYNA Developers Forum*, 2011.
- [56] A. Franco and G. Royer-Carfagni. Critical issues in the design-by-testing of annealed glass components. *Engineering Structures*, 99:108–119, 2015.

# Appendix A

## Material tests specimen size

**Table A.1:** Geometrical dimensions of the 100x20 mm flexural test specimens, all measurements in mm. Width and height are averaged.

Specimen	Length	Width	Height	Specimen	Length	Width	Height
1	100.41	20.19	4.01	19	99.93	20.02	4.02
2	100.07	20.01	3.99	20	99.97	20.15	4.02
3	99.92	20.01	4.01	21	100.05	20.05	4.02
4	100.08	20.15	4.04	22	100.04	20.12	4.02
5	99.93	19.99	4.02	23	99.90	20.15	4.03
6	99.96	20.12	4.04	24	100.07	20.07	4.01
7	99.93	20.00	4.03	25	100.03	20.07	4.03
8	100.01	20.10	4.02	26	99.97	20.04	4.03
9	100.00	20.04	4.01	27	100.01	20.08	4.03
10	100.00	20.06	4.04	28	100.05	20.04	4.01
11	100.00	20.09	4.02	29	99.95	20.02	4.02
12	100.07	20.11	4.00	30	100.24	19.99	4.01
13	100.06	20.03	4.05	31	100.09	20.11	4.02
14	99.98	20.08	4.02	32	99.96	20.11	4.02
15	100.04	19.97	4.02	33	99.94	19.99	4.01
16	100.06	20.03	4.01	34	100.11	20.01	4.02
17	100.20	20.03	4.02	35	100.00	20.07	4.00
18	99.95	20.11	4.02				

**Table A.2:** Geometrical dimensions of the 200x40 mm flexural test specimens, all measurements in mm. Width and height are averaged.

Specimen	Length	Width	Height	Specimen	Length	Width	Height
1	199.99	39.98	4.01	18	200.05	40.03	4.00
2	199.95	40.01	4.00	19	199.97	40.07	4.00
3	199.95	40.08	4.05	20	200.00	40.04	4.01
4	199.93	40.03	4.04	21	199.98	39.95	3.99
5	200.08	40.07	4.02	22	199.97	39.89	4.00
6	200.04	40.04	4.02	23	199.99	39.98	4.01
7	199.93	39.99	4.01	24	199.97	40.02	4.00
8	199.90	40.11	4.02	25	199.97	40.02	3.99
9	200.00	40.08	4.02	26	199.95	40.08	3.98
10	199.95	39.95	4.02	27	199.92	40.03	3.98
11	199.93	40.00	4.02	28	199.93	40.14	4.00
12	200.12	39.98	4.03	29	200.02	40.18	3.99
13	199.90	40.13	4.00	30	199.95	40.15	4.02
14	200.01	40.07	4.01	31	199.95	40.11	4.03
15	199.93	40.01	4.02	32	200.04	40.04	3.98
16	199.97	40.05	4.03	33	200.00	40.04	3.99
17	199.91	40.05	4.00	34	199.97	40.04	4.03

**Table A.3:** Geometrical dimensions of the 300x60 mm flexural test specimens, all measurements in mm. Width and height are averaged.

Specimen	Length	Width	Height	Specimen	Length	Width	Height
1	300.12	60.13	3.95	18	300.00	60.04	3.96
2	300.09	60.05	3.97	19	299.94	60.09	3.95
3	300.02	60.00	3.96	20	300.03	60.03	3.94
4	299.97	60.04	3.97	21	300.04	60.09	3.93
5	300.06	60.05	3.96	22	300.12	60.20	3.93
6	299.92	60.12	3.96	23	299.95	60.08	3.94
7	300.06	60.11	3.94	24	300.09	60.01	3.93
8	300.04	60.13	3.95	25	300.07	59.98	3.94
9	300.06	60.16	3.94	26	300.06	59.98	3.95
10	299.96	60.10	3.95	27	300.13	60.02	3.94
11	300.09	59.98	3.94	28	300.12	60.12	3.93
12	300.07	60.08	3.95	29	300.13	60.14	3.96
13	300.00	59.97	3.95	30	300.12	60.11	3.94
14	300.01	60.07	3.95	31	300.10	60.18	3.95
15	300.07	60.02	3.92	32	300.05	60.15	3.96
16	300.00	60.18	3.94	33	300.08	60.08	3.92
17	300.12	59.95	3.96	34	300.09	60.05	3.94

# Appendix **B**

## Bending test specimens post-failure

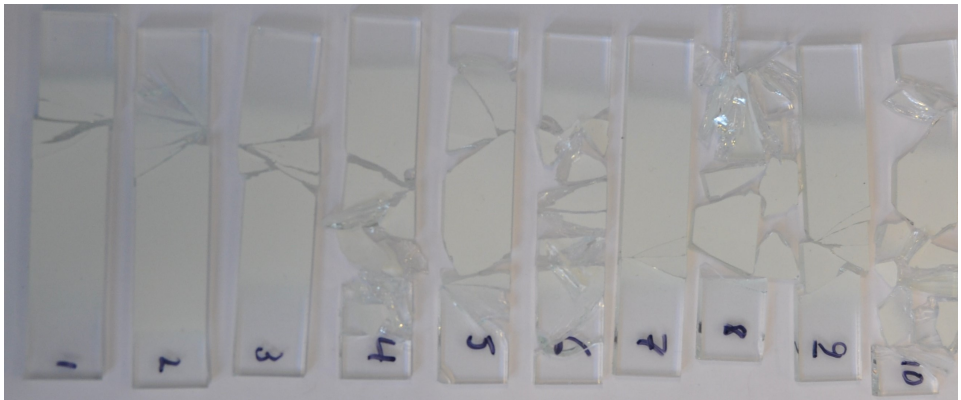


**Figure B.1:** Small test specimens 1 to 10.



**Figure B.2:** Small test specimens 11 to 30.

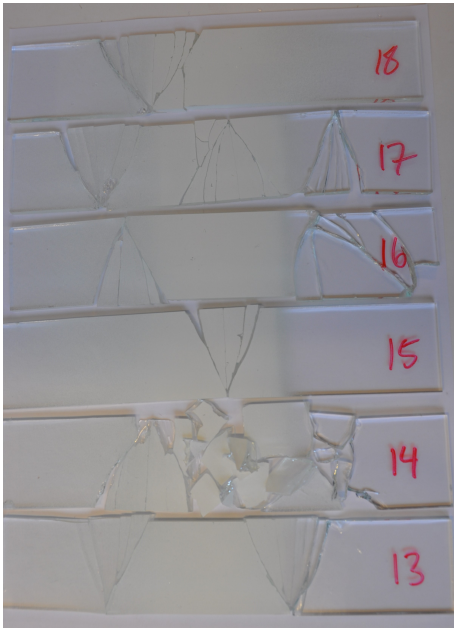
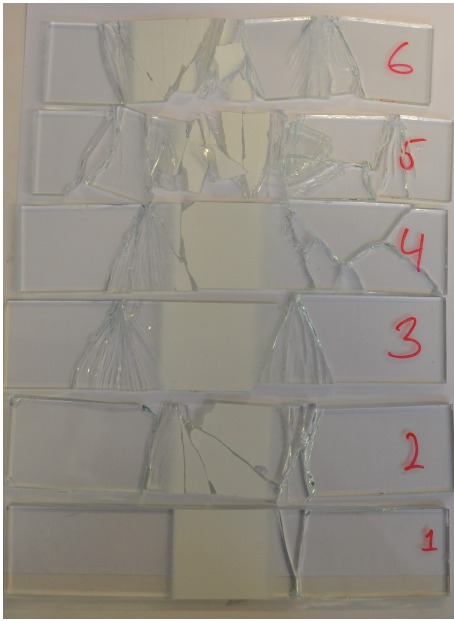


**Figure B.3:** Medium test specimens 1 to 24.

---

---



# Appendix C

## Weibull plots for medium and large specimens

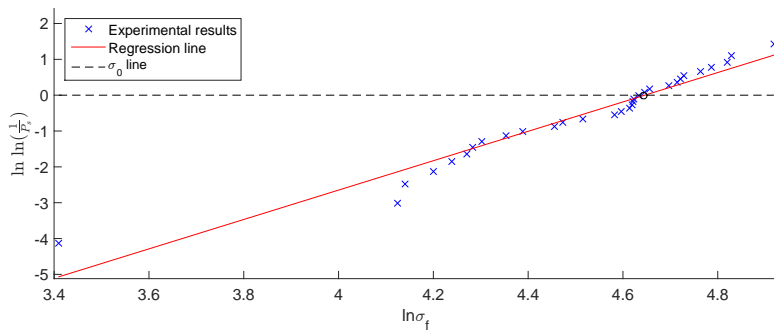


**Figure C.1:** Regression fit of Weibull parameters, medium samples.

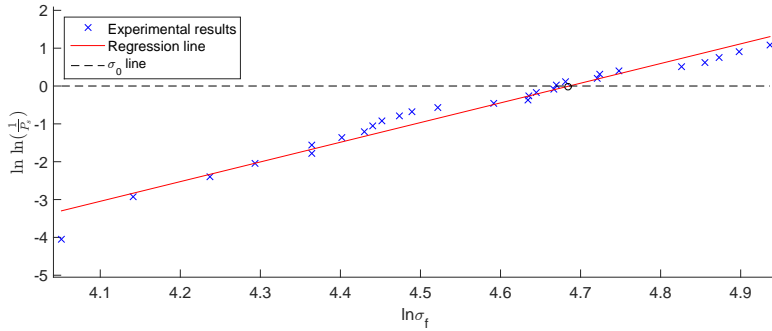
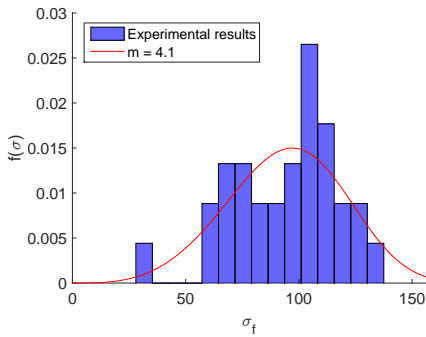
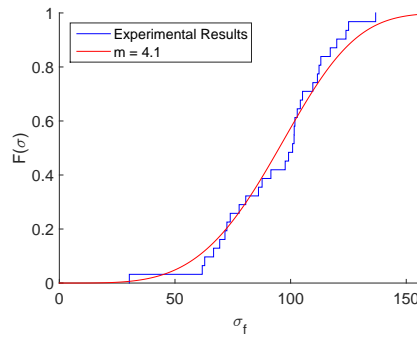


**Figure C.2:** Regression fit of Weibull parameters, large samples.

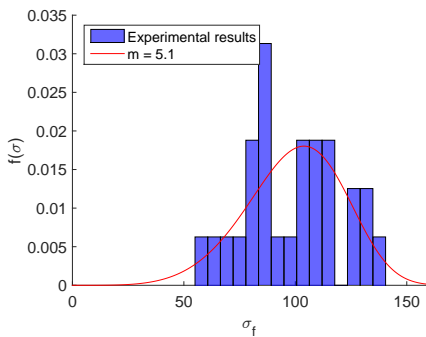


**(a)**

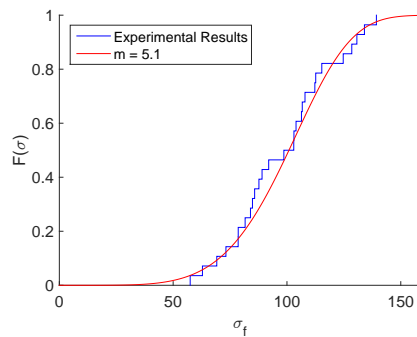


**(b)**

**Figure C.3:** (a) Probability density, and (b) cumulative probability density compared with experimental results, small samples.



**(a)**



**(b)**

**Figure C.4:** (a) Probability density, and (b) cumulative probability density compared with experimental results, small samples.

# Appendix D

## Component test overview

**Table D.1:** Overview of all three point bending tests.

Test number	Support type	Tightening moment	Comments
1	Rubber	5 Nm	
2	Rubber	5 Nm	
3	Rubber	5 Nm	Precracked, invalid
4	Rubber	5 Nm	
5	Rubber	10 Nm	
6	Rubber	10 Nm	
7	Rubber	10 Nm	
8	Rubber	10 Nm	With grease
9	Rubber	20 Nm	
10	Rubber	20 Nm	
11	Rubber	20 Nm	Precracked, invalid
12	Rubber	20 Nm	
13	Rubber	-	Loose top plate, with grease
14	Rubber	-	Without top plate, with grease
15	Teflon	10 Nm	
16	Teflon	10 Nm	
17	Teflon	10 Nm	
18	Aluminium	10 Nm	
19	Aluminium	10 Nm	
20	Aluminium	10 Nm	Precracked
21	Aluminium	-	Without top plate

**Table D.2:** Overview of all component tests.

Test <sup>1</sup>	Plate (#)	$P_a$ (bar)	$P_r$ (bar)	Failure	Comments
MG-5.7-01 <sup>2</sup>	1	5.7	$\approx 1.9$	✓	
MG-5.7-02	2	5.7	1.92	✓	
MG-5.7-03	3	5.7	1.88	✓	
MG-1.6-01	4	1.6	0.64	✗	
MG-2.1-01	4	2.1	0.78	✗	
MG-2.6-01	4	2.6	0.98	✗	
MG-3.6-01	4	3.6	1.25	✓	
MG-2.6-02	5	2.6	0.93	✗	
MG-2.6-03	6	2.6	0.97	✓	
MG-2.6-04	7	2.6	0.98	✓	
MG-3.6-02	8	3.6	1.16	✓	
MG-3.6-03	9	3.6	1.23	✓	
MG-3.6-04	10	3.6	1.56	✓	
MG-2.1-02	11	2.1	0.75	✗	
MG-2.1-03	12	2.1	0.74	✗	
LG-5.7-01	13	5.7	1.77	✗	
LG-6.7-01	13	6.7	1.89	✗	
LG-7.7-01	13	7.7	2.00	✗	
LG-8.5-01	13	8.5	2.33	✗	
LG-10.3-01	13	10.3	2.76	✓	Ruptured PVB
LG-9.6-01	14	9.6	2.37	✗	
LG-9.6-02	15	9.6	2.38	✓	
LG-9.6-03 <sup>3</sup>	16	8.8	-	✓	Failure in one glass pane
LG-9.6-04	17	9.6	2.37	✓	Failure in one glass pane
LG-8.6-01	18	8.6	2.32	✗	
LG-8.6-02	19	8.6	2.42	✗	
LG-10.3-02	20	10.3	2.68	✓	
LG-10.3-03	21	10.3	2.76	✓	

<sup>1</sup> MG – Monolithic glass, LG – Laminated glass

<sup>2</sup> No output data. The driver pressure was however noted, and is found comparable to the rest of the test series MG-5.7

<sup>3</sup> Membrane ruptured too early creating a lower pressure than desired, and no output data. The driver pressure was however noted, and is found comparable to test series LG-8.6

# Appendix E

## LS-DYNA Keywords

usermat\_smm.k

```

*KEYWORD
$$$$$$$$$$$$$$$$$$$$$$$$$$$$$$$$$$$$$$$$ SMM MATERIAL CARD $$$$$$$$$$$$$$$$$$$$$$$$$$$$$$$$$$$$$$$$$
*MAT_USER_DEFINED_MATERIAL_MODELS
$#      MID      RO      MT      LMC      NHV      IORTHO      IBULK      IG
      1 2.5000E-9      41      24      60      0      1      2
$#  IVECT  IFAIL  IHTERM  IHYPER  IEOS      LCMA
      1      1      0      0      0      0
$#  BULK  SHEAR  EFLAG  YFLAG  RMAPFLAG  HFLAG  VFLAG  TFLAG
42.85e+03 29.51e+03      1      1      2      0      0      0
$#  DFLAG  SFLAG  STFLAG  E      PR  SIGMA0  KSI  SIGMAC
      3      2      003 72.00e+03 0.220000      1e9      0.1      113.00
$#  DELTAC  nfip  xminsc  xmaxsc  mwsc  muwsc  v0sc
      1E-5      1      57.5      157.7      4.130      0.300      18.00e3      0
$$$$$$$$$$$$$$$$$$$$$$$$$$$$$$$$$$$$$$$$ Define $$$$$$$$$$$$$$$$$$$$$$$$$$$$$$$$$$$$$$$$$
*DEFINE_COORDINATE_VECTOR
$#      cid      xx      yx      zx      xv      yv      zv      nid
      1 1.000000      0.000      0.000      0.000      1.000000      0.000      0

```

```
*KEYWORD
$$$$$$$$$$$$$$$$$$$$$$$$$$$$$$$$$$$$$$$$ SBMM MATERIAL CARD $$$$$$$$$$$$$$$$$$$$$$$$$$$$$$$$$$$$$$$$$
*MAT_USER_DEFINED_MATERIAL_MODELS
$#      mid      ro      mt      lmc      nhv      iortho      ibulk      ig
      4 2.5000E-9      42      24      25      0      23      24
$#  ivect      ifail      itherm      ihyper      ieos      lmca      unused      unused
      1      1      0      1      0      0
$      E11      E22      E33      V12      V23      V31      G12      G23
      72000.0      72000.0      72000.0      0.22      0.22      0.22 29508.197 29508.197
$      G31      af      k0      E0      Gf      Dc      Nfipt      k0_min
29508.197      2.0 0.001157 72000.0      0.01      0.99      1.0 5.000E-4
$      k0_max      mw      uw      V0      delta_Gf      p6      p7      p8
      0.0015      4.13      0.0      200.0      0.01      0.0 42857.143 29508.197
```

---

```
$$$$$$$$$$$$$$$$$$$$ Layered Laminated Glass $$$$$$$$$$$$$$$$$$
*MAT_LAMINATED_GLASS_TITLE
Layered_LG
$#      mid      ro      eg      prg      syg      etg      efg      ep
      8  2.300E-9  72000.0  0.22  200.0  1.0  0.001  220.0
$#      prp      syp      etp
      0.4      11.0      9.0
$#      f1      f2      f3      f4      f5      f6      f7      f8
      0.0      0.0      0.0      0.0      0.0      0.0      0.0      0.0
$#      f1      f2      f3      f4      f5      f6      f7      f8
      0.0      0.0      1.0      1.0      1.0      1.0      0.0      0.0
*INTEGRATION_SHELL
$#      irid      nip      esop      failopt
      4      14      0      1
$#      s      wf      pid
      1.0  0.084034      2
      -1.0  0.084034      2
      0.816514  0.084034      2
      -0.816514  0.084034      2
      0.633027  0.084034      2
      -0.633027  0.084034      2
      0.449541  0.084034      2
      -0.449541  0.084034      2
      0.266055  0.084034      2
      -0.266055  0.084034      2
      0.133028  0.039916      2
      -0.133028  0.039916      2
      0.043578  0.039916      2
      -0.043578  0.039916      2
```

---







